Doctoral theses at NTNU, 2021:218

Augusto Matheus dos Santos Alonso

Multi-Purpose Coordinated Control of Distributed Energy Resources in Transactive AC Microgrids

Doctoral thesis

NTNU
Norwegian University of Science and Technology
Thesis for the Degree of
Philosophiae Doctor
Faculty of Information Technology and Electrical
Engineering
Department of Electric Power Engineering

NTNU
Norwegian University of
Science and Technology

Augusto Matheus dos Santos Alonso

Multi-Purpose Coordinated Control of Distributed Energy Resources in Transactive AC Microgrids

Thesis for the Degree of Philosophiae Doctor

Trondheim, September 2021

Norwegian University of Science and Technology
Faculty of Information Technology and Electrical Engineering
Department of Electric Power Engineering

NTNU
Norwegian University of
Science and Technology

NTNU
Norwegian University of Science and Technology

Thesis for the Degree of Philosophiae Doctor

Faculty of Information Technology and Electrical Engineering
Department of Electric Power Engineering

ISBN 978-82-326-6603-4 (printed ver.)
ISBN 978-82-326-5663-9 (electronic ver.)
ISSN 1503-8181 (printed ver.)
ISSN 2703-8084 (online ver.)

Doctoral theses at NTNU, 2021:218

Printed by NTNU Grafisk senter

I dedicate this PhD thesis to my parents, Dirce and Mauro, for their endless support, which has allowed me to pursue my dreams so far in life.

Eu dedico esta tese de doutorado aos meus pais, Dirce e Mauro, por seu suporte infindável, o qual me possibilitou ir em busca de meus sonhos até aqui.

Abstract

Pervasive penetration of distributed energy resources (DERs), usually constituted by renewable energy sources and/or storage systems along with their interfacing inverters, are pushing AC electrical grids toward a power electronics-based paradigm. Although the presence of DERs in power grids brings more flexibility of operation and the decentralization of energy generation allows us to obtain more efficient power dispatch, it is imperative to achieve proper control over the existing inverters to support the synergistic integration of multiple electric apparatuses. This is particularly true from the perspective of inverter-dominated AC microgrids (MGs), which rely on the implementation of coordination strategies to adequately exploit DERs to support controlled power dispatchability, power quality interventions, as well as accessibility to energy markets.

Within such a context, this thesis presents a coordinated control strategy capable of supporting multiple operation modes for transactive AC MGs through a model-free, plug-and-play and topology-independent steering of inverters. Such a control approach, namely Generalized Current-Based Control (GCBC), is capable of accommodating inverters of assorted operational natures, being of a dispatchable (d-DER) or non-dispatchable (nd-DER) nature, relying on a centralized unit and on low-bandwidth communication links. By flexibly coordinating DERs, the strategy supports the implementation of active current sharing among inverters, also endowing compensation of reactive currents, as well as offering distributed and selective harmonic mitigation. In addition, the control approach is capable of coping with intermittent energy generation profiles, which are typical of nd-DERs. As another feature, the proposed coordination strategy provides proportional current sharing without being affected by line impedance parameters, in contrast to the conventional droop control method. Above all, the GCBC strategy is capable of managing an interconnected MG to operate as a single controllable entity, providing full controllability over its power dispatch to an upstream grid, allowing it to trade energy services in transactive energy markets.

The merits of the GCBC strategy are thoroughly assessed throughout this thesis by means of simulation and experimental results, based on multiple MG prototypes focusing on the low-voltage (LV) perspective, ensuring that the method is feasible for implementation in real-life applications. Numerous MG scenarios are evaluated, such as under limited power capabilities, considering the presence of non-ideal voltage waveforms, as well as upon communication issues, ensuring that the GCBC approach endures operation under adverse conditions. Moreover, it is experimentally demonstrated that the method is also capable of improving voltage quality in weak LV MGs

of homogeneous features, as an indirect outcome of the proportional sharing of non-active currents.

Lastly, advanced control functionalities are devised by flexibly adapting the GCBC strategy, endowing LV MGs with the capacity to shape their operation to behave as a variable and selective resistor, which supports a more efficient operation of the distribution grid and favors the damping of harmonic resonances. As another advanced functionality, distributed compensation of active and reactive unbalanced currents is also possible, based on concepts from the Conservative Power Theory. Moreover, voltage regulation can be ensured for the MG by means of an automatic scheme incorporating the GCBC, allowing the possibility to concomitantly increase energy exploitation from nd-DERs. Finally, considerations on the integration of optimization methods highlight that further capabilities can be formulated upon the adoption of the GCBC strategy.

Sammendrag

En omfattende integrasjon av distribuerte energikilder (DERer), som består av fornybare energisystemer med tilhørende omformere, representerer et paradigmeskifte for AC strømnett i form av økt bruk av kraftelektronikk. Selv om bruken av DERer i lavspenningsnettet muliggjør en mer fleksibel drift av nettet, og desentralisering av energikildene tillater en økt effektivitet, er det helt avgjørende å ha tilstrekkelig kontroll over eksisterende omformere for å utnytte potensialet i dem. Dette gjelder særlig for omformerdominerte mikronett, som er avhengige implementering av koordinerte strategier for å utnytte DERer til kontrollert kraftregulering, forbedring av spenningskvalitet, samt tilgjengelighet til elektrisitetsmarkedet.

Denne avhandlingen presenterer en koordinert reguleringsstrategi for mikronett. Strategien kan levere flere systemtjenester, og reguleringen legger til rette for plug-and-play av omformere, uavhengig av topologien til nettet. Denne strategien, kalt Generalized Current-Based Control (GCBC), kan integrere omformere basert på både regulerbare (d-DER) og ikke-regulerbare (nd-DER) energikilder. Strategien er avhengig av en sentralisert kontrollenhet samt et kommunikasjonssystem med lav båndbredde. Ved hjelp av fleksibel koordinering av DERer støtter strategien deling av aktive strømmer mellom omformere, kompensasjon av reaktive strømmer, samt tilbyr distribuert og selektiv harmonisk demping. I tillegg kan strategien håndtere intermitterende energiproduksjonsprofiler, som er typiske for nd-DERer. I motsetning til den konvensjonelle statikk-metoden er den foreslåtte strategien også i stand til å gi proporsjonal strømdeling uten å være påvirket av linjeimpedansparametere. Fremfor alt er GCBC-strategien i stand til å styre et sammenkoblet mikronett for å fungere som én enkelt kontrollerbar enhet, samt å ha full kontrollerbarhet over kraftutvekslingen med et overliggende nett, slik at mikronettet kan handle energitjenester i bilaterale energimarkeder.

Aspektene ved GCBC-strategien blir grundig gjennomgått i denne avhandlingen ved hjelp av simulering og eksperimentelle resultater, basert på flere lavspente (LV) mikronett-prototyper, for å sikre at metoden er mulig å implementere i ekte applikasjoner. Flere mikronett-scenarier blir evaluert, for eksempel ved begrenset effekt, under ikke-ideelle spenningsforhold, samt ved kommunikasjonsproblemer. Dette sikrer at GCBC-strategien fungerer også under ugunstige forhold. Videre er det eksperimentelt demonstrert at metoden er i stand til å forbedre spenningskvaliteten i svake LV mikronett, noe som er et indirekte resultat av proporsjonal deling av ikke-aktive strømmer.

Til slutt utvikles avanserte kontrollfunksjoner ved fleksibel tilpasning av GCBC-strategien, hvilket gir LV mikronett muligheten til å oppføre seg som en variabel og selektiv motstand, som støtter en mer effektiv drift av distribusjonsnettet og bidrar til

demping av harmoniske resonanser. En annen avansert funksjonalitet er distribuert kompensasjon av aktive og reaktive ubalanserte strømmer, basert på konsepter fra «Conservative Power Theory». Videre kan spenningsregulering utformes for mikronettet ved hjelp av en strategi som inkluderer GCBC, slik at man samtidig kan øke energiutnyttelsen fra nd-DERer. Betraktninger rundt integrering av optimaliseringsmetoder fremhever at ytterligere funksjonalitet fortsatt kan legges til ved bruk av GCBC-strategien.

Resumo

A contínua expansão do uso de recursos energéticos distribuídos (REDs), normalmente constituídos de fontes de energia renovável e/ou sistemas de armazenamento com seus respectivos inversores de potência, tem incorporado a eletrônica em potência como panorama para redes elétricas CA. Embora a presença de REDs em tais redes traga maior flexibilidade de operação e a descentralização da geração de energia possibilite despacho de potência mais eficiente, é essencial que se imponha um controle adequado sob inversores para garantir uma operação harmoniosa com os múltiplos dispositivos elétricos existentes. Tal requerimento é de particular importância em microrredes CA com alta imersão de inversores, as quais requerem a implementação de estratégias de controle coordenado para adequadamente explorar REDs, visando obter controlabilidade perante despacho de potência, intervenções para melhoria da qualidade da energia, e também acessibilidade a mercados de energia.

Dentro de tal contexto, esta tese de doutorado apresenta uma estratégia de controle coordenado capaz de prover múltiplos propósitos operacionais para microrredes CA com características transativas. Tal abordagem rege a operação de inversores sem necessitar conhecimento prévio das características da microrrede, independentemente da topologia elétrica, e ofertando operacionalidades *plug-and-play*. Esta estratégia, nomeada *Generalized Current-Based Control* (GCBC), é capaz de acomodar inversores de características diversas, sendo de natureza despachável (d-RED) ou não-despachável (nd-RED), com base em uma unidade centralizadora e em canais de comunicação de banda estreita. Através da coordenação flexível de REDs, a estratégia suporta a implementação de compartilhamento de correntes ativas, tão bem quanto a compensação de correntes reativas, além da mitigação distribuída e seletiva de harmônicos. Ademais, a estratégia de controle é complacente com perfis intermitentes de geração de energia, os quais são comuns em nd-REDs. Além disso, outra vantagem se refere à capacidade de prover compartilhamento de correntes entre inversores de forma proporcional às suas capacidades, sem interferência das características de impedâncias de linha, diferente do método convencional de controle *droop* (i.e., controle por inclinação). Acima de tudo, a estratégia GCBC é capaz de gerenciar uma microrrede CA interconectada para operar como uma entidade única controlável, provendo controlabilidade total sob seu despacho de potência para a rede de distribuição, permitindo a negociação de serviços energéticos em mercados de energia transativos.

Os méritos da estratégia GCBC são amplamente avaliados ao longo desta tese, por meio de simulação e resultados experimentais, com base em múltiplos protótipos

de microrrede com foco em baixa tensão, garantindo que o método é viável a implementações práticas reais. Diversos cenários de microrrede são analisados, tal como sob limitação de capacidades de potência, considerando a presença de tensões não ideias, e também perante complicações relacionadas à comunicação de dados, certificando que a estratégia GCBC é capaz de operar sob condições adversas. Ainda, demonstra-se através de resultados experimentais que o método de controle é capaz de prover melhoria da qualidade da tensão em microrredes fracas de baixa tensão que apresentam características homogêneas, como um resultado indireto do compartilhamento proporcional de correntes não ativas.

Finalmente, funcionalidades de controle avançadas são flexivelmente derivadas com base na abordagem GCBC, possibilitando que uma microrrede seja capaz de modelar sua operação para se comportar como um resistor variável e seletivo, o qual suporta uma operação mais eficiente da rede de distribuição, ainda favorecendo o amortecimento de ressonâncias harmônicas. Como outra funcionalidade avançada, compensação distribuída de correntes ativa e reativa de desbalanço pode ser também ofertada, com base em conceitos advindos da Teoria de Potência Conservativa. Ademais, regulação de tensão pode ser implementada para microrredes, com base em um esquema de controle automático incorporando a estratégia GCBC, possibilitando ainda uma exploração de energia aprimorada para nd-REDs. Por último, considerações sob a integração de métodos de otimização também ressaltam que funcionalidades adicionais podem ser formuladas com base na adoção da estratégia GCBC.

Ackowledgements

Above all, I would to thank God, for giving me the strength to overcome the difficult times endured during the period of this PhD project.

I thank my parents, Mauro and Dirce, and my brothers, Lucas and Felype, for supporting and motivating me at all times. It is also impossible to write any acknowledgements without thanking my future wife, Mariana, for her love and tender company throughout all these years.

Most of my time working on this PhD project was spent at UNESP/Sorocaba-Brazil, and I thank all my colleagues for the talks, and the company during the many days and nights spent in the lab. A particular thanks goes to Wesley A. Souza, Eduardo V. Liberado, Luis A. O. Arenas, Rubens T. Hock Jr., Marcelo N. Tirolli, and José A. O. Filho. Moreover, I am grateful to the professors from the *Group of Automation and Integrated Systems (GASI)* at UNESP, particularly to Flávio A. S. Gonçalves and Helmo K. M. Paredes, for their technical support and teaching during the courses I undertook in Brazil.

I also had the pleasure of spending some time at NTNU/Trondheim-Norway, and to participate as a member in the *Power Electronic Systems and Components (PESC)* group. This period was very fruitful from both personal and professional perspectives, and I foremost thank my friends Andreas Giannakis, Erick F. Alves and Spyridon Chapaloglou, who also represent many other amazing people that I was luckily able to meet. I also thank Fredrik T. B. W. Göthner for the technical interaction during the conference paper C.2., as well as for helping me out with the *Sammendrag* of this thesis. From the staff side, I thank Bodil V. Wold and Åshild U. Meistad for making my stay at NTNU more pleasant. Lastly, I thank Santiago S. Acevedo and Salvatore D'Arco, from *SINTEF Energy*, for supporting me on my short experience at the *National Smart Grid Laboratory*.

I am very grateful to the *São Paulo Research Foundation (FAPESP)*, for the grant 2017/24652-8, which provided me with financial support for this PhD project, as well as for the grant 2018/22172-1 that allowed me to develop part of my research at NTNU. I also thank FAPESP for the grant 2016/08645-9, since this thesis is incorporated into a larger thematic project. To conclude, I thank the *Research Council of Norway*, since my Cotutelle agreement is a direct outcome of the cooperation between UNESP and NTNU, which was initiated with the *NB_POCCREI* project (grant f261735/H30).

I thank the evaluation committee of my mid-term (qualifying) examination, Prof.

Josep M. Guerrero from Aalborg University, Prof. Mohammad Amin from NTNU, and Prof. Pericle Zanchetta from University of Nottingham, for their insightful comments on my project, which oriented me to direct toward completion.

I am lucky to have had three amazing professors guiding me throughout the journey of this PhD project. First, I deeply thank my co-supervisor, Prof. Danilo I. Brandão, for the intensive support given on technical aspects comprised within this project, whenever I needed it. He was fundamental to all the achievements related to this project.

From the NTNU side, I am very thankful for having Prof. Elisabetta Tedeschi as my main supervisor. It has been an enormous pleasure to learn from her during the course I undertook at NTNU, and I thank her for technically supporting me along the entire duration of this project. Especially, I express my appreciation for her, as she always provided me with access to whatever was needed for my project, as well as for making my stay in Norway an unforgettable experience.

Last, but not least, I must thank my main supervisor at UNESP, Prof. Fernando P. Marafão, for conducting me throughout the most challenging and fruitful professional times of my life. I will be ever grateful to him, not only for the technical guidance throughout my master and PhD degrees, but also for giving me opportunity to pursue my professional dreams. I owe to him most of the (limited) technical knowledge I have attained during the last few years.

Contents

List of Tables

List of Figures

List of Acronyms and Abbreviations

AC	Alternating Current
APC	Active Power Curtailment
AVG	Average
CB	Circuit Breaker
CCM	Current Controlled Mode
CPT	Conservative Power Theory
D	CPT's Distortion Power
d-DER	Dispatchable DER
DC	Direct Current
DER	Distributed Energy Resource
DFT	Discrete Fourier Transform
DRA	Demand Response Aggregator
DSO	Distribution System Operator
DSP	Digital Signal Processor
DST	Distribution System Transformer
ESS	Energy Storage System
GCBC	Generalized Current-Based Control
ICT	Information and Communication Technology
LC	Inductive and Capacitive Output Filter
LCL	Inductive-Capacitive-Inductive Output Filter
LPF	Low-Pass Filter
LV	Low-Voltage

MAF	Moving Average Filter
MG	Microgrid
MG-TES	Microgrid Transactive Energy System
MGO	Microgrid Operator
N	CPT's Unbalance Power from
nd-DER	Non-dispatchable DER
P	CPT's Active Power
P2P	Peer-to-Peer
PCC	Point-of-Connection
PF	CPT's Power Factor
PLL	Phase-Locked-Loop
PoC	Point-of-Connection of a DER
PRep	Proportional-Repetitive
PRes	Proportional-Resonant
Q	CPT's Reactive Power
RES	Renewable Energy Source
RLS	Resistive Load Synthesis
RMS	Root Mean Square
SCS	Sinusoidal Current Synthesis
SG	Smart Grid
SoC	State-of-Charge
TES	Transactive Energy System
THD_i	Total Harmonic Distortion of a Current
THD_v	Total Harmonic Distortion of a Voltage
TSO	Transmission System Operator

UI	Utility Interface
VCM	Voltage Controlled Mode
VPP	Virtual Power Plant
X/R	Ratio Between Inductance and Resistance of Line Impedances

List of Symbols and Variables

$\star$	Refers to the main experimental setup (single-phase MG)
$\dagger$	Refers to the experimental setup from Section 5.8 (three-phase MG)
^{3ph}	Refers to the experimental setup from Section 6.4 (three-phase MG)
$\|\|$	In-phase component
$\perp$	Quadrature component
^{INV}	Refers to the simulation circuit of Section 4.4.2
$\alpha_{h\|\|}$	GCBC in-phase scaling coefficient for harmonic order h
$\alpha_{h\perp}$	GCBC quadrature scaling coefficient for harmonic order h
γ_{Na}	Percentage of compensation for the active unbalanced current parcel
γ_{Nr}	Percentage of compensation for the reactive unbalanced current parcel
γ_{OV}	Activation variable of the active and reactive voltage control
γ_{RLS}	Activation variable of the RLS-based coordination approach
θ_{1m}	Synchronization angle for the fundamental component
θ_{hm}	Synchronization angle for harmonic component at order h
θ_s	Phase shift of a waveform
ω_o	Fundamental angular frequency
ω_j	Angular frequency at a DER j
δ_1	Constant for the regulation of steps in current dispatch
B	A MG node from the main simulation testbench
C_f	Capacitor of LC and LCL filters
$i(t)$	Time-domain current
i^{DER}	Time-domain current of a DER

i^{DER*}	Time-domain reference current of a DER
i^{Grid}	Time-domain current of the grid
i^{P*}	Time-domain reference current for active power injection
i^{o}	Time-domain output current of a DER at its PoC, or at the MG PCC
i_c	Time-domain capacitor current
i_{a_m}	Fryze's time-domain active current of a phase *m*
i_{na_m}	Fryze's time-domain non-active current of a phase *m*
i^*_{Anc}	Time-domain reference current for ancillary service provision
i^*_{ESS}	Time-domain reference current for an ESS
$i^b_{a_m}$	CPT's balanced active current of a phase *m*
$i^b_{r_m}$	CPT's balanced reactive current of a phase *m*
$i^u_{a_m}$	CPT's unbalanced active current of a phase *m*
$i^u_{r_m}$	CPT's unbalanced reactive current of a phase *m*
I_{Col}	Collective current
I_{RMS}	RMS current
I^*_h	Reference peak current to be shared by DERs at harmonic order *h*
I^{DERj}_h	Peak current of a DER *j* at harmonic order *h*
I^{DERj}_{nom}	Nominal peak current of a DER *j*
$I^{DERj}_{1\|\|max}$	Maximum active current generated by a DER *j*
$I^{DERj}_{1\|\|sto}$	Maximum active current stored by a DER *j*
I^{DERt}_h	Total peak current of DERs participating in the GCBC at harmonic order *h*
$\hat{I}^{DERt}_h$	Estimated total peak current of DERs at harmonic order *h*
I^{DERt}_{nom}	Total nominal peak current of DERs participating in the GCBC
$I^{DERt}_{1\|\|max}$	Total maximum peak current of DERs participating in the GCBC
$I^{DERt}_{1\|\|sto}$	Total stored peak current of DERs participating in the GCBC

I_h^{Grid}	Peak current of the grid at harmonic order *h*
I_h^{Grid*}	Reference peak current for the grid at harmonic order *h*
$\overline{I_{1\|\|}^{Grid}}$	Upper limit for the active current dispatch of the MG
$\overline{I_{1\perp}^{Grid}}$	Upper limit for the reactive (inductive) current dispatch of the MG
$\underline{I_{1\|\|}^{Grid}}$	Lower limit for the active current absorption of the MG
$\underline{I_{1\perp}^{Grid}}$	Lower limit for the reactive (capacitive) current dispatch of the MG
I_h^L	Peak current of loads, considering losses and non-participating DERs
$I_h^{L(b)}$	Balanced component of I_h^L after CPT decomposition
$I_h^{L(u)}$	Unbalanced component of I_h^L after CPT decomposition
I_h^{UI}	Peak current of the UI at harmonic order *h*
I_h^{UI*}	Reference peak current for the UI at harmonic order *h*
$\sqrt{\Delta I}$	Total current capability of all DERs participating in the GCBC
$\sqrt{\Delta I^{DER_j}}$	Total current capability of a DER *j*
ΔI	Quadratic total current capability of all DERs at actual step of the GCBC
ΔI_{old}	Quadratic total current capability of all DERs at previous step of the GCBC
j	*j*-th DER (*j*=1,2,3,...,*J*)
k	Actual control cycle
f_s	Sampling frequency
f_{sw}	Switching frequency
f_{GCBC}	GCBC algorithm interruption frequency
K_P	Proportional gain
K_I	Integral gain
K_f	Repetitive gain
K_{damp}	Gain of the active damping loop
L_B	Load connected to a node *B*

L_i	Inverter-side inductor of LC and LCL filters
L_g	Grid-side inductor of a LCL filter
m	Refers to phase m of an electric circuit
P^{Fryze}	Fryze's active power
P_{max}^{DERj}	Maximum active power of a DER *j*
P_{nom}^{DERj}	Nominal active power of a DER *j*
Q_{max}^{DERj}	Maximum (inductive) reactive power of a DER *j*
Q_{min}^{DERj}	Maximum (capacitive) reactive power of a DER *j*
Q_{nom}^{DERj}	Nominal reactive power of a DER *j*
r_{dDERs}	Proportion ratio among d-DERs
v^{Grid}	Time-domain voltage of the grid
v^{DERj}	Time-domain voltage of a DER *j* at its PoC
V_{RMS}^{DERj}	RMS phase voltage of a DER *j* at its PoC
V_{RMS}^{Grid}	RMS phase voltage of the grid
V_{Col}	Collective voltage
$\bar{V}$	Average of RMS voltages
$\bar{V}^{lim}$	Threshold for overvoltage detection
$\bar{V}_{lower}^{lim}$	Critical limit for undervoltage condition
$\bar{V}_{upper}^{lim}$	Critical limit for overvoltage condition
T_D	Time delay
T_s	Sampling time
T_{GCBC}	GCBC algorithm interruption time
x_h	Unitary reference signal at harmonic order *h*
Z_L	Line impedance

Chapter 1

Introduction

1.1 Background and Motivation

Decarbonization is a growing trend in the energy sector [1], and renewable energy generation plays a vital role in supporting such an energy transition [2], pushing electric power systems toward new operational and economic paradigms [3]. The immediate request to integrate renewable energy sources (RESs) into electrical grids is tied to benefits, such as the decentralization of generation, which increases the reliability in power dispatch [4]. In addition, integration of RESs provides a more diverse energy matrix that favors economic gains [5]. Nevertheless, as the proliferation of RESs increases, previously unknown technical and policy-related challenges arise [6], demanding research into new operational and regulatory strategies [7] for electric power systems.

Typically, RESs are small-scale energy generators that operate interconnected to electrical grids, by means of power electronic converters. Such an incorporation of power interfacing devices to RESs is part of the concept of distributed energy resources (DERs) [8]. In fact, DERs may also comprise energy storage systems (ESSs), and other complementary embedded technologies and functionalities, such as communication interfaces and remote control capabilities [9]. Hence, although RESs are in the spotlight of the actual energy transition [3], their potential benefits to electric systems cannot be fully exploited without the conceptualization of DERs.

In AC electrical systems, DC-AC power converters (i.e., so-called inverters) are the main electronic units of DERs in relation to the provision of controlled power conversion from RESs (e.g., photovoltaic- (PV) and wind-based generators), as well as from ESSs. A schematic of an inverter-based DER connected to an AC power system is depicted in Fig. 1.1. Converting power through inverters is possible due to their power electronics infrastructure [10], which allows the possibility to modulate voltage and current waveforms through the commutation of power switches. Concomitantly, the control algorithms embedded to such inverters are the ones responsible for dictating the operational features of DERs [11], adapting their voltages and currents according to energy generation and grid quantities. For instance, DERs can be managed to pursue local or global goals [12], leading to enhanced operation at their particular electric

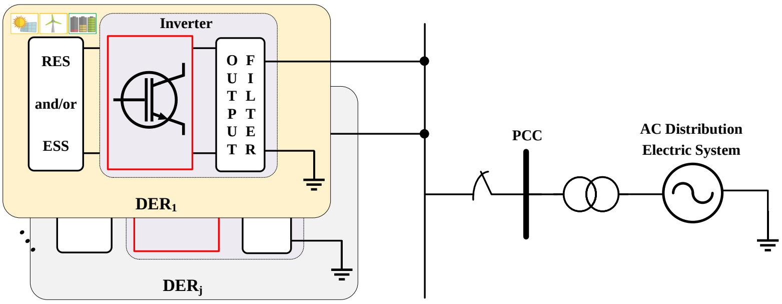

Figure 1.1: Schematic of a DER composed of a RES or ESS, and its inverter connected to an AC distribution system.

nodes, or at their entire interconnected grid, respectively.

Conventional inverters existing within DERs are commonly designed to only process active power, providing a dispatch of RESs' generated energy to the electrical grid. However, in recent years, led by the trend for *Smart Grids* (SGs) [12, 13], the concept of smart inverters has enlightened new perspectives on the purpose of such equipment [14, 15]. Beyond the provision of active power conversion, smart inverters (also called multifunctional inverters) offer the possibility to employ their rated capabilities in services related to power conditioning and grid support [16]. Thus, flexible implementation of power quality interventions, and more sophisticated power distribution planning strategies have become possible [17].

To implement such a perspective, the control flexibility of inverter-based DERs can be exploited to offer ancillary functionalities, such as voltage support to the grid [18], compensation of power oscillations and unbalanced currents [14], mitigation of reactive and harmonic components [19], and many others [15]. Moreover, since information and communication technologies (ICTs) are intrinsic to SGs, communication features are becoming compulsory for inverters [8]. This consequently allows them to support remote control and interoperability, while broadening their applications to scenarios of cooperative and coordinated operations [14, 20].

As more and more multifunctional abilities are being incorporated into electrical grids, especially from the perspective of low-voltage (LV) power systems, the locally-oriented operation of inverters is doomed to become obsolete. This occurs because operation of DERs under individualized perspectives (i.e., purely local) does not take into account the status of other equipment or the overall needs of the grid. Moreover, non-coordinated DER actions may interfere with the proper functioning of their neighboring inverters [21], as well as impairing grid stability [22]. To corroborate such undesired effects of interacting DERs, one can observe issues like the multi-timescale coupling among their control loops [23], and the generation of circulating currents caused by the lack of synergy during their parallel operation [21].

On the other hand, as reinforced in [23], if proper coordination among multifunctional inverters is formulated, more reliability and robustness can be achieved from both local and global operational perspectives. Thus, the coordinated control of DERs not only offers enhanced use of inverters' power capabilities, but also decreases the undesired side-effects of their local functioning. Furthermore, proper coordination of ancillary services devised by smart inverters dispersed over AC grids can even optimize the profitability of prosumers (i.e., DERs' owners that also comprise local consumption) [24]. Moreover, this also supports the offering of energy management features to benefit entities at power system levels [25].

The importance of coordinating inverters is further evidenced in the so-called weak grids, which are power systems comprising low short-circuit ratio and small inertia constant [26]. In such a scenario, the significant presence of DERs potentially affects the grid capability to maintain steady and compliant voltage profiles. Consequently, this results in a chain effect that may interfere with the adequate operation of loads and grid-tied converters [26], as well as potentially lead to the propagation of non-idealities (e.g., harmonic distortions) [27] to adjacent distribution grids [28].

This condition is particularly frequent, and critical, in weak microgrids (MGs), which are defined by [29] as power systems that: *i)* present clearly established electrical boundaries; *ii)* comprise a considerable amount of loads and interconnected DERs; *iii)* have the capability to act as a single controllable entity, with respect to its point-of-connection (PCC) with an upstream grid (see Fig. 1.1); and that *iv)* are able to operate both interconnected and islanded (i.e., under autonomous mode [30]). Given all the particularities of MGs, their design, operation and management have been extensively explored in the literature [31, 32, 33, 34], often converging on the conclusion that proper coordination of DERs is imperative.

Since ICT is being widely incorporated into the infrastructure of electric grids, along with the fact that MGs can be interpreted as individual entities, smartness can also be extended to how such systems behave and operate. Smart MGs, for instance, are systems that are intelligently self-sufficient (i.e., internally exploiting their resources to be fully independent) [35]. Moreover, they are capable of dynamically interacting with external agents to optimize internal and external financial and operational objectives [36].

As a result, if a smart MG is flexibly modeled and managed to act according to market and technical requirements, it can accordingly take part in controlled energy transactions [37]. Hence, smart MGs possess the means to interact with external agents (e.g., the distribution system operator (DSO), aggregators or other MGs) to trade market-regulated energy services. Among the examples of such services provided by LV MGs, one can find controllable power dispatchability [25], and power quality support to achieve more robust operation of distribution grids [38].

The summary presented in Fig. 1.2 represents the scalable complexity of how the context of RESs and SGs is impacting on how equipment (such as inverters) and power systems (such as MGs) are evolving and interacting with other entities. It can be noted that, although each of the previous discussions may be seen as an independent topic, all concepts are fundamental pieces of the overall infrastructure of real SGs. Although the practical model of SGs is complex, extending from consolidated concepts like automation and digitalization, up to emerging ideas such as the energy internet [39], it can be first realized by intelligently operating equipment that supports basic principles, such as interoperability.

The background of this PhD thesis is also immersed within the multidisciplinary context found in Fig. 1.2. By assimilating different SG concepts, the scope of this thesis encompasses the idea of how multiple technological principles (e.g., smart inverters, coordinated control, energy services) can be integrated to obtain the flexible operation of MGs. Beyond basic management features, the consideration of non-ideal operational conditions is also of interest to this thesis, not to mention the importance of accounting for market-oriented applicability. Thus, in summary, the grounds of this thesis take into consideration the employment of smart inverters as potential tools to improve the management of MGs, under diverse operational conditions, also investigating possibilities to broaden the provision of ancillary energy services focusing on the LV perspective.

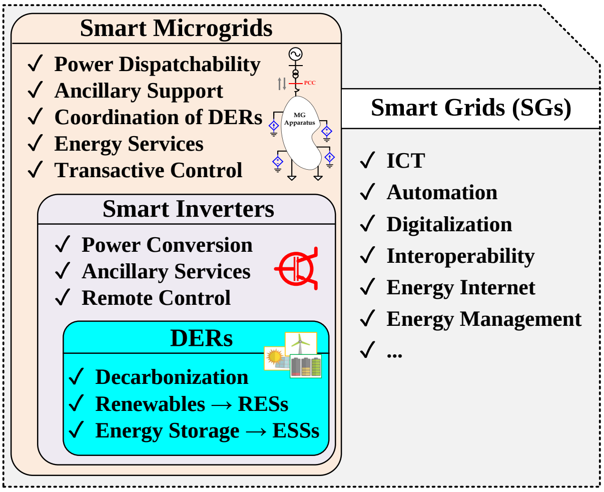

Figure 1.2: Background context of DERs, smart inverters and MGs within the scenario of SGs.

1.2 Main Goals and Contributions

1.2.1 Main Goals of the PhD Thesis

This PhD thesis is grounded in the perspective of a smart AC MG comprising a significant amount of DERs of different natures, considering that their inverters have the capability to operate as multifunctional devices offering ancillary services. The targeted scenario holds homogeneous features, indicating that DERs, loads and line impedances are fairly evenly distributed throughout the MG. In addition, since a MG acts most of the time under the interconnected mode [5], this thesis also focuses on the features of its operation as a single-controllable entity, assessing how it can contribute to the support of an upstream distribution network.

Based on the above-mentioned conceptualization, the major objective of this thesis is to develop a coordinated control strategy to allow transactive and multi-purpose steering of DERs dispersed over an AC MG, focusing on the LV perspective. The transactive control aspect of such a strategy [40] is intended to support the possibility for the MG to trade energy services with external agents. Consequently, the flexibility to achieve market-oriented management over active power dispatchability, in addition to the extended provision of ancillary services, is offered. Furthermore, the proposed multi-purpose feature relates to the fact that, beyond providing controllable power extraction from DERs, distributed compensation of unwanted current components, as well as voltage regulation, can be pursued.

Another goal of this thesis is to ensure that the proposed coordination of inverters is valid under non-ideal operational scenarios, such as non-sinusoidal voltages, abnormal voltage scenarios, as well as under ICT-related issues. Such goals imply that, by providing flexible steering of DERs in a MG, both local and global objectives related to power exploitation, power quality, grid support, and market-oriented actions can be obtained.

The main goals of this thesis are explicitly highlighted as follows. They specify the idea of developing a coordinated control strategy that grants:

1. *Model-free formulation and flexible implementation*

   In order to deploy the strategy, features that facilitate its real implementation are desirable, for the sake of practicality and commercial attractiveness. Hence, a goal is set by developing a strategy that is: *i)* topology independent, *ii)* model-free, and *iii)* plug-and-play.

   The topology independence of the strategy strives to make it applicable to AC MGs, regardless if they are based on single- [41], three-phase, or other polyphase circuits [42]. The model-free aspect implies that knowledge of MG parameters (e.g., line impedance characteristics, location of DERs or loads, features of transformers, etc.) are not essential for the adequate and proportional steering of DERs [43]. In addition, the plug-and-play feature relates to the self-adjusting capability of the control strategy to dynamically rearrange the coordination of inverters during changes in the MG;

2. *Adjustable active power conversion*

   Since the main purpose of DERs is to inject active power into grids, it is important to achieve controllability over such functionality. Thus, energy exploitation can efficiently occur without affecting grid performance. Additionally, as power generation profiles may be intermittent or limited, variability in the local operation of DERs should be supported. Lastly, DERs of a dispatchable (e.g., endowing ESSs) and non-dispatchable (e.g., PV- or wind-based) nature may exist (i.e., herein denoted as d- and nd-DERs), so that the strategy must cope with their synergistic operation;

3. *Distributed compensation of unwanted currents*

   In AC MGs, reactive, harmonic and unbalanced current components are tied to the lowering of energy efficiency and deterioration of power quality [27]. Hence, the control strategy intends to exploit dispersed inverters to also provide distributed compensation of reactive currents, as well as selective mitigation of harmonics. The compensation of unbalanced currents is also considered for particular implementations;

4. *Operation upon adverse scenarios*

   In general, LV MGs are known to be weak systems, in which voltage waveforms cannot always be ideal (i.e., sinusoidal with constant magnitude). Consequently, the goal of ensuring that the proposed coordinated control strategy presents robust operation under non-ideal scenarios is accounted for. In particular, this thesis presents an assessment of the control approach upon scenarios of distorted voltages, as well as considering voltage ride-through challenges. Another research target is to demonstrate the features of the strategy under the occurrence of ICT-related issues, such as faulty communication links and delays in data transmission;

5. *MG dispatchability and support to transactive control*

   The key factor in the MG participation in energy transactions [37] is the ability to achieve full power dispatchability. This thesis has the objective of demonstrating that, by adequately coordinating DERs, the energy flow at the MG PCC can be regulated to achieve decoupled active, reactive and harmonic controllability. Consequently, access to market-oriented transactions of active power flow is individually possible. In addition, the reactive and harmonic power flow control at the PCC can support the planning of power dispatch for the upstream grid and provide high power factor operation, respectively, being interpreted as marketable energy services. Finally, full controllability over active and non-active currents at the PCC also offers the possibility for the MG to operate under self-consumption mode [44] (i.e., neither depending on the upstream grid, nor significantly affecting its operation).

6. *Voltage regulation capability*

   While exploiting DERs in distribution systems, it is important to ensure that voltage profiles are maintained within acceptable ranges [8], foremost in the internal nodes of the MG. With this in mind, this thesis also strives to develop a coordinated control strategy that sustains the regulation of voltage profiles, if overvoltage conditions occur internally to the MG. The availability of several DERs to contribute to voltage regulation is also taken into account.

7. *Experimental validations*

   Since the development of the coordinated control strategy reaches the power electronics layer, it is important to validate the applicability of the proposed functionalities to real-life implementations. As a result, beyond demonstrating computational simulations, laboratory scale prototypes have been set up to experimentally assess the performance of the coordination approach.

1.2.2 Contributions of the PhD Thesis

This thesis explicitly presents the following scientific and nonscientific contributions, which are also evidenced by the scientific publications presented in Section 1.3:

Scientific Contributions

1. The development of a centralized strategy that provides multi-purpose coordinated control of inverters in transactive MGs. The coordination approach, so-called Generalized Current-Based Control (GCBC), is formulated based on the analysis of electrical currents flowing within the MG, also considering power exchange interactions with the upstream distribution grid at the PCC. The GCBC encompasses all the features previously explained in Section 1.2.1 for goal 1, while also endowing control capabilities to achieve goals 2 to 5.

2. A systematic assessment of the features of the proposed coordination approach is realized, by means of computational simulations and extensive experimental work, being carried out on multiple simulation testbenches and laboratory-scale MG prototypes. Beyond evaluating non-ideal scenarios of operation, comparative studies with another well-known coordination strategy (i.e., droop control

[31]) are conducted to highlight the particularities and contributions of the proposed method;

3. An innovative approach is proposed to devise a resistive shaping for the PCC of an interconnected MG, considering that the upstream distribution grid operates while suffering from distorted voltages. The method provides high power factor operation and, upon the existence of resonant components, it supports harmonic resonance damping, which minimizes deterioration of voltage quality. In addition, the control approach holds improved performance when compared to strategies that aim to fully mitigate harmonic currents;
4. A method to steer DERs to achieve distributed and decoupled compensation of unbalanced currents in MGs, without requiring the implementation of virtual impedance control loops [31], nor the extraction of sequence components. Such an approach incorporates the Conservative Power Theory (CPT) [45] for generating reference currents for the compensation purposes;
5. Taking advantage of the MG power dispatchability, an automatic voltage regulation scheme is formulated. It is demonstrated that the energy exploitation of non-dispatchable inverters can be enhanced without optimization algorithms, while ensuring that overvoltage conditions are mitigated internally to the MG. This occurs by the synergistic active and reactive power control of d- and nd-DERs. Additionally, the proposed strategy allows the possibility to integrate DERs into voltage regulation regardless of their location in the MG;
6. An extended outlook on the power dispatchability of transactive MGs is presented, demonstrating that multiple ancillary services can be provided. Moreover, a transactive control framework for MGs is designed, relying on the steering of DERs to offer the flexible provision of energy services in the power system level, thus supporting accessibility to electricity markets.

Nonscientific Contributions

1. Two main contributions relate to UNESP/Sorocaba-Brazil. The first one concerns the implementation of two experimental MG prototypes being: *i)* one composed of three-phase inverters; and *ii)* one devised by the realization of technical improvements in a previously existent single-phase platform. Beyond the fact that both testbenches can be used in future research, they lead to the second contribution, which is the incorporation of these experimental infrastructures into the activities executed for the thematic project "*Interdisciplinary Research Activities in Electric Smart Grids*" [46], which is funded by *FAPESP*;
2. Two last contributions relate to NTNU/Trondheim-Norway. This PhD thesis is also a direct outcome of the "*Norwegian-Brazilian Collaboration on*

Power Theories and Cooperative Control for Renewable Energy Integration (NB_POCCREI)" project [47], which was funded by the the *Research Council of Norway*. Additionally, the interactions resulting from this thesis led to a Cotutelle agreement for a double degree PhD, taking part in strengthening the scientific cooperation between NTNU and UNESP.

1.3 List of Publications

During the three-year period of this PhD project, the main scientific findings have been published in the following journal and conference articles. Such publications present results obtained as a direct outcome of this PhD research, also comprising additional contributions in correlated topics.

Journal Papers:

J.1) **A. M. S. Alonso**, D. I. Brandao, E. Tedeschi, and F. P. Marafao, “Resistive Shaping of Interconnected Low-Voltage Microgrids Operating Under Distorted Voltages,” *IEEE Transactions on Industrial Electronics*, 2021. Accepted

J.2) **A. M. S. Alonso**, L. O. Arenas, D. I. Brandao, E. Tedeschi, and F. P. Marafao, “Automatic Overvoltage Control of Distributed Energy Resources Supporting Enhanced Energy Exploitation in Interconnected Microgrids,” *IEEE Transactions on Sustainable Energy*, 2021. Under Review

J.3) **A. M. S. Alonso**, J. H. Oliveira, D. I. Brandao, J. P. Bonaldo, H. K. M. Paredes, and F. P. Marafao, “A Multifunctional Grid-Tied Inverter for Two-Phase Three-Wire Networks Based on the Conservative Power Theory,” *IEEE Transactions on Power Delivery*, 2021. Under Review

J.4) **A. M. S. Alonso**, D. I. Brandao, E. Tedeschi, and F. P. Marafao, “Distributed Selective Harmonic Mitigation and Decoupled Unbalance Compensation by Coordinated Inverters in Three-Phase Four-Wire Low-Voltage Networks,” *Electric Power Systems Research*, vol. 186, pp. 1–14, 2020.

J.5) **A. M. S. Alonso**, D. I. Brandao, T. Caldognetto, F. P. Marafao, and P. Mattavelli, “A Selective Harmonic Compensation and Power Control Approach Exploiting Distributed Electronic Converters in Microgrids,” *International Journal of Electrical Power & Energy Systems*, vol. 115, pp. 1–15, 2020.

J.6) **A. M. S. Alonso**, B. R. Pereira Jr., D. I. Brandao, and F. P. Marafao, “Optimized Exploitation of Ancillary Services: Compensation of Reactive, Unbalance and Harmonic Currents Based on Particle Swarm Optimization,” *IEEE Latin America Transactions*, vol. 19, no. 2, pp. 314-325, 2021.

J.7) L. S. De Araujo, **A. M. S. Alonso**, and D. I. Brandao, “Decentralized Control of Voltage- and Current-Controlled Converters Based on AC Bus Signaling for Autonomous Microgrids," *IEEE Access*, vol. 8, pp. 202075–202089, 2020.

J.8) J. P. Bonaldo, J. A. O. Filho, **A. M. S. Alonso**, F. P. Marafao, H. K. M. Paredes, "Modeling and Control of a Single-Phase Grid-Connected Inverter with *LCL* Filter," *IEEE Latin America Transactions*, vol. 19, no. 2, pp. 205-259, 2021.

J.9) D. I. Brandao, W. M. Ferreira, **A. M. S. Alonso**, E. Tedeschi, and F. P. Marafao, "Optimal Multiobjective Control of Low-Voltage AC Microgrids: Power Flow Regulation and Compensation of Reactive Power and Unbalance," *IEEE Transactions on Smart Grid*, vol. 11, no. 2, pp. 1239–1252, 2020.

J.10) D. I. Brandao, L. S. Araujo, **A. M. S. Alonso**, G. L. dos Reis, E. V. Liberado, and F. P. Marafao, "Coordinated Control of Distributed Three- and Single-Phase Inverters Connected to Three-Phase Three-Wire Microgrids," *IEEE Journal of Emerging and Selected Topics in Power Electronics*, vol. 8, no. 4, pp. 3861–3877, 2020.

Conference Papers:

C.1) **A. M. S. Alonso**, L. O. Arenas, R. T. Hock Jr., H. Guillardi Jr., H. K. M. Paredes, F. A. S. Goncalves, and F. P. Marafao, "Experimental Implementation of a Single-Phase Microgrid: A Flexible Resource for Research and Educational Activities," in *2021 IEEE 16th Brazilian Power Electronics Conference (COBEP)*, 2021. Accepted

C.2) **A. M. S. Alonso**, F. Göthner, D. I. Brandao, F. P. Marafao, and E. Tedeschi, "Power- and Current-Based Control of Distributed Inverters in Low-Voltage Microgrids: Considerations in Relation to Classic Droop Control," in *2020 15th International Conference on Ecological Vehicles and Renewable Energies (EVER)*, 2020, pp. 1–10.

C.3) **A. M. S. Alonso**, L. C. Afonso, D. I. Brandao, E. Tedeschi, and F. P. Marafao, "Considerations on Communication Infrastructures for Cooperative Operation of Smart Inverters," in *2019 IEEE 15th Brazilian Power Electronics Conference and 5th IEEE Southern Power Electronics Conference (COBEP/SPEC)*, 2019, pp. 1–6.

C.4) **A. M. S. Alonso**, H. K. M. Paredes, J. A. O. Filho, J. P. Bonaldo, D. I. Brandao, and F. P. Marafao, "Selective Power Conditioning in Two-phase Three-Wire Systems Based on the Conservative Power Theory," in *2019 IEEE Industry Applications Society Annual Meeting*, 2019, pp. 1–6.

C.5) **A. M. S. Alonso**, D. I. Brandao, F. P. Marafao, and E. Tedeschi, "Coordinated Control of Parallel Power Conditioners Synthesizing Resistive Loads in Single-Phase AC Microgrids," in *2019 21st European Conference on Power Electronics and Applications (EPE '19 ECCE Europe)*, 2019, pp. 1–9.

C.6) **A. M. S. Alonso**, D. I. Brandao, E. Tedeschi, and F. P. Marafao, “Distributed Harmonic Compensation in Single-Phase Low-Voltage Microgrids,” in *XXII Brazilian Conference on Automation (CBA)*, 2018, pp. 1–8.

The above-mentioned publications support multiple chapters of this thesis, and they can be mapped according to Table 1.1. Moreover, it is highlighted that the following three additional papers are currently being written: *i)* one journal paper, being an extension of "C.2", which has been invited for possible publication in *IEEE Transactions on Industry Applications*; *ii)* one journal paper comprising the results from Section 5.5; and *iii)* one conference paper composed of discussions presented in Chapter 2.

Table 1.1: Mapping of publications to chapters.

Chapter	**2**	**3**	**4**	**5**	**6**
Journal	-	*J.3, J.4, J.5, J.8*	*J.4, J.5, J.7, J.10*	*J.5*	*J.1, J.2, J.4, J.6* *J.8, J.9, J.10*
Conference	-	*C.2, C.3, C.6*	*C.1, C.2, C.6*	*C.6*	*C.4, C.5*

1.4 Structure of the Thesis

Besides its introductory part, this thesis is structured into six additional chapters, aiming at plainly conveying the ideas and contributions comprised within the proceeding discussions.

Firstly, in Chapter 2, the transactive aspect of MGs is presented. The concept of Transactive Energy Systems (TESs) is introduced, and the MG power dispatchability is discussed as a means to offer energy services, constituting a market-oriented outlook.

Chapter 3 explains the MG and DER topologies considered within this thesis, and it presents the basic formulation of the proposed multi-purpose coordination of DERs (i.e., the GCBC approach). The hierarchical control infrastructure of the strategy, as well as its flexibility to control multiple current components, is thoroughly explained.

The multiple functionalities and transactive features of the GCBC strategy are demonstrated in Chapter 4, in which extensive simulations and experimental results are discussed. Moreover, additional operational considerations, such as the MG transition modes and a comparison with the droop control approach, are discussed.

Adverse operational scenarios, such as under distorted voltages, upon ICT-related issues, and consideration of the matter of power coupling among DERs, are assessed in Chapter 5. The goal of the discussions in this chapter is to show that the GCBC approach is flexible and resilient for implementation in weak LV MGs.

Advanced control functionalities related to the resistive shaping of MGs, distributed compensation of unbalanced currents, and voltage regulation capabilities are provided in Chapter 6. Moreover, a brief discussion about the integration of optimization approaches to the coordination strategy is also given.

Lastly, Chapter 7 presents the final conclusions of the PhD thesis, and offers proposals for the development of future works.

Chapter 2

Microgrid Transactive Energy as a Framework for the Coordination of Smart DERs

2.1 Introduction

From a business perspective, the aggregation of DERs into AC distribution grids imposes challenges to energy trading due to the decentralization of market players. This occurs because each DER owner can be interpreted as an individual market player, resulting in complex profiles of power demand and supply to be resolved [48]. Consequently, energy trading strategies incorporating a high amount of DERs should cope with multiple players and their distinct market objectives.

Although the participation of DER owners in energy markets can be determined by diverse approaches [49], the concept of peer-to-peer (P2P) trading is among the most diffused ones. This is because P2P architectures offer the possibility to take into consideration the particular market goals of each participant [50], meaning that trading occurs according to consumer-centric energy transactions. Consequently, each agent (e.g., DER owner or prosumer) is a market player that sells or buys energy from another individual, such as its neighboring DER, the DSO, or MGs [50]. However, as discussed in [51], such a consumer-centric approach presents a scalability problem, as complexity in management of energy transactions increases proportionally to the number of market players.

On the other hand, when such agents are integrated into a community-based perspective, as depicted in Fig. 2.1, more scalability is attained, since energy trading is handled collectively through a centralized management entity [51]. From the perspective of an AC MG, such a centralized unit is usually called as MG central controller (MGCC) [52]. Thus, the MGCC has two main roles: *i)* to represent a community of DERs in P2P markets, acting as a single player, by controlling the MG dispatchability to meet external energy demands and offer ancillary services; and *ii)* to coordinate the operation of elements internally to the MG, aiming to fulfill punctual demands of energy services from consumers/prosumers, as well as to meet their financial objectives.

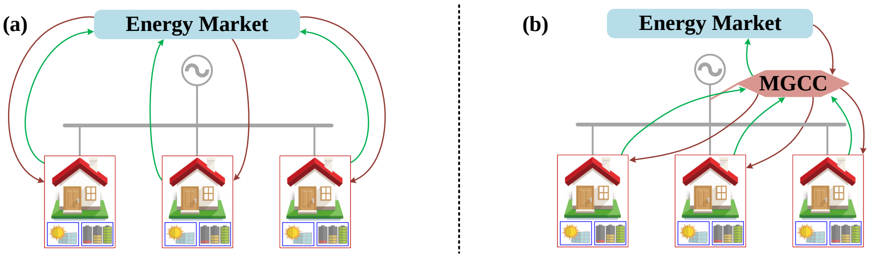

Figure 2.1: (a) Consumer-centric versus (b) community-based participation of DER owners in energy markets under the perspective of transactive MGs.

Taking into account aspects beyond market concerns, the MGCC can also be interpreted as a demand response aggregator (DRA) [53]. This means that the MGCC flexibly controls the MG to match internal and external energy demands, responding to grid conditions and market inputs, through the management of dispatchable and non-dispatchable grid apparatuses [54]. Finally, it is mentioned that the MGCC could also operate, and participate in energy markets, through the supervision of a MG operator (MGO) [37] that manages clusters of MGs [55]. However, since the perspective of MG clusters is outside the scope of this thesis, the MGO can be disregarded.

2.1.1 The Microgrid Transactive Energy Concept

By integrating market-oriented actions, demand response functionalities, and either consumer-centric or community-based management of DERs, the concept of MG transactive energy systems (MG-TES) arises [37]. First, transactive energy is an approach relating to the trading of energy services among participating entities. Thus, the conception of TESs allows market players to actively negotiate and establish contractual agreements to manage the demand and supply of electric power [56]. Moreover, in addition to the exchange of usable energy (i.e., control over active power), ancillary actions provided by market participants can also be interpreted as tradeable energy services [57]. Consequently, energy transactions may incorporate the trading of grid-support functionalities to strive for the enhanced operation of MGs and their interconnected power systems.

To support the implementation of MG-TESs, three main sectors need to be considered to endow transactive features [58]: *i)* the management sector; *ii)* the control sector; and *iii)* the market sector. They are further explained as follows:

- *Management sector*: An architecture has to be adopted to determine how the MG will operate, with regard to the management strategy of its internal elements. Such management can occur based on architectures that are centralized (e.g., as using a MGCC), distributed (e.g., based on multiple management units), or others approaches (e.g., game-theoretic, internet-based, so forth [39]). Additionally, this sector also establishes which roles will be played by the MG in energy markets (e.g., which energy services will be traded). For instance, a transactive MG can interact with one or multiple players, such as other MGs, DRAs, the DSO, the transmission system operator (TSO), or others. Another possibility would also be to manage the MG as an asset within the context of virtual power plants (VPPs) [59, 60]. Hence, the MG can trade particular services based on its internal energy planning, as well as according to the market demands at the time of establishing business interactions. For example, a MG can engage in contractual relations with its neighboring MG to offer ancillary services [61]. At the same time, it can trade active power dispatch with an interconnected upstream grid (e.g., DSO) [62];

- *Control sector*: This sector establishes the means for coordinating the operation of DERs to follow a given operational direction imposed by the MG management sector. In other words, a transactive control framework is defined within this level, determining how DERs need to operate to allow the MG to operate as a single controllable entity endowing dispatchable features. Additionally, the control strategy is also responsible for ensuring adequate operation of loads and other non-dispatchable grid elements, thus allowing the MG to deliver or utilize the sold or bought energy services, respectively;
- *Market sector*: This sector is characterized by the economic aspects of the transactions, establishing mathematical formulations for dynamic pricing and bidding, according to the availability of energy assets and participating players [37, 58]. Consequently, a transactive MG requires the employment of financial methodologies to support its business interactions, respecting market regulations. For example, the MG needs to determine price tags for its available provision of different energy services, or it needs to know when prices are advantageous to buy energy/services from other players. As inputs, the market sector uses economic goals, energy generation and consumption profiles, as well as the nominal capabilities of the MG, usually pursuing financial benefits. As outputs, operation setpoints quantitatively define the power dispatch of the MG, as well as its ancillary service provision, always respecting contractual constraints.

In Fig. 2.2, a summarized overview of the infrastructure behind the implementation of MG-TESs is given. Note that a transactive system is formed by a conglomeration of market-oriented and energy concepts comprising multiple players. Each player presents its own goals and assets, interacting with other agents according to market rules and the establishment of contractual relations. Moreover, an electrical infrastructure forms the backbone of the system, relying on technical and financial synergistic interactions among all participating agents to achieve adequate operation.

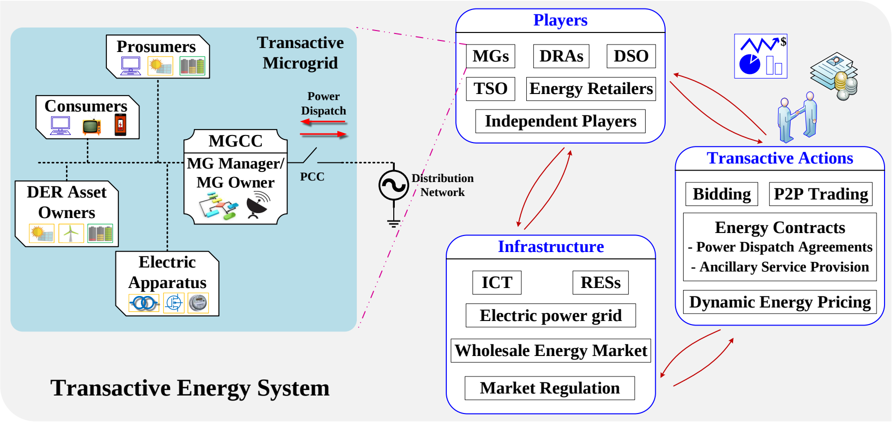

Figure 2.2: Summarized infrastructure of a TES incorporating MGs.

Particularly for the scenario of a MG coping with community-based management of DERs [51], its participation in TESs can be characterized by two main features. The first one is the capability to interact with other external agents, which indicates that communication needs to be considered to exchange information used for market and management purposes. The second feature relates to the flexibility of providing controllable power flow at the MG PCC, since this is the interaction point with external agents, from the physical point of view. Additionally, extending the perspective of energy control, by shaping voltages and currents at the MG PCC, different behaviors can be emulated to provide ancillary functionalities [25].

Although the consideration of market formulations is important to MG-TESs [58], this is beyond the scope of this thesis. Herein, the context of a MG relying on a centralized management architecture is adopted. Moreover, this thesis focuses on the control aspects required to coordinate DERs under a community-based perspective. As a result, a transactive control framework is discussed in Section 2.2, taking advantage of coordinated DERs to allow a LV MG to participate in energy transactions, and to flexibly offer ancillary service capabilities. Such a framework is used as a point of reference to later formulate a control strategy in Chapter 3.

2.2 A Flexible Framework for Microgrid Transactive Control

A framework to achieve generalization and flexibility of operation for the control sector of transactive MGs is herein presented. Such a control framework relies on six major aspects that, if incorporated into the coordination principles of inverter-interfaced DERs, can merge market and technical requirements of MG-TESs. These six aspects are presented in Fig. 2.3, indicating a subdivision into three main groups.

The first group comprises two fundamental technical features that allow a MG to operate as a transactive system. To trade energy with external agents, the MG needs to steer DERs to support a dispatchable PCC (or multiple interconnection terminals, if that is the case [63]). This means that, with respect to an upstream grid, the MG should adjust the coordination of inverters to bidirectionally control the power flow being imported or exported [64]. Such a feature is necessary because energy transactions are mainly formulated on the basis of power dispatch and consumption. In addition, if power dispatchability is sufficiently flexible to incorporate several purposes into a singular action, the possibility of offering ancillary services is broadened to a power system perspective [25]. In parallel, the second feature supporting the access to energy transactions is the capability to physically interact with external agents, which is usually determined by ICT infrastructures. Thus, communication is indispensable, even when a MGCC is not implemented for the MG management. Otherwise, it becomes difficult to quantify the MG capabilities and to devise adequate power control at the PCC.

The second group supporting flexible transactive control comprises market-oriented features, which bring economic reasons to light. Fundamentally, a MG operating under the grid-connected mode needs to obey interconnection contracts that establish limits for power dispatchability, and ensure grid code compliance [65]. Such contracts are obtained from market interactions between the MG and its upstream grid, and they constrain the flexibility to offer whichever energy services are desired by the MG manager. Nonetheless, under the presumption of meeting interconnection requirements, the MG can respond to any operation inputs established from overlaying market interactions. For instance, a MG may sell a certain amount of active power exportation to the DSO at a given time period, achieving such functionality by only setting this setpoint for the PCC power dispatchability [66]. Of course, energy planning and

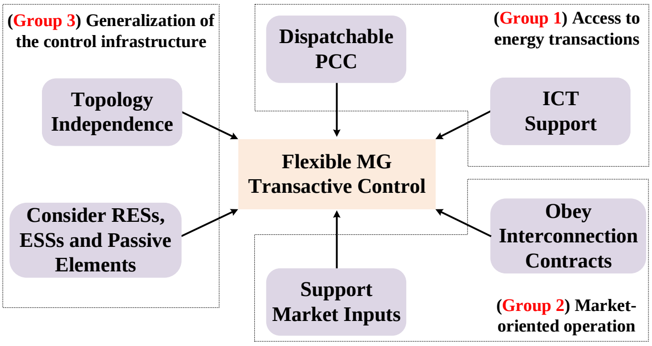

Figure 2.3: Proposed flexible framework for the transactive control of MGs.

forecasting are matters that need to be considered, and, referring to Fig. 2.3, this is not achievable without implementing the first group (i.e., dispatchable PCC and ICT support). Providing an answer to market inputs is also valid to the provision of energy services, as the active and reactive power dispatch of the MG can be devised to support, for example, voltage and frequency response, as well as to emulate spinning reserves and other behaviors [67].

The third group highlighted in Fig. 2.3 refers to the generalization of the control framework, extending its applicability to generic MGs. Since TESs may incorporate MGs of different natures, such as those designed under single-phase [41], poly-phase [42, 68], and mixed infrastructures [69], achieving a framework independent of topologies brings appealing market accessibility. For example, different MGs operating according to similar transactive control frameworks can be grouped as networked market players [70], providing integration of energy capacities to become more important agents in energy planning. The concept of model-free control is also incorporated within such topology independence, giving support to simplifying the coordination of DERs. In addition, if a strategy supports independent control over each phase of the MG, a higher degree of freedom is obtained for the provision of energy services [71].

Last, it is important for a control framework to accommodate DERs operating according to different natures [11, 72], allowing more functionalities to be offered, and increasing the flexibility of operation of the MG. Coordinated operation of dispatchable elements, such as ESSs, is capable of supporting precise controllability over the power flow at the PCC [43], while also being key elements of the economic profitability of MGs [73]. Additionally, without non-dispatchable generation, it is not trivial for MGs to reach a desired level of operational independence from the upstream grid and other market players, since more power needs to be imported. Consequently, the existence of nd-DERs should be incorporated into any control framework targeting transactive MGs. It is also important to highlight that, although such a transactive control framework mainly targets LV MGs in this thesis, it is can also be extended to perspectives at medium and high voltage levels [74].

2.3 An Outlook on Ancillary Service Provision Devised by Transactive Microgrids

So far in this thesis, it has been highlighted that offering ancillary services is comprised within the context of MGs operating as market players. Nonetheless, transactive MGs capable of providing multifunctionalities in the literature [37, 57, 58, 67] mainly focus on grid-support actions related to energy dispatch. This means that an AC MG offering ancillary services is mostly considered as an entity capable of exporting active and reactive power, under the perspective of demand response, to particularly benefit an upstream grid. Herein, discussions highlight that dispatchable MGs can play more diversified roles than the traditional demand response features (e.g., power reserves, load leveling, capacity firming [25, 67]), thus shedding light on the outlook of emerging ancillary services.

First, it is important to clarify that ancillary service provision in transactive MGs with dense penetration of DERs can be looked at from two different perspectives. The first one relates to the internal aspects of the MG, in which smart inverters are coordinated to offer multifunctionalities to support enhanced operation downstream from the PCC. On the other hand, the controllability of the MG as a single entity can be seen from another perspective, in which ancillary services are offered to the interconnected distribution grid or to any other external entity. This means that DERs can be coordinated for the provision of services that target technical or economic benefits upstream from the MG PCC.

2.3.1 Ancillary Service Support Downstream from the PCC

By looking internally into the MG, multiple ancillary services can be provided, as depicted by some examples shown in Fig. 2.4. For instance, Fig. 2.4(a) represents the scenario in which DERs can be coordinated to operate as voltage-controlled sources, providing grid support downstream from the PCC by regulating voltage magnitude and frequency [11]. Other capabilities, related to compensation of reactive power and suppression of harmonic currents, are also depicted in Fig. 2.4(b), in which it is seen that DERs can operate counteracting unwanted behaviors from loads and other MG elements [27].

Ancillary service provision related to internal voltage regulation in LV MGs is also

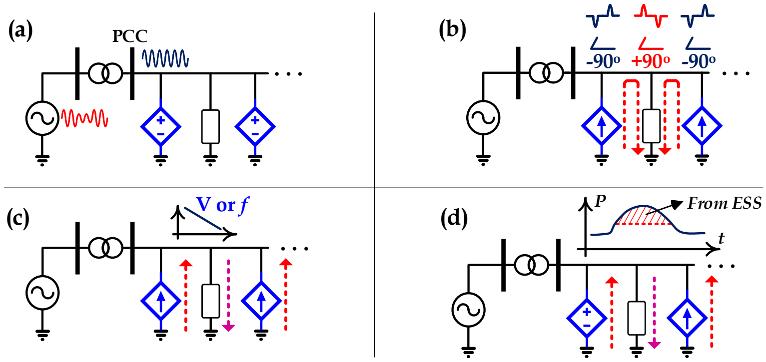

Figure 2.4: Examples of ancillary services provided internally to MGs (i.e., downstream): (a) regulation of voltage magnitude and frequency; (b) compensation of reactive power and harmonic currents; (c) active and reactive power control for voltage regulation; and (d) internal peak shaving functionality.

another important energy service demonstrated in Fig. 2.4(c). DERs can typically rely on controllable active and reactive power injections to respond to deviations in voltage profiles [75]. Finally, Fig. 2.4(d) shows that other advanced MG control functionalities, such as internal peak shaving [76] and routing of inner power flow [77], can be adopted as a means to achieve more sophisticated MG management through the steering of different DERs. Yet, many other functionalities can be devised for ancillary support in MGs [78].

Nonetheless, within the context of MG-TES, the internal offering of ancillary services is not necessarily important when the market participation of a MG is considered. This means that, although the provision of multifunctionalities downstream from the MG PCC is important, the MG mainly regulates its market participation based on external interactions. For that reason, discussions in this section focus upon the outlook of energy services provided outward to the MG (i.e., offered to the upstream grid or other market players).

2.3.2 Ancillary Service Support Upstream from the PCC

Now, looking externally into the MG, other multiple energy services can be realized, as long as DERs can be coordinated to control the dispatchability at the PCC respecting internal grid code requirements. In Fig. 2.5 a few of these services are depicted. Let us consider the scenario of n AC MGs connected in parallel to a bus (B_{mains}) from an upstream grid. If at least one of these MGs can implement a control framework similar to the one presented in Section 2.2, its PCC can be shaped to the provision of multiple ancillary services.

For instance, a possible grid-support feature is the capability of a dispatchable MG to control its active and reactive power dispatch to regulate voltage magnitude and frequency at B_{mains}. Due to uneven power dispatch and consumption in parallel MGs, the voltages and frequency imposed by the upstream grid can deviate from acceptable limits, requiring actions such as transformer tap changing and the adjustment of active and reactive power dispatch [79]. As seen in Fig. 2.5(a), a transactive MG can adjust the setpoints of its absorption or injection of active power, or even provide reactive power injection, to support voltage and/or frequency regulation [80]. This can be done autonomously by measuring voltages at its PCC, or can be commanded by either the DSO or by neighboring MGs. Thus, the MG can trade voltage regulation functionalities with external agents.

The market interactions of a MG can also allow it to engage in contractual relations to supply neighboring MGs at certain time periods, as shown in Fig. 2.5(b). Such an energy supply service can incorporate injection/absorption of precise amounts of reactive power, in order to avoid penalties caused by low power factor. Moreover, absorption (i.e., storage) of active power can also be realized as an ancillary action,

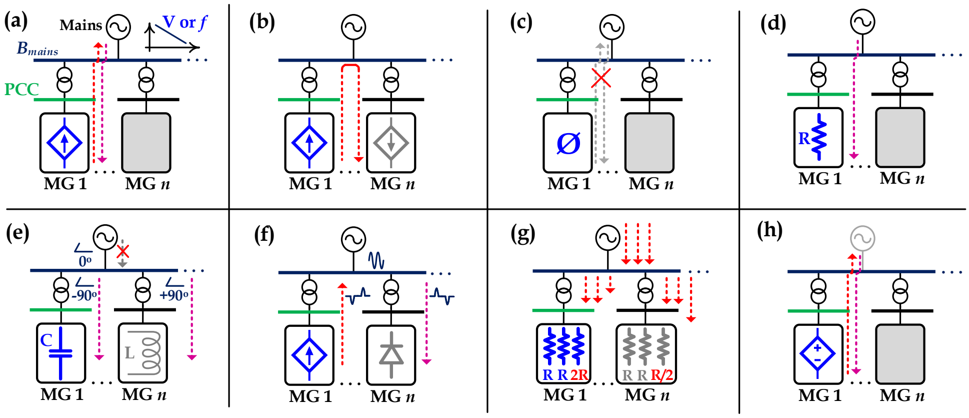

Figure 2.5: Transactive MGs with dispatchable PCC supporting the offering of multiple ancillary functionalities as external energy services: (a) voltage and frequency regulation by controllable power dispatch; (b) power supply of neighboring MGs; (c) self-consumption mode; (d) resistive shaping; (e) inductive or capacitive shaping; (f) compensation of harmonics; (g) correction of unbalanced power dispatch; and (h) multiple MGs forming the grid upon faults or after natural disasters.

balancing energy dispatchability in a bus like B_{mains} [81]. Consequently, actions interrelating networked MGs can occur without intervention from the upstream grid, which can bring economic benefits for MGs and increase energy efficiency.

Other interesting ancillary functionalities allow a transactive MG to emulate different behaviors according to what is desired by the upstream grid. For instance, if full controllability over the dispatch of fundamental and harmonic currents is supported by the MG, null power flow through the PCC can be imposed. In other words, this means that DERs can entirely supply the MG's internal needs. Thus, the MG can be seen as a self-sufficient entity that does not rely on the power dispatch provided from the mains, as depicted in Fig. 2.5(c).

The MG's self-consumption functionality is useful for lowering the burden of the grid, upon restricted levels of power demand and supply [25, 44]. Besides, the MG causes minimum impact on the operation of the distribution system under such an operational mode. Similarly, Fig. 2.5(d) shows that the MG can be self-sufficient only in non-active power, allowing the DSO to mainly deliver usable energy (i.e., interpreting the MG as a pure resistor at the PCC), which minimizes losses at the distribution system, and supports voltage regulation. Note that the only difference between these last two modes of Figs. 2.5(c) and 2.5(d) is the power terms shared among DERs internally to the MG.

As shown in Fig. 2.5(e) reactive power consumption in LV systems usually presents a predominantly inductive behavior due to the features of residential and commercial loads. Hence, a dispatchable MG could also operate as a single multifunctional device [25], offering compensation of reactive power. To provide that feature, an upstream grid can buy from a transactive MG the flexibility to dispatch specific amounts of either inductive or capacitive power. Consequently, dual operations can be realized by parallel MGs, allowing the mains to principally interpret their integrated behaviors as a resistive load (i.e., similarly to Fig. 2.5(d)), or even as in Fig. 2.5(c), if no active power needs to be supplied in steady state operation.

Two additional ancillary services relate to the provision of power quality interventions on a power system scale [81]. The case in Fig. 2.5(f), for example, demonstrates that MGs with dispatchable harmonic capabilities can support compensation of distortion currents drawn by neighboring MGs. Yet, services could be offered to improve the damping of harmonic resonances propagated throughout the distribution system [82], which is of particular interest from the LV perspective [83]. Of course, this functionality is only possible if the impact of dispatching harmonics through distribution transformers and electric conductors has previously been assessed. As another possibility, if the employed control framework is capable of controlling power dispatch through the PCC at each phase individually, support can also be given to balance the power dispatch. This is, for instance, depicted in Fig. 2.5(g), when MG n demands unbalanced currents, another neighbouring MG with transactive features can be demanded by the DSO to counterbalance such an unwanted effect. One challenging research topic behind these power quality-oriented actions, however, relates to the pricing of such ancillary services in energy markets [84].

Finally, in Fig. 2.5(h) one can see a scenario in which the upstream grid is absent (i.e., also representing a faulty condition), and there is no other entity imposing the voltage and frequency references for the overall electric system. This is a typical scenario occurring upon natural disasters [85, 86]. If an interconnected MG presents dispatchable voltage-controlled converters, they can be coordinated to form a grid-forming unit. Consequently, one or multiple transactive MGs could form the grid and supply critical loads for a certain amount of time [85], during the mains absence. Of course, this is only realistic if control strategies are adopted to detect such an abnormal condition and adjust the steering of DERs, knowing that MGs have to present sufficient power capability to provide that functionality for a short period of time [87]. Since this a complex scenario for what concerns MGs' management, as well as for the control of DERs given their limited nominal ratings, strategies such as load shedding and re-dispatch must be concomitantly considered [88].

Overall, it is reinforced that the above-mentioned ancillary services are examples of the under-explored potential of transactive MGs incorporating full dispatchability into their operations. Such features, which are endowed by the adoption of a flexible transactive control framework, are used as motivation for the following chapters of this thesis. Most of these services not only can be applied to LV MGs, but also at medium and high voltage levels, and for some perspectives of active distribution networks [89].

2.4 Chapter Conclusions

In this chapter, the basic concepts behind the implementation of transactive AC MGs were highlighted, demonstrating that many operational aspects need to be taken into account prior to devising the coordination of DERs. For instance, a transactive management architecture needs to be understood to structure the external interactivity of the MG. Concomitantly, the intended market participation of the MG needs to be clarified, since functionalities supporting tradeable energy services should be considered while formulating a coordinated control strategy.

A transactive control framework was also discussed in this chapter, proposing six main pillars (i.e., dispatchable PCC, ICT support, interconnection contracts, market inputs, multiple DERs, and topology independence) to support the implementation of MG-TESs. By following such control principles, flexibility of operation can be attained for MGs implementing community-based management of DERs, considering that a centralized manager (i.e., the MGCC) takes responsibility for market interactions. The coordination of inverters proposed within this thesis incorporates all six pillars, although it does not address matters: *i)* existing for the determination of market inputs, such as market models [40]; or *ii)* business-/policy-related actions required to establish MG interconnection contracts [65].

An extended outlook on the ancillary provision of transactive MGs was also presented, indicating that multiple energy services are tradeable, if the coordination of DERs flexibly supports full power dispatchability at the PCC. It was discussed that ancillary services may refer to either functionalities improving the internal operation of an AC MG, or control capabilities that shape the MG to act according to different principles. With regard to multifunctionalities offered internally to the MG, this thesis focuses on the features related to the sharing of currents among DERs, allowing active power control and compensation of reactive, harmonic and unbalance currents. In addition, internal voltage regulation determined by active and reactive power control of DERs is discussed. On the other hand, the provision of ancillary actions externally to the MG, lying within the subject of this thesis, relate to: *i)* the full self-consumption mode of operation; *ii)* the flexible controllability over reactive power dispatch [66]; as well as *iii)* the capability to shape a resistive behavior at the PCC [90].

Chapter 3

Coordinated Control of DERs in Low-Voltage Microgrids

3.1 Introduction

In this section, a centralized control strategy for the coordination of multiple DERs existing in a LV MG is devised. However, before presenting such a control approach, some premises are discussed with regard to the topology of the MG infrastructure, and concerning the structure of the considered DERs. Having the scenario of application well defined, the Generalized Current-Based Control (GCBC) strategy is explained, demonstrating that the coordination of DERs can be devised by the analysis of current terms flowing within the MG. Moreover, besides its simple formulation and multipurpose operational capabilities, it presents model-free and plug-and-play features.

3.2 Considered Microgrid Topology

This thesis focuses only on the scenario of LV power systems that present limited size, considering significant penetration of inverter-based DERs of different operational natures (i.e., being of a dispatchable and non-dispatchable nature). As discussed in Chapter 1, such a perspective characterizes the premise of residential LV MGs that are integrated into distribution networks.

Such MGs are formed by the aggregation of loads and DERs under a community-based synergy, and they can operate under either islanded or grid-connected mode. When the MG operates islanded, even though this scenario occurs sporadically in relation to its overall amount of operating hours [5], the need for reliable power supply takes precedence over transactive features [91]. Moreover, it is evident in the literature that in-depth research has been performed for the management and coordination of DERs in islanded MGs [31, 32, 33], rather than the aspect of interconnected MGs.

As a consequence, the overall MG panorama of this thesis is revealed. This thesis strives for further exploring inverter-dominated LV MGs while operating interconnected to an upstream grid, taking into account their participation in transactive markets. Therefore, two main aspects are important to the foundation for developing a multi-purpose coordination of DERs, being: *i)* the features of the MG electric infrastructure (e.g., its topology and *X/R* ratio of line impedances); and *ii)* the homogeneity of the MG elements, particularly with regard to DERs, loads and line impedances.

First, the MG electric infrastructure is described by the placement of the distribution system transformer (DST) and the feature of line impedances. The DST is responsible for providing galvanic insulation for the MG, also operating as an interface element that supports electric interconnection to the upstream distribution grid. The main consideration about this interface transformer is that its placement in the MG defines a single PCC. Thus, this thesis considers that there is only one electrical point at which power exchange between the MG and the upstream grid occurs. Additionally, it is highlighted that the existence of the DST is not mandatory for the control strategy herein developed, as long as the MG presents only one PCC, which is typically the case for radial topologies [92]. The scenario of multi-terminal MGs [74] (i.e., comprising multiple interconnections points) [93] is not within the scope of this study. This latter perspective is disregarded due to the fact that multi-terminal MGs require increased complexity to achieve controllable power dispatchability [93].

Since MG nodes are connected by cables that ought not to be idealized, the features of line impedances are important. For the herein considered MG scenario, line impedances are characterized by a low *X/R* ratio (i.e., $X/R < 1.0$). This means that they present resistive behavior, instead of the predominantly inductive characteristic found in long distribution or transmission systems. Such a consideration copes with the expectations of typical LV systems (e.g., as found in residential MGs) [11]. Moreover, in general, the inductive feature of line impedances in such LV systems can be neglected [11], resulting in no significant voltage phase shifts occurring throughout electrical nodes (i.e., for the cases in which the MG presents limited size). This consideration is important for the control features of the coordination strategy of DERs described in Section 3.5, as well as later discussed in Section 5.8.

The second important aspect (i.e., homogeneity) of the considered MG infrastructure relates to the uniformity of the placement and features of its elements. This aspect specifically refers to the physical disposition of line impedances, as well as to the locations and power densities of DERs and loads. By stating that homogeneous line impedances exist [94], for instance, one determines that electric conductors present a similar impedance value per length. In addition, this indicates that the distances between adjacent electric nodes are fairly similar throughout the MG. Likewise, the homogeneity of DERs relates to their uniform distribution over the MG, as well as to their low discrepancy in power density (i.e., they present power ratings of a similar range). With regard to loads, homogeneity basically consists of having uniform distribution of power demand within the MG.

The importance of determining such a homogeneous aspect for the considered MG is tied to the facts that losses turn out to be minimized while steering inverters proportionally to their nominal ratings [95], and that voltage quality improvement can be obtained as an indirect outcome of DERs' coordination. The former fact is discussed throughout Chapter 4, and the latter is explored in Section 5.5. Having discussed the most important aspects of the MG infrastructure, the grid topology used as main reference hereon is presented in Fig. 3.1. Such an MG infrastructure is based on the consolidated CIGRE's LV European benchmark presented in [96], considering slight modifications with respect to DERs and loads. It is important to reinforce that only the residential branch of the testbench from [96] is used.

From Fig. 3.1, one can directly comprehend the aforementioned MG aspects. Note that the upstream grid is connected to the MG through the DST. Distribution systems usually comprise three conductors for each phase (a, b, and c), and the MG is composed of four-wires (i.e., three phases plus neutral). A circuit breaker (CB_{MG}) is responsible for isolating the MG, if required. The MG also presents a PCC, at which voltages and currents need to be measured for attaining bidirectional power flow controllability.

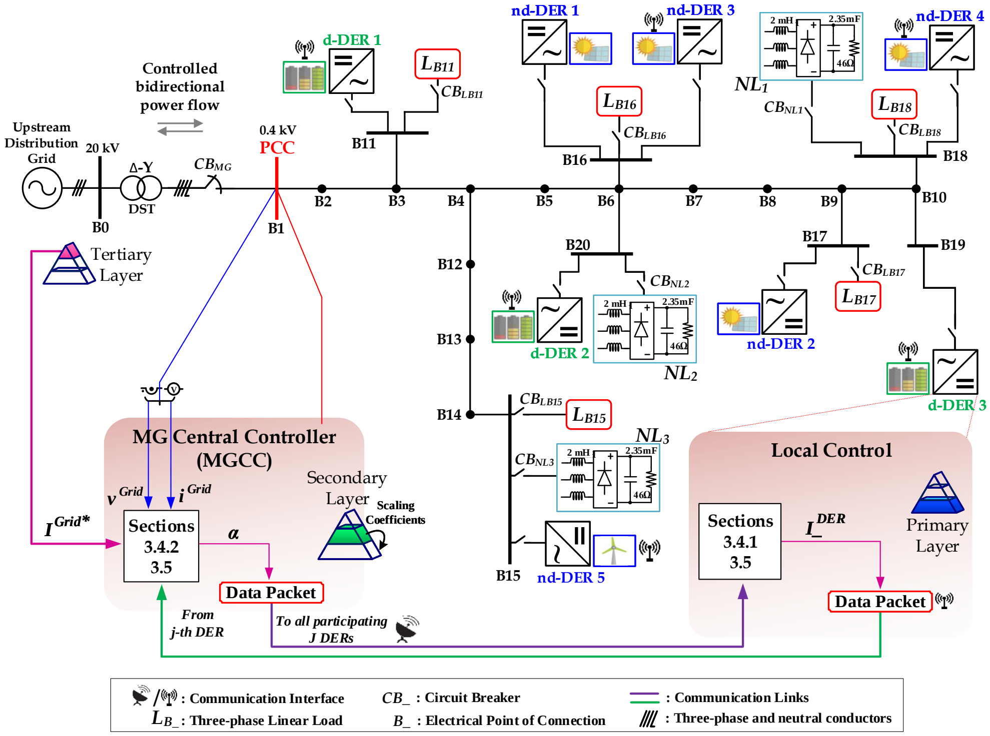

Figure 3.1: Electrical infrastructure and control topology of the considered LV MG, based on the residential branch of the CIGRE LV European benchmark [96].

As mentioned in Chapters 1 and 2, the considered MG strives for a community-based participation of DERs in energy markets. Consequently, a centralized control unit (i.e., MGCC) is placed at the PCC, managing the MG operation and giving support for a centralized coordination of DERs. As in any centralized approach, communication means must exist for exchanging information among the participating elements, which are basically comprised of DERs. Thus, an ICT infrastructure is considered, establishing low-bandwidth communication links for data exchange [97]. In addition, communication is used as a means for the MG's participation in transactive markets, by exchanging information with other players, such as the DSO. The MG transactive control coordinates DERs based on a three-layer hierarchical architecture that is further explained in Section 3.4.

In contrast to the original MG layout from [96], this thesis considers the existence of both linear (L_B) and non-linear (NL) loads. Fig. 3.1 shows that such loads are uniformly dispersed in the MG. Yet, since non-linear loads usually impair power quality in MGs [27], another reason for their implementation is to study how coordinated DERs can be used to offer ancillary services to minimize detrimental effects. With regard to the DERs in the MG, they present either dispatchable (i.e., d-DER) or non-dispatchable (i.e., nd-DER) natures (see Fig. 3.1). In addition, two further categories are considered, characterized by either the presence of a communication interface or the absence of it. A more detailed discussion about the operational features of DERs and their control loops is provided in Section 3.3.

Finally, it is reinforced that, even though islanded MG operation is not within the scope of this thesis, such a condition is a possible scenario [91], and it should not be neglected. Thus, discussions about this operational mode are presented in Section 4.4.1 to demonstrate that the multi-purpose coordination of DERs also copes with such a scenario.

3.3 Topology and Control of the Considered DERs

3.3.1 Considered DERs and their Respective Functionalities

To cope with more realistic scenarios, the MG targeted in this thesis considers two main categories of inverter-based DERs: nd-DERs and d-DERs. Both of these categories present particular control functionalities, which are briefly described herein, being also depicted in Table 3.1.

With regard to nd-DERs, two groups (namely, type A and type B) are taken into account. Type A inverters operate as ordinary distributed generators. This means that their major goal is to feed-in active power to the MG, rather than performing multifunctionalities to contribute to grid support. Consequently, those inverters are

Table 3.1: Features and functionalities of the considered DERs.

		Dispatchable	Communication (Remote Control)	Active Control	Reactive Control	Harmonic Control
nd-DER	**Type A**	✗	✗	✓	✗	✗
	Type B	✗	✓	✓[†]	✓	✓
d-DER		✓	✓	✓	✓	✓

[†] Not performed under coordinated control.

not capable of injecting reactive or harmonic currents. Moreover, they do not present a communication interface, which also restricts their participation in communication-dependent strategies of coordinated control.

On the other hand, type B nd-DERs are smart inverters that comprise non-dispatchable energy generation at their DC side. They present communication interfaces, being also able to offer functionalities to support an improved operation of the MG, as advised by the recommended standards [8]. Among several possible multi-functionalities [14, 15], focus is primarily given to the control of reactive and harmonic currents. Additionally, since remote management is possible for such nd-DERs, they can participate in coordinated control strategies to provide ancillary services. Nonetheless, due to their lack of power dispatchability, active power control cannot be considered under a coordinated perspective.

Lastly, d-DERs comprise inverters capable of supporting power dispatchability features, as they present non-intermittent energy systems at their DC side, such as ESSs. Due to their nature, they can be employed in most functionalities desired for DERs, providing not only active power conversion, but also participating in ancillary actions if they present remaining power capabilities. Such inverters embed communication interfaces, making them the most important devices of the multi-purpose coordination strategy presented in this thesis.

3.3.2 Topology and Control of DERs

The power electronics perspective of the DERs, considered for most of the simulated scenarios in this thesis, takes into account three-phase three-leg inverters with LCL output filters. The use of the LCL topology is adopted due to its improved filtering capability, which allows the possibility to minimize the harmonic effects caused by the high frequency switching of an inverter [98]. The single-phase equivalent circuit of the considered DERs is depicted in Fig. 3.2. Moreover, a generalized implementation of the control loops of nd- and d-DERs is presented.

Typically, commercial grid-tied inverters behave as current sources [11] (i.e., namely current controlled mode (CCM)), to comply with grid codes more effectively.

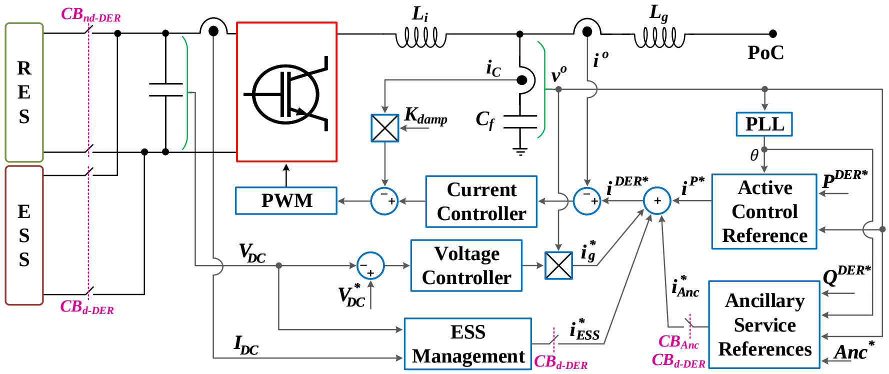

Figure 3.2: Control model of the considered DERs (single-phase equivalent circuit).

Consequently, since the main focus of this thesis is to support the transactive aspect of the MG (i.e., being most important when it operates interconnected), all d- and nd-DERs are assumed to operate under CCM. Such a control principle is commonly adopted for nd-DERs in the literature [11], given that it is also one of the possible operational modes of d-DERs [30, 72]. Moreover, it is important to highlight that, d-DERs could also be driven as voltage-controlled sources (i.e., voltage controlled mode (VCM)), if desired. However, in that case, VCM d-DERs would need to generally implement triple loop control approaches [99], as they should adjust their output voltage in order to follow a given current reference for their grid current loop [100].

Note that in Fig. 3.2 the generic difference in topology between nd-DERs and d-DERs is the energy system at their DC side. For nd-DERs, the circuit breaker $CB_{nd\text{-}DER}$ is closed, connecting the RESs to their inverters (i.e., already considering possible DC-DC conversion stages [19]). On the other hand, d-DERs consider the circuit breaker $CB_{d\text{-}DER}$ closed, which integrates an ESS into the inverter, making it into a dispatchable unit. Yet, even though LCL output filters are adopted for the inverters, any other topology could be employed (e.g., LC and L filters), as long as the grid-side current (i.e., $i^o(t)$) can be controlled or estimated [101]. This is required to achieve the appropriate stiffness and coordination of DERs, as it will be further explained in Section 3.5.

With particular reference to the control model, Fig. 3.2 shows that many control loops can be implemented, according to the operational nature of the DERs. Two basic control aspects are mentioned: *i)* the need for adequate synchronization with voltages at the point-of-connection (PoC) of a DER, which requires the implementation of a phase-locked-loop (PLL) algorithm; and *ii)* the modulation strategy of the inverter's power switches, which is determined by the pulse-width modulation (PWM) approach. In order to control the inverter under CCM, two main loops are required.

The first one, which is the voltage control loop, is responsible for regulating the voltage (V_{DC}) at the DC bus of the inverter, being usually implemented with proportional integral (PI) regulators. The output of this regulator is multiplied by the PoC voltage (v^o) to obtain the reference current (i_g^*) responsible for stabilizing the DC link voltage. Additionally, the voltage loop is designed to be much slower than the response of the current loop [102], knowing that the latter constitutes the second main control target. The current loop is responsible for providing adequate tracking of the reference current $i^{DER*}(t)$ of the inverter. Moreover, if the control design is devised directly in the time domain (i.e., *abc* frame), as performed in this thesis, proportional resonant (PRes) [102] or proportional repetitive (PRep) [103] controllers are interesting alternatives to attain null steady-state error. The models of the current regulators of DERs can be found in Appendixes B.1.3 and C.1.2 .

The term $i^{DER*}(t)$ comprises all the functionalities offered by a DER operating under CCM. For instance, as type A nd-DERs only control active current, just a control block to generate the active current reference (i^{P*}) is required [104] (see Fig. 3.2). Such a reference is calculated based on a setpoint of active power (P^{DER}), which usually comes from maximum power point tracking (MPPT) algorithms. When it comes to type B nd-DERs, they operate as the type A ones, but with an additional control block for generating the reference current i_{Anc}^*, which is responsible for offering ancillary services. Many functionalities can be incorporated into i_{Anc}^* by adequately setting reactive power setpoints (Q^{DER*}), or by selecting other services based on the variable Anc^* [16, 19, 104]. As an example, Anc^* could activate the generation of harmonic current references for compensation purposes [104].

Compared to type B nd-DERs, the control of a d-DER operating under CCM requires an additional block, which is responsible for adequately exploiting the ESS. This occurs because a dispatchable source requires complementary management actions, for example, battery-based ESSs need to account for state-of-charge (SoC) conditions [105]. The reference i_{ESS}^* is usually the one responsible for adding such a control feature to d-DERs. Finally, it is mentioned that the active damping control strategy used in [104] is adopted by implementing the gain K_{damp}, which scales the capacitor current (i_c) feeding the output of the current controller [106]. Such an approach is needed since the LCL filter is known to add one extra pole to the control plant of the inverter, which complicates the control design, and may cause undesired oscillations, or even bring instability concerns [106, 107].

3.4 Hierarchical Control Architecture

The MG management and multi-purpose coordination of DERs presented in this thesis is designed with a grounding in a hierarchical architecture [31, 108]. Such an approach allows the possibility to organize multiple operational goals and manage actions (i.e., from DERs and the MGCC), according to levels of priority and requirements related to computational processing capabilities, as well as based on communication requirements. A three-layer topology is defined for the hierarchical MG architecture, following a multi-rate processing approach that considers: *i)* the need for adequate local (i.e., nodal) operation of DERs; *ii)* integrated actions of several dispersed inverters (i.e., coordinated control of DERs); and *iii)* global management of the MG based on internal and external objectives, such as the ones related to compliance with grid codes and energy contracts, as well as the offer of controllable power dispatchability and ancillary services.

In accordance with this concept, three layers of control are responsible for the entire operation of the MG and its interaction with an upstream power grid through its interconnection point. In Fig. 3.3 an overview of this architecture is presented, summarizing the scope of the control layers. The primary layer basically comprises all the local configurations and algorithms required to adequately control each DER connected to the MG. The secondary control establishes the means for coordinating DERs based on global and local expectations of operation. The tertiary layer supports the MG interaction with external market or regulatory players, allowing it to respond to external energy demands, as well as providing intelligent and/or optimal management and exploitation of MG elements. A more detailed explanation about each hierarchical control layer is presented as follows.

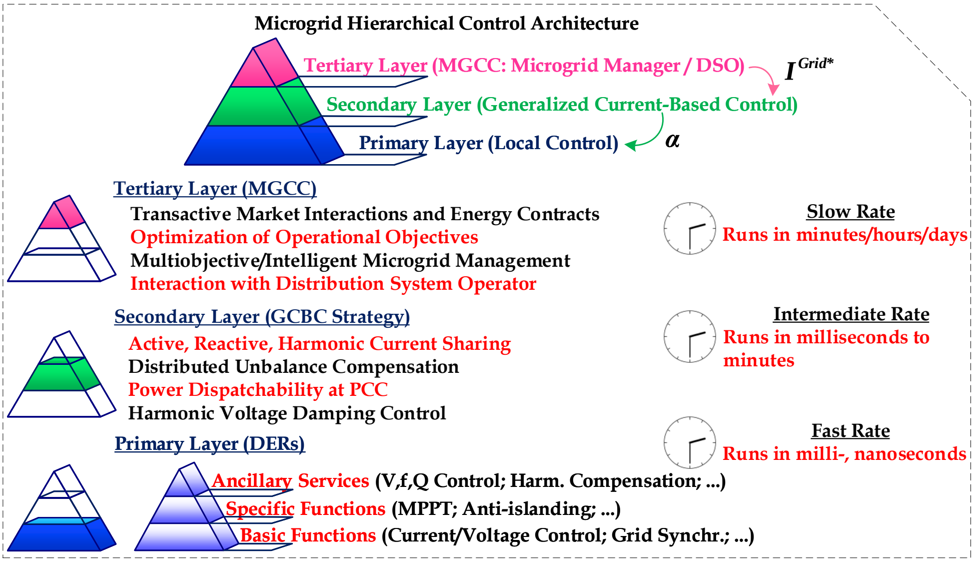

Figure 3.3: Proposed MG architecture with hierarchical layers and multi-rate control.

3.4.1 Primary Layer Control

This control layer is implemented locally at each DER. Its main responsibility is to guarantee that DERs attain adequate electric connection to the MG. Thus, reliable operation and compliance with local grid codes [109] are achieved. This is possible by adequate control algorithms that manage the processing of local currents and voltages modulated by each inverter.

As seen in Fig. 3.3, this primary level of control comprises basic, specific and ancillary services [19]. Consequently, an individual DER can offer power conversion from RESs or ESSs coupled to its DC voltage bus, concomitantly considering protection features and grid synchronization. Moreover, multifunctional actions can be enabled, giving local support to the MG if required [110]. Those local functions can be efficiently performed regardless of the status of other grid nodes. In addition, the local control of DERs does not rely on communication, which ensures that MG stability is not impaired under faulty exchange of information between the MGCC and DERs [111].

Since this level deals with the control of switching power electronics devices, it must run under a fast processing rate from nano- to milliseconds, depending on how the local voltage and current controllers are implemented. Moreover, the interactions of this hierarchical layer with the upper one occur directly through a low-bandwidth communication link, which exist for DERs comprising remote control capabilities [8]. Recalling Fig. 3.1, one can note that the primary control layer is processed only locally at the DERs, and it may use communication links to interact with the MGCC. As an outcome of the interactions among the primary and secondary layers, scaling coefficients (α) provided by the MGCC are used in the calculation of the local current references (i^{DER*}) of a DER. Such coefficients are explained in the following section, and the relation between i^{DER*} and α is explained in Section 3.5.

It is finally reinforced that, since this thesis also considers the existence of nd-DERs characterized by the absence of communication interfaces (i.e., type A inverters), such devices only present the primary layer of control implemented for ruling their local operations. This means that such DERs operate based on their own operational principles and local goals.

3.4.2 Secondary Layer Control

Traditionally, secondary layers of MG hierarchical approaches are implemented for correcting voltage amplitude and frequency deviations caused by the primary control [31, 108], especially for droop-based strategies. Moreover, secondary control may include additional coordinated functions to improve the MG operation, such as voltage stabilization, reduction of distribution and conversion losses, accurate load power sharing and disturbances compensation [112]. Nevertheless, a droop-free control approach is designed in this thesis, implying that this layer implements fairly different control concepts.

The secondary layer herein presented is primarily responsible for the coordination of DERs, as well as for controlling MG operations. As can be seen in Fig. 3.1, this layer is entirely processed at the MGCC, which must be placed at the PCC in order to support controllability over the power flow at this point. To coordinate the steering of DERs, the MGCC must gather information from all participating inverters, and the GCBC strategy is used as a framework to exploit them according to the desired objectives.

Thus, as presented in Fig. 3.3, the secondary control level ensures that active, reactive and harmonic current sharing is adequately attained among participating DERs, by means of the GCBC algorithm. Furthermore, by the simple and flexible formulation of the GCBC discussed in Section 3.5, the MG can impose different conditions of power flow at the PCC to comply with market and contractual requirements. The offer of ancillary energy services such as the compensation of unbalanced current or voltage components, as well as voltage regulation and damping of harmonic resonances, is also managed at this layer. Consequently, the secondary control provides the means to offer the transactive ancillary provision discussed in Chapter 2.

One important aspect of this layer is that it requires communication capabilities to ensure an exchange of information with the primary and tertiary layers. With respect to the former, the MGCC demands information about electric quantities from DERs, returning them control coefficients (α) that scale their participation in the coordinated functionalities (e.g., active power injection, reactive current compensation, so forth). Relating to the latter (i.e., tertiary layer), the secondary control requires inputs for enabling the proper MG functionalities, also demanding setpoints (I^{Grid*}) that determine the status of the power flow at the PCC (see Fig 3.1). The complete meaning of the terms α and I^{Grid*} are explained along with the GCBC strategy in Section 3.5.

Lastly, it is stated that a time rate of milliseconds to minutes is required to operate this control layer, since it relies on the data exchange with both primary and tertiary layers, which present faster and slower processing times, respectively.

3.4.3 Tertiary Layer Control

This top layer is implemented as a means for attaining proper interactions with external energy players (e.g., DSO, DRAs, other MGs, etc), and concomitantly monitoring the MG functionalities devised to several internal and external purposes. Such tertiary control is usually implemented at the MGCC to facilitate the integration with the other layers, and it incorporates the energy market aspects that allow the MG to participate in transactive relations. It is highlighted that there is no impediment for this layer to be remotely settled in a computational unit dispersed over the electrical system. Basically, the tertiary layer comprises all the information about the overall energy generation, and power consumption profiles expected for the MG within a certain time period (e.g., hours, days, months). As a consequence, in possession of such information, the MG manager can determine the needs and capabilities related to power dispatchability, thus allowing a planned market participation.

Another role of this layer is to establish interconnection contracts with the DSO. Due to stability and power planning matters, in order for a MG to be coupled to a distribution system, it has to comply with contractual requirements. Such requirements can basically be translated into limits for the dispatch or absorption of active and reactive power, also determining compliance with power quality standards at the PCC [65]. Despite the fact that such operational boundaries can change throughout the lifetime of a MG, they are important parameters for regulating the offer of energy services, becoming fundamental within the control aspects devised by the secondary layer. For instance, upper ($\overline{I^{Grid}}$) and lower ($\underline{I^{Grid}}$) contractual limits (i.e., later explained in Section 3.5) constrain the MG power dispatchability, therefore they need to be considered within the GCBC strategy.

As presented in Fig. 3.3, the tertiary layer is also responsible for incorporating optimization [66] or intelligent control algorithms [113] into the MG management. This is an interesting possibility because the MG operation and the coordination of DERs can be devised according to approaches that not only provide multi-purpose operation, but are also able to extract the most from the system capabilities. Thus, the operation of the tertiary layer can extend the coordination of DERs to functionalities that lead to an even more sophisticated MG management.

A longer timeframe is needed for the operation of the tertiary layer, running from minutes to days, since it handles data and interactions of slow nature (i.e., market relations, energy planning, etc.). In addition, due to the possible implementation of complex algorithms (e.g., used for market decisions and optimized MG operation) high computational capability is usually required.

3.5 Generalized Current-Based Control of DERs

3.5.1 GCBC Strategy: Premises

The GCBC strategy is herein devised as a centralized approach that coordinates inverters to offer multiple operational functionalities. Following the aforementioned hierarchical infrastructure, the steering of DERs occurs based on the analysis of peak currents flowing within the MG. More specifically, such peak (i.e, magnitude) currents are analyzed for all DERs participating in the coordinated control strategy, as well as for the currents flowing through the MG PCC. Therefore, scaling coefficients (α) can be calculated to adjust the currents being processed by the inverters. The GCBC strategy is primarily processed at the MGCC, relying on communication means to achieve bidirectional data exchange with DERs.

The GCBC approach is formulated considering in-phase (i.e., subscript "$_{||}$") and quadrature (i.e., subscript "$_{\perp}$") components of currents in relation to PoCs or PCC voltages, and no load currents need to be measured, which provides interesting scalability to applications in LV MGs. Considering a generic time domain current flowing through a node, $i(t)$, its in-phase component, $i_{||}(t)$, is characterized by a waveform that presents no phase-shift in relation to the voltage of that same node. Similarly, the quadrature element, $i_{\perp}(t)$, is defined by the current component that is orthogonal to that voltage. Thus, one can reconstruct $i(t)$ based on Eq. 3.1.

$$i(t) = i_{||}(t) + i_{\perp}(t) \tag{3.1}$$

Since the GCBC approach relies on the analysis of current components, three premises are important: *i)* the reason for using peak current terms; *ii)* the choice of providing MG management based on currents instead of power terms; and *iii)* the formulation of a centralized approach.

The initial premise relates to the fact that, following a cooperative perspective in which many DERs may exist, the analysis of currents flowing within a LV MG is usually not practicable under a time-domain perspective. This occurs because the status of several DERs needs to be processed in a coordinated way. Consequently, even though communication links might present fast transmission rates, currently it would not be realistic to implement it in real-life applications of MG control, given the existing technologies [114]. Usually, low-bandwidth communication is used for MG management [114, 115]. Thus, instead of analyzing time domain current components (i.e., instantaneous magnitude and phase), one can use their peak values as parameters, as has been done for the GCBC strategy. By using peak currents as control parameters, a simplified implementation method can be devised for the coordination strategy, since a reduced amount of data is analyzed and transmitted through low-bandwidth channels.

With regard to the second premise, it is known that power-based coordination of DERs is more commonly considered in the literature [108, 116, 117], due to its simplified interpretation and straightforward implementation. Nonetheless, power-based coordination of DERs is not trivial to be formulated when non-ideal operational aspects are faced, such as upon the existence of harmonics and unbalanced components in currents or voltages. By choosing a current-based approach, more flexibility can be attained to interpret the physical interactions occurring within the MG, and in some cases, the coordination of DERs to achieve proportional power sharing might be facilitated [118, 119, 120].

Lastly, the choice of a centralized approach is due to the operational feature of the MG. Since this thesis focuses on MGs that are interconnected and intend to participate in transactive energy markets, the ICT infrastructure is a fundamental element. Additionally, the MG power dispatchability cannot be adequately controlled unless a monitoring unit assesses the power flow through the PCC. Consequently, such quantification of the power flow should also be accounted for while coordinating inverters. Yet, another aspect is that power sharing among DERs can be more accurately devised if communication is employed [121]. Thus, although centralized MG management may present limitations tied to the dependence on communication links and the centralization of data processing [108], if properly designed, it can offer more flexibility of operation, as well as superior performance, than distributed or decentralized strategies [122].

3.5.2 The GCBC Strategy for Coordination of DERs

Let us consider that in an interconnected LV MG there is a number *J* (i.e., *j=1,2,3,...,J*) of DERs that are interfaced by inverters. Any DER can be controlled by the GCBC strategy, so long as they present communication interface and remote control capabilities. Particularly for the case of nd-DERs, due to their feature of presenting intermittent and non-dispatchable generation, active power control is not usually considered for coordination. However, nd-DERs can still participate in the coordinated control strategy (e.g., concerning reactive and harmonic control), if they present the remaining power capability and can operate as a multifunctional device.

Herein, the peak value (I) of a current component from a DER or from the PCC will be denoted by I^{DER} and I^{Grid}, respectively, being required for explaining the GCBC strategy. Additionally, the following fundamental concept is highlighted: given a time-domain current ($i(t)$) composed of *H* harmonic components (i.e., *h=1,2,3,...,H*), it can be rewritten at any time according to Eq. 3.2. Note that such a definition considers an AC time-domain signal of unity amplitude that determines the in-phase ($x_{h_{||}}$) or quadrature ($x_{h_{\perp}}$) synchronism of the current components, respectively. Such synchronism is always achieved in relation to the voltage of that same node of the electric circuit.

$$i(t) = \sum_{h=1}^{H} (I_{h_{||}} \cdot x_{h_{||}} + I_{h_{\perp}} \cdot x_{h_{\perp}}) \tag{3.2}$$

The GCBC strategy requires the implementation of three main tasks to steer DERs. They are: *i)* the local evaluation of electrical quantities at DERs and PCC; *ii)* the processing of the GCBC algorithm at the MGCC; and *iii)* the local current reference setting at DERs. The summarized scheme presented in Fig. 3.4 demonstrates how

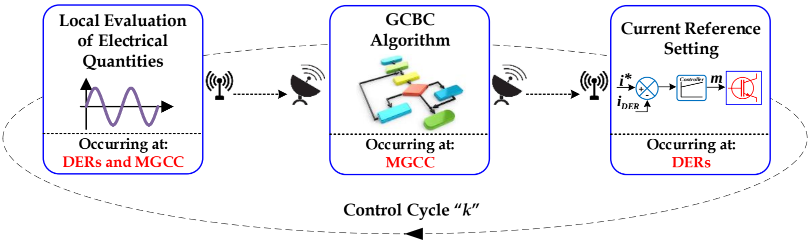

Figure 3.4: Three main tasks of the GCBC strategy for coordination of DERs.

these three tasks are integrated into the GCBC strategy. One can note that, given a control cycle "k", the GCBC tasks are processed sequentially at different locations of the MG, using communication links to adjust the currents injected by DERs at the final step. Each of these tasks is thoroughly explained below.

i) Local Evaluation of Electrical Quantities

This procedure is required to process the electrical quantities (i.e., voltage and currents) at the nodes of interest. It occurs at each DER and at the MGCC. The main goal of this procedure is to detect the peak values of the currents flowing through the respective PoCs and PCC. For instance, let us consider the time-domain local output current of a DER, $i^o_m(t)$, in which *m* stands for the respective phase of a generic circuit (e.g., *m* = *a, b* or *c*, for three-phase topology). The scheme demonstrated in Fig. 3.5(a) is then used for extracting the magnitude of the in-phase ($I^o_{h||_m}$) and quadrature ($I^o_{h\perp_m}$) peak currents of $i^o_m(t)$. Of course, since this procedure occurs at DERs and the PCC, one finds that $I^o_{hm} = I^{DER_j}_{hm}$ for each *j*-th DER, and $I^o_{hm} = I^{Grid}_{hm}$ for the PCC.

The decomposition of current components is performed for all harmonic orders (h) that need to be controlled. For instance, by controlling the fundamental in-phase component, $I^o_{1||_m}$, active current control is obtained. Similarly, reactive current control occurs based on $I^o_{1\perp_m}$. The components of upper harmonic orders (i.e., for *h=3,5,7,9,...,H*), $I^o_{h||_m}$ and $I^o_{h\perp_m}$, are responsible for the regulation of non-fundamental currents (i.e., compensation of harmonics). Furthermore, it is already noticeable that the GCBC strategy performs a per-phase analysis of currents. Consequently, it can easily be applied to any topology of electric circuits (i.e., single-, three-, or other polyphase systems).

The local evaluation required by the GCBC starts by measuring the local currents and voltages (v^o_m) of a PoC or PCC, as seen in Fig. 3.5(a) (i.e., $v^o_m = v_m^{DERj}$ for DERs, or $v^o_m = v^{Grid}_m$ for the PCC). The voltage measurements feed a PLL algorithm, which gives the fundamental synchronization angle θ_{1m}. Later, θ_{1m} is used for calculating the synchronization angles $\theta_{hm} = h \cdot \theta_{1m}$ that provide the references for the harmonic frames. Moreover, it should be noted that, if such angles feed cosine and sine trigono-

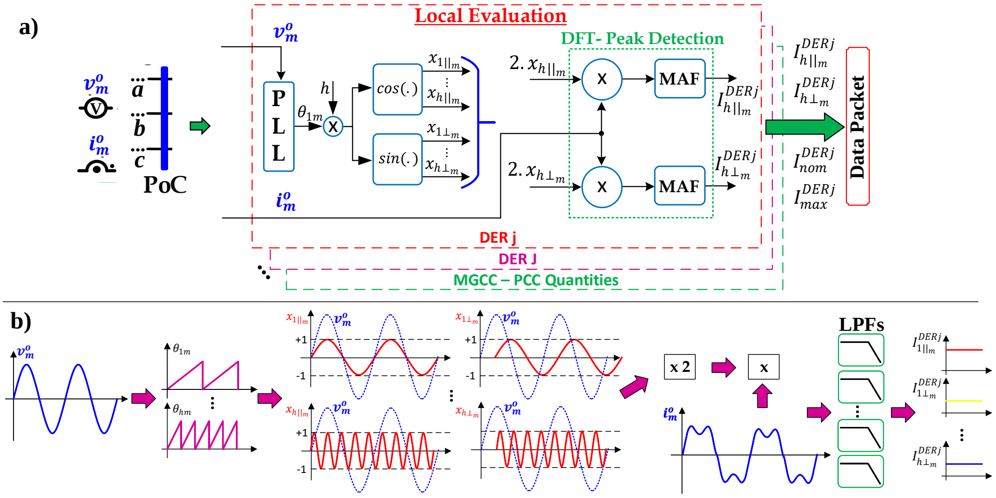

Figure 3.5: Local evaluation of electrical quantities required for the GCBC strategy. (a) Summarized scheme; and (b) graphical demonstration of the procedure in (a).

metric functions, the aforementioned unity reference signals, $x_{h||_m}$ and $x_{h\perp_m}$, can be obtained for the in-phase and quadrature orientations. Another important aspect is that the chosen PLL algorithm must be robust enough to endure operation under non-ideal voltage conditions, such as for the cases of applications in weak LV MGs. Under that premise, the PLL algorithm presented in [123] is considered for this thesis.

In possession of $x_{h||_m}$ and $x_{h\perp_m}$, as well as of the node current $i_m^o(t)$, one can use a discrete Fourier transform (DFT) [124] as a means for calculating the peak values of the targeted current components. Here, a discrete implementation of the Fourier transform is used in view of a digital implementation of the method in a processor, which requires only a low computational burden. The adopted DFT is devised in Fig. 3.5(a) by means of moving average filters (MAFs) that act as low-pass filters (LPFs), allowing simple digital implementation. Moreover, due to the feature of this implementation, the peak current terms $I_{h||_m}^o$ and $I_{h\perp_m}^o$ are average quantities that could assume either positive or negative values, depending on how $x_{h||_m}$ and $x_{h\perp_m}$ interact with $i_m^o(t)$. For instance, attaining a positive value for $I_{1||_m}^o$ would indicate an injection of active power. On the other hand, power absorption (i.e., storage) would result in a negative[1] value for $I_{1||_m}^o$.

Another highlight is that, if desired, other approaches for the calculation of the peak currents [125, 126] could be devised, guaranteeing compatibility with the fol-

---

[1] The negative peak value (i.e., negative magnitude) of a periodic current component does not present mathematical meaning. Such a definition is an abstraction, given that the peak detection scheme from Fig. 3.5 can indicate if a current component is either in-phase or 180°-shifted in relation to $x_{h||_m}$ or $x_{h\perp_m}$. For the case of having a 180°-shifted current signal, a negative peak value is obtained.

lowing steps of the GCBC algorithm. A time-domain formulation is chosen within this thesis due to its simple digital implementation and easier adaptability to extend the operation to more advanced control functionalities, as demonstrated in Chapter 6. Finally, note that in Fig. 3.5(b) a graphical representation of the discussed local evaluation is presented to further clarify how the peak currents are calculated.

As the last step of this procedure, all the peak currents calculated (i.e., $I^{o}_{h||_m}$ and $I^{o}_{h\perp_m}$) are gathered to compose a data packet, which is subsequently sent to the MGCC, as shown in Fig. 3.5(a). Along with such terms, other peak current terms need to be inserted into this data packet. Such quantities are the nominal current rating of that *j*-th DER ($I^{DERj}_{nom_m}$), the maximum active current that it can generate ($I^{DERj}_{1||max_m}$), and the maximum active current that it can store ($I^{DERj}_{1||sto_m}$) if an ESS exists.

The per-phase term $I^{DERj}_{nom_m}$ is a constant related to the nominal apparent power of that inverter (i.e., $A^{DERj}_{3\Phi}$, for a three-phase system). It can be easily calculated, for example, according to Eq. 3.3, in which $V^{DERj}_{RMS_m}$ is the root mean square (RMS[2]) *m*-phase voltage of that DER. In this thesis, all RMS variables for voltages and currents are given by capital letters, always presenting the subscript "$_{RMS}$" to distinguish them from the peak value definition.

$$I^{DERj}_{nom_m} = \frac{\sqrt{2} \cdot A^{DERj}_{3\Phi}}{3 \cdot V^{DERj}_{RMS_m}} \tag{3.3}$$

The term $I^{DERj}_{1||max_m}$ characterizes the capability of a *j*-th DER to inject active current, either considering the implementation of MPPT algorithms for its RES (i.e., if it is a nd-DER) or based on the usage of stored power (i.e., if it is a d-DER). Lastly, the term $I^{DERj}_{1||sto_m}$ can be attained based on the SoC of the ESS, as typically performed for battery systems [127]. Therefore, $I^{DERj}_{1||sto_m}$ is only applied to the case of d-DERs.

As expected, since the MGCC is responsible for performing the local evaluation of electrical quantities at the PCC, the calculated terms $I^{Grid}_{h||_m}$ and $I^{Grid}_{h\perp_m}$ are only used locally. Thus, they do not need to be transmitted to DERs at any moment.

ii) Processing of the GCBC Algorithm at the MGCC

The second task of the coordination strategy is to process the GCBC algorithm at the MGCC. Such an algorithm needs to be periodically processed, utilizing data packets transmitted by the DERs. Thus, let us consider a given control cycle "*k*" that is initiated at the beginning of a periodic window of the MG management. As

---

[2] The RMS value of a generic voltage is given by $V_{RMS} = \sqrt{\frac{1}{T} \cdot \int_0^T v^2(t)dt}$, while for a generic current it is $I_{RMS} = \sqrt{\frac{1}{T} \cdot \int_0^T i^2(t)dt}$, having T as the period of these signals.

explained in Section 3.4.2, such a control window can be designed to operate between milliseconds and minutes, according to the MG needs. This cycle "k" is only updated at the next control interruption, resulting in "$k = k + 1$". Thus, once cycle "k" starts, the MGCC pulls the data packets processed by DERs, just as explained for the step of local evaluation of electrical quantities. Likewise, the local peak currents from the PCC are also calculated. Again, it is considered that J DERs are participating in the coordinated control strategy.

Having information about the status of all participating DERs and the PCC, and knowing that H harmonic orders need to be controlled, the following calculation is performed. Firstly, the total current contribution of the J DERs is computed, for each harmonic order h, as given by Eqs. 3.4 and 3.5. This process is performed for the in-phase ($I_{h||_m}^{DERt}$) and quadrature ($I_{h\perp_m}^{DERt}$) current components. Herein, the superscript "^{t}" will stand for the total quantities of the MG (i.e., with relation to all J DERs participating in the GCBC strategy).

$$I_{h||_m}^{DERt}(k) = \sum_{j=1}^{J} I_{h||_m}^{DERj}(k) \tag{3.4}$$

$$I_{h\perp_m}^{DERt}(k) = \sum_{j=1}^{J} I_{h\perp_m}^{DERj}(k) \tag{3.5}$$

A similar calculation has to be performed for the nominal capabilities of the DERs ($I_{nom_m}^{DERj}$), as well as for their maximum generation ($I_{1||max_m}^{DERj}$) and storage ($I_{1||sto_m}^{DERj}$) peak currents. This procedure is realized as shown in Eqs. 3.6 to 3.8. At this point, the MGCC knows the actual participation of DERs in the overall status of the MG operation. Eq. 3.7 demonstrates that DERs may even have different generation profiles, ones which do not require additional processing of the analyzed current quantities to obtain coordination among DERs.

$$I_{nom_m}^{DERt}(k) = \sum_{j=1}^{J} I_{nom_m}^{DERj}(k) \tag{3.6}$$

$$I_{1||max_m}^{DERt}(k) = \sum_{j=1}^{J} I_{1||max_m}^{DERj}(k) \tag{3.7}$$

$$I_{1||sto_m}^{DERt}(k) = \sum_{j=1}^{J} I_{1||sto_m}^{DERj}(k) \tag{3.8}$$

Hence, knowing that the MGCC also possesses the information about the currents flowing through the PCC (i.e., $I^{Grid}_{h||_m}$ and $I^{Grid}_{h\perp_m}$), the summed current contribution ($I^{L}_{h||_m}$ and $I^{L}_{h\perp_m}$) of all MG elements, including the passive or non-controlled ones, can be devised. This is conducted based on the PCC and DERs' current components at the cycle "k", and according to Kirchhoff's current law. Such a current reconstruction is based on Eqs. 3.9 and 3.10. Besides, a graphical demonstration is presented in Fig. 3.6 to facilitate the understanding of such interpretation.

$$I^{L}_{h||_m}(k) = I^{DERt}_{h||_m}(k) + I^{Grid}_{h||_m}(k) \tag{3.9}$$

$$I^{L}_{h\perp_m}(k) = I^{DERt}_{h\perp_m}(k) + I^{Grid}_{h\perp_m}(k) \tag{3.10}$$

A few notable aspects need to be mentioned with regard to these two load current terms. Firstly, one can note that the left-hand side of Eqs. 3.9 and 3.10 not only comprises the currents drawn by the loads that may exist within the MG, $I^{L}_{h||_m}$ and $I^{L}_{h\perp_m}$ also incorporate all the power losses occurring in line impedances and other dissipative elements. Additionally, DERs that do not participate in the GCBC strategy are also considered within these terms. Another important remark is that Eqs. 3.9 and 3.10 are only valid due to the limited size of the considered MG, its homogeneous characteristic, and the low *X/R* feature of its line impedances, which guarantees that voltage shifts are not significant, as discussed in Section 3.2.

Lastly, note that, if the J DERs are able to share the amount of peak currents given by $I^{L}_{h||_m}$ and $I^{L}_{h\perp_m}$, the current flow through the PCC will become null. This is an operational premise of the GCBC algorithm, which defines the amount of peak current that should be shared among DERs, in order to achieve different desired objectives. If DERs are able to achieve $I^{L}_{h||_m} = 0$ and $I^{L}_{h\perp_m} = 0$ for all significant harmonic orders, the MG will operate under full self-consumption mode [44] in a steady-state condition. Consequently, the MG would not depend on the upstream grid, aside from the fact of forming the grid (i.e., imposing the voltages and frequency at the PCC).

Now, the GCBC algorithm takes into consideration the transactive aspect of the MG operation, which demands a controllable power flow through the PCC. Such a

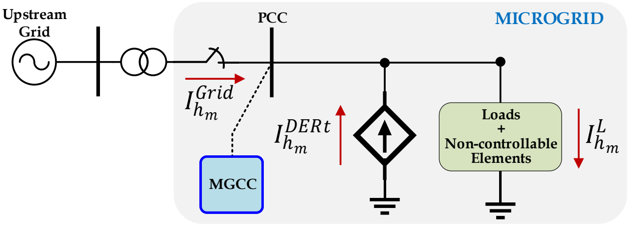

Figure 3.6: Kirchhoff's current law applied to the MG peak current analysis.

power flow can be translated into current signals that must be drawn or dispatched by the MG, considering that it is interpreted as single entity from the DSO perspective. Thus, let us define such signals as reference peak currents at each h harmonic order, namely $I_{h||_m}^{Grid*}$ and $I_{h\perp_m}^{Grid*}$.

These terms establish the amount of peak current that must circulate at the PCC, even after fulfilling the MG internal current needs (i.e., $I_{h_m}^{L}$). Consequently, these terms are usually set by the DSO, or by transactive deals, through interactions at the tertiary layer. For instance, if $I_{1||_m}^{Grid*}$ is a non-null positive quantity, this means that the overall operation of the MG is seen by the upstream grid, as a load drawing active currents. On the other hand, if $I_{1||_m}^{Grid*}$ is a negative quantity, it means that the MG is exporting (i.e., dispatching) active power. It is also important to remember that, due to contractual relations with the upstream grid, such PCC reference terms are constrained to active and reactive power dispatch limits, resulting in Eqs. 3.11 and 3.12, respectively.

$$\underline{I_{1||_m}^{Grid}} \leq I_{1||_m}^{Grid*} \leq \overline{I_{1||_m}^{Grid}} \qquad \forall\, I_{1||_m}^{Grid*} \in \mathbb{R} \tag{3.11}$$

$$\underline{I_{1\perp_m}^{Grid}} \leq I_{1\perp_m}^{Grid*} \leq \overline{I_{1\perp_m}^{Grid}} \qquad \forall\, I_{1\perp_m}^{Grid*} \in \mathbb{R} \tag{3.12}$$

Then, one can define the currents that need to be shared by the DERs, at the next control cycle "*k+1*", namely $I_{h||_m}^{*}(k+1)$ and $I_{h\perp_m}^{*}(k+1)$. Such references can be calculated according to Eqs. 3.13 and 3.14, which can be expanded to Eqs. 3.15 and 3.16.

$$I_{h||_m}^{*}(k+1) = I_{h||_m}^{L}(k) - I_{h||_m}^{Grid*}(k+1) \tag{3.13}$$

$$I_{h\perp_m}^{*}(k+1) = I_{h\perp_m}^{L}(k) - I_{h\perp_m}^{Grid*}(k+1) \tag{3.14}$$

$$I_{h||_m}^{*}(k+1) = I_{h||_m}^{DERt}(k) + I_{h||_m}^{Grid}(k) - I_{h||_m}^{Grid*}(k+1) \tag{3.15}$$

$$I_{h\perp_m}^{*}(k+1) = I_{h\perp_m}^{DERt}(k) + I_{h\perp_m}^{Grid}(k) - I_{h\perp_m}^{Grid*}(k+1) \tag{3.16}$$

Finally, in order to coordinate DERs to achieve current sharing over multiple harmonic orders, $I_{h||_m}^{*}$ and $I_{h\perp_m}^{*}$ are used to calculate scaling coefficients (i.e., namely $\alpha_{h||_m}$ and $\alpha_{h\perp_m}$). Such a calculation is devised by means of Eqs. 3.17 and 3.18. The term $\sqrt{\Delta I_m}$ is defined as the overall peak current capability of the MG, and it needs to be used to achieve proportional current sharing among DERs, while respecting their power ratings. This term must be adjusted iteratively according to the calculation of each scaling coefficient, as depicted in Fig. 3.7.

$$\alpha_{h||_m} = \frac{I_{h||_m}^{*}(k+1)}{\sqrt{\Delta I_m}}, \qquad \forall\, \alpha_{h||_m} \in \mathbb{R} : -1 \leq \alpha_{h||_m} \leq +1 \tag{3.17}$$

$$\alpha_{h\perp_m} = \frac{I^*_{h\perp_m}(k+1)}{\sqrt{\Delta I_m}}, \qquad \forall\, \alpha_{h\perp_m} \in \mathbb{R} : -1 \leq \alpha_{h\perp_m} \leq +1 \tag{3.18}$$

Such a correction of $\sqrt{\Delta I_m}$ follows a sequential order, having active current control processed first, reactive control next, and the in-phase and quadrature harmonic orders are processed last. Particular attention must be given to active current control because active current injection or absorption must be related to $I^{DERt}_{1||max_m}$ and $I^{DERt}_{1||sto_m}$, respectively. Note that, since each step of this procedure is based on orthogonal subtractions, by using the DERs' estimated currents (i.e., given by $\hat{I}^{DERt}_{h||_m} = \alpha_{h||_m} \cdot \sqrt{\Delta I_m}$ or $\hat{I}^{DERt}_{h\perp_m} = \alpha_{h\perp_m} \cdot \sqrt{\Delta I_m}$) at "*k+1*", overcurrents are prevented. Additionally, such phasorial calculations also guarantee that their current capabilities are respected. The scheme in Fig. 3.7 uses two auxiliary variables (ΔI_m and $\Delta I_{m_{old}}$), which hold the quadratic value of the overall current capability at the actual and previous calculation steps, respectively. It should ultimately be remarked that, if desired, for whatever MG management reason, the sequence of the iterative calculation of $\sqrt{\Delta I_m}$ can be flexibly readjusted.

Finally, further explanations are given about the scaling coefficients, $\alpha_{h||_m}$ and $\alpha_{h\perp_m}$. These coefficients are within the range of $[-1, +1]$, and if they are equal to +1 or -1, it indicates that all the DERs' current capacity, at a given harmonic order h, is used. As expected, if these coefficients are null, no current control is performed at the respective harmonic order. In particular, when looking into the coefficients of the fundamental order, one can generally understand the coordination purpose of the DERs.

For instance, the term $\alpha_{1||_m}$ relates to active current control, and it indicates that power injection is demanded by the DERs (i.e., if $\alpha_{1||_m} > 0$), or that absorp-

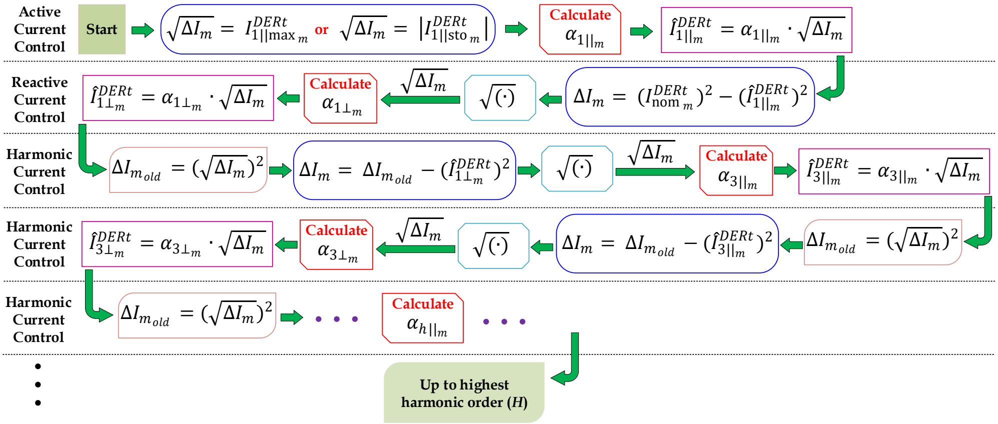

Figure 3.7: Iterative calculation of DERs' current capability ($\sqrt{\Delta I_m}$).

tion/storage is commanded (i.e., if $\alpha_{1||_m} < 0$). On the other hand, the term $\alpha_{1\perp_m}$ implies that inductive or capacitive behavior is provided by the DERs, if $\alpha_{1\perp_m} > 0$ or $\alpha_{1\perp_m} < 0$, respectively. Yet, by using the non-fundamental scaling coefficients (i.e, $\alpha_{h||_m}$ and $\alpha_{h\perp_m}$, for $h \geq 2$), the MG manager has a means to implement distributed and selective compensation of harmonic currents. Of course, for the case of nd-DERs not comprising ESS, $\alpha_{1||_m}$ cannot assume negative values, as $I_{1||sto_m}^{DERj}$ is null. Besides, since the GCBC algorithm can also be employed to coordinate active filters [128], a similar idea would apply, resulting in $\alpha_{1||_m}$ being always null, as $I_{1||max_m}^{DERj} = I_{1||sto_m}^{DERj} = 0$.

This task of the GCBC strategy terminates by gathering in a data packet the scaling coefficients, of all harmonic orders to be controlled. Sequentially, this data packet is broadcast to all participating DERs within the MG, so they can adjust their current injections as given by the next step of the GCBC approach.

iii) Current Reference Setting at DERs

The final procedure of the GCBC strategy is responsible for setting the right current references to be injected by the DERs. This task occurs only at each DER, and it uses the scaling coefficients transmitted by the MGCC. Let $i_m^{DERj*}(t)$ be the time-domain current reference of the phase *m*, for each *j*-th DER participating in the coordination strategy. Such a reference can then be constructed similarly to Eq. 3.2, in which the unity reference signals (i.e., $x_{h||_m}^{DERj}$ and $x_{h\perp_m}^{DERj}$) come from the local evaluation of the electrical quantities realized by that *j*-th DER. Thus, the final current reference used for that DER is given by Eqs. 3.19 to 3.20, which can be summed up to result in Eq. 3.21, similarly to Eq. 3.1.

$$i_{||_m}^{DERj*}(t) = \sum_{h=1,3,5,...}^{H} \left(\alpha_{h||_m} \cdot \sqrt{\Delta I_m^{DERj}} \cdot x_{h||_m}^{DERj} \right) \tag{3.19}$$

$$i_{\perp_m}^{DERj*}(t) = \sum_{h=1,3,5,...}^{H} \left(\alpha_{h\perp_m} \cdot \sqrt{\Delta I_m^{DERj}} \cdot x_{h\perp_m}^{DERj} \right) \tag{3.20}$$

$$i_m^{DERj*}(t) = i_{||_m}^{DERj*}(t) + i_{\perp_m}^{DERj*}(t) \tag{3.21}$$

In such equations, the current capability of each respective DER ($\sqrt{\Delta I_m^{DERj}}$) is used. This variable is calculated in the same way as for the total current capability of the MG ($\sqrt{\Delta I_m}$), following the same iterative scheme presented in Fig. 3.7. However, for $\sqrt{\Delta I_m^{DERj}}$, only the local quantities of that specific *j*-th DER must be used (i.e., $I_{nom_m}^{DERj}$, $I_{1||max_m}^{DERj}$, and $I_{1||sto_m}^{DERj}$).

A final remark is made with regard to the per-phase controllability provided by the GCBC strategy. Note from Eq. 3.21 that the current reference for a DER is locally constructed based on the evaluations performed at each phase *m*, even for the three-phase topology. This indicates that, for the case of single-phase MGs, the GCBC is performed only for one phase. On the other hand, for three-phase MGs, the GCBC application depends on the topology of the inverters. For instance, if three-leg DERs exist, only two phases need to be controlled [129], being the modulation of the third leg obtained from Kirchhoff's current law. Hence, the GCBC needs to be implemented considering two phases to adequately coordinate such DERs.

For the case in which three-phase four-leg DERs exist (i.e., in a three-phase four-wire MG) [130], as it will be discussed in Section 6.4, the GCBC is applied to three phases, controlling the DER's neutral leg by Kirchhoff's current law. Based on this concept of operation, the coordination strategy can be applied to any MG topology (e.g, such as two-phase three-wire circuits [42]). Additionally, although being outside the scope of this thesis, such a per-phase coordination can even be employed for steering single-phase DERs arbitrarily connected to three-phase MGs, or it can concomitantly coordinate single- and three-phase DERs, as done in [68] and [71], respectively.

3.6 Chapter Conclusions

In this chapter, a model-free coordinated control strategy was devised to steer DERs in AC MGs. Although being applicable to generic voltage levels, the approach is particularly interesting from the LV perspective due to the feature of line impedances, which commonly present a low *X/R* ratio. The strategy, so-called Generalized Current-Based Control (GCBC), is formulated by means of the analysis of peak currents, and it takes advantage of a three-layer hierarchical architecture that incorporates multi-rate control aspects. Consequently, the cooperative operation of the controlled inverters is able to consider operational features ranging from the power electronics level, up to the perspective of power systems planning. Since the strategy is devised under a per-phase control approach, it is flexible enough to be implemented in LV MGs of generalized circuit topologies.

The considered MG topology and control modeling of the adopted DERs has also been presented. Discussions about MG infrastructure indicated that the proposed coordination approach focuses on LV systems of limited size and that present homogeneous features. It has also been discussed that the GCBC strategy is suitable for coordinating DERs of different natures (i.e., dispatchable or non-dispatchable behavior), also considering variability in power generation. As an example of the multiple operational objectives offered by the GCBC strategy, it has been highlighted that the MG manager is able to coordinate DERs to perform active and reactive current sharing, as well as distributed and selective harmonic compensation. Moreover, the power flow of the MG at the PCC can be flexibly controlled, ensuring that power dispatchability is offered to comply with contractual requirements and demands for transactive actions.

Chapter 4

Multi-Purpose Coordination of DERs Devising Flexible Microgrid Operation

4.1 Introduction

Herein, the multi-purpose feature of the GCBC strategy is demonstrated and validated, being later complemented by the non-ideal operational scenarios and advanced control functionalities presented in Chapters 5 and 6, respectively. Firstly, the main MG testbench implemented for simulations results is discussed, and the main laboratory prototype used for experimental validations is presented. Most of the proposed functionalities and features of the GCBC strategy are experimentally assessed, as a means to certify the feasibility of the approach to real-life applications.

Three main operational purposes are firstly presented, demonstrating the capability of the coordination method to provide active, reactive and harmonic control. Thus, it is shown that DERs can be steered to achieve proportional active current sharing, distributed compensation of reactive currents, as well as selective mitigation of harmonics. The MG power dispatchability is then presented, showing that DERs can be coordinated to provide a controllable power flow at the PCC, certifying the transactive aspect of the strategy. Since different DERs may exist in a LV MG, it is shown that nd- and d-DERs can be coordinated by the GCBC, and that it can handle the possibility of supporting variable generation profiles for the RESs.

Lastly, additional operational considerations are presented to demonstrate two aspects. The first is related to the MG's capability of transitioning between grid-connected and islanded modes, ensuring that the GCBC strategy does not negatively affect the synergistic operation of DERs or grid. The second aspect highlights how the cooperative method realized by the GCBC compares to the well-known droop control strategy.

4.2 Microgrid Simulation Testbench and Experimental Prototype

4.2.1 Main Simulation Testbench

As discussed in Section 3.2, this thesis relies on the CIGRE's European LV benchmark [96] as the main reference for computational simulations. This testbench, which is a three-phase four-wire circuit, is herein used for all simulation results, apart from Sections 4.4.2 and 5.7 that use another MG circuit for the sake of simplicity.

The MG is implemented as demonstrated in Fig. 3.1 (one can also see a simplified layout in Fig. 4.1(a)), comprising: *i)* a delta-wye DST interconnecting the MG with the upstream grid; *ii)* line impedances between electric nodes (*B_*); *iii)* several circuit breakers (*CB_*) that connect the MG PCC, loads and DERs; *iv)* linear and nonlinear loads (unbalanced loads are only considered in Section 6.4); and *v)* eight DERs. With regard to the DERs, they are modeled based on three-phase three-leg inverters connected to phases *a*, *b* and *c*. Additionally, the eight inverters are considered to be three d-DERs (i.e., d-DER$_1$ to d-DER$_3$), two nd-DERs without communication interface (i.e., nd-DER$_1$ and nd-DER$_2$), and three nd-DERs with communication interface (i.e., nd-DER$_3$ to nd-DER$_5$). Thus, such inverters operate according to the premises presented in Section 3.3.

The physical and operational parameters of the above-mentioned MG elements are

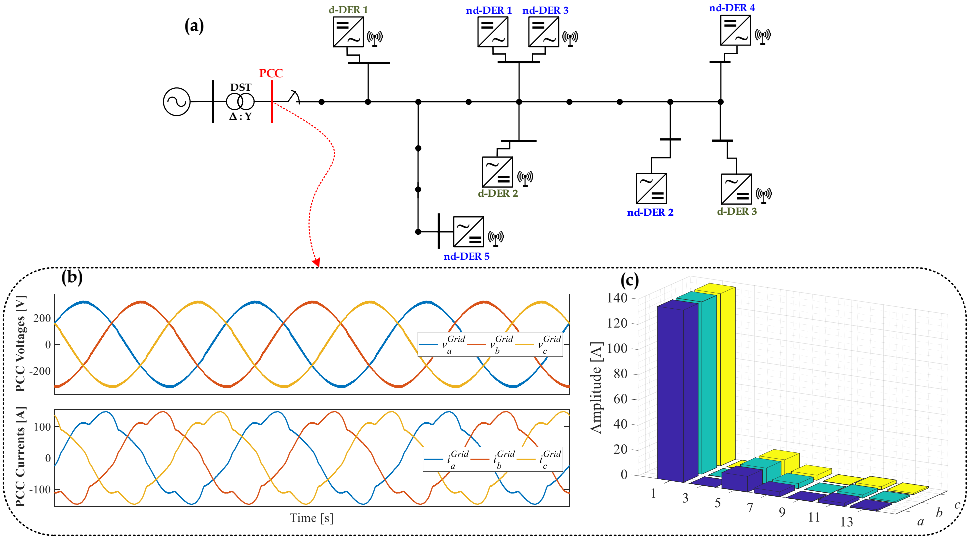

Figure 4.1: Simplified layout of the adopted MG, and preliminary simulation results. (a) MG layout; (b) voltages and currents at PCC; and (c) harmonic content of the load currents.

presented in Tables 4.1 and 4.2. The parameters of line impedances are available in Appendix B.1.2. Moreover, for this testbench, DERs are modeled considering *LCL* filters with an active damping loop (i.e., as in Section 3.3). Additionally, PRep current controllers are devised to control the DER's output current ($i_m^{DERj}(t)$) directly in time-domain (i.e., without requiring axis transformations), ensuring zero steady-state error while tracking $i_m^{DERj*}(t)$. The model of these current controllers are presented in Appendix B.1.3. Yet, RESs and DC bus voltage controllers are idealized in simulations by using constant voltage sources. Herein, the variable r_{dDERs} is defined as the current ratio between d-DER$_1$ (or d-DER$_3$) and d-DER$_2$, being used to assess their proportionality while performing current sharing. For instance, Table 4.2 shows that $r_{dDERs} = 1.75$ for simulations using the main MG testbench.

MATLAB/Simulink®, version R2018a, is used as a simulation platform for implementing the MG. Besides, a time step of 1.33 μs is set for simulations, using a fixed-step discrete solver. Since the GCBC is based on a hierarchical control architecture that uses multi-rate control, delays are emulated in simulation by zero order sample holders, achieving the required different processing times of the approach. For instance, DERs run with sampling time equal to T_s, and the GCBC processing time, at the MGCC, is set to process data packets at each cycle of the line voltage (i.e, $T_{GCBC} = 20$ ms). Since the tertiary layer is much slower than the other two control

Table 4.1: MG parameters used for simulation results.

Parameter	**Value**
Line-to-line voltage at the DST's primary side	20 kV$_{\text{RMS}}$
Line-to-line voltage at the DST's secondary side	400 V$_{\text{RMS}}$
MG frequency (f_o)	50 Hz
DST's reactance	0.016 Ω
DST's apparent power ($A_{3\Phi}^{DST}$)	500 kVA
Loads[‡]	**Value**
L_{B11} (resistive-inductive)	$A_{3\Phi} = 13.50$ kVA with $PF = 0.54$
L_{B15} (resistive-inductive)	$A_{3\Phi} = 13.50$ kVA with $PF = 0.54$
L_{B16} (resistive-inductive)	$A_{3\Phi} = 12.50$ kVA with $PF = 0.75$
L_{B17} (resistive-inductive)	$A_{3\Phi} = 5.90$ kW with $PF = 1.00$
L_{B18} (resistive-inductive)	$A_{3\Phi} = 5.60$ kVA with $PF = 0.82$
Non-linear Loads: NL_1, NL_2, NL_3 (AC side inductor, DC side capacitor and resistor)	2 mH, 2.35 mF, 46 Ω

[‡] See Fig. 3.1 for the disposition of loads within the MG.

Table 4.2: DERs' parameters used for simulation results.

	nd-DERs	**d-DERs**
DER[‡] Number	**Apparent Power [kVA]**	
1	8	35
2	8	20
3	12	35
4	12	-
5	12	-
Nominal current ratio between d-DERs ($r_{dDERs} = 35/20$)	1.75	
***LCL* Filter and Control Parameters**		
Inductors: L_i and L_g	3.5 and 1.5 mH	1.8 and 0.8 mH
Filter capacitor (C_f)	2.2 μF	2.2 μF
Active damping gain (K_{damp})	4.8 p.u.	2.5 p.u.
PRep controller: K_P and K_f gains	0.38 and 0.47 p.u.	0.26 and 0.28 p.u.
Additional Parameters (All DERs)		
DC link voltage (V_{DC})	750 V	
Switching frequency ($f_{sw} = 1/T_{sw}$)	15 kHz	
Sampling frequency ($f_s = 1/T_s$)	15 kHz	

[‡] See Fig. 3.1 for the disposition of DERs within the MG.

levels, its current references used for the MG dispatchability are considered constant throughout the simulated cases, unless otherwise stated. A picture of the implemented MG testbench, in MATLAB/Simulink, is provided in Appendix B.1.1.

As a preliminary simulation result, the MGCC measurements for the voltages and currents at the PCC, considering all DERs disabled (i.e., not processing any currents) are shown in Fig. 4.1(b). Thus, only the currents being drawn by the loads are seen in such a simulated case. It can be noted that, at normal operational conditions, the MG presents sinusoidal voltages and distorted load currents. Since linear and nonlinear elements are drawing power from the upstream grid, the currents at the PCC are also phase-shifted in relation to the voltages. This indicates that, besides providing active current to the loads, the MG must endure operation considering the circulation of reactive and harmonic currents, respectively.

The harmonic spectrum of the load currents at PCC is presented in Fig. 4.1(c), demonstrating that the most significant harmonic terms are the 5th, 7th, 11th and 13th orders. The apparent (*A*), active (*P*), reactive (*Q*) and distortion (*D*) power terms at the PCC for Fig. 4.1(b), as well as the power factor (*PF*), are also provided in Table 4.3. It can be noted that a significant amount of these four power terms exist at the PCC, and that the MG operates with non-unity power factor (i.e, 0.93). It is important to stress that, hereon, all the presented powers terms and *PF* are calculated based on the CPT, as

Table 4.3: Three-phase steady state powers and PF at the PCC, and MG power losses for the main MG simulation testbench.

PCC Powers	
A	67.69 kVA
P	55.55 kW
Q	39.98 kVAR
D	7.32 kVA
PF	0.80
Losses	804 W

in [45]. One can refer to Appendix A.1 for further explanations about the CPT power and current terms. The overall power losses over the line impedances are additionally computed for this scenario (i.e., having loads connected the MG, while all DERs are disconnected). Such losses are calculated by summing the power dissipation at all nodes, and for the three phases. The per-phase loss of a node is based on the expression $R_{Z_m} \cdot I^2_{RMS_{Z_m}}$, in which R_Z is the resistance of that piece of line impedance, while $I_{RMS_{Z_m}}$ is the RMS current flowing through it.

4.2.2 Main Experimental Prototype

A single-phase laboratory-scale MG prototype [131] is used as the main platform to perform the experimental validations within this thesis. Exception is only made to Sections 5.8 and 6.4, in which two other MG prototypes are used to demonstrate specific aspects of particular functionalities of the GCBC strategy. These other two prototypes are explained in the sections of their respective uses.

The equivalent circuit of the single-phase MG prototype is depicted in Fig. 4.2. Moreover, a picture of the entire MG prototype is presented in Fig. 4.3 and an extended explanation about the implementation of this MG is found in Appendix C.1. The upstream grid is formed by a 30 kVA AC grid emulator, from REGATRON®, model TC-ACS-30-528-4WR, which is coupled to the MG PCC. The MG nodes are interconnected through line impedances (Z_{L1} to Z_{L5}), having Z_{L1} = Z_{L2} = Z_{L3} = Z_{L4} = $2.Z_{L5}$ = *0.5 mH*. Three loads are considered for the MG operation, one being composed of an IT8616 electronic load (L_1) from ITECH® (i.e., emulating a constant 16 Ω resistor), and two passive loads; one an inductive load (L_2 = 40 *mH*) and the other a non-linear load (L_3).

The non-linear load is a full-wave diode rectifier having an inductor (*5 mH*) at its AC side, and a capacitor bank (*2.35 mF*) in parallel with a resistor (*41.8* Ω) at its DC side. The MG elements can be switched on or off by means of circuit breakers (*CB_*). Yet, DPO3000 TEKTRONIX® oscilloscopes were used for acquiring current and voltage waveforms, and a DPO3PWR power analysis module was used to quantify the amplitude of harmonic components and the phase shift between voltage and current.

Most importantly, such a MG prototype presents three inverters. Two of them are controlled as dispatchable units (i.e., d-DERs*: d-DER$_1^\star$ and d-DER$_2^\star$), being ruled by the GCBC strategy. The third inverter operates as a non-dispatchable unit (i.e., nd-DER$_1^\star$), only injecting active power into the MG when desired, and not participating in the GCBC approach. Note that the inverters referred for this main experimental prototype are denoted by the superscript "$\star$" to more easily distinguish them from the ones used in the simulation. The d-DERs* present *LC* output filters, while the nd-DER* uses a *LCL* output filter with passive damping resistor (R_d). The DERs* are driven under CCM (i.e., as controlled current sources), and they use proportional-resonant (PRes) current controllers modeled as in [102]. More details about the model of such controllers are found in Appendix C.3.

All inverters present constant DC voltage sources at their DC buses, being: one KEYSIGHT® model N8937APV, one CHROMA® model 62050H-600S, and a third

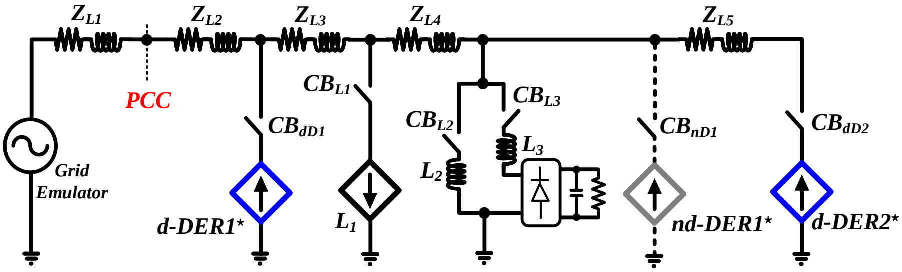

Figure 4.2: Equivalent circuit of the single-phase MG prototype assembled for experimental results.

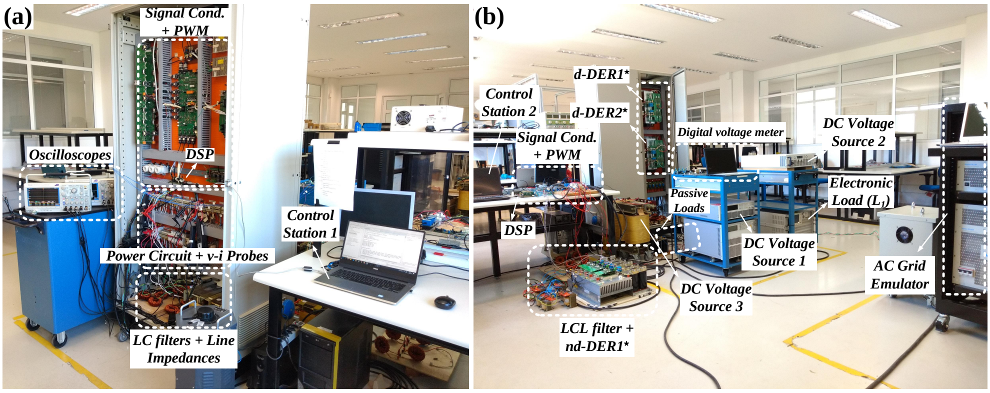

Figure 4.3: Experimental prototype of the single-phase MG: (a) front, and (b) back views.

one built with a variac, an isolating transformer, and a diode bridge. The two d-DERs* are controlled by a TMS320F28335 digital signal processor (DSP) from Texas Instruments®, which processes the current controllers of both inverters and the code required for implementing the GCBC strategy. The nd-DER* runs based on another independent TMS320F28335 DSP. The parameters of the DERs* used for experimental results are available in Table 4.4. For such a prototype, the current ratio between d-DER$_2^\star$ and d-DER$_1^\star$ is named $r_{dDERs^\star}$.

Similarly, in Section 4.2.1, a preliminary experimental result is presented in Fig. 4.4, demonstrating how the MG operates when the loads are connected to the circuit. For this result, all DERs* were considered to be disabled (i.e., not processing any currents). It is emphasized that, due to simplicity and safety concerns, this single-phase MG prototype was emulated considering line-to-neutral grid voltage of 127 V$_{\text{RMS}}$ at 60 Hz (i.e., in contrast to the simulation testbench, which is three-phase, and considered phase voltage of 240 V$_{\text{RMS}}$ at 50 Hz).

From Fig. 4.4 it is noticeable that, although having sinusoidal voltages at the PCC, the current demanded by the MG loads was distorted and phase-shifted in relation to the voltages. Thus, as demonstrated in Table 4.5, the MG presents a considerable amount of active, reactive and distortion powers at the PCC. Additionally, a significantly low power factor was achieved for the MG, mainly due to the circulation of reactive power. The harmonic components of the PCC currents are also presented in Table 4.5. It can be noted that, beyond the fundamental component, the most significant harmonic terms causing current distortion are the odd ones, from the 3rd up to the 9th orders. The total harmonic distortion (THD$_{\text{i}}$) of the PCC current, caused by the

Table 4.4: Parameters of DERs in the single-phase MG prototype used for experiments.

Parameter	**Value**
d-DERs	
d-DER$_1^\star$ nominal peak current	15 A$_{\text{pk}}$ ($\approx$ 3 kVA)
d-DER$_2^\star$ nominal peak current	20 A$_{\text{pk}}$ ($\approx$ 4 kVA)
Nominal current ratio between d-DERs* ($r_{dDERs^\star} = 20/15$)	1.33
LC filter: L_i and C_f	3.0 mH and 2.2 μF
Switching and sampling frequencies	12 kHz
DC link voltage (V_{DC})	270 V$_{\text{DC}}$
nd-DER	
nd-DER$_1^\star$ nominal peak current	15 A$_{\text{pk}}$ (i.e., $\approx$ 3 kVA)
LCL filter - Inductors: $L_i^{'}$ and L_g	1.0 mH and 1.0 mH
LCL filter - Capacitor ($C_f^{'}$) and Damping Resistor (R_d)	3.3 μF and 1 Ω
Switching and sampling frequencies	18 kHz
DC link voltage (V_{DC})	270 V$_{\text{DC}}$

Table 4.5: Powers and harmonic current components at PCC for Fig. 4.4.

PCC Powers		Harmonics	
A	1501 VA	***h=1***	12.2 $\mathrm{A_{RMS}}$
P	980 W	***h=3***	2.31 $\mathrm{A_{RMS}}$
Q	1148 VAR	***h=5***	0.63 $\mathrm{A_{RMS}}$
D	315 VA	***h=7***	0.26 $\mathrm{A_{RMS}}$
PF	0.65	***h=9***	0.19 $\mathrm{A_{RMS}}$

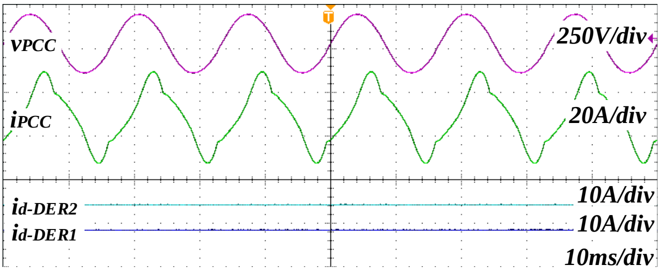

Figure 4.4: Experimental result: single-phase MG operating with all loads connected and with DERs* disabled. From top to bottom: PCC voltage and current, d-DER$_2^{\star}$ and d-DER$_1^{\star}$ currents.

loads, is 19.5%.

Having demonstrated the features of the main simulation testbench, and of the main experimental prototype, the results of the multiple operational purposes supported by the GCBC strategy are discussed in the following sections.

4.3 Multi-Purpose Coordination of DERs

In this section, four main functionalities offered by the GCBC strategy are presented. First, the capability to offer active and reactive power control is demonstrated through simulation and experimental results. Thus, inverters are coordinated to share the fundamental components of load currents. Second, the capability to achieve selective and distributed harmonic compensation is demonstrated. Third, the transactive control aspect of the MG is shown by dynamically controlling the active and reactive power dispatch at the PCC. Last, a final scenario demonstrates that the basic features of GCBC strategy cope with the existence of DERs with variable generation capability.

4.3.1 Active and Reactive Current Control

The results for these two operational purposes are divided into two parts. Initially, simulation results carried out on the MG testbench of Figs. 3.1 and 4.1 demonstrate how the GCBC strategy allows the possibility to coordinate DERs to achieve proportional active and reactive current sharing. Additionally, the dynamic response of the coordination strategy is shown by considering load steps. The plug-and-play feature of the approach is also assessed by abruptly disconnecting one DER that participates in the cooperative operation.

Later on, experimental results validate each individual aspect of operation of the GCBC strategy. For instance, the independent control over the active and reactive current terms is demonstrated, as well as their concomitant implementation. Moreover, the transient behavior of controlled DERs is assessed in experiments, highlighting the applicability of the GCBC method to real-life applications.

4.3.1.1 Simulation Results

Let us consider the main MG testbench adopted for simulation (i.e., the one explained in Section 4.2.1), in which an initial state was given by only having all loads connected to the MG (i.e., just as in Fig. 4.1(b)). Additionally, all eight DERs (i.e., five nd-DERs and three d-DERs) were already connected to the MG, not injecting any currents at first. Thus, simulation results are presented in Fig. 4.5, in which the voltages and currents at the PCC are demonstrated, along with the currents from a nd-DER and from a d-DER. Such results were divided into four intervals (Int.) to better show the GCBC operation.

Initially, at Interval I, only loads were drawing currents, just as in Fig. 4.1(b). At 0.3 s, all nd-DERs were initiated, injecting active power at full capability (i.e., 1 p.u.) to fulfill their major operation goal. Note that, by doing so, the nd-DERs' currents were practically in-phase with the PCC voltages (i.e., indicating active current injection). Then, after reaching steady state, it can be seen that the maximum amplitudes of the PCC currents were reduced, and that such currents were still distorted and phase-shifted. Table 4.6 complements such a result demonstrating that the active power (P) was the power term mainly affected by the operation of the nd-DERs (see Table 4.3 as reference), while a considerable amount of reactive and distortion powers still remained at the PCC.

Moreover, the DERs' collective [132] currents (I_{col}^{DERj}) are presented in Fig. 4.6 to qualitatively compare their participation in current sharing. The collective current from a DER is defined by $I_{col}^{DERj} = \sqrt{(I_{RMS_a}^{DERj})^2 + (I_{RMS_b}^{DERj})^2 + (I_{RMS_c}^{DERj})^2}$, recalling that $I_{RMS_a}^{DERj}$, $I_{RMS_b}^{DERj}$ and $I_{RMS_c}^{DERj}$ are the RMS phase currents. Note in Fig. 4.6 that nd-DER$_1$ and nd-DER$_2$ injected the same amount of current, since they presented the same nominal power (i.e. 8 kVA). This also occurred with nd-DER$_3$ to nd-DER$_5$, as they had the same power capabilities.

Then, at Interval II in Fig. 4.5, the GCBC was initiated, coordinating d-DERs to

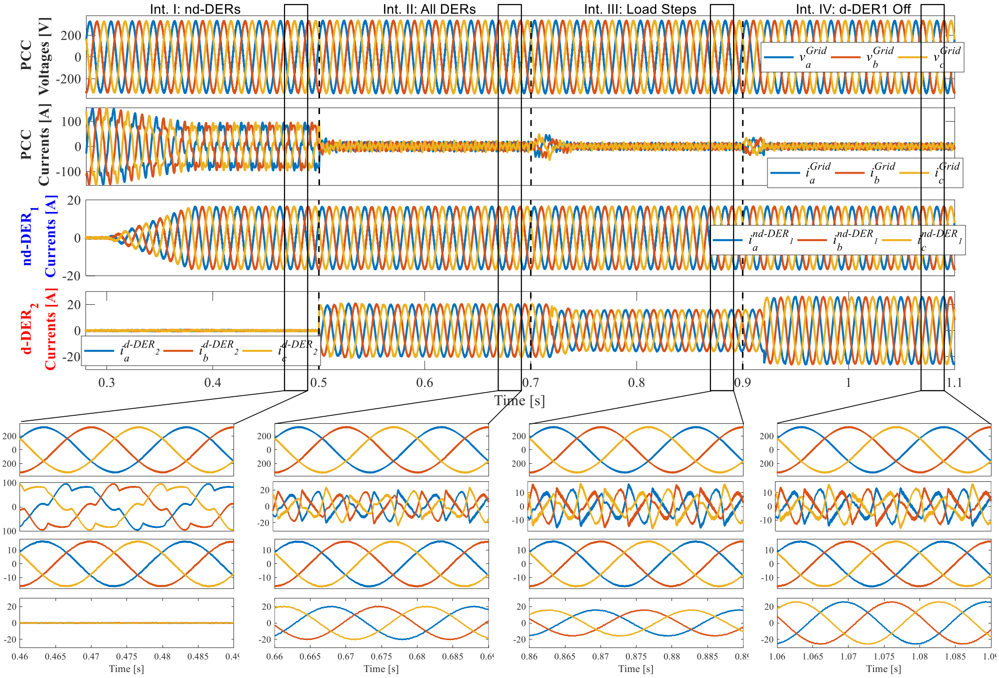

Figure 4.5: Simulation results: active and reactive current sharing capability. Interval I: only nd-DERs injecting active currents; Interval II: d-DERs sharing active and reactive currents; Interval III: load steps; Interval IV: d-DER$_1$ abruptly disconnects. From top to bottom: PCC voltages and currents, nd-DER$_1$ and d-DER$_2$ currents.

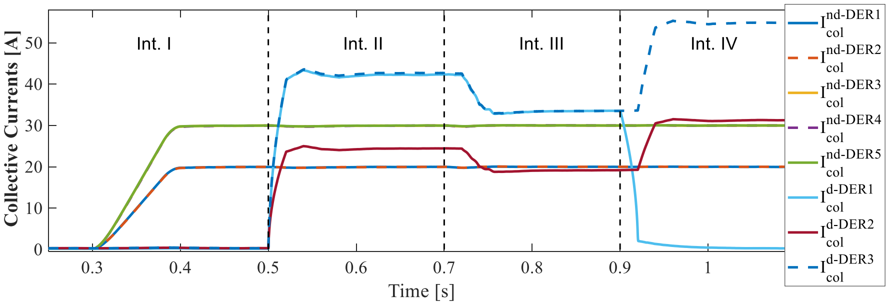

Figure 4.6: DERs' collective currents during simulations in Fig. 4.5.

perform active and reactive current control. Thus, the goal was to steer d-DERs to share the active and reactive current demanded by the loads within the MG. Since these were the only targeted operational purposes, the terms $I_{1||}^{Grid*}$ and $I_{1\perp}^{Grid*}$ used in the GCBC algorithm were considered to be null at this point (i.e., no power dispatch is expected). As d-DERs started receiving scaling coefficients (i.e., $\alpha_{1||}$ and $\alpha_{1\perp}$), they

Table 4.6: Three-phase steady state powers at the PCC, and overall power losses for Fig. 4.5.

PCC Powers				
	Int. I	Int. II	Int. III	Int. IV
A [kVA]	43.63	7.20	5.28	4.98
P [kW]	5.92	0.79	0.05	0.04
Q [kVAR]	42.56	0.16	0.01	0.16
D [kVA]	7.54	7.16	5.28	4.95
Losses [W]	344	146	212	300

rapidly adjusted their current injections. For instance, it can be noted in Fig. 4.5 that after a few fundamental cycles (i.e., approximately two to three cycles) the d-DERs had already reached steady state. In the zoom-in-view of this interval, it is also seen in detail that the nd-DERs currents did not change, and that d-DER$_2$ (as all d-DERs) processed currents that were phase-shifted in relation to the PCC voltages. As a result, it can be seen in Table 4.6 that the P and Q were significantly lower than during the previous interval.

Since the active and reactive current components were mostly supplied by the DERs, the PCC currents became visually more distorted, indicating that primarily harmonics flowed through the PCC. Knowing that the grid voltages were sinusoidal, the D power in Table 4.6 also demonstrates that mostly distortion currents were seen at the PCC. Yet, note that, by having D practically maintaining its amount from Interval I to II, this indicates that the fundamental current sharing provided by the GCBC was decoupled from harmonic components of higher orders.

Another important feature of the GCBC strategy can be interpreted from the collective currents in Fig. 4.6. As the d-DERs reached steady state operation, it is clear that d-DER$_1$ and d-DER$_3$ processed the same amount of collective current during this interval, being approximately 42.69 A. On the other hand, d-DER$_2$ processed 24.47 A of collective current, which is 1.74 times smaller than the ones from d-DER$_1$ and d-DER$_3$. Since a proportional current sharing among coordinated DERs is desired for the MG's operation, such collective values indicate that this goal was achieved. If one recalls the nominal powers of the d-DERs (see Table 4.2), the baseline ratio between d-DER$_1$ and d-DER$_2$ (also between d-DER$_3$ and d-DER$_2$) is $r_{dDERs} = 1.75$, which was very close to the one obtained during simulations (i.e., 1.74). Consequently, it is demonstrated that the GCBC was able to offer proportional current sharing among coordinated DERs, under a model-free approach.

At Interval III, a dynamic change on the MG was emulated by abruptly disconnecting two loads at the same time, i.e. a linear load (L_{B16}) and the nonlinear load at node *B18* (see Fig. 3.1). The circuit breakers of such loads were switched off at 0.7

s, being visible that a step disturbance occurred at the PCC currents immediately after this action (see Fig. 4.5). Such a disturbance occurred at the PCC because the GCBC relies on communication links to adjust the currents injected by the DERs. Thus, note that, after 0.7 s, the d-DER$_2$ currents only started to be adjusted after approximately one fundamental cycle, which was the data transmission speed set for simulations.

As the MGCC sensed a different current flowing through the PCC, the scaling coefficients calculated by the GCBC algorithm were automatically readjusted to update the current setpoints of the DERs. The GCBC scaling coefficients responsible for the active and reactive current control are depicted in Fig. 4.7 for the entire simulation period, demonstrating that the MG operation was constantly monitored and readjusted according to the operational goals. After reaching steady state, the active and reactive currents injected by the d-DERs presented smaller amplitude than in the previous interval, as the load power demand became lower (see zoom-in-view of Interval III in Fig. 4.5).

It can be seen from Table 4.6 that even though a different operational condition occurred within the MG, the GCBC strategy was able to adequately coordinate DERs to achieve similar results, as in previous intervals. Note that the active and reactive powers were practically shared by DERs, not demanding a significant amount of such terms to be provided by the upstream grid. Yet, as can also be seen from the zoom-in-view in Fig. 4.5, mostly harmonic currents flowed through the PCC. With regard to Fig. 4.6, it is understood that the d-DERs still shared currents proportionally to their power capabilities.

A final simulation case is demonstrated at Interval IV, representing the plug-and-play feature of the GCBC strategy. This case shows how the GCBC acted when DERs connect or disconnect from the MG. As explained in Chapter 3, at the beginning of each control cycle "k", the MGCC pulls information from all the DERs willing to participate on the coordinated control. Thus, when a coordinated DER was disconnected from the MG (i.e., for whatever safety or local management reasons), this unit was

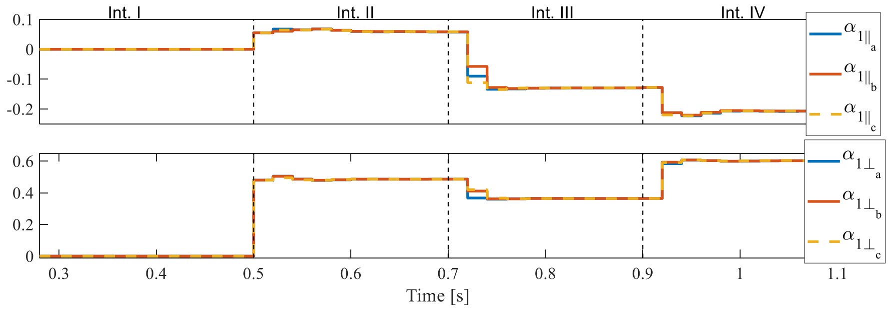

Figure 4.7: GCBC scaling coefficients during simulations in Fig. 4.5.

disregarded for the coordinated operation. Consequently, as the MGCC updated the list of participating DERs at the cycle "k", the nominal current capabilities of the MG (i.e, $I_{h||_m}^{DERt}$, $I_{1||max_m}^{DERt}$ and $I_{1||sto_m}^{DERt}$) were also calculated considering this new status, readjusting the steering of the inverters.

At 0.9 s in Fig. 4.5, d-DER$_1$ was abruptly disconnected from the MG, requiring the GCBC strategy to readjust the coordination of DERs. Similar to Interval III, since the DER disconnection occurred after a control cycle was initiated, the GCBC was only able to start responding to this change at the next control cycle "k + 1". Thus, note that after approximately one fundamental cycle, the currents of the d-DER$_2$ started to be readjusted. For this case, since d-DER$_1$ was disconnected, its currents needed to be shared by the other d-DERs to maintain null active and reactive current flow at the PCC. This can be noted in the currents injected by d-DER$_2$, which had their amplitudes increased. In addition, this change was also noticed in Fig. 4.7, by the significant step occurring in the active and reactive control scaling coefficient.

Table 4.6 and Fig. 4.6 offer some final considerations about this simulated case. For the former, again, it can be seen that mostly harmonics flowed through the PCC, practically maintaining the distortion power demand of the previous interval. The latter shows that the collective currents still followed the expected proportion ratio, as d-DER$_3$ injected 54.87 A, and d-DER$_2$ processed 31.29 A, resulting in $r_{dDERs} = 1.75$.

A final remark, considering all simulated cases in Fig. 4.5, can be made about the overall power losses shown in Table 4.6. By steering DERs to achieve null power flow at the PCC, such losses tended to reduce because generation was closer to consumption, as well as by the fact that the MG presented homogeneous features. Note for instance that, even though all intervals presented losses much lower than the load baseline of 804 W (see Table 4.3), at Interval IV they were higher than during Interval III. This occurred because the distribution of DERs became less homogeneous when d-DER$_1$ was disconnected. A similar analogy applies to Intervals II and III, as the losses became higher for the latter, since the homogeneity of power consumption was reduced by the disconnection of the two loads.

4.3.1.2 Experimental Results

Now, experimental results using the single-phase MG prototype explained in Section 4.2.2 are presented. Let us consider the equivalent circuit of Fig. 4.2, knowing that only d-DER$_1^\star$ and d-DER$_2^\star$ were connected to the MG (i.e., nd-DER$_1^\star$ did not inject any currents, since CB_{nD1} was switched off). All linear loads, as well as the non-linear one, were considered to be connected, drawing currents from the upstream grid, as in Fig. 4.4. Thus, the experimental results of the GCBC steering the two d-DERs* are presented in Fig. 4.8.

Firstly, in Fig. 4.8(a) it is demonstrated how the GCBC coordinates the DERs* to achieve only active current control. Note that, since only $I^*_{1||}$ was being controlled, the d-DERs* injected sinusoidal currents that were practically in-phase with the grid voltages (i.e., v_{PCC}). As a result of having the active current being shared by the DERs*, the PCC current became phase-shifted by 93° in relation to the voltage, beyond presenting distortions. This indicates that mainly reactive and harmonic current

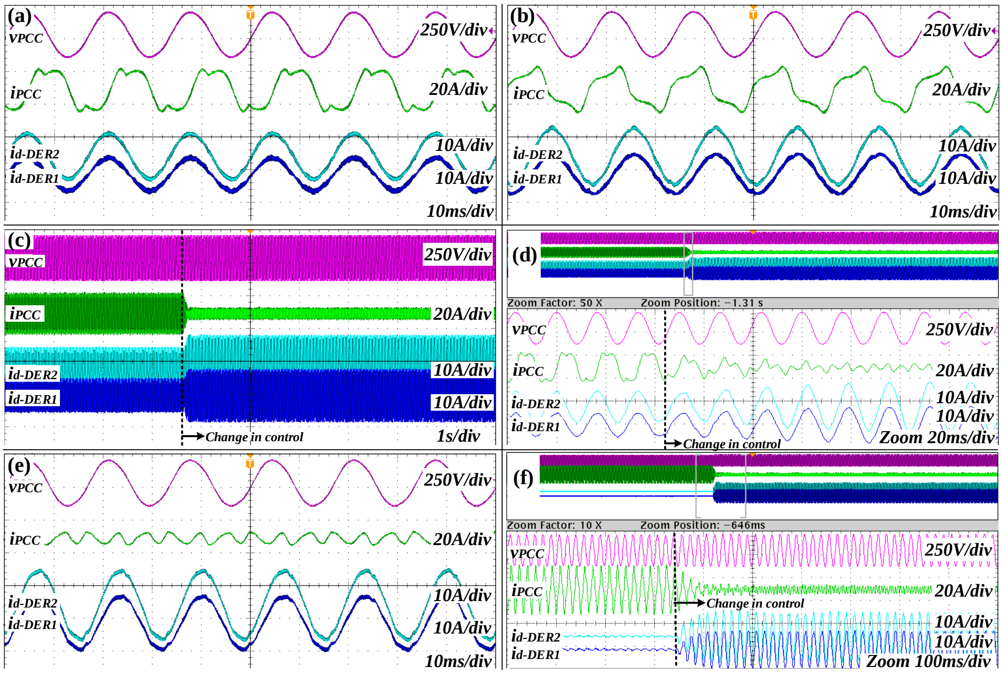

Figure 4.8: Experimental results: active and reactive current sharing. (a) active current control; (b) reactive current control; (c) transition from active to fundamental current control; (d) zoom-in-view of (c); (e) fundamental current control; and (f) initialization of the fundamental current control. From top to bottom: PCC voltage and current, d-DER$_2^\star$ and d-DER$_1^\star$ currents.

Table 4.7: Steady state powers and PF at the PCC for Fig. 4.8.

	PCC Powers		
	Active Control (Fig. 4.8(a))	Reactive Control (Fig. 4.8(b))	Fundamental Control (Fig. 4.8(e))
A [VA]	1204.76	1075	314.6
P [W]	-68.52	1044	-67.61
Q [VAR]	1164.05	-47.49	-32.22
D [VA]	302.18	330.20	305.7
PF	0.00	0.97	0.00

components were drawn from the upstream grid emulator, respectively.

In Table 4.7, the powers calculated for this case are seen, thus reinforcing the statement. Note that *P* (i.e., the active term) has been fully shared by the DERs*, and that Q and D (i.e., reactive and distortion terms, respectively) remained practically the same comparing to the load scenario (see the baseline in Table 4.5). Consequently, it can be inferred that the GCBC approach achieved control over the active current, coordinating DERs* to provide current sharing, without affecting the reactive and harmonic components. The remaining harmonic currents at the PCC led to a THD$_{\text{i}}$ of 23.6%.

Additionally, since accurate proportional sharing was provided by the GCBC approach, the currents of the DERs* presented similar waveforms, having d-DER$_2^\star$ injecting a current with higher amplitude than d-DER$_1^\star$, due to its greater nominal capability. Recalling the baseline for the current ratio between these DERs (i.e., $r_{dDERs^\star} = 1.33$, as presented in Table 4.4), this experimental case led to a proportional sharing given by $r_{dDERs^\star} = 4.93/3.54$, which results in 1.39. Thus, such a result shows that the expected current injection ratio between DERs* was practically obtained, proving that the GCBC also provided accurate proportional active current control during experiments.

A second experimental case is seen in Fig. 4.8(b), in which the reactive current sharing capability of the GCBC was assessed. By controlling $I^*_{1\perp}$, the reactive currents drawn by the loads were injected by the d-DERs*. This can be observed by the phase-shifted currents of the inverters (i.e., in relation to v_{PCC}), which were also proportional to each other. For this case, a proportion ratio of $r_{dDERs^\star} = 6.03/4.31 = 1.39$ was obtained, once again proving that the DERs* shared currents proportionally to their nominal capabilities. As a result, the PCC currents presented minimized phase shift in relation to the PCC voltage (i.e., approximately 12.90$^{\text{o}}$). It is highlighted that this phase shift still existed due to a small amount of reactive current at the PCC, even though the most significant content of this parcel has been shared by the DERs*.

Analyzing the results provided in Table 4.7, one can note that mainly active and distortion powers were seen at the PCC. This caused the MG to operate under a higher power factor (i.e, $PF = 0.97$) than the load scenario, as seen from the upstream grid perspective. Since harmonic currents were not being shared by the DERs*, the PCC current was still highly distorted, presenting THD$_{\text{i}}$ of 28.5%. It is worth reinforcing that the THD$_{\text{i}}$ term uses the amplitude of the fundamental current components in its calculation [133]. Consequently, it is natural to obtain results, for the active and reactive control cases, that are higher than the reference case of $THD_i = 19.5\%$ (i.e., when only loads were connected to the MG, as in Fig. 4.4).

The next two experiments, shown in Figs. 4.8(c) and 4.8(d), demonstrate the transition between operational purposes. For these experiments, the first stage was the active current control scheme shown in Fig. 4.8(a). Then, once a change in control was set by the MGCC, causing the scaling coefficients of the GCBC to be adjusted, both active and reactive current control were performed simultaneously by the d-DERs*. From Fig. 4.8(c) it becomes clear that such a transition did not cause any overvoltage or overcurrents within the MG, allowing DERs* to smoothly transition over the changes in control references. Additionally, from Fig. 4.8(d), the response time of the DERs* demonstrates as rapid response to the change in control setpoints. Thus, once the reactive current control was added to the operation, after approximately three to four fundamental cycles, the system reached steady state operation, sharing both fundamental components of the load currents.

The steady state operation of the MG is depicted in Fig. 4.8(e), when the GCBC was providing both active and reactive current sharing. It can be noted that mainly distortion currents were flowing through the PCC, and that the d-DERs* still shared sinusoidal and proportional currents. A ratio of $r_{dDERs^\star} = 7.45/5.75 = 1.29$ was obtained for this case, which demonstrates that the concomitant offering of multiple functionalities did not affect the expected proportional sharing of currents between DERs*. In contrast to methods such as conventional droop control [31], the GCBC strategy was able to provide accurate fundamental current sharing among DERs* without requiring knowledge of the line impedances interconnecting them.

The powers calculated at the PCC also reinforce some particularities of the control method. The active and reactive powers were significantly lower, and the distortion power, again, remained fairly close to the baseline state. Thus, this proves that mainly harmonic components were flowing through at the PCC, relieving the upstream grid from the burden of providing active and reactive powers for the proper functioning of the loads.

A final result is also shown in Fig. 4.8(f) to demonstrate the transient behavior of the GCBC strategy while steering DERs* to share active and reactive currents. For this result, the initial stage considered that DERs* were idling (i.e., following a current reference of 0 A), and then the MGCC initiated the GCBC at a second instant, later reaching a steady state operation similar to Fig. 4.8(e). Note that the operation did not cause any overcurrents or overvoltages, and rapidly (i.e., in about 4 fundamental cycles) converged to a steady state. Yet, it is evident that proportional sharing was maintained at all instants.

4.3.2 Selective Harmonic Compensation and Full Current Control

Now, two additional operation purposes of the GCBC strategy will be presented. Firstly, it is demonstrated that the GCBC is capable of providing distributed and selective harmonic compensation, achieving low harmonic distortion for the PCC currents. Secondly, the concomitant active, reactive and harmonic current control capabilities of the approach are shown, highlighting the fact that the MG can operate under full self-consumption mode. The main features of the coordination of DERs are initially assessed by simulation results, then further detailed by means of experimental results.

4.3.2.1 Simulation Results

Let us consider the same MG scenario discussed in Section 4.3.1.1 (i.e., the one about active and reactive current control). As previously mentioned, such control over the active and reactive currents is decoupled from the harmonic control. To reaffirm this from the perspective of harmonic control, simulation results are presented in Fig. 4.9, being split into three intervals.

The first simulation case (i.e., Interval I), up to 0.5 s, brings the same scenario as

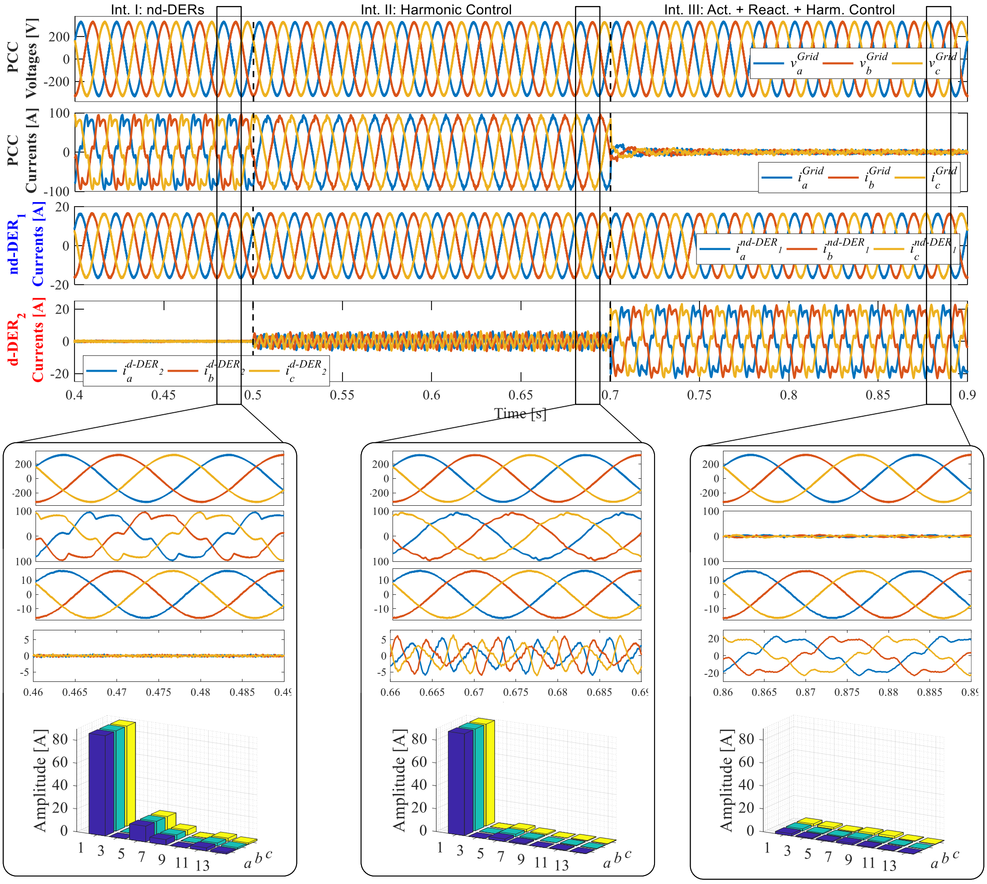

Figure 4.9: Simulation results: harmonic and full current sharing capability. Interval I: only nd-DERs injecting active currents; Interval II: d-DERs sharing harmonic currents; Interval III: d-DERs sharing active, reactive and harmonic currents. From top to bottom: PCC voltages and currents, nd-DER$_1$ and d-DER$_2$ currents, and harmonic spectrum of PCC currents.

earlier demonstrated, in which the MG control was initiated by setting the five nd-DERs to inject active power at full capacity. Since coordinated current control was not performed at this interval, the currents at the PCC were considerably distorted, presenting THD_i of 16.96%, 16.94% and 16.95%, for phases a, b and c, respectively. Additionally, one can note the harmonic spectrum of the PCC currents in the zoom-in-view of Interval I in Fig. 4.9. It is clearly seen that, beyond the fundamental component, the harmonic components presenting most significant amplitudes were the ones from the 5th, 7th, 11th, and 13th orders. The collective currents of the DERs are also presented in Fig. 4.10, showing that the nd-DERs injected constant active power throughout all simulation intervals, and according to their nominal ratings.

The harmonic current control provided by the GCBC was then initiated at Interval II, commanding d-DERs to share the in-phase ($I^*_{h||}$) and quadrature ($I^*_{h\perp}$) components greater than the fundamental (i.e., $h > 1$). It is reinforced that the GCBC algorithm was set in simulations to share the odd harmonic terms, from the 3rd up to the 13th orders. The result in Fig. 4.9 shows that, as d-DERs started sharing the selected harmonic currents, the PCC currents became much less distorted than during the first interval. For instance, a THD_i of 3.64%, 3.70% and 3.69% was obtained for phases a, b and c, respectively. This reduction in distortion can be also evidenced by the harmonic spectrum shown in the zoom-in-view of Fig. 4.9, and by analyzing the D power and the current amplitudes in Table 4.8. Note that the 5th, 7th, 11th and 13th harmonic orders were significantly reduced.

Furthermore, the zoom-in-view of Interval II in Fig. 4.9 indicates that, even though d-DERs were sharing harmonic currents, this action did not cause any impact on the currents injected by the nd-DERs, or in voltages. Additionally, the PCC currents were still phase shifted in relation to the voltages, since reactive control was not set. The scaling coefficients responsible for coordinating this harmonic current sharing among d-DERs (i.e., for phase a) are presented in Fig. 4.11. Observe that the $\alpha_{h||}$ and $\alpha_{h\perp}$ coefficients, at each harmonic order controlled, were frequently adjusted to achieve the desired operational goal. Moreover, the control coefficients of the fundamental

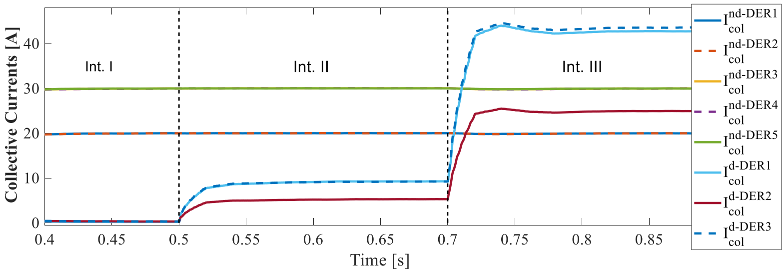

Figure 4.10: DERs' collective currents during simulations in Fig. 4.9.

Table 4.8: Three-phase steady state powers and harmonic current amplitude (for phase a) at the PCC, and overall power losses for Fig. 4.9.

PCC Powers				**Harm. Amplitude [A$_{\text{pk}}$]**			
	Int. I	Int. II	Int. III		Int. I	Int. II	Int. III
A [kVA]	43.63	43.50	1.81	**h=1**	88.24	89.08	1.96
P [kW]	5.92	5.82	0.94	**h=5**	13.75	1.78	0.79
Q [kVAR]	42.56	43.08	0.29	**h=7**	4.70	1.03	1.24
D [kVA]	7.54	1.61	1.51	**h=11**	2.71	0.58	0.40
Losses [W]	344	341	142	**h=13**	1.30	0.32	0.18

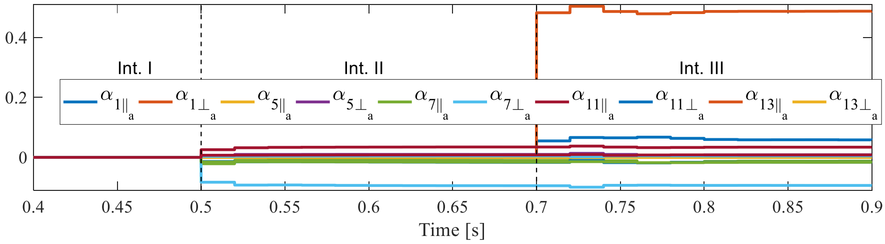

Figure 4.11: GCBC scaling coefficients (for phase a) during simulations in Fig. 4.5.

currents, $\alpha_{1||}$ and $\alpha_{1\perp}$, remained null during Intervals I and II.

The powers calculated at the PCC, seen in Table 4.8, reinforce the fact that the harmonic control practically did not affect the P and Q powers, ensuring decoupled compensation. It is also highlighted that, since the GCBC approach only tackled a few selected harmonic orders, the harmonics of higher order still circulated at the PCC, limiting the reduction of the power D. Yet, the collective currents in Fig. 4.10 show that the three d-DERs proportionally shared the burden of supplying the targeted harmonics. For instance, d-DER$_1$ and d-DER$_3$ shared approximately 9.21 A of collective currents, while d-DER$_2$ processed 5.29 A, which results in a proportion ratio of $r_{dDERs} = 1.74$, being close to the expected 1.75 value.

The last simulation interval in Fig. 4.9 demonstrates that active, reactive, and harmonic current control can be performed concomitantly by the GCBC. Hence, if DERs can be managed to give support to such an operational condition, the MG becomes fully self-sufficient in terms of power demand [44], not depending on the upstream grid for that. This result is demonstrated at Interval III of Fig. 4.9, starting at 0.7 s. Note that after approximately three voltage cycles, the MG reached steady state operation, relying on the d-DERs to share the fundamental and selected harmonic terms.

As d-DERs provided current sharing, the currents flowing through the PCC presented significantly low amplitudes, supporting close to null power flow through the PCC.

Note in Table 4.8 that the *P*, *Q*, and *D* powers were reduced to minimum amounts, reinforcing the fact that the MG operated targeting full self-consumption mode. The amplitude of the active, reactive and harmonic currents in Table 4.8, and the harmonic spectrum shown in Fig. 4.9 for Interval III, also prove that the harmonic currents were significantly reduced at the PCC. Moreover, once again Fig. 4.10 proves that proportional sharing was maintained by the d-DERs. For this case, the proportion ratio was $r_{dDERs} = 1.74$.

A final comment can be made about the power losses within the MG. As earlier discussed in Section 4.3.1.1, since the MG became practically self-sufficient during Interval III, the minimum condition of power loss was obtained (i.e., comparing to the three simulated cases). Nonetheless, this result is approximate to the 146 W attained for Interval II in Table 4.6 (i.e., for the result only considering active and reactive currents). This indicates that, even though harmonic currents are important from a power quality perspective [133], particularly for this MG scenario, their role in power loss minimization over line impedances is not as significant as the fundamental currents.

4.3.2.2 Experimental Results

An experimental validation is now presented to certify the practical applicability of the harmonic and full current control functionalities devised by the GCBC strategy. Let us again consider the single-phase MG prototype discussed in Section 4.2.2, along with the preliminary experimental state of Fig. 4.4, in which all the linear and nonlinear loads existing within the MG were drawing currents. Experimental results are shown in Fig. 4.12, and they sequentially validate three aspects: *i)* the harmonic compensation capability; *ii)* the concomitant sharing of harmonic and reactive currents; and *iii)* the full current control feature, as well as its behavior during load steps. It is worth reinforcing that only the two d-DERs* participated in the coordinated control, and nd-DER$_1^\star$ was disconnected from the circuit (see Fig. 4.2).

Initially, in Fig. 4.12(a), the steady state condition of the harmonic compensation case is depicted. During this case, d-DER$_1^\star$ and d-DER$_2^\star$ were sharing the harmonic components of the 3rd and 5th orders, achieving low distorted current at the PCC, especially compared to the baseline of Fig. 4.4. Visually from Fig. 4.12(a) one can already see that the PCC current resembled a sinusoidal waveform, even though it was still phase shifted in relation to the voltage, as reactive compensation was not performed. Based on Table 4.9 a quantitative analysis can also be conducted. When only loads were connected to the MG, a distortion power (*D*) of 315 VA existed at the PCC, being reduced to approximately 58 VA after the GCBC strategy was enabled. In addition, note that the current amplitude of the 3rd and 5th harmonics became considerably lower. The fundamental component of the PCC current remained practically the same, ensuring decoupled harmonic compensation.

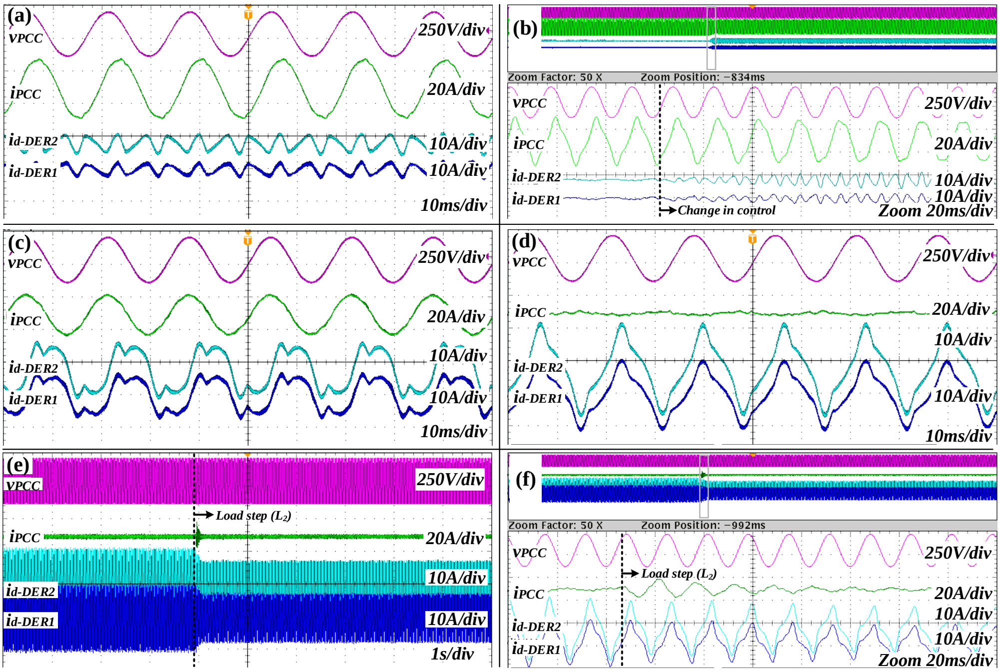

Figure 4.12: Experimental results: harmonic and load current sharing capabilities. (a) harmonic current control; (b) initialization of the harmonic control; (c) reactive and harmonic control; (d) full current control; (e) full current control during load step; and (f) zoom-in-view of (e). From top to bottom: PCC voltage and current, d-DER$_2^\star$ and d-DER$_1^\star$ currents.

Table 4.9: Steady state powers, PF, and harmonic current amplitudes at the PCC for Fig. 4.12.

	PCC Powers		
	Harmonic Control (Fig. 4.12(a))	Harm. + Reac. Control (Fig. 4.12(c))	Full Control (Fig. 4.12(d))
A [VA]	1533.00	1047.00	98.27
P [W]	983.70	1044.00	-73.30
Q [VAR]	1174.00	-20.19	-14.05
D [VA]	58.81	78.04	65.70
PF	0.64	0.99	0.00
	Harmonic Amplitude [A$_{\text{RMS}}$]		
h* = *1	12.2	8.54	0.62
h* = *3	0.18	0.18	0.08
h* = *5	0.17	0.27	0.11

The final THD$_{\text{i}}$ of the PCC was reduced from 19.50% to 2.92%, which represents a significant improvement in current distortion. For this case, d-DER$_2^\star$ processed 1.88 A$_{\text{RMS}}$, whereas d-DER$_1^\star$ injected 1.42 A$_{\text{RMS}}$ into the MG. Thus, the proportion ratio between the DERs resulted in $r_{dDERs^\star} = 1.32$, which indicates an appropriate balance in power demand between inverters, as the reference for proportional sharing was 1.33.

The initialization of the above mentioned result of Fig. 4.12(a) is shown in Fig. 4.12(b). During the startup of the harmonic compensation action, the d-DERs* began operation tracking a null current reference (i.e., not injecting any currents) until the GCBC was enabled and control coefficients were sent to them. Note that there were no inrush currents, and neither was the voltage affected by the enabling of the GCBC strategy (see Fig. 4.12(b)). After a few fundamental cycles (i.e., approximately four to five), the inverters were able to adequately share the targeted harmonic currents drawn by the loads. Besides, proportional sharing of the harmonic currents occurred even during the transient states. It is important to mention that, besides the slow cyclic feature of the GCBC strategy, the dynamics of the digitally implemented current controllers of the DERs* also influence their response time during experimental results.

The next experimental case, shown in Fig. 4.12(c) depicts the capability of coordinated DERs to achieve concomitant reactive and harmonic current compensation. This feature is particularly interesting because, even without having generated or stored energy at the DC side of an inverter (i.e., as a PV-based DER at night), compensation of reactive power and harmonics can be performed. Thus, multifunctional inverters can operate similarly to active power filters [42, 128, 134] under such a condition. The result in Fig. 4.12(c) represents that scenario, but under a cooperative perspective. Observe that, as the d-DERs* shared $I^*_{1\perp}$, along with $I^*_{h||}$ and $I^*_{h\perp}$ (i.e., for $h > 2$), the PCC current became practically in-phase with the voltage, also presenting low distortion. For instance, a small phase deviation of 4.70^{o} occurred between the PCC voltage and current during this case. Yet, a THD$_\text{i}$ of 3.62% was obtained, which can be considered low comparing to the load baseline of 19.50%.

From Fig. 4.12(c) it also visible that d-DER$^\star_2$ processed a current with higher amplitude than d-DER$^\star_1$ (e.g., the former injected 5.95 A$_\text{RMS}$, against 4.46 A$_\text{RMS}$ of the latter). Hence, the proportion ratio among them was $r_{dDERs^\star} = 1.33$, exactly reaching the expected value. The results in Table 4.9 reinforce the effectiveness of the reactive and harmonic compensation. Note that Q was practically fully mitigated, while D also presented significant reduction. The amplitudes of the components of the PCC current also show that the harmonic parcels achieved similar values (i.e, comparing to the previous case), and that the fundamental component was partially reduced due to the harmonic compensation.

Since mainly active power flowed through the PCC, a high power factor of $PF = 0.99$ was reached for this operation. By looking at it from the DSO perspective, such a coordinated control feature is interesting because the distribution system may interpret the MG mainly as a resistive load (i.e, during steady state operation). Such a result can be linked to the discussions about ancillary services provided by transactive MGs, made in Chapter 2. Consequently, an optimized power dispatch can be planned for the upstream grid, reducing overloading and losses throughout the distribution system [135], as apparent power can be reduced.

The final three experimental cases (i.e., Figs. 4.12(d) to 4.12(f)) show the operational purpose of achieving full current control for the MG. As clearly seen in Fig. 4.12(d), by coordinating the d-DERs* to also share the reference ($I^*_{1||}$), along with the reactive and most significant harmonic current terms, the PCC current became practically null. This can be demonstrated by the power terms in Table 4.9. Note that P, Q and D became considerably lower, indicating that only 98.27 VA was flowing through the PCC, in comparison to the approximately 1500 VA being demanded by the loads. The amplitude of the PCC currents also shows that the fundamental and harmonic components being controlled by the GCBC strategy achieved minimum values.

Proportional use of DERs*' current capabilities was also maintained. While concomitantly sharing the active, reactive and harmonic components, d-DER$_2^\star$ and d-DER$_1^\star$ processed 7.79 A_{RMS} and 5.87 A_{RMS}, respectively, thus achieving a proportion ratio of $r_{dDERs^\star} = 1.32$. Moreover, once again, this result of full current control can be interpreted from the upstream grid perspective. If the MG is able to operate under full self-consumption mode, as in Fig. 4.12(d), its electric impact on the upstream grid operation is minimum, giving support to a more robust integrated operation between the MG and its interconnected grid.

The dynamics of such full current control functionality are evidenced in Figs. 4.12(e) and 4.12(f), by applying a load step to the MG. At a given instant, the inductive load (L_2) had its circuit breaker switched off (see Fig. 4.2), reducing the MG power demand. Note in Fig. 4.12(e) the d-DERs* smoothly transiting through this change in the MG, without suffering from overcurrents, and stably operating until steady state was reached. The zoom-in-view of this transition is shown in Fig. 4.12(f), reaffirming that the PCC voltage was not affected by this action. Additionally, after approximately four cycles, the amplitude of the PCC current was again considerably lower. Finally, it can be observed that proportional current sharing was maintained even during transient stages.

4.3.3 Flexible Microgrid Power Dispatchability

In this section, the GCBC functionality behind the main transactive aspect of operation of LV MGs is demonstrated. Beyond coordinating DERs to achieve full current control, the MGCC has the possibility to flexibly control the power flowing through the PCC, ensuring that precise amounts of active and reactive currents are dispatched to, or drawn from, the upstream grid. Thus, beyond making sure that the MG obeys the contractual and technical limits of the operation (i.e., with regard to power demand/dispatch), surplus generated energy can be sold in transactive markets, or can be bought and stored in ESSs. Herein simulation and experimental results demonstrate such an operational feature of the GCBC strategy.

4.3.3.1 Simulation Results

Let us consider an initial scenario in which nd-DERs are injecting nominal active power, while d-DERs are being coordinated to achieve full self-consumption mode for the MG (i.e., just as presented at Interval III for Fig. 4.9). This condition is considered as a preliminary state of operation, namely Interval I, in the following simulation results.

Therefore, the MG power dispatchability provided by the GCBC strategy can be explained based on Fig. 4.13, according to the following additional three intervals that demonstrate, respectively: *i)* the controlled active current dispatch; *ii)* the concomitant active and reactive current dispatch; and *iii)* the controlled drawing of active currents at the PCC. For the following simulation scenarios, the upper and lower limits for the active and reactive current flow at the PCC (i.e., as the contractual MG operation limits) were set to $\overline{I^{Grid}_{1||_m}} = \overline{I^{Grid}_{1\perp_m}} = 200A_{pk}$ and $\underline{I^{Grid}_{1||_m}} = \underline{I^{Grid}_{1\perp_m}} = -200A_{pk}$, respectively. Firstly, at Interval II (i.e, beginning at 0.5 s in Fig. 4.13), the active current control provided by the GCBC was adjusted to consider a non-null reference for the PCC, by setting $I^{Grid*}_{1||_m}$ to -100 A_{pk}. The goal behind this operation is to only dispatch active power to the upstream grid. Thus, one can observe in the zoom-in-view of this interval that, once the d-DERs reached steady state operation, the PCC currents became low distorted, presenting 180$^{\text{o}}$ of phase shift in relation to the PCC voltages. Such a phase shift indicates that the flow of active power is directed toward the upstream grid (i.e., being dispatched by the MG).

The purple horizontal line giving reference to the value of $I^{Grid*}_{1||_m}$ (see the PCC currents plot) explicitly shows that the coordinated control was able to steer the d-DERs to accurately reach the desired peak current reference. Beyond the 180$^{\text{o}}$ phase shift existing between the PCC voltages and currents, the active power dispatch is reinforced in results by the negative value of the *P* power obtained at the PCC, as shown in Table 4.10. For this case, since active, reactive and harmonic control were decoupled, *P* was -49.32 kW, whereas the other power terms remained low (i.e., just as in the full current control scenario shown earlier in Section 4.3.2). One can also note in Table 4.10 that the amplitude of the fundamental component at the PCC was 99.22 A_{pk}, which proves an adequate active current control, as the reference was $I^{Grid*}_{1||_m} = -100$ A_{pk}.

It can be additionally observed in Fig. 4.13, and on the DERs' collective currents in Fig. 4.14, that the nd-DERs did not suffer any impact from the controlled current dispatch provided by the GCBC strategy, ensuring synergistic operation with the d-DERs. Besides, the d-DERs maintained an adequate proportional injection of cur-

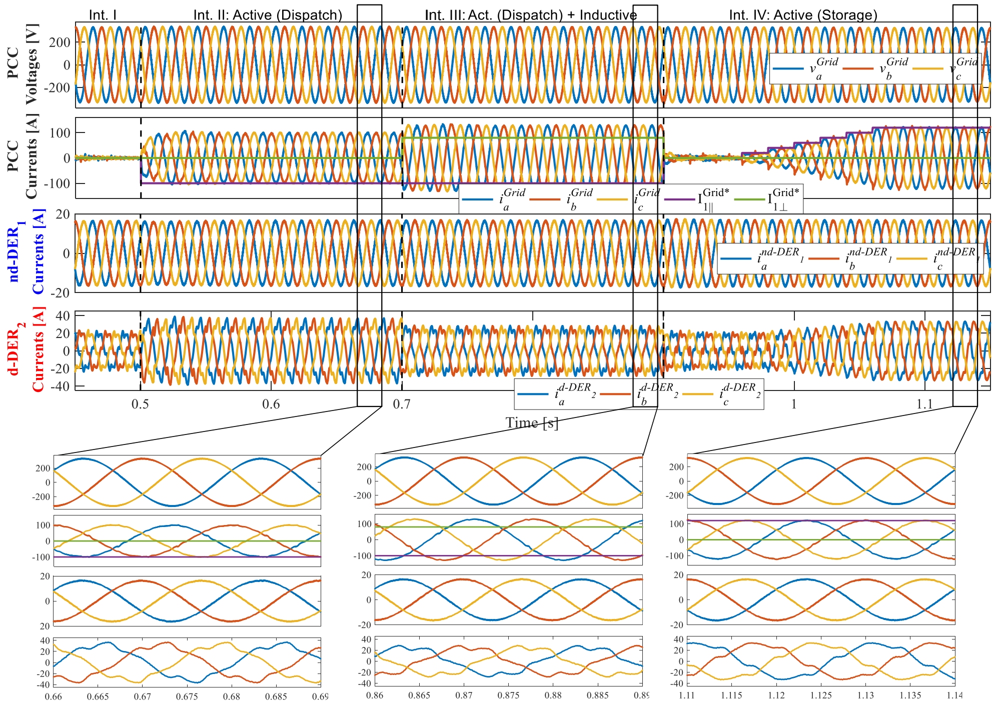

Figure 4.13: Simulation results: power dispatchability at the MG PCC. Interval I: full current control; Interval II: active power dispatch; Interval III: active and reactive power dispatch; and Interval IV: active power storage. From top to bottom: PCC voltages and currents, nd-DER$_1$ and d-DER$_2$ currents.

Table 4.10: Three-phase steady state powers and harmonic current amplitude (for phase a) at the PCC, and overall power losses for Fig. 4.13.

PCC Powers				**Harm. Amplitude [A$_{pk}$]**			
	Int. II	Int. III	Int. IV		Int. II	Int. III	Int. IV
A [kVA]	49.35	63.32	58.01	**h=1**	99.22	127.97	119.96
P [kW]	-49.32	-48.65	57.99	**h=5**	0.64	0.02	0.06
Q [kVAR]	0.88	40.52	-1.03	**h=7**	0.69	0.13	0.08
D [kVA]	1.52	1.35	1.05	**h=11**	0.37	0.08	0.06
Losses [W]	567	720	786	**h=13**	0.45	0.07	0.07

rents, presenting a ratio of $r_{dDERs} = 1.74$, remembering that the baseline was 1.75 for simulations. The scaling coefficients calculated by the GCBC algorithm, which are shown in Fig. 4.15, also demonstrate that the d-DERs were coordinated to provide fundamental and harmonic control. It is evident in Fig. 4.15 that, as a step was applied to $I_{1||_m}^{Grid*}$ (i.e., at 0.5 s) the active current control coefficient ($\alpha_{1||_m}$) was rapidly adjusted to provide the desired dispatch for the MG.

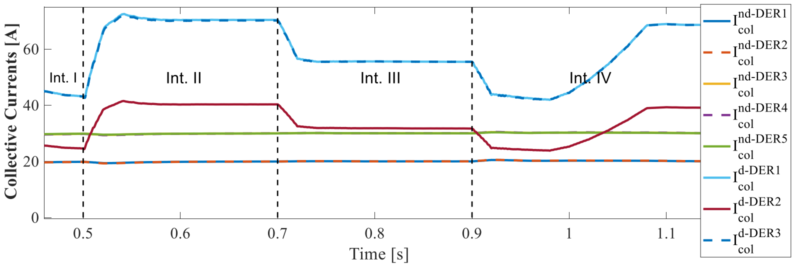

Figure 4.14: DERs' collective currents during simulations in Fig. 4.13.

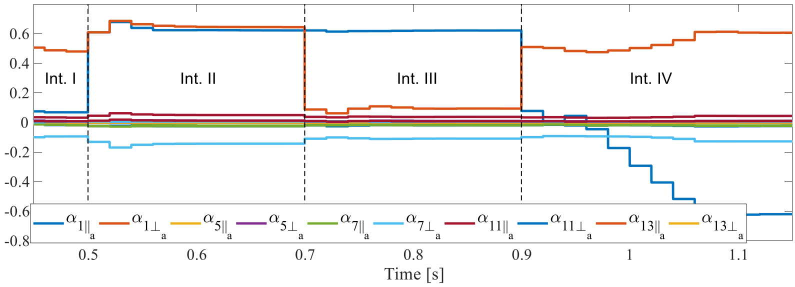

Figure 4.15: GCBC scaling coefficients (for phase a) during simulations in Fig. 4.13.

Another interesting particularity of the GCBC strategy can be seen in Fig. 4.15. Even though the GCBC achieves decoupled control, by increasing the active power dispatch of DERs to meet the PCC demand, the voltages at internal MG nodes tend to rise [136] (such as for the PCC node). Consequently, this action naturally causes the loads to increase the drawing of reactive and harmonic currents. Nevertheless, note that the GCBC scaling coefficients (i.e., other than $\alpha_{1||_m}$) were also automatically readjusted, allowing the possibility to maintain proper performance in power sharing. Discussions about such a scenario, concerning the influence of DERs on voltage profiles, are presented in detail in Chapter 6.

The next simulated scenario in Fig. 4.13 (i.e. Interval III), shows a case in which reactive current dispatch is demanded, concomitantly to the active current dispatch. At 0.7 s, $I_{1\perp_m}^{Grid*}$ was set to +80 A$_{\text{pk}}$ (see green horizontal line in the PCC currents plot), demanding inductive current to flow through the PCC, along with the -100 A$_{\text{pk}}$ active current dispatch per-phase. Note in the zoom-in-view of this interval that the PCC current waveforms became phase-shifted in relation to the voltages, presenting a lagging behavior (i.e., as expected for an inductive feature). The control transitions that enabled the active and reactive power dispatch, respectively at Intervals II and III, occurred smoothly, even though abrupt changes were set to the $I_{1||_m}^{Grid*}$ and $I_{1\perp_m}^{Grid*}$ current references. Thus, the results indicate that the GCBC strategy coordinates DERs to provide power dispatchability, without causing overcurrents or overvoltages. Yet, if desired, the reactive current dispatch provided by the GCBC strategy could achieve the dual operation of Interval III, which would impose a capacitive behavior by setting $I_{1\perp_m}^{Grid*}$ negative.

Table 4.10 demonstrates that the P and Q terms were adequately controlled during Interval III, indicating that an integrated current dispatch comprising both active and reactive currents was obtained. For instance, note that the three-phase power P was -49.32 kW, which results in -95.55 A_{pk} per phase at the PCC (i.e., $I_{1||_m}^{Grid} = \sqrt{2} \cdot P/(3 \cdot V_{RMSm}^{Grid})$), while Q led to a per-phase reactive current of 79.58 A_{pk}. Additionally, as during Interval II, the power D was practically unaffected by the concomitant active and reactive power dispatch.

The last simulated scenario in Fig. 4.13 shows how the GCBC controls the drawing of active currents at the PCC. Looking only at the power dispatch perspective, this case is usually a transactive control action of MGs to take advantage of the cheap selling of energy from external agents [137]. Hence, by buying cheap energy and storing it in ESSs, the MG can later use it for its own needs (e.g., as for peaking purposes [76]), or even sell it back in the energy market at higher prices.

On the other hand, if one looks at the ancillary perspective of this action [64], it can provide support to the upstream grid on the regulation of voltage profiles, as absorption of active power tends to limit voltage rise [136]. Then, the last simulation result in Fig. 4.13 depicts such operationality. First, at Interval IV the previous active and reactive current dispatch references were set to zero, at 0.9 s. After a few cycles, $I_{1||_m}^{Grid*}$ was adjusted, being increased at each cycle until a reference of +120 A_{pk} was obtained (see purple line in the PCC currents plot). It is highlighted that $I_{1||_m}^{Grid*}$ could also be readjusted according to a ramp behavior without impairing current sharing effectiveness. Simulations consider abrupt current steps because they represent a more challenging scenario.

The zoom-in-view of this interval in Fig. 4.13 demonstrates the steady state operation of the MG, in which the PCC currents were still low distorted, but now in-phase with the voltages. Note that the peak reference for the PCC currents was once again adequately followed, indicating proper coordination of the d-DERs. The results in Table 4.10 also reinforce that a per-phase current dispatch of 119.96 A_{pk} was obtained for the fundamental component, being mostly composed of active currents, as only the power P presented significant value. The proportion ratio of 1.71 that was attained for this case, along with the collective currents seen in Fig. 4.14, also indicates that proportional steering of the d-DERs occurred during this interval.

4.3.3.2 Experimental Results

The experimental validation of the flexible power dispatchability provided by the GCBC strategy is herein presented, being also based on the main single-phase MG prototype explained in Section 4.2.2. Again, the case in which all linear and non-linear loads were connected to the MG, and nd-DER$_1^\star$ was disconnected, is considered as baseline. The experiments show four following transactive features: *i)* active current dispatch at the PCC; *ii)* reactive dispatch devising inductive behavior; *iii)* reactive dispatch devising capacitive behavior; and *iv)* concomitant active and reactive current dispatch at the PCC. All experimental results are seen in Fig. 4.16.

The first result, depicted in Fig. 4.16(a), shows the steady state operation of the MG when d-DERs* were sharing the active, reactive and harmonic currents of the loads, additionally providing active current dispatch. For this case, a reference of $I_{1||}^{Grid*} = -10A_{pk}$ was established for the operation, leading the d-DERs* to share currents with a higher amplitude than when only full current control was performed (see Figs. 4.12(d) and Fig. 4.16(a)). Moreover, looking at the PCC current, interesting

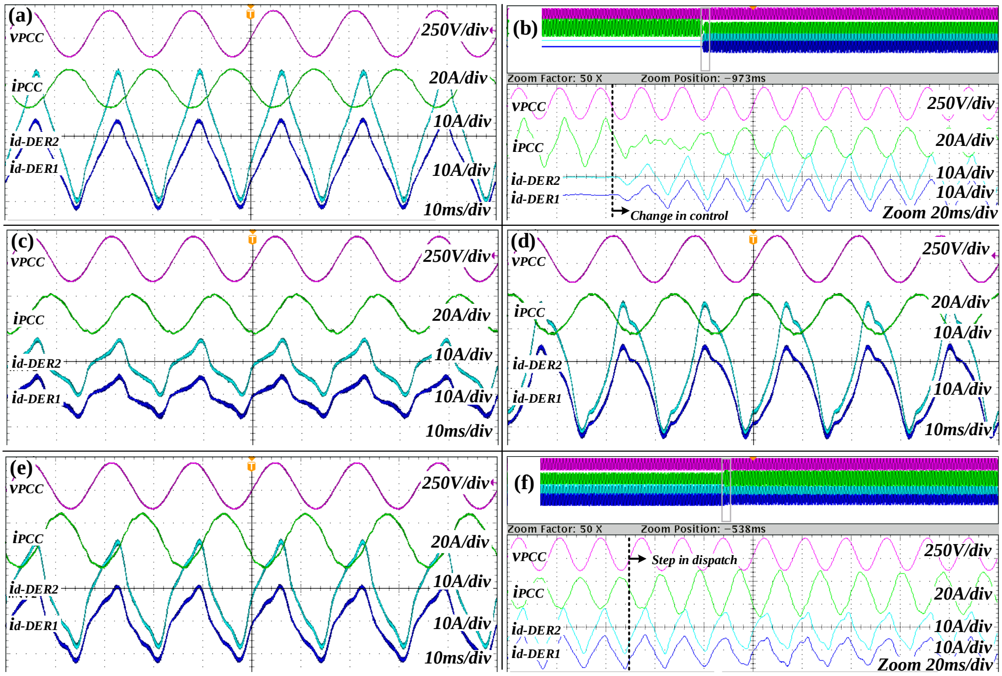

Figure 4.16: Experimental results: active and reactive power dispatchability at PCC, with concomitant full current control. (a) active current dispatch at PCC; (b) initialization of the active current dispatch; (c) reactive inductive current dispatch at PCC; (d) reactive capacitive current dispatch at PCC; (e) active and reactive current dispatch at PCC; and (f) Change in current dispatch. From top to bottom: PCC voltage and current, d-DER$_2^\star$ and d-DER$_1^\star$ currents.

particularities can be highlighted. Observe that this current resembled a sinusoidal waveform, also presenting phase opposition in relation to the PCC voltage. In fact, the phase of this current was 173.6^{o} (i.e., being close to 180^{o}), which indicates that mainly active power circulated at the PCC, and that it was being dispatched to the grid emulator.

The results in Table 4.11 reiterate the fact that mainly active power was seen at the PCC, as can be noted by the practically negligible *Q* and *D* powers. Besides, since *P* was negative, this also indicates power flowing towards the upstream grid. Visually looking at Fig. 4.16(a), one can also note that the amplitude of i_{PCC} practically remained within one unit of the oscilloscope window, which considered a scale of 20 A/div. Thus, the goal of achieving $I_{1||}^{Grid*} = -10A_{pk}$ was obtained (i.e., resulting in a current waveform with 20 A peak to peak). Such control performed by the GCBC strategy caused d-DER$_1^\star$ to process 11.08 A$_{\text{RMS}}$, whereas the d-DER$_2^\star$ processed 8.11 A$_{\text{RMS}}$. Thus, a ratio of $r_{dDERs^\star} = 1.36$ was obtained, practically respecting the reference value of 1.33.

The initialization of the case of Fig. 4.16(a) is shown in Fig. 4.16(b). Like other previous experiments, the d-DERs* started following a null current reference until a change in the MG management initiated the GCBC strategy. Note that the inverters started performing active, reactive and harmonic control, at the same time as the active current dispatch. After approximately four cycles, all the unwanted currents (i.e., reactive and harmonic terms) were adequately shared by the inverters, and the active power dispatch reached the desired operational point. Proportional current sharing was maintained throughout the transient states, without leading to any overcurrents, nor overvoltage.

The GCBC strategy also features the capability to provide reactive current controllability at the PCC, which can even be flexibly adjusted to shape the MG to present either an inductive or a capacitive behavior. The inductive power dispatchability of the MG is experimentally validated by the result in Fig. 4.16(c). This steady state result was achieved while setting active, reactive and harmonic control to be performed,

Table 4.11: Steady state powers at the PCC for Fig. 4.16.

	PCC Powers			
	Active (Fig. 4.16(a))	Inductive (Fig. 4.16(c))	Capacitive (Fig. 4.16(d))	Act. + Induct. (Fig. 4.16(e)
A [VA]	1058.00	1024.00	1092.00	1439.00
P [W]	-1051.00	17.65	-7.27	1017.00
Q [VAR]	-16.47	1023.00	-1082.00	1014.00
D [VA]	35.10	50.88	104.10	78.79

along with the consideration of having $I_{1\perp}^{Grid*} = +10A_{pk}$. By analyzing the PCC current for this case, one can note that it was practically sinusoidal, also lagging with respect to the voltage, which indicates an inductive behavior at the PCC. The phase shift between the PCC current and voltage was 88.97^{o}, being very close to the expected value of 90^{o}. This inductive behavior can also be visually seen during the zero crossings of the voltage waveform, which practically correspond to the peaks of the PCC current waveform. Table 4.11 reiterates that mainly positive reactive power was seen at the PCC. The proportion ratio between DERs* was adequately reached as well, being 1.38 for this case, as d-DER$_{1}^{\star}$ and d-DER$_{2}^{\star}$ processed 4.81 and 3.47 A_{RMS}, respectively.

The dual operation (i.e, the capacitive current dispatch) has its steady state experimental result presented in Fig. 4.16(d), after setting $I_{1\perp}^{Grid*} = -10A_{pk}$. Observe that, instead of having i_{PCC} with a lagging waveform (i.e., as for the inductive behavior), it presented a leading characteristic during this case. The phase shift obtained was -90.40^{o}, precisely demonstrating that the PCC current was ahead of the voltage. Additionally, it is clearly visible in Fig. 4.16(d) that this current was low distorted and presented an amplitude close to the 10 A_{pk} value targeted. Table 4.11 also reaffirms that mainly the Q power was seen at the PCC, presenting a negative value, which also provides an indication of the capacitive behavior.

This flexibility of the GCBC strategy to provide reactive current control at the PCC, shaping the MG to present either inductive or capacitive behavior, is of particular interest to the upstream grid, as mentioned in Chapter 2. Such a reactive power dispatch provided by LV MGs can be understood as energy services, which can be tradeable in transactive energy markets, giving support to enhance the operational stiffness of the distribution system. For instance, by shaping interconnected MGs to present controllable reactive behaviors, the DSO can employ dynamic management strategies to regulate voltage profiles, as well as to compensate for possible inductive or capacitive features of power distribution cables in longer power systems [138].

Another experiment shows the concomitant control of the active and reactive currents at the PCC. The steady state condition of this case is presented in Fig. 4.16(e), knowing that the active and reactive current references set for the PCC were $I_{1||}^{Grid*} = +10A_{pk}$ and $I_{1\perp}^{Grid*} = +10A_{pk}$, respectively. It can be noted that the waveform of i_{PCC} was lagging the voltage, presenting phase shift of 134.9^{o}, which indicates that not only an inductive current was measured at the PCC (i.e., since the phase shift was not around 90^{o}).

In addition, Table 4.11 shows that the P and Q powers were practically the same, which reinforces that the GCBC was able to steer DERs* to provide adequate control over the active and reactive currents. These power terms also indicate that the peak values of the active and reactive currents were fairly close to the expected value. For instance, for the active current, one can calculate $1014W/127V_{RMS} = 7.98A_{RMS}$, which results in $I_{1||}^{Grid} = 11.29A_{pk}$. The proportion ratio obtained for this case was also adequate, being 1.34, as d-DER$_1^\star$ and d-DER$_2^\star$ processed 6.98 $\mathrm{A_{RMS}}$ and 9.41 $\mathrm{A_{RMS}}$, respectively.

The last experiment is presented in Fig. 4.16(f) to demonstrate the transient behavior of the DERs*. This case has two stages, in which the first one is given by Fig. 4.16(a), and the second one results in the steady state condition of Fig. 4.16(e). For that, at a certain time, a control change in the coordination strategy occurs, allowing the d-DERs* to additionally consider the sharing of $I_{1\perp}^{Grid*} = +10A_{pk}$, beyond the processing of $I_{1||}^{Grid*} = +10A_{pk}$ that was taking place at the initial stage. Observe in Fig. 4.16(f) that, as the control change occurred, the reactive current dispatch was added to the operation without causing any unwanted behavior in the currents of the d-DERs*, or in the PCC current and voltage. Moreover, the strategy was able to steer the inverters proportionally to the their nominal capacities at all times.

4.3.4 DERs of Assorted Operational Natures and Variable Generation Capabilities

Inverter-dominated LV MGs usually comprise multiple RESs and ESSs, which present particular operational natures, beyond the fact that power generation intermittency is likely to exist for some of these generation systems. Thus, once a coordinated control strategy is employed in such MGs, it is imperative to cope with the existence of DERs of a varied nature (i.e., being nd- and d-DERs). Additionally, the control strategy should endure operation when DERs face variable energy generation profiles.

Although the previous simulation and experimental scenarios have demonstrated that the GCBC strategy is capable of accommodating both nd- and d-DERs, it has not been shown how the MG operates when the primary energy sources of nd-DERs present variable generation. Moreover, since two types of nd-DERs (i.e., characterized by either the presence or absence of communication interface) are considered within this thesis, it is important to also demonstrate how the GCBC performs under such a scenario. Therefore, the following simulation and experimental results demonstrate these two features of the strategy.

4.3.4.1 Simulation Results

Let us again establish an initial operational condition, being presented at Interval I in Fig. 4.17, in which the main MG testbench is used, having all eight DERs connected to it, as well as all loads (see Fig. 3.1). Firstly, it was considered that the five nd-DERs were injecting active power at nominal capability (i.e, 1 p.u.), whereas the three d-DERs were being coordinated by the GCBC strategy to achieve full current control. Consequently, one can see in Fig. 4.17 that most of the load currents were provided by the DERs, as the PCC currents were significantly low.

At this point, it is important to remember that nd-DER$_1$ and nd-DER$_2$ do not present a communication interface, therefore, not being controlled by the GCBC approach at any moment. On the other hand, nd-DER$_3$ to nd-DER$_5$ present a communication interface and can participate in the sharing of non-active currents (i.e., reactive and harmonic components), if they present remaining power capability while injecting their generated energy. Then, at 0.5 s in Fig. 4.17, a variation in the energy generation profile of nd-DER$_1$ and nd-DER$_2$ was considered, abruptly imposing a reduction of 50% in the inverters' active power injections. By looking at the currents of nd-DER$_1$ at Interval II, one can easily identify such a sudden change, noting that their amplitudes were reduced by half. The collective currents of the DERs, which can be seen in Fig. 4.18, also demonstrate that the amount processed by these two nd-DERs went from 20 A to 10 A.

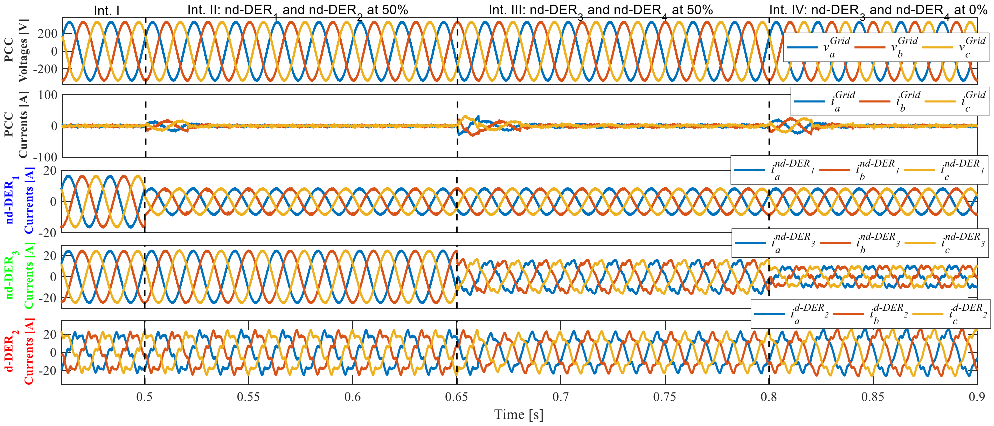

Figure 4.17: Simulation results: full current control considering assorted inverters and variable generation capability. Interval I: nd-DERs at 100% generation capability; Interval II: nd-DER$_1$ and nd-DER$_2$ at 50% generation capability; Interval III: nd-DER$_3$ and nd-DER$_4$ at 50% generation capability; and Interval IV: nd-DER$_3$ and nd-DER$_4$ at 0% generation capability. From top to bottom: PCC voltages and currents, nd-DER$_1$, nd-DER$_3$ and d-DER$_2$ currents.

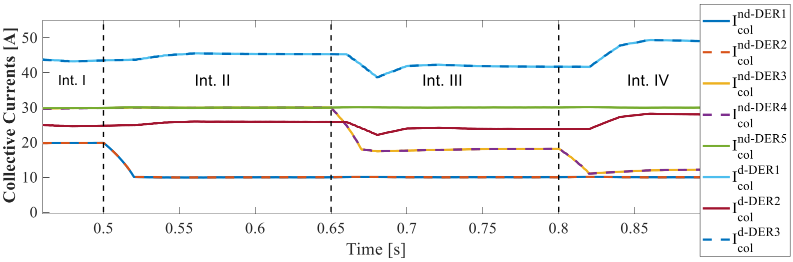

Figure 4.18: DERs' collective currents during simulations in Fig. 4.17.

Most importantly, observe in Figs. 4.17 and 4.18 that the currents from the other nd-DERs practically did not change. The d-DERs, in contrast, had to adjust their current injections to maintain the current sharing performance (see d-DER$_2$ currents in Fig. 4.17, and the scaling coefficients in Fig. 4.19). The steady state powers during Interval II are shown in Table 4.12, reinforcing that d-DERs were able to adjust their operations to achieve low amounts of active, reactive and distortion components flowing through the PCC.

During the next simulation scenario seen at Interval III, beginning at 0.65 s in Fig. 4.17, the energy generation variability of the other nd-DERs (i.e., the ones comprising communication interface) is depicted. While having nd-DER$_1$ and nd-DER$_2$ maintaining active power injection at 50% of their capabilities, the energy generation of nd-DER$_3$ and nd-DER$_4$ were also abruptly reduced by half. Consequently, these two additional nd-DERs operating at 50% of energy generation presented remaining power capability, which could be used to deploy ancillary actions.

In addition, as nd-DER$_3$ and nd-DER$_4$ comprise the communication interface, the MGCC knows about their current injection statuses, which allowed them to be incorporated into the coordinated operation. It should be highlighted that, during all inter-

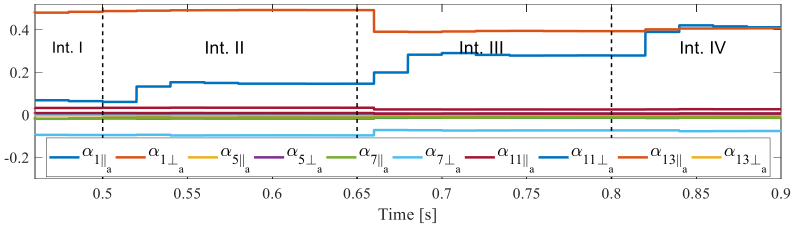

Figure 4.19: GCBC scaling coefficients (for phase a) during simulations in Fig. 4.17.

Table 4.12: Three-phase steady state powers at the PCC and at the DERs for Fig. 4.17. Units: P [kW], Q [kVAR], and D [kVA].

	Int. II			**Int. III**			**Int. IV**		
	P	Q	D	P	Q	D	P	Q	D
PCC	0.03	0.00	0.93	0.00	1.50	0.96	0.00	0.78	0.89
nd-DER$_1$	4.02	-0.05	0.16	4.02	-0.04	0.15	4.01	-0.04	0.15
nd-DER$_2$	4.02	-0.05	0.15	4.00	-0.04	0.16	4.01	-0.04	0.15
nd-DER$_3$	12.08	-0.12	0.40	6.07	1.98	0.80	0.09	2.43	0.93
nd-DER$_4$	12.10	-0.12	0.44	6.08	1.97	0.81	0.08	2.43	0.93
nd-DER$_5$	12.01	-0.12	0.37	12.01	-0.12	0.37	11.99	-0.12	0.37
d-DER$_1$	5.50	8.50	3.21	10.11	6.53	2.48	14.77	6.36	2.46
d-DER$_2$	3.16	4.87	1.84	5.79	3.73	1.44	8.42	3.63	1.44
d-DER$_3$	5.54	8.55	3.24	10.14	6.53	2.52	14.75	6.37	2.51

vals simulated in Fig. 4.17, nd-DER$_5$ was the only nd-DER operating injecting active power at 100% capacity, which can be visualized in Fig. 4.18. This was performed to demonstrate that the GCBC strategy is resilient, even having DERs of similar operational features facing different energy generation profiles.

It can be seen in Fig. 4.17 that nd-DER$_3$, as well as nd-DER$_4$, started to process reactive and harmonic currents during Interval III. Even though transient currents appeared at the PCC, due to the sudden change in the energy generation of these two nd-DERs, the GCBC algorithm was able to rapidly (i.e., in about two fundamental cycles) adjust the scaling coefficients. Therefore, Table 4.12 shows that a similar performance was maintained at the PCC, presenting low amounts of the P, Q and D terms, especially if compared to the load baseline of $P = 55.55$ kW, $Q = 39.9$ kVAR and $D = 7.32$ kVA. Besides, observe in Fig. 4.18 that the currents injected by nd-DER$_1$, nd-DER$_2$ and nd-DER$_5$ were not affected.

Another important discussion needs to be made about the proportional current sharing provided by the GCBC strategy. By coordinating nd-DERs to only share reactive and harmonic currents, their participation in the GCBC strategy is proportional to their remaining capabilities. This means that their active current injections are subtracted from their nominal ratings, according to the iterative calculation of $\sqrt{\Delta I_m}$ in Fig. 3.7.

The results in Table 4.12 during Interval III can be taken as example, in which it is shown that nd-DER$_3$ and nd-DER$_4$ injected 6 kW of active power, whereas d-DER$_1$ (and d-DER$_2$, as they have same ratings) processed approximately 10 kW. Hence, making an approximation, it can be considered that voltages throughout the MG roughly present similar magnitudes, so Fig. 3.7 can be interpreted by power terms. This allows one to calculate the following available capability for d-DER$_1$ to share reactive power: $Q_{aval}^{d-DER_1} = \sqrt{(A^{d-DER_1})^2 - (P^{d-DER_1})^2}$, which gives $Q_{aval}^{d-DER_1} = \sqrt{(35000)^2 - (10000)^2} = 33.54$ kVAR. The same calculation can be performed for nd-DER$_3$, resulting in $Q_{aval}^{nd-DER_3} = \sqrt{(12000)^2 - (6000)^2} = 10.39$ kVAR. Note that the ratio between the power availabilities from such d- and nd-DERs was approximately 3.22, indicating that the former DERs should process reactive power approximately three times higher than the latter ones. Now, from Table 4.12, it is possible to verify that the ratio between the reactive powers of such DERs was 3.29 (i.e., 6.53 kVAR/1.97 kVAR). Thus, it is proved that proportional sharing was maintained, even under variable energy generation capabilities.

A last simulation case is shown at Interval IV of Fig. 4.17, abruptly imposing a null generation capability only for nd-DER$_3$ and nd-DER$_4$. As a result, such nd-DERs did not have the capability to inject active power into the grid anymore. However, they could still continue to be coordinated to participate in the sharing of reactive and harmonic currents. Note in Figs. 4.17 and 4.19 that the strategy was able to adequately accommodate the DERs upon such a scenario, reaching steady state after approximately three cycles. Moreover, from Table 4.12 it is seen that nd-DER$_3$ and nd-DER$_4$ practically did not process active power, which reflected on the increased P values attained for d-DER$_1$ to d-DER$_3$, if compared to Interval III. As such nd-DERs presented more available power capability, the sharing of reactive and harmonic components was also readjusted by the GCBC. Thus, this case demonstrates that the GCBC approach is also able to accommodate active filtering devices that potentially exist within the MG, and that intend to cooperate with DERs.

4.3.4.2 Experimental Results

Experimental validations are herein presented to show that the GCBC strategy is able to coordinate DERs of assorted operational natures, as well as upon variable energy generation profiles, in real-life implementations. The experiments use the main single-phase MG prototype mentioned in Section 4.2.2, considering all linear and non-linear loads connected to it (see Fig. 4.2), with the results divided into three cases. For the first two cases, two DERs are considered; one operating as a dispatchable unit, and the other one as a non-dispatchable unit that participates in the GCBC. For the last case, a third inverter is connected to the MG, operating as an nd-DER without communication interface. During all cases, the coordination of inverters strives to attain full current control, sharing the active, reactive and harmonic current terms drawn by the loads.

The first case is depicted in Fig. 4.20(a), considering that d-DER$_1^\star$ and d-DER$_2^\star$ were the two inverters connected to the MG. To emulate a scenario comprising assorted inverters, only for this section, d-DER$_1^\star$ was configured to be driven as an nd-DER. Thus, it injected its generated active current into the MG under a local perspective. Additionally, d-DER$_1^\star$ could also be coordinated to share reactive currents, as well as harmonics of the selected 3rd and 5th orders, if the remaining capability was available. Even though d-DER$_1^\star$ operated as a non-dispatchable inverter, its nomenclature as a d-DER* was maintained for the sake of organization.

The result in Fig. 4.20(a) shows the steady state operation of the MG, considering that d-DER$_1^\star$ was injecting active current at 20% of its nominal rating. Consequently, in Table 4.13 it is seen that d-DER$_1^\star$ injected 251.3 W of active power, while d-DER$_2^\star$ was responsible for providing the remaining active power demanded by the loads. One can note that the P power seen at the PCC was low, being -48.49 W, in comparison to the baseline of 980 W. This demonstrates that the GCBC was able to steer d-DER$_2^\star$ to process the remaining active power that was not supplied by d-DER$_1^\star$. In parallel, as d-DER$_1^\star$ had most of its power capability idling, the GCBC strategy strived to integrate the operations of both DERs* for what concerns the sharing of reactive and harmonic current demanded by loads.

As a result of such cooperation, Fig. 4.20(a) shows that both DERs* processed

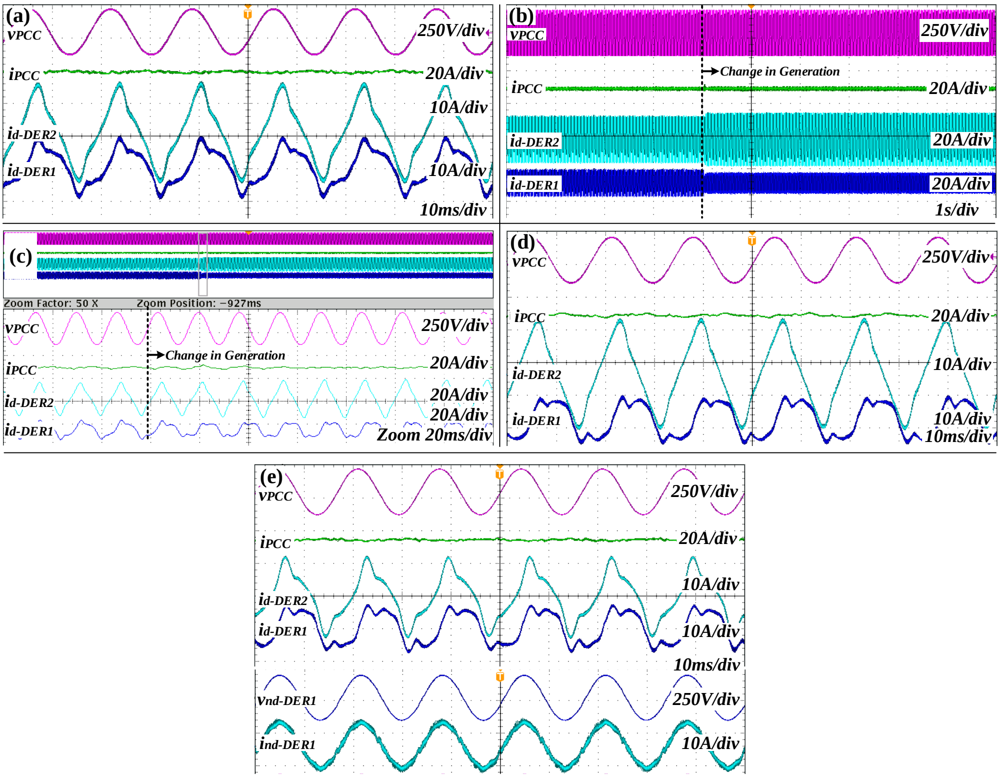

Figure 4.20: Experimental results: full current control with assorted inverters and variable generation capability. (a) d-DER$_1^\star$ emulates an nd-DER with 20% of generation capability; (b) d-DER$_1^\star$ emulates an nd-DER transiting from 20% to null generation capability; (c) zoom-in-view of (b); (d) steady state condition of (c); (e) case (d) considering nd-DER$_1^\star$ injecting active power. From top to bottom: PCC voltage and current, d-DER$_2^\star$ and d-DER$_1^\star$ currents. The results in (e) were measured using two oscilloscopes using AC line trigger mode.

Table 4.13: Steady state powers at the PCC and the DERs for Fig. 4.20. Units: P [W], Q [VAR], D [VA].

	Fig. 4.20(a)			**Fig. 4.20(d)**			**Fig. 4.20(e)**		
	P	Q	D	P	Q	D	P	Q	D
PCC	-48.49	7.67	101.4	-36.0	47.1	77.9	-31.2	-16.9	110.4
d-DER$_2^\star$	826.5	647.8	203.3	1154	573.2	187.8	460.0	679.2	231.2
d-DER$_1^\star$	271.3	542.3	184.5	-7.5	584.5	176.3	9.51	556.5	169.6
nd-DER$_1^\star$	0.0	0.0	0.0	0.0	0.0	0.0	591.4	2.7	74.4

currents that were phase shifted in relation to the PCC voltage, being also highly distorted. Therefore, the PCC current became practically null, indicating that full current control was adequately attained by the operation. Nonetheless, in contrast to previous experimental cases, the currents of both DERs did not present similar and proportional waveforms, as the inverters were playing different roles. From Table 4.13 this can also be seen, as both DERs* injected non-proportional values of P, also processing reactive and harmonic powers that do not appear to be proportional at first sight.

However, it is important to remember that, as explained during simulations, the current sharing proportionality should only be considered based on the remaining capabilities of the inverters (i.e., after considering active current injection). Further analyzing the obtained power terms for this case, the proportion ratio between the DERs was 1.19. Consequently, this result indicates an adequate sharing of currents, as a reference ratio of 1.21 can be theoretically calculated.

The second experimental case is depicted in Figs. 4.20(b) to 4.20(d). This case shows the transient and steady state results when the active current generation profile of d-DER$_1^\star$ was reduced from 20% to 0%, causing this inverter to resemble the operation of an active filter. In 4.20(b), the instant at which such a change occurred at the d-DER$_1^\star$ is shown. The zoom-in-view of this transition is presented in Fig. 4.20(c), demonstrating that such an action did not cause disturbances in the PCC voltage, nor in the currents seen at the PCC or processed by the DERs*. After approximately three cycles, the GCBC was able to adequately adjust the currents injected by the inverters.

The steady state waveforms for this case are seen in Fig. 4.20(d) demonstrating that d-DER$_1^\star$ processed a current explicitly different from d-DER$_2^\star$, as it operated only sharing reactive and harmonic currents. However, the powers shown in Table 4.13 prove that proportional power sharing was obtained for the reactive and harmonic components. For instance, one can calculate 1.38 kVA of remaining capability for d-DER$_2^\star$ (i.e., $\sqrt{1800^2 - 1154^2}$), which was close to the nominal capability of d-DER$_1^\star$ (i.e., 1.34 kVA, see Table 4.2). Thus, the two inverters should process similar amounts of Q and D powers, which was the case for the results in Table 4.2 (see that the DERs*' non-active powers were practically the same).

As a final experiment, the case in Fig. 4.20(e) is complementary to Fig. 4.20(d), demonstrating the insertion of one additional non-dispatchable inverter to the MG, which is nd-DER$_1^\star$ (see Fig. 4.2). It is reinforced that the previous operational conditions of Fig. 4.20(d) were maintained. Thus, nd-DER$_1^\star$ was added to the MG to operate injecting active power (i.e., 591.4 W), as can be seen by the low distorted and in-phase current in Fig. 4.20(e), as well as in Table 4.2. Since one more inverter injected the active currents being drawn by the loads, the GCBC approach was able to indirectly measure this condition at the PCC currents, later adjusting the coordination of the other DERs*. Consequently, note that the currents from d-DER$_1^\star$ and d-DER$_2^\star$ presented lower amplitudes than during the previous case, and the current flow through the PCC remained significantly lower.

Finally, it is also highlighted that, since d-DER$_2^\star$ reduced its active power injection, it presented more remaining capability. Hence, this inverter ended up processing more reactive and harmonic currents than d-DER$_1^\star$ (see Q and D powers in Table 4.2). Nonetheless, such current sharing still occurred proportionality to the remaining capabilities of the two DERs*, achieving $r_{dDERs^\star} = 1.22$, knowing that the reference proportion ratio was 1.29 during this case. Thus, the experiments proved the feasibility of the GCBC strategy to accommodate inverters of different operation natures, as well as to cope with different generation profiles.

4.4 Complementary Operational Considerations

A variety of scenarios can be faced by LV MGs, and DERs can be coordinated according to several control strategies that offer particular advantages and disadvantages. Although the GCBC strategy is derived with a primary focus on the transactive aspect of a MG, meaning that grid-connected mode is mainly targeted, it is important to clarify how DERs are also coordinated during mode transition, as well as when islanded operation occurs. In addition, since conventional droop control is the most commonly adopted solution for steering inverters in MGs, considerations are offered in this section to highlight the particularities of the GCBC strategy.

4.4.1 Islanded Operation and Transition in Microgrid Modes

By definition, MGs must endure steady state operation under either interconnected or islanded modes [29]. In addition, they must support the transition between such states, by means of smooth maneuvers. Nevertheless, there are many technical challenges behind MG mode transition, such as the need to suppress voltage and current fluctuations [139], the requirement for adequate implementation of re-synchronization strategies for DERs [140], and others [141]. Hence, especially for scenarios of high penetration of DERs [41], it is important to certify that their coordination can endure the dynamic changes occurring in the MG, when transition between modes occurs.

In general, MGs can take advantage of one of the two following alternatives, in order to endure islanded operation and smooth mode transitions. The first alternative (i.e., *Alternative 1*) is the use of any coordination strategy capable of steering multiple inverters (i.e., of dispatchable nature) as voltage controlled sources. The second solution (i.e., *Alternative 2*) considers the existence of a single utility-interactive converter, which forms the MG when the upstream grid is absent. These two approaches are further explained as follows.

- *Alternative 1:*

  For this case, inverters based on only intermittent RESs (i.e., nd-DERs) are usually not considered for grid-forming purposes, resulting in the idea that there must exist d-DERs in the MG to play that role [41]. When the upstream grid becomes absent, d-DERs have to share the burden of forming the grid, controlling voltage magnitude and regulating frequency. Consequently, during the transition from grid-connected to islanded mode, and vice-versa, the coordination strategy must allow DERs to properly re-synchronize and interact with each other without causing undesired electric transients [140].

Although coping with such a requirement is not trivial, strategies like droop control [31, 139], and concepts like virtual synchronous machines (VSM) [142] and virtual oscillators (VOC) [143], can fulfill such a need. The GCBC strategy, however, has not been devised with that focus of operation. Thus, when the GCBC is adopted in a MG without grid-interactive converters, if islanding is detected by d-DERs [144], they must change their local control approach to operate autonomously according to droop-based, VSM or VOC concepts. Since such autonomous approaches have been widely investigated in the literature [30], this thesis does not further address this alternative;

- *Alternative 2:*

  Utility-interactive converters [145] are power electronic interfaces incorporating sophisticated power processing capabilities [100], and they operate based on two main purposes in MGs. The first purpose relates to the interconnected scenario, in which such converters give support to obtain a more robust MG operation, particularly when adverse conditions occur [146] (e.g., under abnormal voltages, under non-linearities in voltages/currents, so forth). Additionally, since utility-interactive converters usually present ESSs, they can support the MG power dispatchability [66]. On the other hand, such converters can also strive for a second purpose, which is the imposition of voltage and frequency references when the MG is islanded [145] (i.e., grid-forming features). Besides, the provision of smooth transition between the MG operation modes is usually expected from such converters [146].

  Thus, when an utility-interactive converter coexists with DERs being coordinated by the GCBC strategy in a MG, synergistic interaction needs to be achieved. Otherwise, the multiple operational purposes offered by the GCBC, or the interesting grid-supporting features of the former converter, cannot be fully exploited to fulfill all MG needs. Since this scenario is not commonly addressed in the literature, discussions are herein presented based on simulation results.

To understand how the GCBC strategy is supported under islanded operation and during MG mode transitions, the existence of an utility-interactive converter needs to be accounted for in the formulation of the control strategy. Herein, a specific utility-interactive converter, namely Utility Interface (UI) [147], is considered on the MG

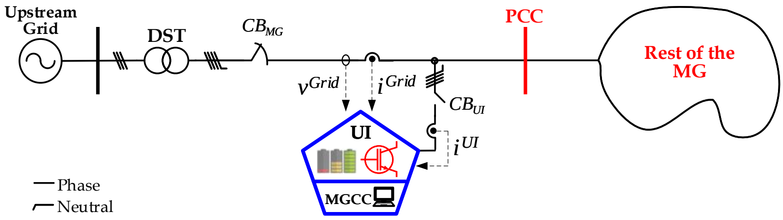

Figure 4.21: Placement of the UI at the LV MG.

topology (i.e., exclusively for this section). The UI is typically designed with a four-leg converter topology, usually considering triple loop controllers [99], and being allocated at the MG PCC. Moreover, due to its powerful computational capabilities, and by the fact that a communication interface is present, it can also incorporate the MGCC within its hardware [145]. The scheme shown in Fig. 4.21 depicts the layout of the UI within the MG.

One can observe that, if the circuit breaker CB_{MG} is switched on, the MG is grid-connected and the UI plays grid-supporting mode. On the other hand, if CB_{MG} is switched off, the UI forms the grid, not affecting the overall coordination of nd- and d-DERs provided by the GCBC. Nonetheless, the UI imposes a new perspective for the MG, and the previous formulation of the GCBC (i.e., presented in Chapter 3) is no longer valid. Based on Fig. 4.21, let us then formulate this new MG perspective, keeping in mind that v_m^{Grid} and i_m^{Grid} are the *m*-phase voltage and current drawn from the upstream grid, and i_m^{UI} is the UI current.

When the GCBC strategy is initiated at a control cycle "*k*", the reconstruction of the currents demanded by loads (i.e., also incorporating losses and non-participating DERs), which was previously given by Eqs. 3.9 and 3.10, can be re-written considering the UI peak currents. Hence, having the PCC as the reference node, $I^L_{h||_m}$ and $I^L_{h\perp_m}$ are now formulated according to Eqs. 4.1 and 4.2, respectively.

$$I^L_{h||_m}(k) = I^{DERt}_{h||_m}(k) + I^{Grid}_{h||_m}(k) + I^{UI}_{h||_m}(k) \tag{4.1}$$

$$I^L_{h\perp_m}(k) = I^{DERt}_{h\perp_m}(k) + I^{Grid}_{h\perp_m}(k) + I^{UI}_{h\perp_m}(k) \tag{4.2}$$

Consequently, the reference currents ($I^*_{h||_m}$ and $I^*_{h\perp_m}$) required for coordinating the participating DERs at the cycle "*k+1*" result in Eqs. 4.3 and 4.4.

$$I^*_{h||_m}(k+1) = I^L_{h||_m}(k) - I^{UI*}_{h||_m}(k+1) - I^{Grid*}_{h||_m}(k+1) \tag{4.3}$$

$$I^*_{h\perp_m}(k+1) = I^L_{h\perp_m}(k) - I^{UI*}_{h\perp_m}(k+1) - I^{Grid*}_{h\perp_m}(k+1) \tag{4.4}$$

These two equations demonstrate that the operation of the UI is independent from the steering of DERs, allowing it to offer grid-supporting functions at the PCC, while coexisting in synergy with other coordinated inverters. Moreover, note that the reference currents for the UI (i.e., $I_{h||_m}^{UI*}$ and $I_{h\perp_m}^{UI*}$) make it a participant in the power dispatchability of the MG [66]. Therefore, the UI can use the capability of its ESS, or even its generated energy (i.e., if RESs are considered on its topology), to dispatch active and reactive power aiming at supporting the transactive aspects of the MG.

Finally, Eqs. 4.3 and 4.4 also indicate that, when the MG operates under islanded mode, the upstream grid is absent, resulting that $I_{h||_m}^{Grid*}$ and $I_{h\perp_m}^{Grid*}$ are null. Since the UI acts forming the grid, $I_{h||_m}^{UI*}$ and $I_{h\perp_m}^{UI*}$ take over the role of $I_{h||_m}^{Grid*}$ and $I_{h\perp_m}^{Grid*}$ (see the similarity with Eqs. 3.9 and 3.10). Thus, if $I_{h||_m}^{UI*} = I_{h\perp_m}^{UI*} = 0$, the DERs controlled by the GCBC strategy drive the MG to full self-consumption mode, relieving the UI from providing power to loads. On the other hand, if $I_{h||_m}^{UI*}$ and $I_{h\perp_m}^{UI*}$ are not null, the UI has to provide or absorb power, ensuring the proper power balance required for islanded MG operation.

4.4.1.1 Simulation Results Considering the Utility Interface Converter

Simulation results are herein presented to demonstrate that the GCBC strategy can cope with the existence of an utility-interactive converter in the MG. To demonstrate this, the main MG testbench presented in Fig. 3.1 and explained in Section 4.2.1 is used, considering that all linear and non-linear loads were connected to the MG, as well as the three d-DERs (i.e., d-DER$_1$ to d-DER$_3$). The nd-DERs were disregarded for the sake of simplicity. In addition, the UI converter was placed at the PCC of that MG, just as depicted in Fig. 4.21. While the complete modeling of the UI can be found in [147], the basic control layout and the parameters used for simulations are briefly described in Appendix B.1.4.

The results considering such an integrated operation of inverters are presented in Fig. 4.22, being split into five intervals. Such intervals show different operational conditions, taking into account the two MG transition modes (i.e., grid-connected and islanded). During Interval I, the MG was interconnected to the upstream grid, also considering that the GCBC strategy was disabled and d-DERs were not sharing any currents. Consequently, since full self-consumption mode was expected for the MG, the UI provided all the currents demanded by the loads. Fig. 4.22 demonstrates a practically null circulation of currents through the PCC, as the UI injected distorted and phase-shifted currents.

At a second instant (i.e., Interval II), the circuit breaker CB_{MG} was switched off, requiring the UI to form the grid in order to ensure proper islanded operation for the MG. The result of this transition shows that neither overvoltages nor overcurrents occurred in the MG. Moreover, the UI was able to regulate the magnitude of the PCC voltages, as well as the MG frequency, without ceasing to feed currents to the loads. During the islanded operation of the MG, the GCBC strategy was enabled to additionally steer the

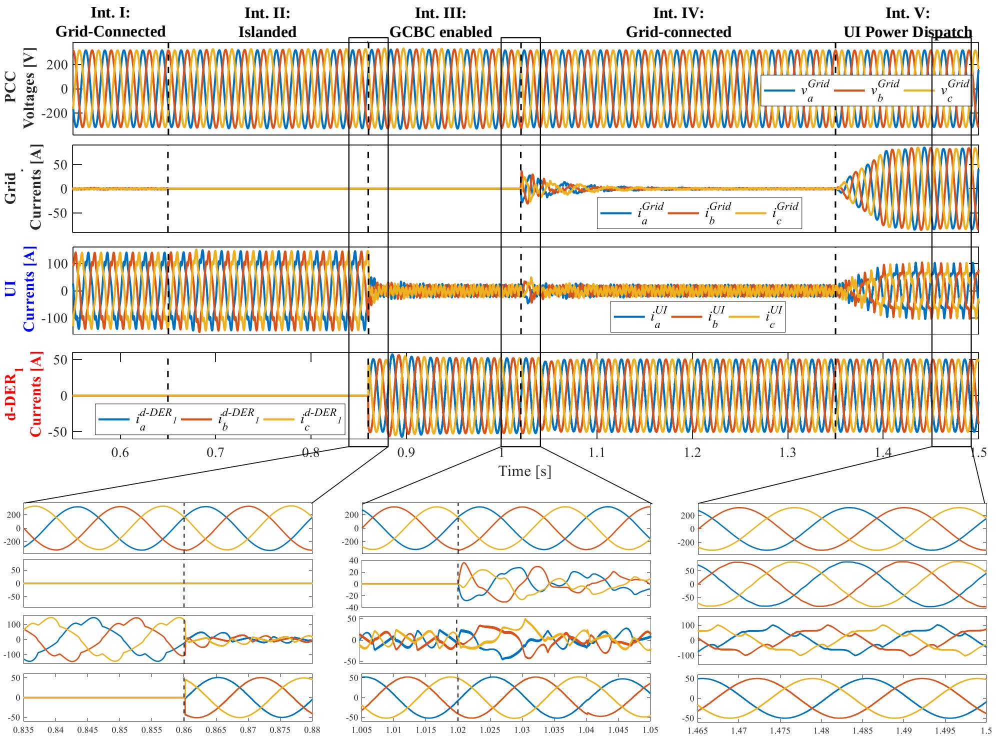

Figure 4.22: Simulation results: MG transiting from interconnected to islanded mode, and vice-versa. Interval I: GCBC disabled and MG interconnected; Interval II: GCBC disabled and MG islanded; Interval III: GCBC enabled and MG islanded; Interval IV: GCBC enabled and MG interconnected; and Interval V: GCBC enabled, MG interconnected, and UI controlling the power flow at PCC. From top to bottom: PCC voltages, grid currents, UI currents, and d-DER$_1$ currents.

three d-DERs to share the active and reactive currents drawn by the loads.

This standalone scenario is depicted in Interval III, and the zoom-in-view of the operational transition is shown in Fig. 4.22. It is observed that, as d-DERs followed their current references to process fundamental currents (see low-distorted waveforms for d-DER$_1$), the UI promptly adjusted its control inputs to provide the remaining load currents. Hence, the UI basically processed harmonic currents, supporting the achievement of a proper power balance for the MG. This result shows that synergistic operation occurred among the UI and the inverters coordinated by the GCBC.

Since d-DER$_1$ to d-DER$_3$ processed collective currents equal to 63.71 A, 36.41 A and 63.68 A (see Fig. 4.23), respectively, it is proven that the expected proportion ratio of 1.75 was obtained (i.e., between d-DER$_1$ and d-DER$_2$, also between d-DER$_3$ and d-DER$_2$). Thus, the proportional current sharing provided by the GCBC was not affected

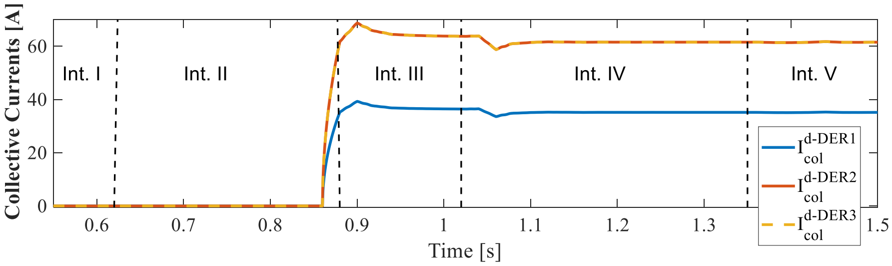

Figure 4.23: DERs' collective currents during simulations in Fig. 4.22.

by the presence of the UI during Interval III. It is also important to highlight that the UI usually endows large-bandwidth control loops [100], which support improved regulation of the output currents, as well as allowing seamless transition for the MG [145]. For such reason, load currents can be adequately supplied at all instants.

For Interval IV, the upstream grid was considered to be active again, requiring the MG to reconnect to it. Note in the zoom-in-view of the transition between intervals III and IV that, even though a small disturbance occurred at the grid currents, the UI was able to promptly counteract it, providing a smooth transition for the MG. Moreover, d-DERs were practically unaffected by the new MG operational status, demonstrating that the UI was incorporated into the MG control, providing proper mode transitions, without impairing the current sharing devised by the GCBC strategy.

Observe that the d-DERs' currents were only adjusted to cope with the slight different voltage amplitudes of the grid voltages, when compared to those imposed by the UI. While in the steady state condition, the upstream grid, the UI, and the d-DERs provided adequate regulation of the MG null current dispatch current. In addition, proportional sharing was attained, as d-DERs presented a ratio of 1.74.

The last simulated scenario, shown at Interval V in Fig. 4.22, demonstrates how the UI participates in the power dispatchability of the MG. For this case, the UI was demanded to process 13 kW per phase, in addition to the provision of the load harmonic currents that were not shared by the d-DERs. As the UI enabled its consumption of active power (i.e., emulating energy storage), the grid currents increased smoothly until steady state operation was reached. It can be seen in the zoom-in-view of this interval in Fig. 4.22 that the grid currents became low-distorted, while being in-phase with the PCC voltages. A peak value of 82.2 A_{pk} was obtained for the per-phase grid currents, which indicates adequate control, as 12.99 kW was drawn from the upstream grid.

Lastly, two aspects can be further observed during this instant. The UI currents presented both fundamental and harmonic components, and the currents from d-DERs were not affected, when compared to Interval IV. This indicates that the load demand for active and reactive currents was still supplied by the coordinated DERs, and the UI complemented the operation supplying the remaining harmonic currents. Thus, the UI could be integrated into the MG dispatchability independently of the coordination of the other inverters.

4.4.2 Considerations in Relation to Classic Droop Control

In the literature [31, 108, 122, 148, 149, 150], droop control is undoubtedly the most commonly adopted strategy for what concerns the coordination of inverters in MGs, especially when cooperative operation is devised under decentralized or distributed control topologies. This occurs because droop-based approaches, in general, steer inverters under VCM (i.e., as controlled voltage sources) [30, 72], requiring only local electrical quantities (e.g., voltages, currents, and/or power terms) to be processed by the inverters. Therefore, power sharing is achieved in a MG based on the tuning of droop gains [11, 31], which are utilized on the local control of the inverters.

Due to its simplicity, conventional droop control can be straightforwardly implemented. Nevertheless, several more elaborate formulations of this method are found in the literature [108, 151], aiming to overcome its commonly faced issues, such as: *i)* inaccurate proportional power sharing; *ii)* dependence on the knowledge of MG physical parameters; and *iii)* sensitivity to droop parameters. Most of the time, adding virtual impedance loops to the control of inverters [152, 153] is the simplest solution to attain improved performance.

With this in mind, this section aims at highlighting some differences in the operational aspects of the GCBC strategy, in relation to the conventional droop control. The main purpose herein is to demonstrate the particularities of the GCBC while coordinating inverters in LV MGs, having the droop concept as a reference method. Focus is given to the aspects related to the active, reactive, and harmonic power sharing capabilities of both methods. Moreover, for the sake of clarity, simulation results take into consideration a simplified single-phase MG circuit, which is described as follows.

4.4.2.1 Simplified MG Circuit and Operational Principles

The LV MG circuit considered in this section is shown in Fig. 4.24, being composed of two inverters, namely INV_1 and INV_2, line impedances (Z_0 to Z_4), as well as two linear loads (Z_{L1} and Z_{L2}) and one non-linear load (Z_{NL}). Note that the loads Z_{L1}, Z_{L2} and Z_{NL} can be switched off by the circuit breakers CB_{L1}, CB_{L2} and CB_{NL}, respectively. In addition, step in line impedances can be emulated by the switch SB_Z, which connects to the MG either Z_3 or Z_4. The MG parameters are summarized in Table 4.14. It is highlighted that both inverters, INV_1 and INV_2, are given these names to easily distinguish them from the other nomenclatures used in previous simulation and experimental results.

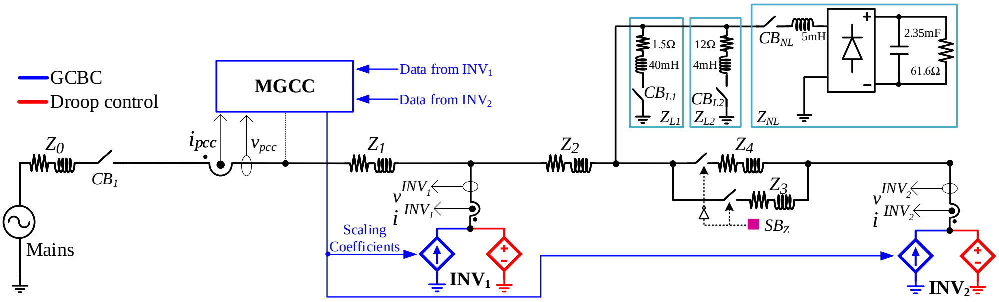

Figure 4.24: Simplified MG circuit adopted for discussions and simulations related to droop and GCBC strategies.

Table 4.14: MG parameters for the simplified single-phase MG circuit of Fig. 4.24.

Parameter	Value
Grid phase voltage and frequency	127 V$_{\mathrm{RMS}}$ at 60 Hz
Line Impedances: $Z_0 = Z_1 = Z_2$	0.038 + j0.005
Line Impedances: Z_3	0.076 + j0.010
Line Impedances: Z_4	0.152 + j0.020
Nominal power of INV$_1$ (A^{INV1})	5 kVA
Nominal power of INV$_2$ (A^{INV2})	3 kVA
Nominal current ratio between INVs ($r_{INVs} = 5/3$)	1.66
Droop gains for INV$_1$: k_{p_1} and k_{q_1}	2.5e^{-5} and 5e^{-5}
Droop gains for INV$_2$: k_{p_2} and k_{q_2}	4.16e^{-5} and 8.3e^{-5}
GCBC processing time (T_{GCBC}):	16.66 ms

Now, the control aspects of this simplified MG will be discussed. Knowing that the GCBC strategy is devised based on the perspective of having the MG operating under interconnected mode, as explained in Section 4.4.1, the inverters are usually driven under CCM (i.e., as controlled current sources). Consequently, for testing the GCBC strategy in this circuit, the inverters were emulated by ideal current sources in simulations (i.e., only for this section).

In addition, an ideal voltage source placed at the PCC imposed the MG voltage and frequency reference, emulating the UI operation. Moreover, the centralized control topology of the GCBC approach states that a MGCC must be allocated at the PCC, in constrast to the classic decentralized droop control. Thus, the MG management relies on a low-bandwidth communication link to exchange data with the inverters. Similarly to previous simulations, the GCBC approach was set for sharing fundamental currents, as well as odd harmonics from the 3rd up to the 13th orders. Yet, since the GCBC strategy was thoroughly explained in Chapter 3, no further discussions are presented.

On the other hand, once conventional droop control is implemented to coordinate inverters in this MG, a decentralized topology is considered. Hence, there is no direct exchange of information between the inverters, nor do they use data links to communicate with a MGCC (see Fig. 4.24). Droop control is usually implemented based on a hierarchical architecture [41], being fully locally implemented at each inverter, as shown in Fig. 4.25. In such a control structure, inner control loops steer the inverters under VCM, using cascaded voltage and current control regulators. The control loops running at each *j*-th inverter take into consideration the MG references for the angular frequency and voltage amplitude (i.e., ω_j^* and E_j^*, respectively). In addition, two droop equations control the cooperative operation of the inverters.

Such droop equations are mathematically formulated by Eqs. 4.5 and 4.6, being ω_j and E_j, the frequency and amplitude of the output voltage of the *j*-th inverter, respectively. P_j and Q_j are the low-pass filtered active and reactive output powers obtained by following their respective control references P_j^* and Q_j^*. For the simulation results, the single-phase power calculation used for the droop control loop was implemented as done in [154], using a low-pass filter time constant of 0.03 s.

$$\omega_j = \omega_j^* - k_{p_j} \cdot (P_j - P_j^*) \tag{4.5}$$

$$E_j = E_j^* - k_{q_j} \cdot (Q_j - Q_j^*) \tag{4.6}$$

Other two important variables are k_{p_j} and k_{q_j}, which are the active and reactive power droop gains, respectively. These two terms are constants responsible for providing proportionality among inverters during power sharing. Thus, they are the terms that are usually tuned when droop control is implemented. For simulations, k_{p_j} and k_{q_j} were tuned based on the main operational condition of the MG, as later explained, having their values presented in Table 4.14. Additionally, the variable ω_j is typically integrated to attain the phase angle θ_j used for the inner control loops, as given by Eq. 4.7. Finally, for the sake of simplicity, and to better depict the comparisons between the droop and GCBC methods, ideal voltage controlled sources were used for implementing the former strategy in simulations.

$$\theta_j = \int \omega_j \cdot dt \tag{4.7}$$

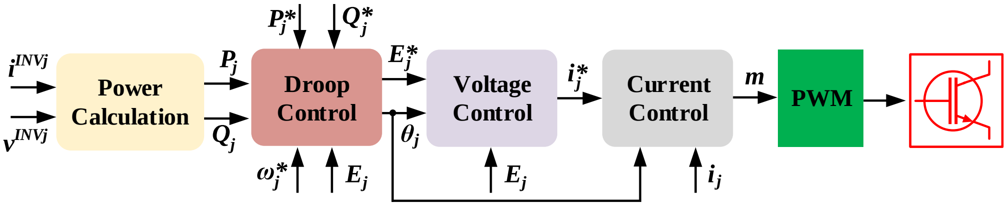

Figure 4.25: Basic hierarchical structure of droop controlled inverters.

4.4.2.2 Simulation Results

The simulation results are divided into two parts. The first one demonstrates how the droop and GCBC strategies compare in steady state condition when linear and non-linear loads exist within the MG. Additionally, their transient responses when loads are abruptly switched on and off are also verified. The second part demonstrates the sensitivity of the strategies to changes in grid impedances. To emulate these changes in MG impedance, the switch button SB_Z is used, modifying the normal operation of the circuit (i.e., with Z_3 switched on) to the case in which Z_4 is connected.

The first simulation results (i.e., for part one) are presented in Fig. 4.26 and in Table 4.15, considering that the inverters are striving for sharing the active, reactive and harmonic currents demanded by the loads. Each of the three intervals in Fig. 4.26 comprise different states for the MG loads. During Interval I, for instance, the linear load Z_{L1} and the non-linear load Z_{NL} are connected to the circuit, while Z_{L2} is switched off (see Fig. 4.24).

From Fig. 4.26 it can be seen that, during Interval I, the two strategies presented similar steady state behavior in relation to active power. Note in Table 4.15 that, for the droop and GCBC strategies, the P powers processed by INV_1 and INV_2 converged to practically the same operational point. Besides, power sharing occurred proportionally to the inverters' nominal capabilities, being $r_{INVs} = 1.67$, which is very close to 1.66 baseline. This is expected because inaccuracy in active power sharing is not usually characteristic of conventional droop control. Due to the fact that w_j is a global MG variable, by using it in Eq. 4.5, the inverters can properly balance their participations in active power sharing, if droop gains are adequately tuned, as occurred during simulations.

In contrast, the voltage amplitude E_j modulated by each droop-controlled inverter follows Eq. 4.6, consequently being affected by voltage drops through line impedances. Hence, mismatches in grid impedances inherently lead to inaccurate reactive power sharing among inverters [155]. The non-proportional power sharing caused by the droop control is evident in Fig. 4.26 (see reactive power plot), as well as in the proportion ratios obtained during this interval (see Q power in Table 4.15). Observe that, although the GCBC strategy was capable of maintaining the expected 1.66 proportion ratio, droop control led the inverters to reach a value of 2.56.

The direct consequence of such an operational condition is that INV_1 had to process much more Q power than INV_2, which may cause unbalanced thermal stress of the inverters within the MG. By looking at the inverter currents in the zoom-in-view of Fig. 4.26, one can also note the difference in current amplitude for the droop control. Since conventional droop control does not typically implement harmonic loops [153], the sharing of distortion power also occurs non-proportionally to the inverters'

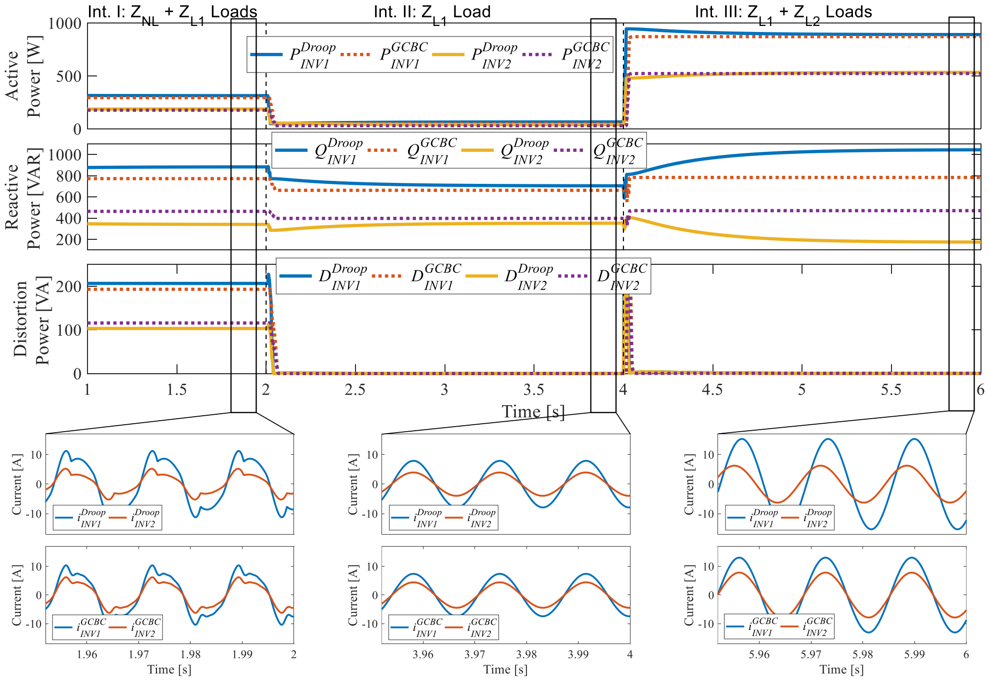

Figure 4.26: Inverters sharing load powers for the droop and GCBC strategies. Interval I: linear (Z_{L1}) and non-linear (Z_{NL}) loads connected; Interval II: linear load (Z_{L1}) connected; and Interval III: linear loads (Z_{L1} and Z_{L2}) connected. From top to bottom: P, Q and D powers, and zoom-in-view of inverters' currents for the droop and GCBC strategies.

Table 4.15: Steady state powers for the inverters and power sharing ratio during results in Fig. 4.26. Units: P [W], Q [VAR], D [VA].

		Int. I			**Int. II**			**Int. III**		
		P	Q	D	P	Q	D	P	Q	D
Droop	INV$_1$	314	884	206	66	705	0.0	891	1046	0.0
	INV$_2$	188	341	103	40	352	0.0	534	174	0.0
	r^{Droop}_{INVs}	1.67	2.59	2.00	1.65	2.00	0.0	1.66	6.01	0.0
GCBC	INV$_1$	296	772	193	50	663	0.0	872	784	0.0
	INV$_2$	177	463	116	30	398	0.0	526	471	0.0
	r^{GCBC}_{INVs}	1.67	1.66	1.66	1.66	1.66	0.0	1.65	1.66	0.0

capabilities. This can be noted in Table 4.15, as r_{INVs} was 2.00 for the droop method, whereas the GCBC approach maintained the 1.66 proportion.

During Interval II, the non-linear load was switched off at 2 s, demonstrating that droop control maintained a similar behavior when compared to Interval I. This case shows that, regardless of the loads existing within the MG, proportional active power sharing was attained when the inverters were controlled by the two strategies (see proportion ratios in Table 4.15). Additionally, reactive power was not shared proportionally by droop-controlled inverters, in contrast to the GCBC approach. Another contrasting feature can be observed in Fig. 4.26, being more evident in the Q power plot. Note that the droop method took longer to reach the steady state condition, requiring approximately 1.0 s after the load step was applied. On the other hand, the CBC strategy took less than 0.25 s. Of course, such accommodation times depend on the time constants of the filters used for implementing the droop strategy, also being affected by the communication time employed for the GCBC method.

For the last simulation case, shown at Interval III, another load step was applied to the MG, switching Z_{L2} on, and increasing the active and reactive power demands seen by the inverters. Fig. 4.26 shows that the accommodation times required for both methods were similar for Interval II, also resulting in accurate active power sharing during steady state. The zoom-in-view of this interval in Fig. 4.26 makes visually evident the effect of the inaccurate reactive power sharing provided by the droop method. Note that this operation caused the two inverters to process currents with different amplitudes and significant phase shift between them, reaching a high proportion ratio of 6.01 (see Table 4.15). On the contrary, the GCBC approach was able to steer inverters following a ratio of 1.66.

The second part of the simulation results will now be presented, showing the behavior of the two coordination strategies when a change in grid impedance occurs at the MG. Knowing that LV MGs are dynamic systems, the sudden connection and disconnection of inverters, as well as of loads, might cause different equivalent grid impedances to be sensed at each node [156]. Consequently, this condition might affect the coordination of inverters for model-based strategies, as well as potentially impairing the proper power sharing even for model-free methods, if they are not robust to variations in grid impedance.

During simulations, the conventional droop and GCBC strategies were tested upon such a condition by applying a line impedance step in the MG, changing the Z_3 by Z_4 (see Fig. 4.24). This result is shown in Fig. 4.27, considering that the initial condition is the same as in Fig. 4.26, but at 2.0 s the switch button SB_Z was enabled. Only the loads Z_{L1} and Z_{NL} were considered to be switched on at all instants in Fig. 4.27.

Then, it can be firstly noted in the results that, once the step is applied, significant overshoot and undershoot occurred at the active powers processed by the droop-controlled INV_1 and INV_2, respectively. Such an overshoot reached around 27% of the steady state active power injected of INV_1, and it was around 20% for the undershoot of INV_2. Additionally, the transient response of these inverters took much longer to settle than during previous cases when load steps were tested. Note that the settling

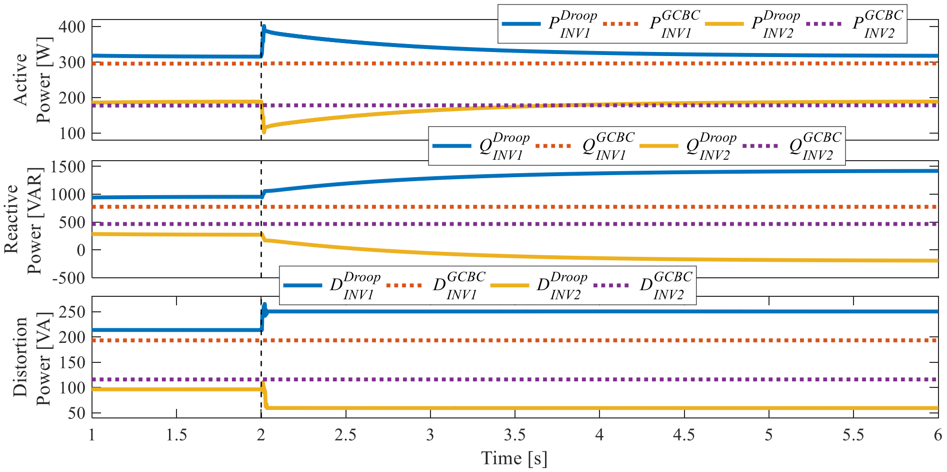

Figure 4.27: Response of the droop and GCBC strategies upon line impedance step. From top to bottom: active, reactive and distortion powers for both inverters.

time was about 3.5 s for this scenario. Nonetheless, steady state proportional power sharing was satisfactorily maintained for P, presenting a ratio of 1.68.

Concerning the reactive and distortion powers, it is also evident that the change in the grid impedance further deteriorated the proportional power sharing capability of the droop control. For instance, besides slow settling time also occurring for the reactive power, proportion ratios of 7.33 and 4.23 were obtained for the Q and D terms. These ratios are significantly different when compared to the baseline of 1.66. Therefore, such results demonstrate how sensitive the conventional droop control approach is to the physical parameters of the MG.

In contrast, due to the model-free feature of the GCBC strategy, it was practically unaffected by the change in grid impedance. However, a shortcoming of the GCBC is that higher energy losses may occur depending on the MG disposition of nodes, as well as on the inverters' ratings. Since proportional sharing of the P, Q and D powers is offered by the GCBC regardless of the grid impedance values, higher energy losses may be faced if the MG presents non-homogeneous features.

In conclusion, these results show that, beyond the particular implementation principles, the conventional droop and GCBC strategies provide different power sharing features while steering inverters in MGs. Droop control has the advantage of straightforwardly supporting islanded operation, while the GCBC approach requires the existence of a grid-forming converter, or that several inverters cooperate for specifically imposing the voltage and frequency references for the MG. In addition, droop control inherently does not rely on communication links, which increases MG reliability [149].

Nonetheless, without implementing virtual impedance loops, proportional reactive and harmonic power sharing are significantly affected in droop-controlled inverters [152]. Additionally, sensitivity to grid parameters might be critical, especially in the scenario of weak MGs, as well as when operating under non-ideal voltage conditions [107]. Finally, a transactive energy aspect is usually expected of MGs, since they generally operate interconnected to an upstream grid. Thus, if the MG manager desires to control the power flow at the PCC using droop-controlled inverters, communication infrastructures and a MGCC are likely to be required [52], as they are for the GCBC. Overall, depending on the MG management perspective, the GCBC strategy may be more interesting due to its multi-purpose operational feature discussed throughout this thesis.

4.5 Chapter Conclusions

This chapter presented the main operational purposes supported by the GCBC strategy. It has been demonstrated that it is possible to coordinate DERs in LV MGs to achieve decoupled control over current terms drawn by loads. In fact, active and reactive currents can be shared by inverters proportionally to their nominal ratings. Concomitantly, the controllability over such fundamental currents gives flexibility to the MG to also regulate the power flow through its PCC, supporting its participation in transactive energy interactions. Moreover, selective distributed harmonic compensation is supported, allowing the possibility to obtain full current control or low current distortion at the PCC, if desired.

It has also been demonstrated that the GCBC approach is capable of accommodating DERs of assorted operational natures (i.e., dispatchable or non-dispatchable), also coping with the intermittency inherent to RESs. Additional considerations highlighted that the coordination strategy can be applied to the MG even during transition modes. Finally, discussions enlightened the differences between the GCBC strategy and the conventional droop control, clarifying the particular implementation and operational features of the latter.

Chapter 5

Current-Based Coordination of DERs upon Adverse Scenarios

5.1 Introduction

Weak[1] MGs commonly undergo adverse operational conditions due to massive penetration of RESs and non-linear loads, and due to disturbances involuntarily imposed by the upstream grid. Abnormal conditions bring additional operational challenges, which need to be properly assessed prior to deploying coordinated control strategies to steer inverters. Among the burdens leading to non-ideal MG scenarios are, for example, the existence of non-sinusoidal voltage conditions, the occurrence of fluctuations in voltage profiles, as well as the case of inverters with limited capabilities to offer ancillary services.

Thus, the main goal of this chapter is to demonstrate that the GCBC strategy is capable of coping with several non-ideal operational scenarios, ensuring reliable and stable operation. It presents the capability of the coordination strategy to endure operation under distorted voltages, voltage ride-through conditions, as well as adequately limiting the participation of DERs to respect their nominal ratings. One additional advantage of the GCBC strategy is also discussed, demonstrating that its current sharing features can indirectly support the purpose of improving voltage quality in weak MGs. A discussion regarding the stability aspects of the control method is presented, being complemented by results demonstrating that communication issues are not a concern from the MG operational perspective. Finally, brief considerations about power coupling are presented to highlight how the GCBC behaves in MGs with line impedances of high *X/R* ratio.

5.2 DERs with Limited Power Ratings

Since the loads existing within the MG present dynamic behavior, often connecting and disconnecting from the grid, inverters sharing powers need to constantly adjust

---

[1] The definition of a weak MG was defined in Section 1.1, being a power system of low short-circuit ratio and small inertia constant [26].

to the required need. Additionally, intermittency in generation or limitation in the number of coordinated inverters may cause the power demand to be higher than the MG's internal energy supply. Hence, coordinated inverters may face demands that exceed their nominal ratings. With this in mind, this section shows that the GCBC strategy is capable of adequately saturating the participation of DERs to respect their available capabilities. Such a functionality is herein discussed based on experimental results seen in Fig. 5.1.

For presenting this feature of the GCBC approach, let us recall the main single-phase MG prototype presented in Section 4.2.2, considering that all loads, as well as d-DER$_1^\star$ and d-DER$_2^\star$ were connected to the MG. However, the nominal current ratings of the d-DERs* were reduced through software by 50% to emulate the limited capabilities. Thus, d-DER$_1^\star$ and d-DER$_2^\star$ presented 7.5 A$_{\text{pk}}$ and 10 A$_{\text{pk}}$ of nominal current capabilities, respectively. Yet, it is considered that full current control is intended for the MG operation, aiming at steering the two d-DERs* to share the active, reactive and selected harmonic currents drawn by the loads.

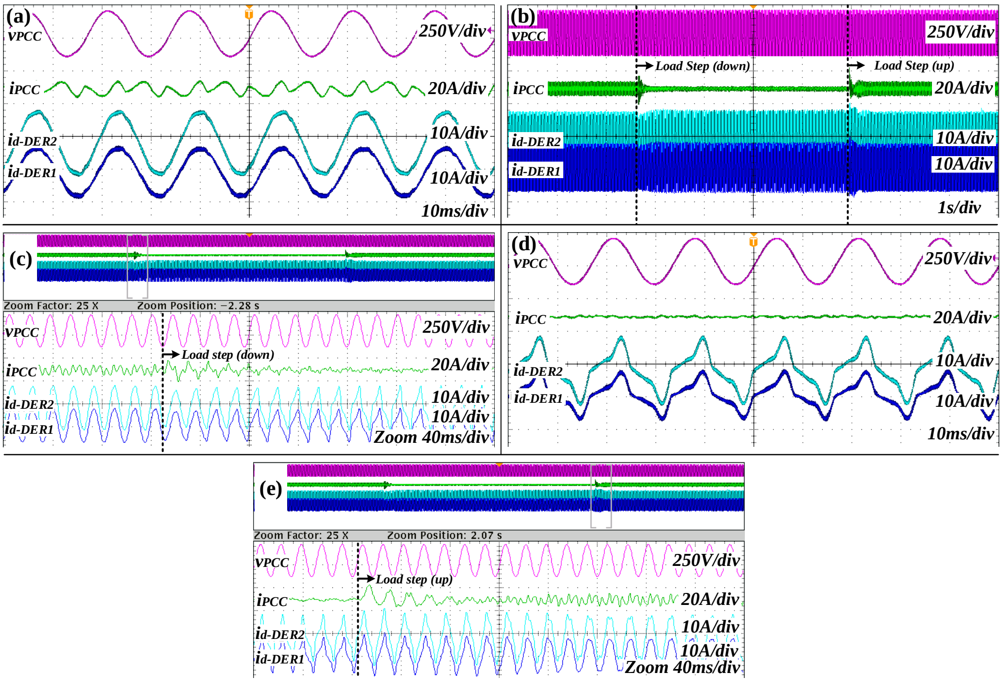

Figure 5.1: Experimental results: full current control under limited power capability. (a) d-DER$_1^\star$ and d-DER$_2^\star$ with 50% smaller ratings than nominal values in Table 4.4; (b) load steps applied disconnecting and connecting load L_2; (c) zoom-in-view of stage one in (b); (d) steady state condition of (c); (e) zoom-in-view of stage two in (b). From top to bottom: PCC voltage and current, d-DER$_2^\star$ and d-DER$_1^\star$ currents.

Then, in Fig. 5.1(a), the steady state behavior of the GCBC strategy while steering both DERs* under such a limited condition is demonstrated. Apart from the reduced current ratings of the DERs*, the scenario in Fig. 5.1(a) is the same as in Fig. 4.12(d), in which it was demonstrated that a null PCC current was obtained when the GCBC was enabled. Nevertheless, in Fig. 5.1(a) the inverters faced a condition in which there was insufficient current capability to completely share load currents (i.e., I_{nom}^{DERt} was limited). Consequently, Fig. 5.1(a) shows that the GCBC algorithm saturated the currents injected by the inverters, in order to respect their available capabilities.

For instance, note that the PCC current was no longer null, presenting both fundamental and harmonic components. The power components calculated for this scenario are seen in Table 5.1, showing that mainly reactive and distortion powers were measured at the PCC. In comparison to the two baselines (i.e., when the MG presented only loads, and when current ratings were not reduced), one can verify that the Q power was only partially provided by the DERs* in Fig. 5.1(a). Moreover, the D power was not tackled at all. This second matter can also be evidenced by the practically sinusoidal DERs*' currents seen in Fig. 5.1(a), indicating that the GCBC only assigned active and reactive current sharing to the inverters.

Such an operational condition was possible due to the saturation scheme discussed in Fig. 3.7, as the GCBC strategy iteratively calculates the DERs*' current capabilities before defining the scaling coefficients. If the inverters had even lower nominal ratings, the strategy could saturate the injection during the assignment of the active current sharing. Similarly, this could occur for harmonics, if I_{nom}^{DERt} was sufficient to only process the active and reactive load currents. For the case of Fig. 5.1(a), d-DER$_2^\star$ and d-DER$_1^\star$ processed 6.79 $\mathrm{A_{RMS}}$ and 5.18 $\mathrm{A_{RMS}}$, respectively. Thus, proportional current sharing occurred even under limited capability (i.e., $r_{dDERs^\star} = 1.31$), as the baseline ratio was 1.33.

Now, in Figs. 5.1(b) to 5.1(d) it is demonstrated that such limited ratings of DERs* do not affect current sharing if load demand is lower than I_{nom}^{DERt}. This is demonstrated by applying a load step to the MG, abruptly switching off the circuit breaker of the

Table 5.1: Steady state power terms at the PCC for Fig. 5.1.

PCC Powers				
	Baselines		This Section	
	Loads	Fig. 4.12(d)	Fig. 5.1(a)	Fig. 5.1(d)
A [VA]	1051	98.27	362.40	79.88
P [W]	980	-73.30	-70.72	6.25
Q [VAR]	1148	-14.05	184.6	-20.60
D [VA]	315	65.70	304.6	73.66

inductive load L_2 (see Fig. 4.2), which reduced the amount of reactive current drawn from within the MG. Observe in Fig. 5.1(b), and in the zoom-in-view of this action in Fig. 5.1(c), that the GCBC approach was able to adequately readjust the currents processed by the inverters, as the load demand was reduced below I_{nom}^{DERt}. It is visible in Fig. 5.1(c) that, even though the mechanical switching of the circuit breaker is slow, after a few fundamental cycles (i.e., approximately seven) the DERs* shared the load currents without causing overvoltages or overcurrents. In addition, the capabilities of the inverters, as well as their proportionality, were also respected during transients. The steady state condition of this new load scenario is shown in Fig. 5.1(d), in which it is visually seen that the PCC current was practically null. The power terms presented in Table 5.1 show that low amounts of P, Q and D terms were flowing through the PCC. The proportion ratio between DERs* was 1.36, reiterating that proportional full current control was reached by the strategy.

Lastly, a dual condition is tested by switching on the load L_2. This can be seen in Figs. 5.1(b) and in the zoom-in-view presented in Fig. 5.1(e). Note that the inverters were able to ride through the disturbance caused by the mechanical switching of the referred circuit breaker, without losing effectiveness in proportional current sharing nor leading to overcurrents in the DERs*. Taking approximately seven cycles after the circuit breaker was switched on, the MG returned to the steady state condition of 5.1(a), respecting the capabilities of the inverters during the transition.

These results show that the GCBC saturation scheme of Fig. 3.7 is efficient, avoiding to impose current demands that are not supported by the DERs*. It is worth reinforcing, however, that it is also important to implement current/power saturators in the inner loops of the inverters to ensure proper local control and redundancy for the coordinated perspective.

5.3 Distorted Voltages

LV power systems are prone to operating with background harmonics in voltages. This is also true for MGs, especially if they are weak systems comprising non-linear loads [26], as well as if they operate interconnected to an upstream grid that may propagate voltage distortions [28]. Thus, it is imperative to certify that the coordination of inverters is not affected if voltages are non-ideal, particularly upon the concern of harmonic distortion.

In order to assess the feasibility of the GCBC strategy while coordinating inverters upon distorted voltages, experimental results are herein discussed. For this case, once again the main MG prototype explained in Section 4.2.2 is used, considering all loads, as well as the two d-DERs* operating at nominal ratings. To obtain the expected non-ideal scenario, the grid emulator functioned as an upstream distribution system imposing fundamental voltage at nominal condition, plus 12.50% of the 3rd harmonic order. Thus, the instantaneous non-sinusoidal grid voltage was $v^{Grid}(t) = 127 \cdot \sqrt{2} \cdot cos(\omega_o \cdot t) + 15.87 \cdot \sqrt{2} \cdot cos(3 \cdot \omega_o \cdot t)$.

The experimental results are presented in Fig. 5.2, in which it can be straightforwardly noted that the grid voltages were significantly distorted (see Fig. 5.2(a)), causing slightly different load currents at the PCC as well (i.e., if compared to Fig. 4.4). Then, each simulated case is explained keeping in mind that the GCBC strategy is firstly set to achieve full current control for the MG operation. A final case demonstrates the GCBC features when only reactive and harmonic current control were set.

In Fig. 5.2(b) a steady state condition of how the DERs* were steered to share the active, reactive and harmonic currents is shown. It is visually evident that, similar to that achieved during the sinusoidal voltage condition (see Fig. 4.12(d)), practically a null PCC current resulted from the current sharing. The PCC quantities presented in Table 5.2 also proves that the power flow through the PCC was practically negligible

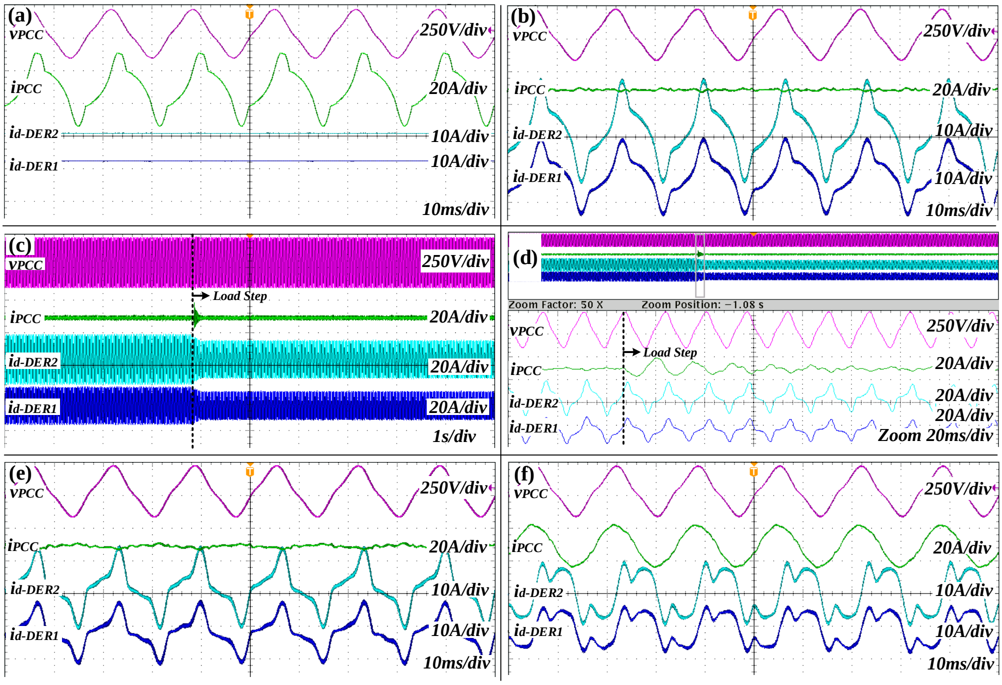

Figure 5.2: Experimental results: full current control under distorted voltage. (a) 12.50% of 3rd harmonic in grid voltage with d-DERs* disabled; (b) active, reactive and harmonic current sharing; (c) load step applied to (b) by disconnecting load L_2; (d) zoom-in-view of (c); (e) steady state condition of (d); (f) reactive and harmonic current sharing only. From top to bottom: PCC voltage and current, d-DER$_2^\star$ and d-DER$_1^\star$ currents.

Table 5.2: Steady state powers and current amplitudes at the PCC for Fig. 5.2.

	Load (Fig. 5.2(a))	Full Control (Fig. 5.2(b))	Full Control (Fig. 5.2(e))	React. + Harm. Control (Fig. 5.2(f))
PCC Powers				
A [VA]	1543	83	121	1102
P [W]	957	-15	-82	1086
Q [VAR]	1157	-10	-23	-27
D [VA]	355	81	84	122
Harmonic Amplitude [$\mathrm{A_{RMS}}$]				
$h = 1$	12.3	0.13	0.74	8.94
$h = 3$	3.23	0.26	0.27	0.26
$h = 5$	0.99	0.14	0.19	0.18

when compared to the load scenario of Fig. 5.2(a). Despite the fact that the grid voltage was highly distorted, proportional currents were processed by d-DER$_1^\star$ and d-DER$_2^\star$, being 6.00 $\mathrm{A_{RMS}}$ and 8.03 $\mathrm{A_{RMS}}$. This proves that the GCBC strategy was robust to operate under non-sinusoidal voltage, also offering proportional current sharing to DERs*, exactly reaching the expected 1.33 proportional ratio.

In Figs. 5.2(c) to 5.2(d) the transient response of the control approach was analyzed by applying a load step to the MG. Again, the inductive load L_2 is switched off from the circuit, requiring the inverters to adjust their current injections in order to maintain the intended full current control. Note in Fig. 5.2(c) that, after the load was removed from the MG, the inverter currents converged to a steady state operation and remained in a stable condition. Coinciding with previously explained results, Fig. 5.2(d) shows that having distorted MG voltage did not cause any impact on the transient behavior of the GCBC strategy. In addition, observe that after approximately four cycles, steady state operation was reached. Thus, the coordination strategy steered the DERs* adequately, respecting their nominal capabilities, and without causing unexpected current spikes.

The steady state result in Fig. 5.2(e) reinforces the discussion about the unaffected behavior of the GCBC approach, which led to low amounts of the P, Q and D powers measured at the PCC (see Table 5.2). The amplitudes of the PCC currents also demonstrate a similar current sharing performance, when compared to the previous scenario of Fig. 5.2(b). As a proportion ratio of 1.30 was obtained for Fig. 5.2(e), it is proved that full current control was achieved by the inverters, and that their balanced participation was ensured.

A final result is presented in Fig. 5.2(f) to demonstrate an important feature of the GCBC strategy. During this case, the coordination approach steered DERs* to provide distributed compensation of the reactive and the selected harmonic currents measured at the PCC. Aside from the fact that the Q and D powers were significantly compensated (see Table 5.2), the obtained PCC current was practically in-phase with the PCC voltage, presenting 1.03^{o} of phase shift. Additionally, proportional power sharing occurred, under a ratio of 1.35.

Nevertheless, it is visible that the PCC current resembled a sinusoidal waveform in Fig. 5.2(f). This occurred as a direct consequence of the GCBC formulation presented in Chapter 3, as the terms $I^*_{h||}$ and $I^*_{h\perp}$ are obtained from the total portion of the load currents. Consequently, these terms lead to selective compensation of harmonic currents, without taking into account the voltage distortions. Although full mitigation of current harmonics seems attractive at first sight (i.e., obtaining sinusoidal waveforms), the literature [19, 157] points out that this might not always be the best operational alternative, depending on the scenario and on the intended MG management. Therefore, further discussions are carried out in Chapter 6, specifically in Section 6.2, to present an advanced operational purpose provided by the GCBC strategy for the case when distorted voltages exist.

5.4 Voltage Ride-Through

Among the many design requirements imposed by modern grid codes and standards [109, 158], grid-tied inverters must present the capability to withstand voltage disturbances. The commonly termed ride-through capability is important to allow DERs to continue operating even if voltages temporarily deviate from nominal magnitudes [8], as long as they are within acceptable limits. Voltage ride-through may occur upon sags, which cause lower magnitudes (i.e., namely, low-voltage ride-through (LVRT)), or upon swells that lead to higher magnitudes (i.e., high-voltage ride-through (HVRT)). Such abnormalities in voltages bring additional challenges to the control of DERs [159], as they may affect: *i)* grid synchronization; *ii)* the power balance between the DC and AC sides of inverters; and *iii)* the dynamic performance of voltage and current controllers.

In brief, voltage ride-through capabilities embedded into the local control of DERs are essential to maintain grid stability [159] and, especially for weak LV MGs, are required to improve reliability of operation. Nonetheless, once operation under an integrated perspective occurs, voltage disturbances should also not affect the coordination of DERs, ensuring that they safely continue to pursue the expected MG goals. Hence, in this section the features of operation of the GCBC strategy are presented with regard to voltage ride-through scenarios. It is demonstrated through experimental results that DERs can endure LVRT and HVRT conditions, without impairing current sharing performance.

The experimental results herein discussed consider the main single-phase MG prototype used within this thesis (see Fig. 4.2), comprising all loads connected to it, as well as having the two d-DERs*. During the results shown in Fig. 5.3, the inverters were, in coordination, targeting the sharing of active, reactive and selected harmonic currents, at all instants. Moreover, since loads were modeled as constant impedances, the drawing of currents varied proportionally to the voltage applied to them. Two scenarios are then presented: firstly, the grid emulator imposes an abrupt voltage sag to study the LVRT capability of the GCBC strategy; and secondly, a sudden voltage swell is applied to the MG, requiring the DERs to endure HVRT.

An overview of the steady state operation of the MG transiting through the different voltage conditions is provided in Fig. 5.3(a). One can note three intervals on the profile of the PCC voltage (see purple waveform). During the initial interval, the nominal condition of the MG (i.e., grid voltage of 127 $\mathrm{V_{RMS}}$) is depicted, having the d-DERs* steadily sharing currents and achieving practically null current flow at the PCC. Later, a sag of 13.33% was applied to the grid voltage, reaching 110 $\mathrm{V_{RMS}}$. Observe that the control strategy allowed the DERs to ride through the change in voltage, returning to stable steady state operation.

Lastly, for the third interval, a sudden swell was emulated, causing the grid voltage to rise from 110 $\mathrm{V_{RMS}}$ to 141.10 $\mathrm{V_{RMS}}$. Even though this step represented a change of approximately 28% in voltage magnitude, the inverters kept sharing currents and reached steady state without resulting in MG instability. Moreover, note in Table 5.3 that the current sharing performance was similar during the LVRT and HVRT cases, occurring proportionally to the d-DERs*' capabilities, and allowing low power flow at the PCC.

Now, Fig. 5.3(b) shows the zoom-in-view of the LVRT transition. It is seen that, as a step was applied to the grid voltage, the d-DERs* suffered an increase in the peak value of their instantaneous currents. This is indeed expected as the current controllers implemented during experiments tend to maintain the power balance between the DC and AC sides of the inverters. Even though such an increase in currents during LVRT

Table 5.3: Steady state powers and current amplitudes at the PCC for Fig. 5.3.

PCC Powers		
	LVRT Case (Fig. 5.3(b))	HVRT Case (Fig. 5.3(c))
A [VA]	118.10	157.12
P [W]	-41.56	-77.18
Q [VAR]	-12.79	-29.19
D [VA]	103.20	126.3
$r_{dDERs^\star}$	1.29	1.31

can be avoided by implementing saturation algorithms [160] on the local controllers of the inverters, the results obtained indicate a non-critical condition for this experiment. The maximum current values reached by d-DER$_1^\star$ and d-DER$_2^\star$ were 15.46 A and 16.76 A, respectively, which still respect the nominal ratings of the inverters. In addition, note in Fig. 5.3(b) that, after two cycles, the current amplitudes were already similar to the previous scenario. The coordinated control was able to keep coordinating the

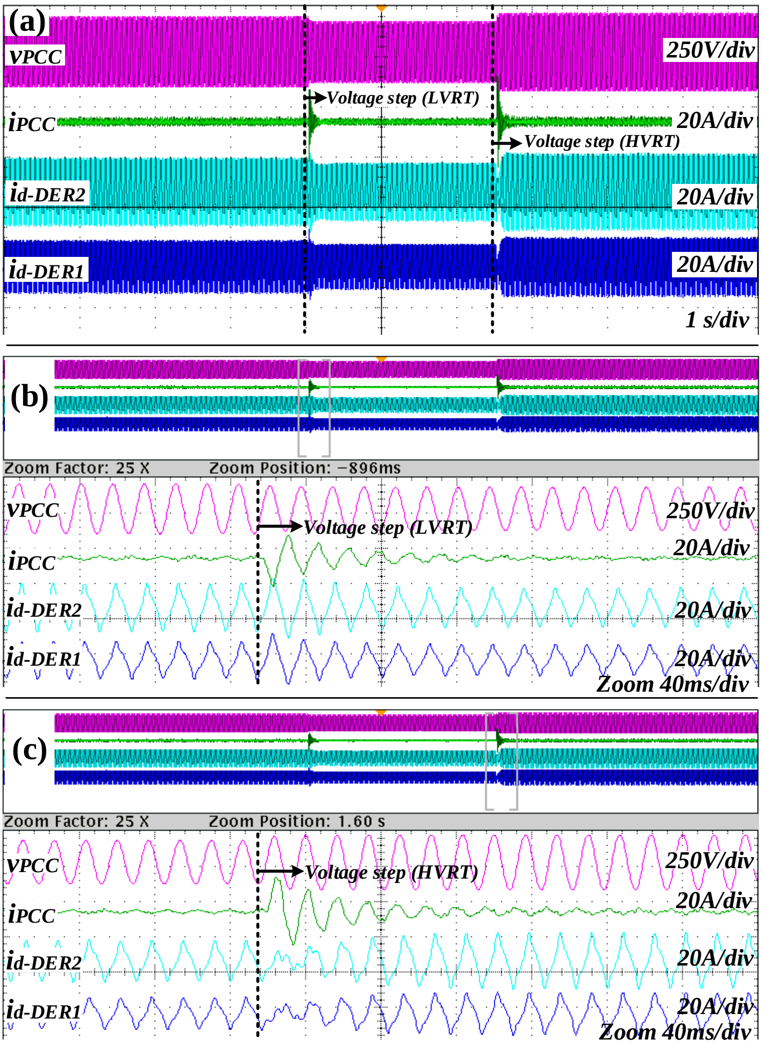

Figure 5.3: Experimental results: full current control under voltage ride-through. (a) Steady state view of voltage steps; (b) Zoom-in-view of a negative step in grid voltage; and (c) Zoom-in-view of a positive step in grid voltage. From top to bottom: PCC voltage and current, d-DER$_2^\star$ and d-DER$_1^\star$ currents.

inverters to achieve current sharing, reaching steady state in approximately five cycles. There was no significant impact on the MG operation, apart from the transitions in currents caused by the local controller of the d-DERs*.

With regard to the HVRT scenario presented in Fig. 5.3(c), one can observe a similar behavior in relation to the coordination provided by the GCBC. After the referred step was applied, significantly increasing the grid voltage, the d-DERs* took approximately five cycles to return to steady state operation, and the proportional current sharing was not ceased during transition instants. Unlike the LVRT scenario, the transient behavior of the d-DERs*' local controllers led to a reduction in current injection, as the magnitude of their PoC voltages increased. Nonetheless, even with the dynamics of the local controllers adding more complexity to the coordination of the inverters, the GCBC strategy was again able to adequately ride through the voltage swell. Even if saturation algorithms were incorporated into the local controllers of the DERs*, no impact would occur on the overall coordinated operation, as the GCBC algorithm only processes and controls average values of currents measured within the MG.

Overall, it has been shown that the GCBC strategy can be implemented for the management of LV MGs, even if voltages may suffer from abnormalities such as sags and swells. The offered coordination of inverters is capable of adjusting their current injections under LVRT and HVRT scenarios, maintaining current sharing effectiveness, as well as rapidly adjusting to different operational conditions.

5.5 Proportional Current Sharing and its Consequences to Voltage Quality

In this section, an interesting particularity related to the proportional current sharing provided by the GCBC strategy is discussed, in terms of its impact on voltage quality. As previously explained in Section 4.4.2, the coordination devised by the GCBC approach allows us to proportionally steer DERs, without requiring knowledge of line impedance parameters. Thus, proportional current sharing is achieved independently of DERs' locations. In addition, steering only occurs based on MG objectives and on the inverters' ratings or capabilities (i.e., depending on the nature of the DERs and their operational goals).

In parallel, an important matter of weak MGs is the fact that, regardless of whether they are under islanded or interconnected mode, the operation of inverters and the existence of non-linear loads may significantly affect voltage quality [133, 161]. This is even more critical for terminal nodes in radial MGs, as voltage drops over consecutive line impedances may lead to: *i)* voltage rise [162] and *ii)* voltage distortions [82], depending on the currents drawn by loads and on how DERs operate. Nonetheless, once a homogeneous MG is considered, the balanced power demand from loads, as well as the uniform distribution of DERs throughout the grid, allow such negative impacts to be minimized, if inverters are adequately coordinated.

Herein, experimental results are presented to demonstrate that, if DERs can be coordinated to proportionally contribute to multiple current sharing purposes within a homogeneous weak MG, voltage quality can be attained as an indirect outcome. Hence, improvement in voltage quality is not only attained for the PCC, but also for the internal MG nodes. Once again, the experiments take into consideration the main single-phase prototype explained in Section 4.2.2, with all elements participating in the MG operation. Consequently, all linear and non-linear loads were connected to the MG, also having the two d-DERs* being coordinated by the GCBC strategy, as well as considering nd-DER$_1^\star$ locally operating injecting active power.

Experimental results are provided in Fig. 5.4, in which the currents and voltages of the three DERs*, and the PCC, are seen. An initial case is presented in Fig. 5.4(a) to explicitly demonstrate the above-mentioned voltage issues occurring in weak MGs comprising non-linear loads and distributed generation. For this case, nd-DER$_1^\star$ operated injecting approximately 591 W, just as was performed during Fig. 4.20(e) in Section 4.3.4.2, whereas the d-DERs* were disabled (i.e., not sharing any currents).

First, it can be noted in Fig. 5.4(a) that the PCC current was distorted, as the loads were drawing harmonic currents. Even though a pure sinusoidal voltage was applied to the grid emulator, due to the harmonic distortions existing in load currents, the PCC voltage presented THD$_v$ of 2.46% (see Table 5.4). By reminding about the harmonic components measured when only loads were connected to the MG (see Table 4.5), the most significant non-fundamental components at the PCC current was the 3rd harmonic

Table 5.4: Amplitudes of voltage harmonic components, and THDv for the PCC and each DER* in Fig. 5.4.

	Voltage Amplitudes [V$_{pk}$]					**THDv [%]**
***h* =**	**1**	**3**	**5**	**7**	**9**	
			Fig. 5.4(a) - GCBC Off			
PCC	171.39	4.04	0.6	0.75	0.13	2.46
d-DER$_1^\star$	165.53	4.34	1.8	0.29	1.05	3.06
d-DER$_2^\star$	167.82	9.25	3.25	0.64	1.5	5.92
nd-DER$_1^\star$	164.35	9.98	3.27	0.5	1.43	6.54
			Fig. 5.4(b) - GCBC On			
PCC	175.08	0.97	1.41	0.47	0.41	1.12
d-DER$_1^\star$	171.79	2.18	1.77	0.57	0.75	2.16
d-DER$_2^\star$	177.73	0.59	3.38	1.48	0.92	2.21
nd-DER$_1^\star$	171.81	2.47	2.17	1.51	1.07	2.53

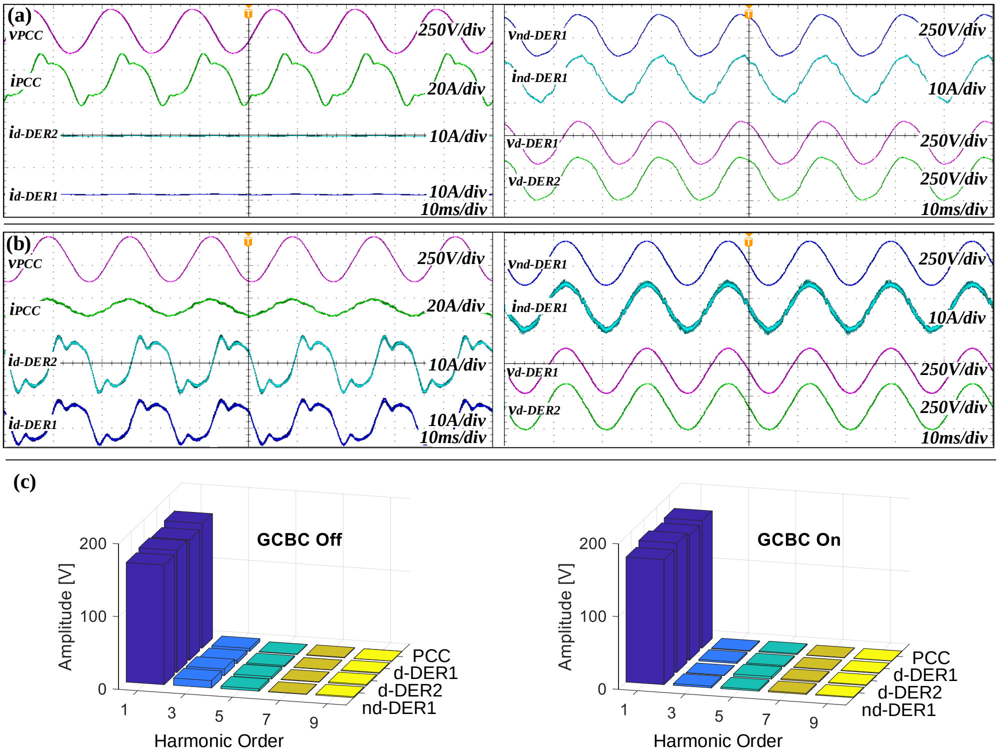

Figure 5.4: Experimental results: voltage quality improvement by distributed compensation of reactive and harmonic currents. (a) PCC and DERs' voltages and currents with GCBC disabled; (b) PCC and DERs' voltages and currents with GCBC enabled; (c) harmonic spectrum of MG voltages. From top to bottom (for (a) and (b)): (left figures) PCC voltage and current, d-DER$_2^\star$ and d-DER$_1^\star$ currents; (right figures) nd-DER$_1^\star$ voltage and current; d-DER$_1^\star$ and d-DER$_2^\star$ voltages.

order, being followed by the 5th order. Now, if one analyzes Table 5.4, it indicates that the distortions found in the PCC voltage during Fig. 5.4(a) were exactly these two components. Observe that the non-linearities in load currents led to a peak voltage of 4.04 V_{pk} at the 3rd harmonic order. This can also be evidenced in the frequency spectrum shown in Fig. 5.4(c), when the GCBC was disabled.

Even worse scenarios of non-sinusoidal voltages appear in the PoCs of the DERs*, than for the PCC. Visually, one can already observe in Fig. 5.4(a) the distorted voltage waveforms obtained for d-DER$_1^\star$, d-DER$_2^\star$, and nd-DER$_1^\star$. Moreover, as expected, d-DER$_2^\star$ and nd-DER$_1^\star$ were the ones presenting the most distorted voltages, as they were located at the terminal nodes of the MG and closer to the loads. The resulting high THD_v, being around 6% for d-DER$_2^\star$ and nd-DER$_1^\star$, was caused by the significant voltage distortions at the 3rd and 5th orders (see Table 5.4), which were most significant in load currents as well. For instance, note that the voltages of d-DER$_2^\star$ and nd-DER$_1^\star$ reached 9.25 and 9.98 V$_\text{pk}$ at the 3rd harmonic, respectively, being totally undesired from the voltage quality perspective [27, 133].

An additional remark is also made in relation the current injected by nd-DER$_1^\star$, since a sinusoidal waveform was not obtained in Fig. 5.4(a). Even though this inverter was controlled to inject only a low-distorted active current, voltage distortions are known to commonly affect the current output of inverters with *LCL* filter, as harmonics flow through their filter capacitor [163]. Thus, this experiment also showed that non-idealities in voltages caused by load currents present a chain effect on the overall robustness of the MG operation. The resulting THD$_\text{i}$ for nd-DER$_1^\star$ was 5.22%, which might be considered inadequate [8], if ancillary services are not being deployed by the inverter.

A contrasting experimental case is then presented in Fig. 5.4(b) to explain the benefits of providing proportional power or current sharing in homogeneous MGs. During this case, the GCBC strategy was enabled to coordinate d-DER$_1^\star$ and d-DER$_2^\star$ to share the loads' reactive and selected (i.e., the 3rd and 5th orders) harmonic currents. As the d-DERs* proportionally shared currents according to their nominal ratings, an adequate proportional ratio of $r_{dDERs^\star} = 1.29$ was obtained, and the PCC current became low-distorted and in-phase with the PCC voltage. Table 5.4 shows that the THD$_\text{v}$ at the PCC was reduced due to this operation, reaching 1.12%. Such steering of the d-DERs* provided a reduction of approximately 75% in the 3rd harmonic distortion at the PCC voltage (see Table 5.4). Furthermore, Fig. 5.4(c) shows that the harmonic spectrum became flatter when the GCBC was enabled, indicating minimization of voltage harmonics.

Looking at the voltages for the other MG nodes in Fig. 5.4(b) (see right-side plots), the benefits of performing proportional current sharing are apparent. The voltage waveforms for all inverters became less distorted, as the burden of voltage harmonics caused by the load currents was compensated under a distributed and proportional perspective. This indirect voltage quality improvement can be observed when the MG presents homogeneous characteristics, since the effort needed to mitigate propagated voltage disturbances is roughly distributed throughout the MG.

Hence, the results show that the distributed current compensation determined by the GCBC strategy allows each inverter to indirectly contribute to local voltage improvement, resulting in roughly uniform voltage profiles, if the MG is homogeneous. A brief theoretical contrast, for instance, can be pointed out in the use of the conventional droop control, considering any generic homogeneous MG. As discussed in Section 4.4.2, droop control would inherently cause inverters to unproportionally share reactive and harmonic currents, as line impedances would have an effect on their actions. Consequently, the amount of harmonic currents flowing from a certain inverter would likely be significantly higher than others, leading to non-uniform distributed compensation of currents, which minimizes the obtained performance in indirect voltage quality improvement.

Table 5.4 shows the numerical performance of the GCBC strategy. By achieving distributed compensation of reactive currents, restoration of the fundamental voltage components occurred, obtaining higher amplitudes at all MG nodes (i.e., becoming closer to the nominal value, which was 179 V_{pk}). Moreover, by offering proportional harmonic current sharing, the amplitudes of non-fundamental voltage components (i.e., particularly for the 3rd order) were significant reduced. For instance, observe that the 3rd harmonic order reduced to 0.59 and 2.47 V_{pk} for d-DER$_2^\star$ and nd-DER$_1^\star$, respectively, being significantly lower than during Fig. 5.4(a). Yet, lower THD_v was also obtained at all nodes, as shown in Table 5.4.

A final side effect of the voltage quality improvement obtained in Fig. 5.4(b) is noticed at the current of nd-DER$_1^\star$. Observe that such a current presented less distortion than during Fig. 5.4(a). This occurred because the reduction in voltage distortion at that PoC led to less harmonic current flowing through the capacitor of the *LCL* filter of nd-DER$_1^\star$. Consequently, an improved performance of the current controller used during the experiments was supported. Therefore, the previously obtained 5.22% THD_i was reduced to 3.23%, demonstrating that the multi-purpose control provided by the GCBC strategy can even benefit inverters not being coordinated.

5.6 Stability Analysis for the GCBC Strategy

In general, coordination of DERs in MGs is deployed to improve system performance, such as by increasing energy exploitation, efficiency and by achieving control flexibility. Nonetheless, when improper coordination of multiple inverters occurs in a MG, their dynamic interactions may lead to undesired operational conditions [23], especially with regard to small signal, transient and voltage stability [164, 165]. Therefore, it is important to study how coordinated control strategies may impact MG stability, so robust operational boundaries can be identified for stable operation [166]. A closed-loop stability analysis is presented in this section, highlighting that the communication-dependency of the GCBC does not negatively affect the overall operationalities of the MG.

5.6.1 Closed-Loop Stability Analysis

From a control theory perspective, the GCBC strategy may be interpreted as a networked control approach [167, 168], in which multiple inverters are seen as slave units driven by a master controller (i.e, the MGCC). Additionally, focusing on the interconnected operational aspect of the MG, the hierarchical control architecture presented in

Section 3.4 determines that the primary control layer already allows DERs to comply with grid codes. Consequently, stable local operation of each inverter can be considered as a premise of the GCBC strategy. Hence, stability can be sufficiently analyzed by considering the matter of time delays on the data exchange needed for the control strategy.

Herein, a simplified analysis of the CBC strategy is presented with regard to closed-loop system stability, being devised in relation to the concern of active current injection, similarly to what was found in [66] and [71]. Since the control strategy is only based on average values, similar schemes could be derived for other current terms. Besides, as the controlled current terms are decoupled and harmonic components are never considered over the bandwidth of local controllers, they independently affect stability. Knowing that stability is assessed herein based on communication delays, the results are analogous for fundamental and non-fundamental current terms. Therefore, only the active current injection is herein analyzed, for the sake of simplicity.

The control scheme of the referred networked system is then derived in Fig. 5.5(a), comprising the MGCC, the communication infrastructure, the local controllers of DERs, as well as the power system. In such a scheme, communication interactions occurring between the the MGCC and DERs are modeled by delays, being represented by a first order system, as in Eq. 5.1. Such time delays, described as T_D, are inherent to the GCBC strategy due to the transmission of data packets, and they should be considered to account for phase margin deviations in the stability analysis. The local controllers of DERs are modeled by first order low-pass filters, as in Eq. 5.2, with a control bandwidth of ω_c, which can be considered as $\omega_c = 2 \cdot \pi \cdot 1200$ rad/s. It is worth mentioning that, since $I_{h||_m}^{Grid*}$ (i.e., MG power dispatchability reference) comes from the tertiary layer and varies very slowly, it can be neglected on the overall stability analysis, as well as in Fig. 5.5(a).

$$H_{T_D}(s) = \frac{1 - s \cdot T_D}{1 + s \cdot T_D} \tag{5.1}$$

$$H_{\omega_c}(s) = \frac{\omega_c}{s + \omega_c} \tag{5.2}$$

Now, it is reminded that the GCBC strategy is periodically processed at the MGCC, under a frequency of f_{GCBC}, which leads to a processing time of T_{GCBC}. Consequently, one can derive the closed-loop discrete control representation of the system, based on the block diagram presented in Fig. 5.5(b), which is the discrete simplification of Fig. 5.5(a). By relating the MG total absorbed current ($I_{1||_m}^{L}(z)$), and the control reference ($I_{1||_m}^{*}(z)$), the transfer function given by Eq. 5.3 is obtained. In Fig. 5.5(b) and Eq. 5.3, z is defined as the discrete domain operator, and $H_{\omega_c}(z)$ is the

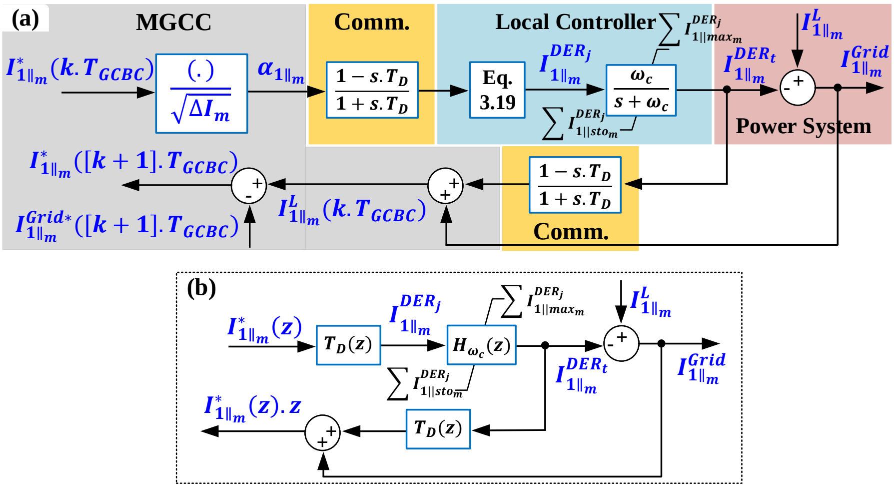

Figure 5.5: Simplified control model of the GCBC strategy, considering communications, used for stability analysis: (a) detailed model and (b) simplified block diagram of the GCBC strategy in discrete domain.

discretized transfer function of the DERs' local controllers.

$$I^*_{1\|_m}(z) = \frac{I^L_{1\|_m}(z)}{z + H_{\omega_c}(z) \cdot T_D(z) \cdot [1 - T_D(z)]} \tag{5.3}$$

The stability analysis of the GCBC strategy can then be performed in the discrete domain by mapping the poles ("×") and zeros ("∘") of Eq. 5.3. In order to analyze the behavior of system, let us consider a generic MG operating with a fundamental frequency of 60 Hz. Thus, for simplicity, this is also set as the interruption frequency of the GCBC strategy at the MGCC, leading to $T_{GCBC} = 1/60$ s. In addition, different time delays are considered, making T_D vary from 1/600 s to 1/6 s during the analysis of the response of the control the system. A time step of 1.66 ms is used for T_D, leading to the mapping of poles and zeros. This is performed to demonstrate how different delays affect on the overall coordination provided by the GCBC approach. The obtained results are shown in Fig. 5.6.

From basic control theory [169], a discrete system is defined to be stable if the closed-loop poles lie within the unity circle in the z-plane. Hence, Fig. 5.6 shows that for all conditions considered for T_D, the poles were inside the expected region, indicating that stability is achieved. Note that the poles also did not touch the boundary of the unity circle (i.e., $z = 1$), which would mean that the system is critically stable. Considering that modern communication systems applied to the scenario of MGs present maximum latency of around 100 ms [170] (i.e., being below the maximum T_D tested), the results from Fig. 5.6 demonstrate that the GCBC does not impair stability.

It can also be observed in Fig. 5.6 that a specific pole of the system tends to move to the right-half side of the z-plane. This is an indication that, as transmission times considered for the communication channels are slower, this pole becomes more dominant [169]. In other words, this means that T_D becomes more important for the stability aspect. Such a condition is reasonable because, as T_D increases, the GCBC strategy takes longer to respond to transients, as it will be later discussed in Section 5.7.2. Thus, the GCBC presents smaller stability margins under the implementation of slow communication [167].

The dual condition, given by the adoption of fast transmission speeds, is also visualized in Fig. 5.6 by the poles lying on the left-half plane, which represents neglecting dominance. If transmission speeds are set to be higher than T_{GCBC}, the MGCC has the capability to interpret the MG status multiple times in a control cycle k, allowing the possibility to promptly adjust the calculation of the scaling coefficients, if desired. Nonetheless, for reasons of practical implementation, there is no need for such a feature, as the steady state performance of the GCBC strategy is not impacted by setting data transmission faster than T_{GCBC}.

A final comment is made with regard to the zeros of the system in Fig. 5.6. Although zeros are known to not affect overall stability [169], by being outside the unity circle, non-minimum phase features may be faced by the system, which, in theory, may limit control bandwidth and decrease the phase margin. Nonetheless, since the

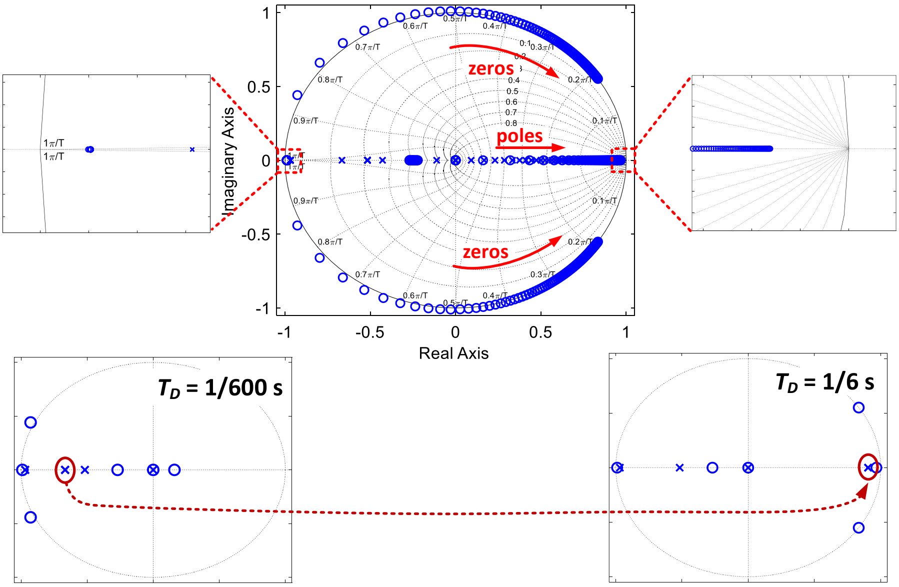

Figure 5.6: Pole and zero mapping, considering T_D varying from 1/600 s to 1/6 s, for the simplified stability analysis of the GCBC strategy.

GCBC relies on an analysis of average quantities, also only controlling current terms up to the bandwidth of the DERs, such limitations are minimized.

5.7 Considerations on Communication Matters

A critical aspect of DER coordination is the possible dependence on communication means, which may reduce MG reliability [171], as well as affect stability [172], if data transmission links are not resilient [111]. Since communication is a bottleneck of the GCBC strategy, faulty data transmission links and the occurrence of delays are addressed in this section to show that they are not critical from a control standpoint.

5.7.1 Faulty Data Transmission Links

Communication-dependent control strategies, in general, present the inherent limitation of requiring data transmissions links to be active to steer DERs. In addition, at any moment, loss of communication may occur for a diverse variety of reasons, such as caused by faults in data transmission channels [173]. Since the GCBC relies on a networked control architecture, it is important to demonstrate how the occurrence of failures in communications is handled without impairing stability. Thus, experimental results demonstrate herein how the MG operates when one or multiple coordinated inverters face loss of communication, making it impossible to exchange data with the MGCC.

Experimental results consider the main single-phase MG prototype of Section 4.2.2, once again having all loads connected, and taking into account only d-DER$_1^\star$ and d-DER$_2^\star$. Both d-DERs* are coordinated by the GCBC strategy and communication failure is emulated by software. As a premise of operation, it is considered that, if such inverters present active communication channels, they must participate in the GCBC to share the active, reactive and harmonic load currents. Otherwise, when communication links are under faulty conditions, the inverter must only operate according to its local goals. Consequently, for the following results, to facilitate understanding, it is considered that d-DERs* do not inject any currents when being locally controlled. A communication speed of 16.66 ms is also emulated in the experiments, allowing the MGCC to start a new control cycle "k" at the beginning of each cycle of the 60 Hz fundamental grid voltage.

Six scenarios are then shown in Fig. 5.7 to demonstrate how the system performs when faults occur at the communication channels of any of the d-DERs*, and how the algorithm proceeds when such links are re-established. Moreover, a case representing the MGCC's communication link under fault is also evaluated. The overall operation of the MG during the aforementioned cases is presented in Fig. 5.7(a). From this result one can note that the d-DERs* present a different status for their communication links

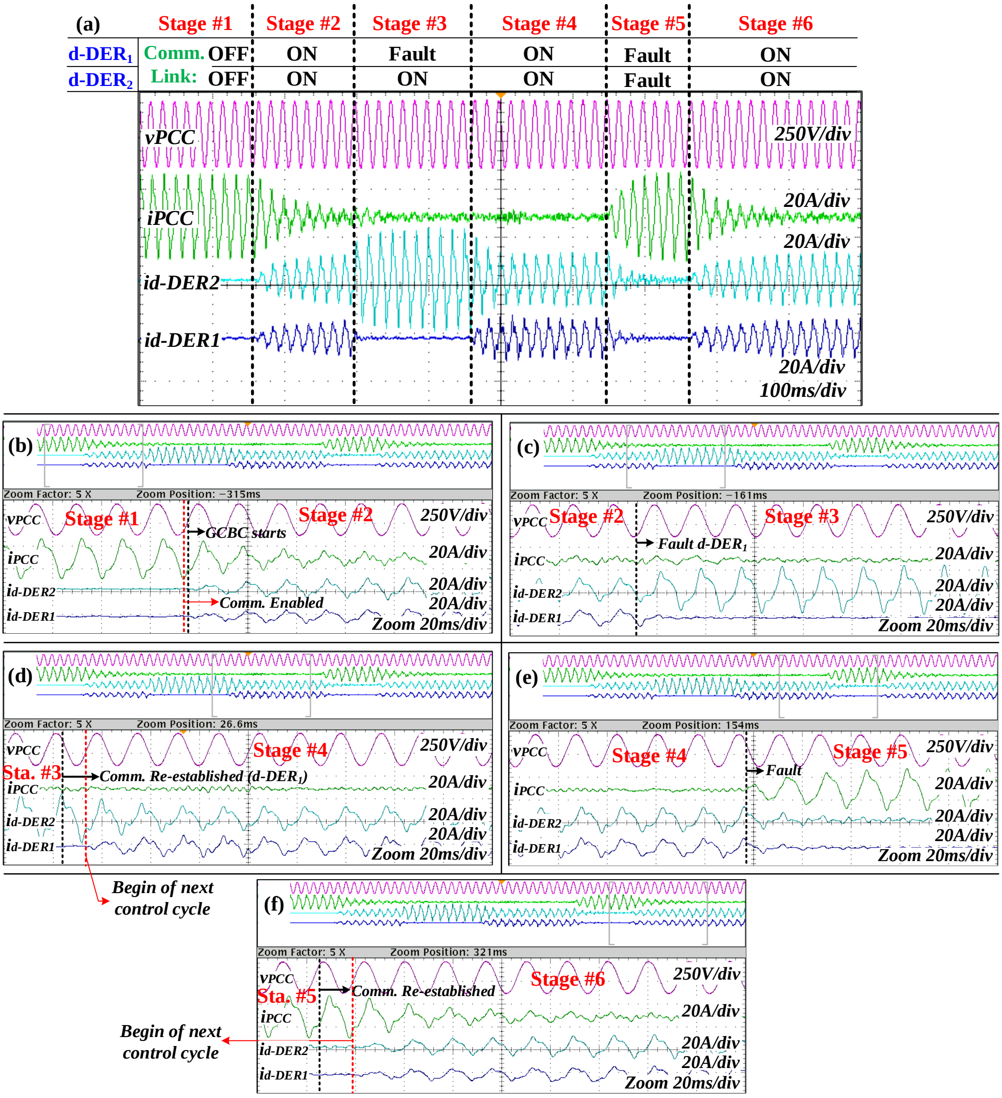

Figure 5.7: Experimental results of the GCBC under faulty communication links. (a) Overall operation considering the six emulated cases; (b) Transition between Stages #1 and #2: GCBC starting; (c) Transition between Stages #2 and #3: communication fault at d-DER$_1^\star$; (d) Transition between Stages #3 and #4: communication re-established at d-DER$_1^\star$; (e) Transition between Stages #4 and #5: communication fault at MGCC; (f) Transition between Stages #5 and #6: communication re-established at MGCC.

at each stage, being each stage further explained based on Figs. 5.7(b) to 5.7(f).

In Stage #1, the locally ruled operation of the DERs* is demonstrated, imposing that communication links are disabled and both inverters are following null current references. The zoom-in-view of this case is seen in Fig. 5.7(b). At a second instant during this result, the communication links of both DERs* are concomitantly activated, allowing the MGCC to obtain data from the participating inverters and proceed with the calculations required by the GCBC strategy. Once scaling coefficients are processed and broadcasted to the DERs*, they start sharing the load currents, similarly to that demonstrated in Chapter 4.

Even before the MG reaches steady state operation in Stage #2, a sudden fault is emulated in the communication channel of d-DER$_1^\star$. Consequently, at an arbitrary moment, this inverter is no longer able to communicate with the MGCC. As this failure is usually locally identified by an inverter [173], d-DER$_1^\star$ was able to promptly set its primary layer control goal to rule its operation. Thus, this action caused d-DER$_1^\star$ to follow a null current reference, as observed in Fig. 5.7(c) during the transition from Stage #2 to Stage #3.

On the other hand, even though d-DER$_1^\star$ was not able to exchange data with the MGCC during Stage #3, d-DER$_2^\star$ was not affected by the fault, allowing it to keep operating according to the desired MG goal (see Fig. 5.7(c)). However, since the MG's total capability changed by the failure at d-DER$_1^\star$, the GCBC had to adjust the scaling coefficients broadcast to d-DER$_2^\star$. This occurred because the MG's capability (i.e, $\sqrt{\Delta I}$) was not the same as that during Stage #2, when d-DER$_1^\star$ was participating in the coordination.

As a result, d-DER$_2^\star$ had to individually supply the currents drawn by the loads to maintain the coordination goal. Of course, if the nominal capability of d-DER$_2^\star$ was reached, the saturation schemes of the strategy would guarantee safe operation, as discussed in Section 5.2. Yet, note that the abrupt disconnection of d-DER$_1^\star$ did not make the GCBC affect the MG overall operation. Fig. 5.7(c) clearly shows that no disturbances were caused at the PCC voltage and current, nor at d-DER$_2^\star$'s current. The plug-and-play feature of the strategy allowed enduring failure in communications, as participation or removal of inverters are interpreted by the MGCC only at the beginning of each new control cycle "k".

Another case can be found in Stage #4, demonstrating how the MG management based on the GCBC strategy would behave when faulty communication links are re-established. This condition is emulated by allowing d-DER$_1^\star$ to suddenly activate its communication channel, allowing it to again exchange data with the MGCC. As noted in Fig. 5.7(d), the re-establishment of d-DER$_1^\star$'s communication link occurred at an arbitrarily instant, which caused this inverter to tardily adjust its current injection. This occurred because the participation on the GCBC strategy is only granted once a new control cycle "k+1" starts. Thus, note that both DERs* returned to provide active current sharing, after a new periodic interruption of the GCBC occurred.

Now, the next case (i.e., Stage #5) shows how the MG operates when the MGCC faces failure in its communication links. The experimental result in Fig. 5.7(e) demonstrates that, as loss of communication was sensed by the d-DERs*, they immediately disregarded the scaling coefficients that were coming from the secondary layer. Hence, operation occurred only based on their local goals, as both d-DERs* processed null currents after the failure. Although inverters could keep operating based on the scaling coefficients attained from the last control cycle, to achieve stronger operational reliability for the MG, they do not do so. This is to cope with the dynamic changes of the MG, as loads and other inverters could connect or disconnected during the faulty condition. Consequently, this new operational state would require the coordination of DERs* to be readjusted, which is not possible due to the unavailable communication means.

Of course, for practical implementations in real-life applications, a waiting time is usually considered to allow more realistic, and less intermittent, interactions among communication interfaces [173]. Thus, according to communication requirements [114], instead of abruptly disregarding the secondary layer, DERs* may maintain their operations for a few milliseconds to seconds, until communication links were indeed considered to be faulty. Such a feature can easily be embedded into the local management of inverters comprising communication interface [8].

The last experiment depicted in Stage #6 demonstrates what happens when the communication capability of the MGCC is re-established, after the failure in Stage #5. From the result shown in Fig. 5.7(f), one can note that communication with DERs* became active after a control cycle was initiated by the MGCC. Consequently, similarly to Stage #4, the inverters were not immediately coordinated by the GCBC strategy and remained processing null currents. Their integrated operation only occurred after a new control cycle was initiated, allowing the MGCC to re-calculate the MG capabilities and set the proper scaling coefficients to achieve the intended operational goal.

5.7.2 Data Packet Delays

The impact of data transmission issues relating to packet delays will now be assessed. Also in this case, the considered study shows that the GCBC can maintain a stable operation. For the following discussions, for the sake of simplicity, computational simulations are carried out based on the simplified MG circuit presented in Section 4.4.2.1 and in Fig. 4.24. The same simulation parameters adopted during the comparative study of the GCBC strategy against droop control are herein used, considering that the two inverters (i.e., INV_1 and INV_2) are sharing the active, reactive and selected harmonic load currents.

Again, the GCBC is emulated with data transmission links supporting the initialization of control cycles at a periodic rate (i.e., T_{GCBC}) of 16.66 ms. It is remarked that delays are emulated during simulations by counters that hold the data packets by a desired time, until they are released to the local control of DERs. To demonstrate the dynamics of the GCBC operating under different scenarios of data packet delays, a load step is emulated during simulations by switching off the linear load (Z_{L1}) (see Fig. 4.24). The second linear load (i.e., Z_{L2}) is considered to be disconnected at all moments.

When a new GCBC control window starts to process data coming from DERs, the following four conditions related to packet delays are likely to occur: *i)* delayed data from the MGCC to DERs (broadcast is halted); *ii)* delayed data from a DER to the MGCC; *iii)* DERs receiving data with different delays from the MGCC within the same control cycle (i.e., normal operation); and *iv)* DERs receiving data with excessive delays from the MGCC at different control cycles (i.e., unusual operation).

The first two conditions have been previously addressed indirectly in this thesis. For instance, the case of *i)* can be interpreted as the result in Fig. 5.7(f), in which the control packets from the MGCC are not immediately sent to inverters, after its faulty communication link is re-established. If the control packets are delayed by a time "D" to be released from the MGCC, DERs will respond slower by at least this same amount of time "D". Thus, such a case does not imply abnormal operational conditions, beyond affecting the settling time of the GCBC strategy.

The second delay condition (i.e, *ii)*) has also been indirectly shown in Fig. 5.7(c), between Stages #2 and #3. From a delay perspective, the result in Fig. 5.7(c) can also be interpreted as a case in which an inverter holds its data packet after the MGCC's requisition. If any DER has its communication link active but its data packet delays to arrive at the MGCC, when a control cycle is initiated, it cannot be considered in the coordination strategy. Hence, at a given control cycle "k", the GCBC only considers a DER as an active participant if its requested data packet arrives on time to proceed with calculations.

The remaining cases, (i.e., *iii)* and *iv)*) will now be addressed. This first case demonstrates the operation of the GCBC strategy when DERs take different times to receive and process the control packets broadcast by the MGCC (e.g., DERs are spread over the MG, presenting different distances to the MGCC). The second case considers the unusual scenario related to the possibility of having excessive delays, which are slower than the period of a given control window. During both cases, the delay characterizing the time to receive control packets broadcast by the MGCC are called D_1 and D_2, respectively for INV_1 and INV_2.

The case of *iii)* can then be depicted in Fig. 5.8(a), with current and voltage waveforms seen in Fig. 5.8(b). Note that the two coordinated inverters present an initial stage (i.e., during cycle "$k = 1$") when the sharing of the load currents occurs accord-

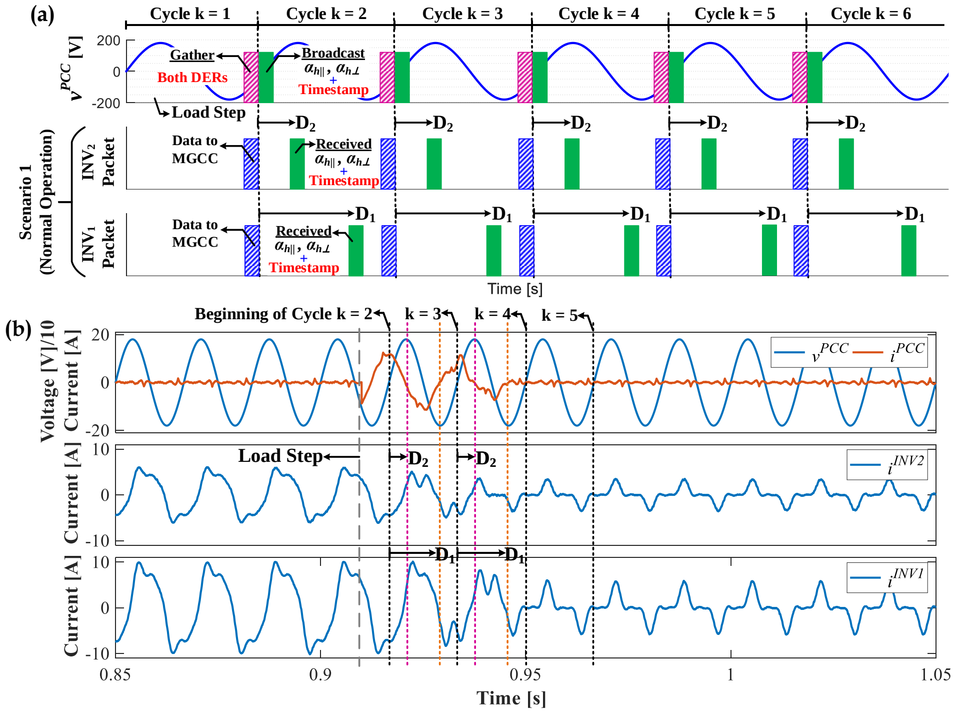

Figure 5.8: Simulation result of the MG operation considering time delays during Scenario 1: constant delays in data packets. From top to bottom: (a) Control windows and time taken for INV_2 and INV_1 to receive data packets from the MGCC; (b) PCC voltage and current, INV_2 and INV_1 currents.

ing to the ideal conditions of data packet transmission. However, at a given instant during "$k = 1$", a load step is applied to the MG by switching off the load Z_{L1}. From that instant onwards, different transmission times are considered for data packets to leave the MGCC and arrive at INV_1 and INV_2.

As the load step occurred during an ongoing control cycle, it is expected for the GCBC algorithm to adjust the calculation of the scaling coefficients at the next window. Thus, the next control cycle should begin intending to gather data from the inverters, as shown by the dashed pink bars in Fig. 5.8(a) (i.e., between "$k = 1$" and "$k = 2$"). During the initiation of this new control window, the MGCC saved a timestamp respective for "$k = 2$", and received from the inverters the expected information about their local quantities (see blue dashed bars in Fig. 5.8(a)). It is worth mentioning that timestamps are common within the structure of data packets, particularly for certain communication protocols [174] adopted by smart inverters [8]. In possession of all required data for the GCBC algorithm, calculations are performed at the MGCC, and the scaling coefficients can be broadcast to the inverters, which now occurs considering constant delays given by D_1 and D_2 (see green bars in Fig. 5.8(a)).

Based on D_1, note Fig. 5.8(b) that INV$_2$ took approximately 1/4 of a fundamental cycle to respond to the new scaling coefficients. On the other hand, INV$_1$ presented a delay of approximately 3/4 (i.e., D_1) to receive such a packet respective to control cycle "k = 2", so its local current references could be updated. Observe that INV$_1$ and INV$_2$ did not present any overcurrents nor instabilities by receiving data packets at different instants. Yet, proportional sharing was maintained regardless of delays. This scenario of having delayed data packets arriving at inverters occurred for the sequential control windows, as can be visualized by the green bars in Fig. 5.8(a).

Even though constant delays were recurrent, data packets were always received during their respective control windows. Therefore, such longer times to receive data packets (i.e., D_1 and D_2) did not have any effect on the overall capability of the GCBC to coordinate inverters. One can observe in Fig. 5.8(b) that, after the load step occurred, the MG operation rapidly converged to steady state operation, similarly to the simulation and experimental results so far discussed within this thesis.

Now, the following discussions are made with regard to the last scenario considered in this section (i.e., case *iv*). For several reasons [173], data transmission in MGs may face uncertain delays [111], which may cause D1 and/or D2 to present random features. Hence, this second scenario depicts a case in which the data packets of given control cycles delay excessively, being only received after the end of their respective control windows. Discussions are conducted based on the simulation results shown in Fig. 5.9, considering the same initial state of the previous scenario shown in Fig. 5.8. Additionally, the same load step is applied to the MG during the control cycle "k = 1".

The pattern of the data transfer from the MGCC to the inverters is seen in Fig. 5.9(a), in which it is observed that INV$_1$ still operated as in Scenario 1, with D1 equal to approximately 1/4 of the period of a fundamental voltage cycle. INV$_2$, however, presented random delays during the control windows "k = 2" and "k = 4" (see red and green bars). At the beginning of "k = 2", the MGCC polled information from the the participating inverters, and broadcast the control data packet. It can be seen from Figs. 5.9(a) and 5.9(b) that INV$_2$ operated similarly to during the previous scenario of Fig. 5.8(b). Nevertheless, the data packet received by INV$_1$ during "k = 2" delayed excessively by a time of D_1', arriving only after a new control cycle started on "k = 3".

Two statements need to be made at this point. The first is a reminder that each control packet sent by the MGCC presents a header with a timestamp [174]. The second relates to the fact that all inverters know which is the current control cycle, based on previous communications established with the MGCC, and on the processing time set for the GCBC strategy (i.e., T_{GCBC}). Consequently, the excessively delayed data packet read by INV$_1$ during "k = 3" must not be used. Observe in Fig. 5.9(b) that

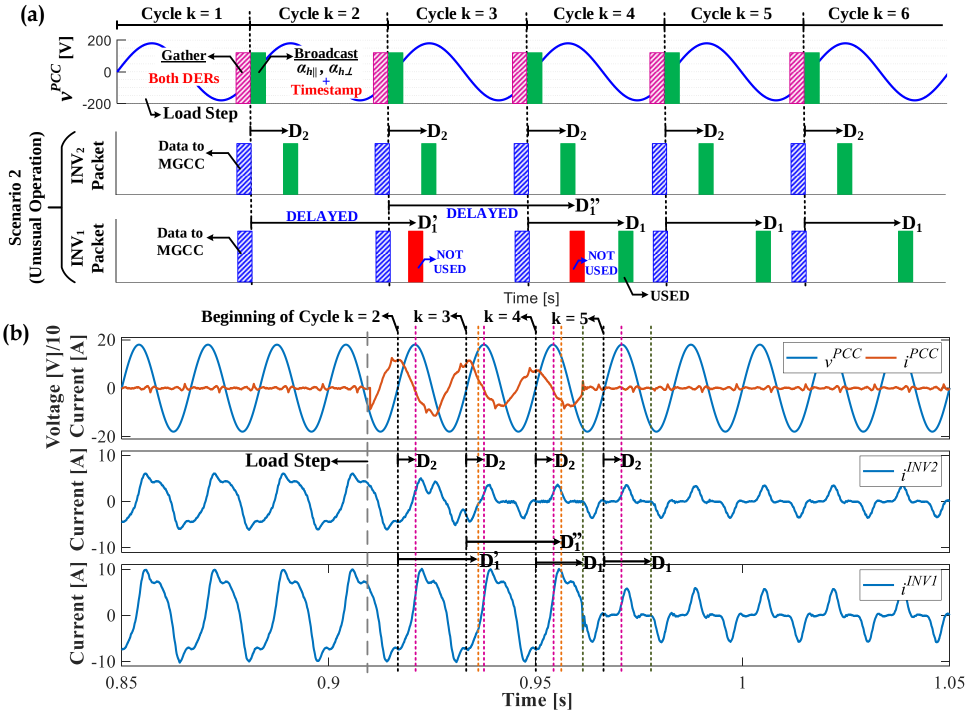

Figure 5.9: Simulation result of the MG operation considering time delays during Scenario 2: excessive delays in data packets. From top to bottom: (a) Control windows and time taken for INV_2 and INV_1 to receive data packets from the MGCC; (b) PCC voltage and current, INV_2 and INV_1 currents.

this inverter did not update its current injection, as the data packet presented an inconsistent timestamp. Since its communication channel was still active and data packets were received, even though delays occurred, INV_1 maintained its current injection unchanged. This is done to avoid intermittency in appropriate current sharing. However, for the case in which excessive delays occur repetitively for prolonged time periods, INV_1 must automatically disregard inputs coming from the secondary layer and operate based on local goals.

Observing cycles "$k = 3$" and "$k = 4$" in Fig. 5.9(a), it is seen that the control packet respective to "$k = 3$" was delayed by D_1''. Consequently, it could not be used by INV_1 again, even though INV_2 kept updating its current injection regardless of a small delay (see Fig. 5.9(b)). Then, once control window "$k = 4$" started, the issue causing delays in the communication of INV_1 was solved, and another control packet arrived after a delay D_1. Since the control packet related to D_1 presented the right timestamp, it is the only one used, allowing INV_1 to promptly respond, as seen in Fig. 5.9(b). Lastly, one can also note that data packet dropouts [114] can be treated similarly to excessively delayed packets, as inverters only update their current references once non-corrupted packets are read at the right control windows.

Finally, it can be concluded that, if data packet delays occur, the GCBC strategy is robust to endure such inconsistencies. Consequently, no impairment occurs at the local operation of primary controllers, and neither is system stability jeopardized. It is also worth noting that the above-mentioned results adopted a short timescale, being of around some fundamental cycles, to simplify understanding. Of course, in practical applications the communication between MGCC and inverters is usually slower, due to the latency of communication interfaces and protocols [114]. However, under such a scenario, delays could be simply seen as a time constants added to D_1 and D_2, not affecting the overall analysis discussed.

5.8 Brief Discussion of Power Coupling

The features of line impedances play a vital role in the deployment of coordinated control strategies in any MG [171]. Depending on how inductive, capacitive or resistive line impedances are, power sharing accuracy can be deteriorated [175], as previously demonstrated for the conventional droop control method in Section 4.4.2. Particularly for MGs comprising predominant inductive line impedances, an additional complication is the coupling existing between the active and reactive powers [176], which does not allow either of these two to be independently regulated without affecting the other. Such a limitation also occurs while controlling non-fundamental currents, being even more challenging, due to the fact that coupling becomes more critical as harmonic order increases [21]. Consequently, power coupling should be avoided as it may lead MGs to instability [155].

In order to tackle power coupling, several methods have been proposed in the literature, mostly taking advantage of virtual impedance loops to achieve decoupled control while offering power sharing [155, 175, 176]. In regard to the GCBC strategy, power coupling is also a concern since coordination of inverters is based on the decomposition of in-phase and quadrature current terms, which are synchronized with the local voltages. For instance, when a *j*-th participating DER decomposes $I_{h\|_m}^{DER_j}$ and $I_{h\perp_m}^{DER_j}$ during the initial steps of the GCBC approach, this procedure occurs synchronized to the voltages of that PoC. Consequently, if the line impedances present sufficient reactance to cause significant phase shifts among voltages (i.e., relating to the PCC and all other PoCs), power coupling will occur. Further comments on that concern can be made by expanding the local current reference of a DER, $i_m^{DERj*}(t)$, which was previously described by Eq. 3.21 in Section 3.5.2.

This time-domain current can be re-written as given by Eq. 5.4, in which $x_{h\|_m}^{DERj}$

and $x_{h\perp_m}^{DERj}$ are substituted by cosine and sine functions, respectively. Such trigonometric functions now consider an additional term relating to the phase (i.e., "$h.\theta_s$") of the current signals, which is calculated with respect to the PCC voltage. Thus, if a MG presents line impedances with the *X/R* ratio high enough, to the point of invalidating the assumption of negligible inductance [11], θ_s will be the factor representing the consequent phase deviations, and leading to power/current coupling. In other words, $\theta_s \neq 0$ makes a constant value of $I_{h||_m}$ and $I_{h\perp_m}$ to be quantified differently across the MG. Hence, inherently resulting in non-accurate coordination of inverters.

$$\begin{aligned} i_m^{DERj*}(t) = \sum_{h=1,3,5,\ldots}^{H} & \{(\alpha_{h||_m} \cdot \sqrt{\Delta I_m^{DERj}}) \cdot \cos(h.\omega_o.t + h.\theta_s) \\ + & \ (\alpha_{h\perp_m} \cdot \sqrt{\Delta I_m^{DERj}}) \cdot \sin(h.\omega_o.t + h.\theta_s)\} \end{aligned} \tag{5.4}$$

Moreover, one can notice from Eq. 5.4 that such a voltage phase shift in relation to the PCC represents an error term, which increases proportionally to the harmonic order "h". Consequently, the system damping ratio decreases as θ_s and h increase, which may cause resonances in the vicinity of the system natural frequency [177]. As a result, $h.\theta_s$ needs to be taken into account while steering parallel DERs.

Nevertheless, if voltage phase shifts are indeed a concern in the MG, they could be overcome by employing low-cost synchrophasor measurement units in the considered network [178], or even GPS-based implementations [179] could be extended to the GCBC strategy. Such two alternative examples would allow us to determine the phase deviation between each participating DER and the PCC with significant precision [180]. Consequently, inverters would be able to correct their current references to achieve decoupled in-phase and quadrature current sharing for fundamental and harmonic terms. Hence, by injecting currents with negligible angle deviations with respect to the PCC voltage, inverters would guarantee adequate damping and stability. Finally, it is worth reinforcing that the LV MG scenario considered within this thesis presents low *X/R* ratio, leading to the fact that voltage phase shifts are typically negligible, and power coupling turns out to not be an important matter.

To emphasize the discussions within this section, and to bring a practical demonstration about such a possible power coupling concern, some brief experimental results are presented as follows.

5.8.1 Experimental Results for the Power Coupling Aspect

In order to verify the implications related to power coupling while implementing the GCBC strategy, a new three-phase MG setup is introduced for the experiments, being shown in Fig. 5.10(a). Such a MG is part of the infrastructure of the *National*

Smart Grid Laboratory [181] managed by NTNU and SINTEF, and the following results consider the use of three DERs†, also relying on an OPAL-RT real-time simulator that operates as the MGCC. This type of simulator would allow us to perform experiments based on power hardware-in-the-loop (PHIL), adjusting the operation of DERs† based on data exchange through optical fiber communication links. As the simulator plays the role of the MGCC, the GCBC strategy runs inside it. Herein the superscript "$\dagger$" will be used to refer to this new experimental setup.

The first of the three DERs† (i.e., DER$_1^\dagger$) is a 200 kVA converter from EGSTON, operating as a controlled voltage source that forms the grid, imposing the voltage and frequency references for the MG. Since DER$_1^\dagger$ acts in this way, under the GCBC strategy, it can be understood as the upstream grid connected to the MG PCC, or as an utility interactive converter. The other two existing 60 kVA DERs†, namely DER$_2^\dagger$ and DER$_3^\dagger$, were built by *SINTEF Energy Research*, being set up to operate as current-controlled inverters during experiments. Both inverters present *LCL* filters, with additional delta-wye transformers at their outputs for obligatory isolation purposes, given that their DC links are fed by a common bidirectional DC bus existing at the laboratory. Line impedances are formed by common commercial LV overhead cables [96].

As noted from Fig. 5.10(a), loads were emulated by DER$_3^\dagger$, which operated drawing any desired current components. On the other hand, DER$_2^\dagger$ was configured to operate ruled by the GCBC strategy, providing control over the targeted load currents computed at the MGCC. The DERs†' current controllers used classic PI regulators devised

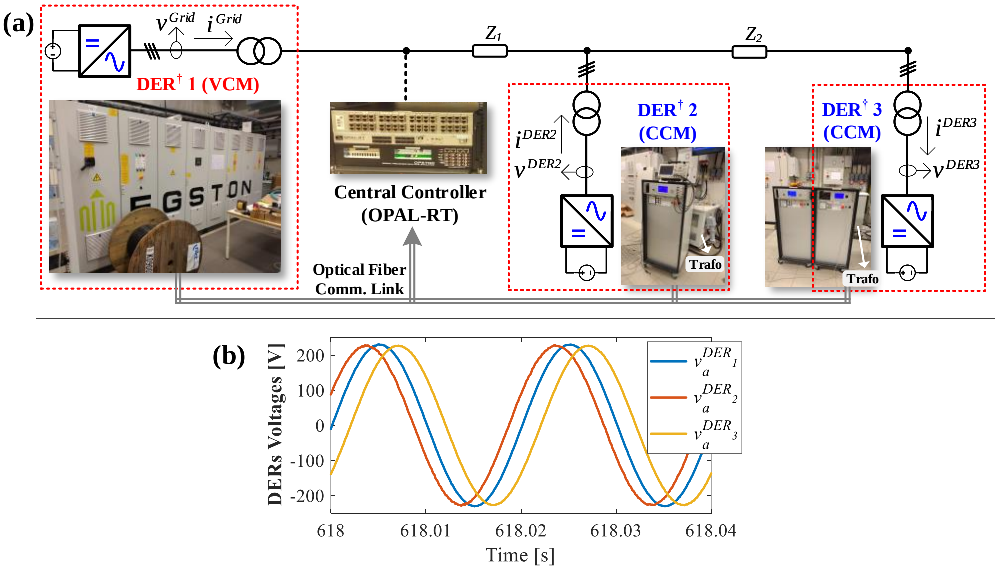

Figure 5.10: PHIL experimental setup used for Section 5.8. (a) Three-phase MG setup; and (b) Instantaneous voltages for all three DERs†.

in the *dq* frame, being locally embedded to their control boards. During experiments, the MG fundamental peak voltage was set to 230 V_{pk} at 50 Hz. Yet, switching and sampling frequencies of 10 kHz were adopted for the inverters, which also had their DC link buses fed with 700 V_{DC}.

A preliminary experimental result is demonstrated in Fig. 5.10(b) to highlight the voltage phase shift existing between the different nodes of the MG. Such a result considered $\text{DER}_2^\dagger$ and $\text{DER}_3^\dagger$ controlling null currents. It is visually evident in Fig. 5.10(b) that the voltages of $\text{DER}_2^\dagger$ and $\text{DER}_3^\dagger$ were significantly shifted in relation to the grid voltage (i.e., $\text{DER}_1^\dagger$'s voltage). More specifically, $\text{DER}_2^\dagger$'s voltage was leading by 25.19°, while $\text{DER}_3^\dagger$'s voltage was lagging by 37.79°. These phase deviations were mainly caused by the transformers placed at the output of the inverters, as the voltage drops over line impedances were small. Therefore, Fig. 5.10(b) presents a clear indication that $\theta_s \neq 0$ for the MG.

Then, the power coupling issue can be visualized by the results shown in Fig. 5.11. For this experiment, the GCBC was implemented to exchange data with the $\text{DER}_2^\dagger$ once in a fundamental cycle (i.e., each 20 ms). Additionally, $\text{DER}_3^\dagger$ was configured to draw 20 A_{pk} of per-phase currents (i.e., $I_{1\perp_m}$), operating as an inductive load. The GCBC strategy was configured to steer only $\text{DER}_2^\dagger$, aiming at supplying the demand of reactive currents initially provided by $\text{DER}_1^\dagger$ (i.e., offering of reactive current control). It is highlighted that only one inverter was considered to be controlled by the GCBC, so a simplified demonstration of the power coupling could be presented. Two intervals were emulated in Fig. 5.11, in which the first shows the GCBC disabled, and the second demonstrates the MG operating when $\text{DER}_2^\dagger$ was controlled to compensate for the reactive currents.

In Fig. 5.11(a) the grid voltages and currents, as well as the currents injected by $\text{DER}_2^\dagger$ and the ones consumed by $\text{DER}_3^\dagger$, are presented. During the first interval, the three-phase reactive power provided by $\text{DER}_1^\dagger$ to supply the load was 8,874.00 VAR. Note that the load currents remained constant during both intervals. Moreover, a small amount of 457.50 W of active power was also measured at $\text{DER}_1^\dagger$ during Interval I (see power plot in Fig. 5.11(b)). Yet, a slight unbalance feature appeared in the grid currents, mainly due to mismatches in the transformers' inductances.

Now, at the second interval, the GCBC was initiated and $\text{DER}_2^\dagger$ was controlled to provide the load reactive currents according to the GCBC strategy. It is noticed from the waveforms in Fig. 5.11(a) that $\text{DER}_2^\dagger$ provided balanced and low-distorted currents, causing the grid currents to significantly reduce their amplitudes. Nonetheless, from Fig. 5.11(b) the coupling between the active and reactive powers, referred to during this section, becomes evident. One can observe the increasing behavior for the active power, even though the reactive power was practically fully provided by $\text{DER}_2^\dagger$, resulting in only -23.82 VAR being measured for $\text{DER}_1^\dagger$. The active power practically

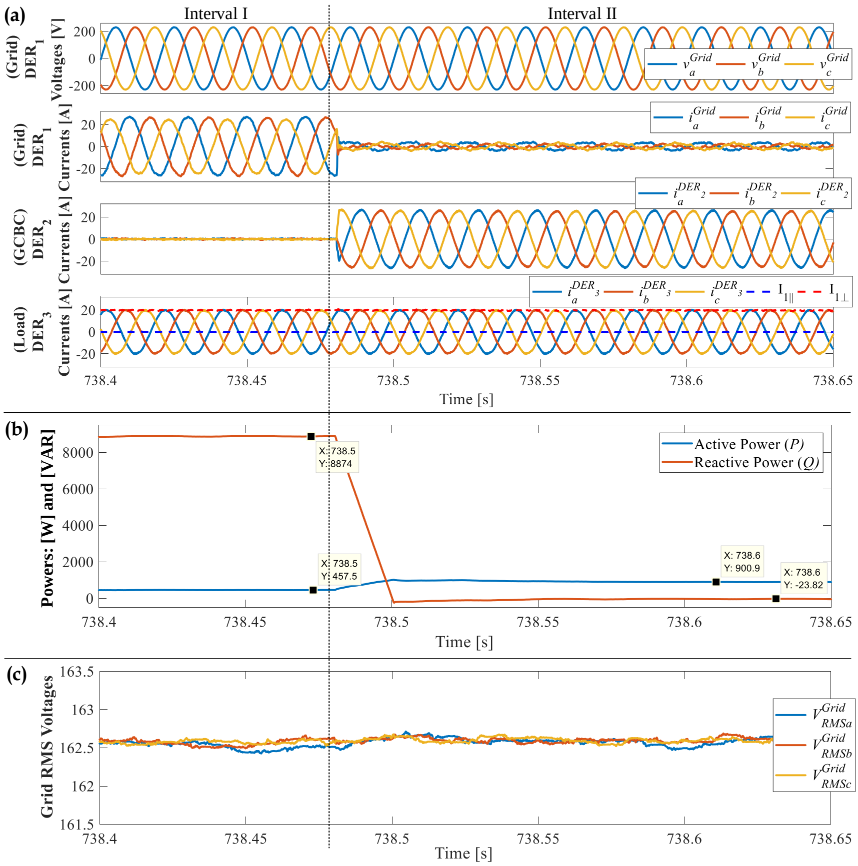

Figure 5.11: PHIL experimental results for the GCBC strategy compensating reactive currents. From top to bottom: (a) Grid (i.e., DER$_1^\dagger$) voltages and currents, DER$_2^\ddagger$ currents, and DER$_3^\ddagger$ currents; (b) Active and reactive power seen at DER$_1^\dagger$; and (c) Grid RMS voltages.

doubled, reaching a value of 900.90 W.

Such an increase in the P power was a direct consequence of the coupling existing between $I_{1||_m}$ and $I_{1\perp_m}$, which was caused by the voltage phase shift existing for this MG. As the load reactive current was supplied by the DER$_2^\dagger$, even though such an inverter only injected $I_{1\perp_m}^{DER_2}$, a different behavior was seen from DER$_1^\dagger$'s perspective, causing $I_{1||_m}^{DER_1}$ to increase. Lastly, the RMS voltages measured for the PoCs of all DERs during both intervals are presented in Fig. 5.11(c). This result demonstrates that the operation of DER$_2^\dagger$ and DER$_3^\dagger$ did not affect voltage profiles, as they remained practically constant during experiments. This also reaffirms the fact that the increased active power measured at the PCC during Interval II was caused by coupled currents.

5.9 Chapter Conclusions

This chapter presented discussions related to how the GCBC strategy steers inverters when non-ideal scenarios occur in a LV MG. For instance, experimental results demonstrated that the coordination of DERs is achieved even if they present limited power ratings. Hence, the control approach allowed the possibility to exploit maximum usage of DERs to provide power control and power quality improvement, respecting their nominal capabilities at all times. Non-idealities in voltages, such as non-sinusoidal waveforms and voltage fluctuations, were also taken into account, showing that DERs can offer multiple control functionalities and present stable operation under such conditions. Moreover, since the strategy provides accurate proportional current sharing, it was shown that DERs can distributedly compensate reactive and harmonic currents, improving voltage quality in homogeneous LV MGs.

As the GCBC strategy is structured based on a hierarchical architecture and can be interpreted as a networked control system, a simplified analysis of the poles and zeros of the system was presented, showing that stability is not a concern, even if slow communication is adopted. Studies of the behavior of the GCBC strategy steering DERs under faults in data transmission channels, as well as under delays in data packets, were also performed. Thus, it was demonstrated that such non-ideal communication conditions are not critical for the overall MG operational goals and stability. Finally, discussions based on theoretical and experimental studies highlighted that power coupling can occur when independent control over fundamental and harmonic currents are intended in MGs with high *X/R* ratios.

Overall, the results presented in this chapter support the idea that, under the scenario of homogeneous LV MGs with low *X/R* ratios, the GCBC strategy can flexibly steer DERs to strive for multiple purposes, even if adverse conditions occur.

Chapter 6

Advanced Control Functionalities for Enhanced Microgrid Operation

6.1 Introduction

Beyond the fact that a LV MG presents dynamic behavior due to interactions occurring among its internal power apparatuses, the interconnection to an upstream distribution grid also brings additional challenges. For instance, non-ideal voltage and current waveforms (e.g., comprising non-linearities and/or asymmetries) may lead to low power factor and malfunctioning of electric equipment [27]. Moreover, as another example, high penetration of DERs in interconnected MGs also causes challenging conditions related to the maintenance of steady voltage profiles [75], as decentralized active power generation is usually tied to voltage rise.

This chapter aims at demonstrating that, if a flexible and multi-purpose coordination of inverters is devised, advanced control functionalities can be offered. Consequently, an enhanced management of MGs and more effective support to the upstream grid can be achieved, particularly when cumbersome operational scenarios are faced. Herein, four main operational scenarios are taken into consideration to highlight advanced MG functionalities [122, 182], being described as follows:

- *Resistive shaping of a LV MG*: non-linearities in voltages are fairly common in LV systems, and the DERs existing in interconnected MGs need to be properly managed to support robust operation [183]. As a result, Section 6.2 discusses a control approach to shape the MG as a variable resistor, achieving higher energy efficiency towards the upstream grid, as well as providing support to damp harmonic resonances;
- *Voltage regulation*: the intermittent and always increasing presence of distributed generation in MGs bring challenges to the maintenance of steady and compliant voltage profiles. Thus, Section 6.3 demonstrates that, if overvoltage conditions occur internally at the MG, the coordination of the DERs based on the GCBC strategy can provide voltage regulation while concomitantly exploiting as much as possible the active power generation from nd-DERs;

- *Compensation of unbalanced currents*: as loads may be arbitrarily connected to poly-phase circuits, MGs may operate with unbalanced currents. As a result, power imbalance often occurs, affecting DSTs' lifespan and bringing additional power quality issues [184]. As a countermeasure, a control scheme based on the GCBC strategy and on the Conservative Power Theory is presented in Section 6.4, aiming at coordinating DERs to achieve distributed compensation of unbalanced currents;
- *Optimal MG operation*: some comments are provided in Section 6.5 to shed light on how the GCBC strategy can also be incorporated into the optimal management of LV MGs.

As a final consideration, it is highlighted that the control functionalities presented herein can also be interpreted as advanced energy services under a transactive control perspective. Consequently, the outlook of energy services and provision of ancillary functionalities are extended, as mentioned in Chapter 2.

6.2 Resistive Shaping of Microgrids under Distorted Voltages

Distorted voltages and currents are an important issue in LV power systems, since they lead to low energy efficiency and deterioration of power quality [185]. Such non-linearities are caused by the increasing presence of nonlinear loads and can be propagated throughout the distribution systems [28]. Moreover, even small voltage distortions may trigger resonances [157] and lead the power system to instability [186]. In particular, this is an inherent concern of weak power systems, such as LV MGs operating interconnected to an upstream grid.

Since MGs operate interconnected most of the time, unless active compensators are placed at their PCC [187], the existing DERs need to be properly coordinated to operate under distorted voltages. Otherwise, reliable operation of DERs is not ensured, and adequate management of the MG as a single-controllable entity is not achieved. Thus, the development of strategies to steer DERs in MGs under distorted voltage conditions is important, being noticeably present in the [28, 107, 183, 188]. Nevertheless, most of the methods found in literature present particularities such as: the consideration of DERs only in islanded MGs [28, 107, 188], sensibility to changes in grid parameters [183], or they do not consider the occurrence of harmonic resonances [148]. Hence, the operation of MGs interconnected to an upstream grid that suffers from voltage distortions is not commonly discussed in the literature.

Concurrently, it has been demonstrated in [19] and [157] that, for the purpose of local applications, harmonic compensation based on the concept of resistive load synthesis (RLS) shows more resonance damping capability than sinusoidal current synthesis (SCS). Besides, RLS-based compensation supports the damping of harmonic propagation throughout distribution grids [82]. Such an RLS principle consists of targeting mitigation of the current harmonics non-proportional to voltages. Thus, the current waveforms resemble the voltage waveforms independently of distortion and/or unbalance (i.e., resistive behavior). On the other hand, SCS-based harmonic compensation results in sinusoidal currents regardless of voltage waveforms. Additionally, another direct consequence of these two approaches is that, based on definitions from modern power theories [45, 189, 190], unity power factor (PF) is only obtained when currents are in-phase to voltages and present proportional waveforms (i.e., PF is the ratio between of active power and the absolute value of complex power). Thus, under distorted voltages, unity PF is only achieved by RLS approaches.

In summary, this section presents an advanced control functionality to coordinate DERs in a LV MG, allowing the possibility to operate it as a single-controllable entity that behaves like a variable resistor. Consequently, the MG PCC can operate with high PF when the upstream grid imposes distorted voltages. Additionally, upon the existence of resonant components, the strategy supports harmonic resonance damping, which minimizes the deterioration of voltage quality. The results discussed in this section also demonstrate that such a complementary functionality: *i)* dampens resonances with more effectiveness than strategies that synthesize sinusoidal currents; and that *ii)* the approach also supports active current sharing among DERs, which allows the MG to operate under full self-consumption mode [44], lessening the burden of power dispatch of the upstream grid, if desired.

6.2.1 RLS-Based Coordinated Control

As demonstrated in Section 5.3, the GCBC strategy inherently presents the capability to provide distributed harmonic compensation following an SCS approach (i.e., harmonic compensation leads to PCC currents resembling sinusoidal waveforms, even under distorted voltages). This occurs because the calculation of scaling coefficients takes into account reference currents based on the grid variables $I_{h||_m}^{Grid}$ and $I_{h\perp_m}^{Grid}$, which comprise all non-fundamental current components.

Nonetheless, in order to achieve a RLS-based coordination of DERs, the GCBC strategy explained in Chapter 3 can easily be modified by further exploiting $I_{h||_m}^{Grid}$ and $I_{h\perp_m}^{Grid}$. Looking into power theory definitions, from the calculation of Fryze's active power (P^{Fryze}) [191], it is understandable that a given time domain current can be decomposed into an active current term, as well as in a non-active term. Thus, for the GCBC strategy, when the MGCC performs the local evaluation of electrical quantities flowing through the MG PCC, the grid instantaneous current, i_m^{Grid}, can be split into an active term ($i_{a_m}^{Grid}$), as well as in a non-active term ($i_{na_m}^{Grid}$), as given by Eq. 6.1.

$$i_m^{Grid} = i_{a_m}^{Grid} + i_{na_m}^{Grid} \tag{6.1}$$

The term $i_{a_m}^{Grid}$ comprises all current components responsible for conveying active power to loads. Consequently, if the term $i_{na_m}^{Grid}$ is compensated, only active power will circulate at that targeted circuit branch, which is the PCC for this case. Based on this concept, Eq. 6.1 can be re-written as Eq. 6.2 to obtain such a current reference for compensation, where V_{col}^{Grid} is the collective[1] voltage for applications in three-phase systems.

$$i_{na_m}^{Grid} = i_m^{Grid} - i_{a_m}^{Grid} = i_m^{Grid} - \frac{P^{Fryze}}{(V_{col}^{Grid})^2} \cdot v_m^{Grid} \tag{6.2}$$

Given $i_{na_m}^{Grid}$, the calculations required for the GCBC strategy can proceed just as presented in Chapter 3. Therefore, to achieve RLS-based coordination of DERs, it is sufficient for them to share the non-active currents measured at the PCC. To do that, $i_{na_m}^{Grid}$ has its peak values decomposed to become the reactive current term ($I_{1\perp_m}^{Grid}$) and the targeted harmonic terms ($I_{h||_m}^{Grid}$ and $I_{h\perp_m}^{Grid}$, for $h > 1$). Note that, by performing such an RLS decomposition, $I_{h||_m}^{Grid}$ and $I_{h\perp_m}^{Grid}$ only comprise the current harmonics non-proportional to voltage harmonics. As a consequence, if they are suppressed, the PCC current will follow a resistive behavior, only presenting harmonics if distortions exist in the grid voltage. This functionality allows the MG to be shaped as a variable resistor, as seen from the upstream grid perspective, giving support to higher energy efficiency and damping of harmonic resonances, as later discussed in Sections 6.2.2 and 6.2.3.

In Fig. 6.1 a scheme summarizes how the RLS-based coordination provided by the GCBC strategy is achieved. Note that the required decomposition of the Fryze's active current only occurs at the MGCC, avoiding additional calculations locally at each inverter. Yet, an additional aspect relates to the variable γ_{RLS}, which is responsible for enabling the RLS functionality. By setting $\gamma_{RLS} = 1$, the distributed compensation of harmonic currents is carried out following a RLS approach.

On the other hand, if $\gamma_{RLS} = 0$, the classic formulation of the GCBC (i.e., presented in Chapter 3) is performed, leading to a SCS-based functionality. The setting of the γ_{RLS} variable is usually regulated at the tertiary control layer, being controlled by the MG manager or by an external agent such as the DSO. Finally, it is highlighted that, if the MG goal is to achieve full self-consumption mode (i.e., sharing of fundamental currents, and harmonic terms both proportional and non-proportional to voltages), the proposed RLS-based can simply be neglected.

---

[1] The grid collective voltage [132] is given by $V_{col}^{Grid} = \sqrt{(V_{RMS_a}^{Grid})^2 + (V_{RMS_b}^{Grid})^2 + (V_{RMS_c}^{Grid})^2}$ (i.e., as for to the collective current shown in Section 4.3.1.1).

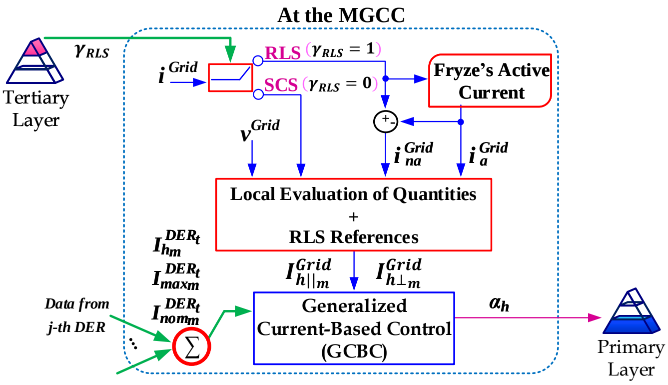

Figure 6.1: Scheme of the GCBC strategy for RLS- or SCS-based coordination of DERs.

6.2.2 High Power Factor Microgrid Operation

Let us consider a scenario for the simulation results, in which the main MG testbench presented in Fig. 3.1 is operating with the upstream grid suffering from distorted voltages at the primary side of the DST. This results in non-linearities of the 7th harmonic order, with 6% of amplitude in relation to the fundamental voltages (e.g., for phase a, $v_a^{Grid} = 400 \cdot cos(\omega_o t) + 24 \cdot cos(7\omega_o t)$). Simulations results are presented in Fig. 6.2, being split into four intervals. For the following results in this section, for the sake of simplicity, only the three d-DERs (i.e., d-DER$_1$ to d-DER$_3$) are considered to be connected to the MG.

Initially, at Interval I, it can be noted in Fig. 6.2(a) how the grid voltages are distorted at the PCC. In addition, considering that d-DERs are idle (i.e., not processing any currents), the load currents are seen at the PCC, being considerably distorted and phase-shifted in relation to the voltages. At this interval, a PF equals to 0.93 is obtained, and the THD$_i$ of the phase currents are approximately 7.70%. Moreover, in Fig. 6.2(b), the PCC currents present several harmonic components, as also evidenced in Fig. 6.3. The most significant harmonics are from the 5th, 7th and 11th orders, being the 7th order the only one existing in the grid voltages.

The GCBC is initiated at Interval II, so the d-DERs are coordinated to share the reactive and harmonic currents seen at the PCC, following the RLS approach. Note in Fig. 6.2(a) that the d-DERs promptly change their current injections, starting to process fundamental and harmonic currents. Besides, such an operation occurs proportionally to their nominal capabilities (e.g., see in Fig. 6.2(e) that d-DER$_1$ and d-DER$_3$ inject the same collective currents, and that d-DER$_2$ injects a collective current around 57% smaller, given that $A^{d-DER_2} \approx 0.57 \cdot A^{d-DER_1}$). Additionally, since d-DERs are following the RLS approach, the PCC currents become in-phase and resemble the voltage waveforms. Fig. 6.3 shows that the harmonic spectrum of the PCC

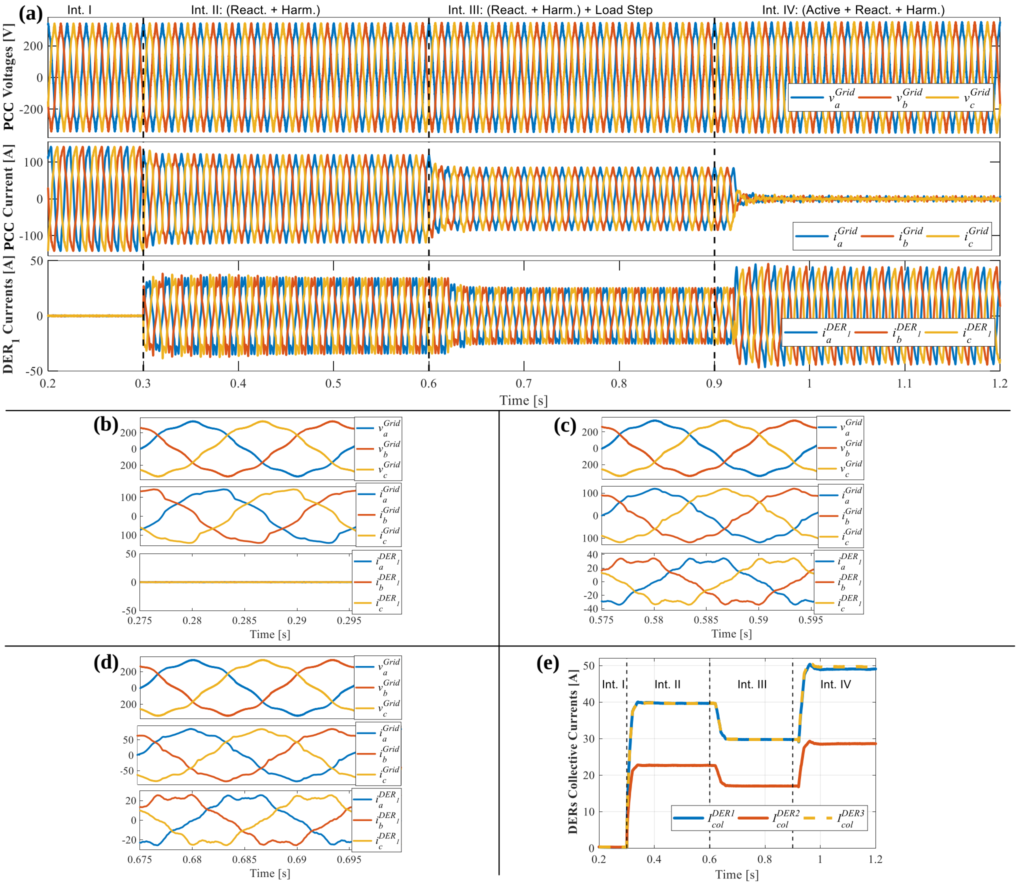

Figure 6.2: Simulation results of the RLS-based coordination for high PF operation. (a) From top to bottom: PCC voltages and currents, and d-DER$_1$ currents; (b) Zoom-in-view of Interval I; (c) Zoom-in-view of Interval II; (d) Zoom-in-view of Interval III; (e) d-DERs' collective currents.

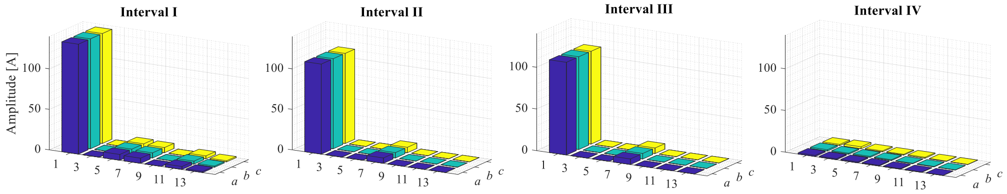

Figure 6.3: Harmonic spectrum of the PCC currents in Fig. 6.2.

currents mostly comprises the fundamental and 7th orders. It is also noticeable that the fundamental is reduced due to the reactive compensation.

In a comparative manner, considering the case in which an SCS approach is implemented for Interval II, the PF at PCC would not be unity (e.g., $PF = 0.982$ was obtained in a simulation result). However, since the proposed approach shapes the MG to synthesize a resistor, the PF at the PCC became 0.999. This indicates that mostly active power flowed through the PCC. Despite the fact that harmonic currents non-proportional to the voltages were compensated, it is reinforced that the RLS approach leads to distorted currents at the PCC. For this case, for instance, the THD_i is 6.29%, 6.28%, and 6.32%, respectively for phase a, b, and c. Besides, Fig. 6.3 shows that only the 7th harmonic order exists.

At Interval III, the dynamic response of such an advanced control strategy is demonstrated. At 0.6 s a load step occurs by suddenly switching off the circuit breakers CB_2 and CB_3, which connect the nonlinear loads in the buses *B16* and *B18* (see Fig. 3.1), respectively. Note in Fig. 6.2(c) that, despite the abrupt disconnection of the loads, the PCC currents promptly change, although neither overcurrent nor overvoltage occurred at the PCC and at d-DERs' PoCs. It is also noticeable that, since the GCBC is set to communicate with DERs each 20 ms, the shared currents started to be readjusted only after one fundamental cycle. Moreover, after two more cycles, steady state is reached, maintaining the features of the RLS approach. Thus, currents are still in-phase with voltages (see Fig. 6.2(c)), and mostly harmonics proportional to the voltages exist. Fig. 6.3 reaffirms that only the 7th order remained at the PCC.

For the last scenario (i.e., Interval IV), the active sharing capability under distorted voltages is presented, having the results shown in Fig. 6.2(a). At 0.9 GCBC is set to control the active current dispatch at the PCC, while also compensating for reactive and harmonic currents. The results show that the GCBC is capable of supporting such a functionality, quickly adjusting the current injections of d-DERs to process active, reactive, and harmonic components. From Fig. 6.3 it is seen that all current terms are practically null at the PCC. Note that, if the most significant current terms flowing through the PCC are shared by the d-DERs, the MG operates (i.e., in steady state) under full self-consumption mode.

Such self-consumption service is commercially found in the local controllers of d-DERs. Besides, it is deemed important since it supports optimized electricity planning of LV grids [44]. However, it can be noticed from the previous discussions that, in this thesis, the concept is expanded to the MG perspective, not only considering active power control, but also providing controllability over reactive and harmonic components.

6.2.3 Support to Harmonic Resonance Damping

Discussions related to the capability of the RLS-based coordinated control on supporting the damping of harmonic resonances are presented in this section. For the following simulation results, a hypothetical resonant load was added to the MG circuit of Fig. 3.1, aiming at emulating harmonic resonances. Such a load was comprised of a line impedance segment and a delta-formed capacitive bank connected to the PCC, as shown in Fig. 6.4.

In LV grids, this type of passive compensator is usually placed close to the DST (i.e., at the PCC) to support voltage regulation, as well as for reactive power compensation [186]. Nonetheless, the interactions of this capacitive filter with line impedances and nonlinear loads may deteriorate voltage quality if resonances are triggered. To demonstrate that, during simulations, only a small amount of 1% of the 7^{th} harmonic order was added to the original sinusoidal grid voltages. Thus, simulation results are presented in Figs. 6.5 and 6.6, and in Table 6.1.

At Interval I in Fig. 6.5(a), and also in Fig. 6.5(b), the outcome of the harmonic resonances caused by the interactions within the MG is demonstrated. The three d-DERs were disabled at this instant. It is seen that PCC voltages became significantly distorted, with much higher THD_{v} value than the 1% of harmonic pollution initially inserted at the grid voltages. Table 6.1 shows that the THD_{v} increased from about 1% to approximately 5% at the PCC due to the resonances. Moreover, even though mainly the 7^{th} order existed in voltages at the secondary side of the DST (i.e., the MG side), a significant amount of the 5^{th}, 7^{th}, 11^{th} and 13^{th} harmonics were also excited at the PCC voltages (see Table 6.1). In Fig. 6.6(a), the DST and PCC voltages are visually compared, showing the detrimental effects of the triggered resonances. Fig. 6.5(b) also shows that the PCC currents were both phase-shifted and distorted (i.e., comprising harmonics non-proportional to the voltages).

For the second interval in Fig. 6.5(a), the GCBC strategy was enabled at 0.3 s, demanding the d-DERs to share the reactive and harmonic currents seen at the PCC, following the RLS approach. By having inverters sharing non-proportional harmonic currents, the PCC voltages started to respond to the changes in current demand, without causing overvoltages. Similarly, the PCC currents did not suffer transient overcurrents. Note that, as the PCC voltages dynamically changed due to the effects of the distributed compensation, the GCBC kept on adjusting the current sharing, until steady state was obtained after about 0.4 s. As a result, in steady state, the currents became proportional to the voltage waveforms (see Fig. 6.5(c)), increasing the damping capability of the MG due to the resistive shaping [157].

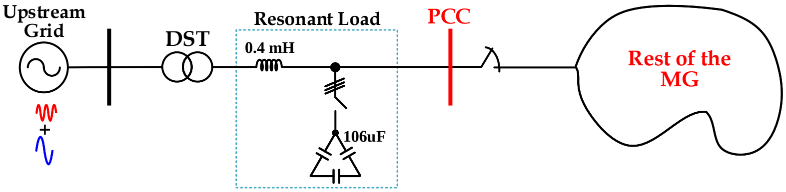

Figure 6.4: Placement of the resonant load at the MG of Fig. 3.1 used for simulations.

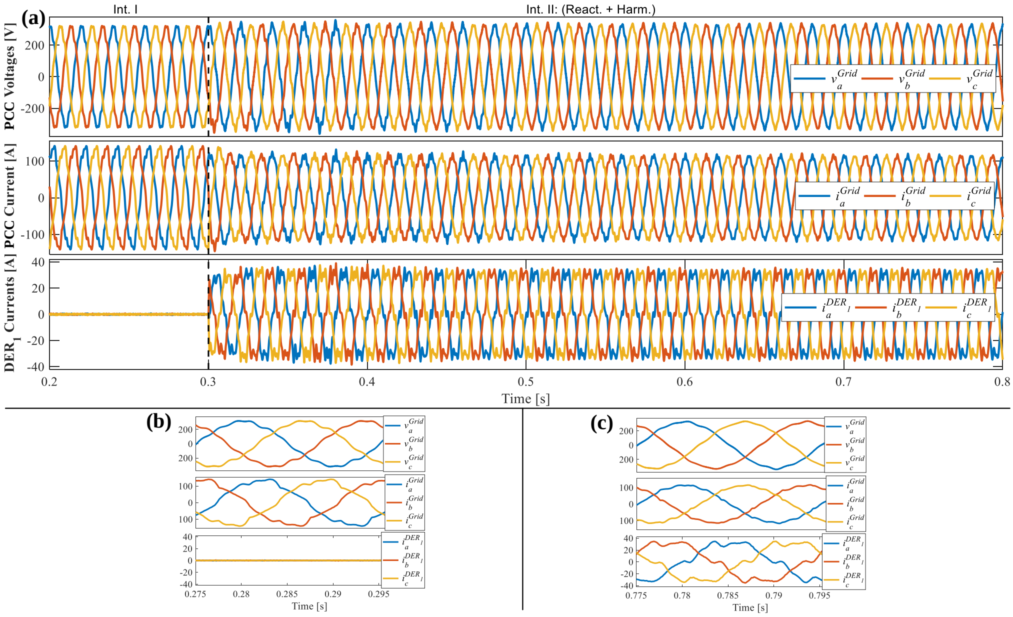

Figure 6.5: Simulation results of the RLS-based coordination for resonance damping. (a) From top to bottom: PCC voltages and currents, and d-DER$_1$ currents; (b) Zoom-in-view of Interval I; (c) Zoom-in-view of Interval II.

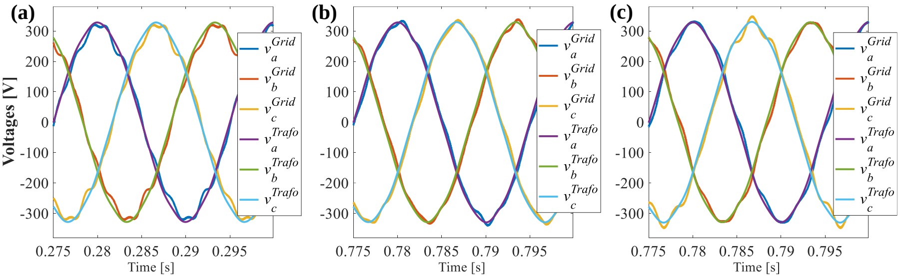

Figure 6.6: Voltages at the DST and at the PCC in Fig. 6.5 during: (a) Interval I; (b) Interval II - RLS; (c) Interval II - SCS.

The direct consequence of shaping the MG as a selective resistor is that most of the harmonic resonances could be suppressed, as seen in Table 6.1. Note that a considerable amount of the 5th, 11th and 13th harmonic distortions were damped. Moreover, the fundamental component was restored to 99% of its nominal value. For instance, for phase *a*, the voltage amplitude was 324.31 V, in comparison to 325.59 V at the secondary side of the DST. Fig. 6.6(b) shows that the PCC voltage waveforms became more similar to the ones from the DST. A THD$_\text{v}$ of approximately 2.5% was obtained for the PCC phase voltages, representing a significant improvement in relation to the previous 5% value. It is important to highlight that the coordination approach based

Table 6.1: Voltage amplitudes and THD_v for the PCC and secondary side of the MG DST for the simulation results of the resonance damping.

	Phase	***a***	***b***	***c***	***a***	***b***	***c***
	Harm.	**DST Voltages**			**PCC Voltages**		
Voltage [V]	**1**	325.59	325.58	325.58	312.54	312.54	312.54
	3	0.01	0.01	0.02	0.01	0.02	0.02
	5	0.04	0.03	0.03	9.54	9.54	9.53
	7	3.40	3.38	3.39	5.59	5.63	5.55
	9	0.05	0.08	0.12	0.27	0.08	0.22
	11	0.15	0.16	0.18	10.71	10.67	10.75
	13	0.05	0.08	0.10	1.44	1.46	1.47
	THD_v [%]	1.05	1.04	1.05	4.96	4.96	4.97
	Harm.	**PCC Voltages - RLS**			**PCC Voltages - SCS**		
Voltage [V]	**1**	324.31	324.22	324.26	324.70	324.53	324.86
	3	0.14	0.20	0.29	0.39	0.33	0.63
	5	0.50	0.43	0.42	0.79	0.18	0.62
	7	6.75	6.61	6.82	11.37	11.0	10.26
	9	0.62	0.99	1.61	6.06	6.64	12.64
	11	1.82	1.92	2.13	0.93	1.46	1.0
	13	0.54	0.84	1.10	0.41	0.65	0.96
	THD_v [%]	2.47	2.44	2.53	4.02	4.02	5.06

on RLS aims to compensate unwanted current components, supporting the damping of harmonic resonances in voltages as a direct consequence. Since the voltage distortions are being imposed by the upstream grid, if a harmonic-free scenario is desired for both currents and voltages, an active compensator ought to be placed at the MG PCC [187].

Finally, a quantitative comparison of the proposed RLS-based coordination against to the SCS concept is presented. A complementary simulation was performed, just as done in Fig. 6.5, but setting the GCBC strategy to share harmonic currents considering the terms proportional and non-proportional to the voltages. By striving to obtain sinusoidal currents upon the same scenario, the suppression of voltage harmonic distortions was minimized. For instance, note in Table 6.1 that, although the 5th and 11th and 13th orders were reduced in relation to the initial PCC stage (i.e., respectively by about 91%, 86%, and 71%), the 7th order was about 82% higher than for the RLS scenario. Yet, additional distortions at the 9th order were significantly triggered.

Thus, this result proves that the SCS approach was less effective than the RLS method in terms of damping of harmonic resonances. Fig. 6.6(c) also demonstrates that voltages were more distorted for the SCS scenario, presenting THD_v of 4.02% for phase *a* and *b*, and of 5% for phase *c* (see Table 6.1). Consequently, the RLS approach improved the damping capability, compared to SCS, by around 38%, 39% and 50%, respectively for phases a, b, and c, considering the THD_v as the figure of merit.

6.2.4 Experimental Results of the RLS-Based Coordination

Experiments are herein presented to validate the capability of the GCBC strategy to provide RLS-based coordination of inverters. In so doing, the main single-phase MG prototype of Section 4.2.2 is considered (see Fig. 4.2), having all loads drawing currents, and only $\text{d-DER}_1^\star$ and $\text{d-DER}_2^\star$ connected to the circuit. Experimental results are presented in Fig. 6.7, considering two main scenarios. In the first scenario, the grid voltage was set to 127 V_rms (i.e., fundamental) at 60 Hz, with additional 15% of the 5th harmonic (i.e., 19 V_rms). For the second scenario, the 15% voltage distortion was changed from the 5th to the 3rd harmonic order.

The initial stage of the experiment is seen in Fig. 6.7(a), depicting the PCC voltage and currents, considering that the two d-DERs* were idling (i.e., not processing currents). From this result, it is evident that the currents presented distortions non-proportional to the voltages. The active and reactive power terms (i.e., once again calculated as in [45]), and the amplitudes of the harmonics of the PCC currents are presented in Table 6.2. Such results demonstrate that the MG operated under low PF, regardless of the grid voltage presenting distortions at the 3rd or 5th harmonic orders. For instance, note in Table 6.2 that the PF was around 0.60 for both voltage scenarios, and that current harmonics at the PCC were more significant for the 3rd and 5th orders.

In Fig. 6.7(b) another experimental result is presented. This case shows the MG operation when the GCBC strategy was enabled, allowing d-DERs* to share the reactive and targeted harmonic currents non-proportional to the PCC voltage. Note that the strategy was able to steer the inverters in proportion to their nominal ratings. For instance, $\text{d-DER}_1^\star$ processed 4.5 A_rms and d-DER_2 6.1 A_rms, which gives $r_{dDERs^\star} = 1.35$, matching the expected proportion of 1.33. As a result, the PCC

Table 6.2: Currents and powers at the PCC during experimental results of Fig. 6.7.

	Harm. Order	**DERs Off - Fig. 6.7(a)**		**Fig.**			
		Dist. at 5th	**Dist. at 3rd**	**6.7(b)**	**6.7(c)**	**6.7(f)**	**6.7(g)**
Current [A_rms]	**1**	12.1	12.0	8.54	8.66	7.88	0.42
	3	2.78	1.32	0.15	0.08	1.16	0.15
	5	1.17	0.62	1.31	1.32	0.05	0.05
	7	0.15	0.27	0.17	0.11	0.26	0.11
	9	0.13	0.15	0.09	0.07	0.15	0.14
	***P* [W]**	940	911	1064	1086	988	-55
	***Q* [VAR]**	1122	1095	-1	9	6	-15
	PF	0.62	0.63	0.99	0.99	0.99	0.0

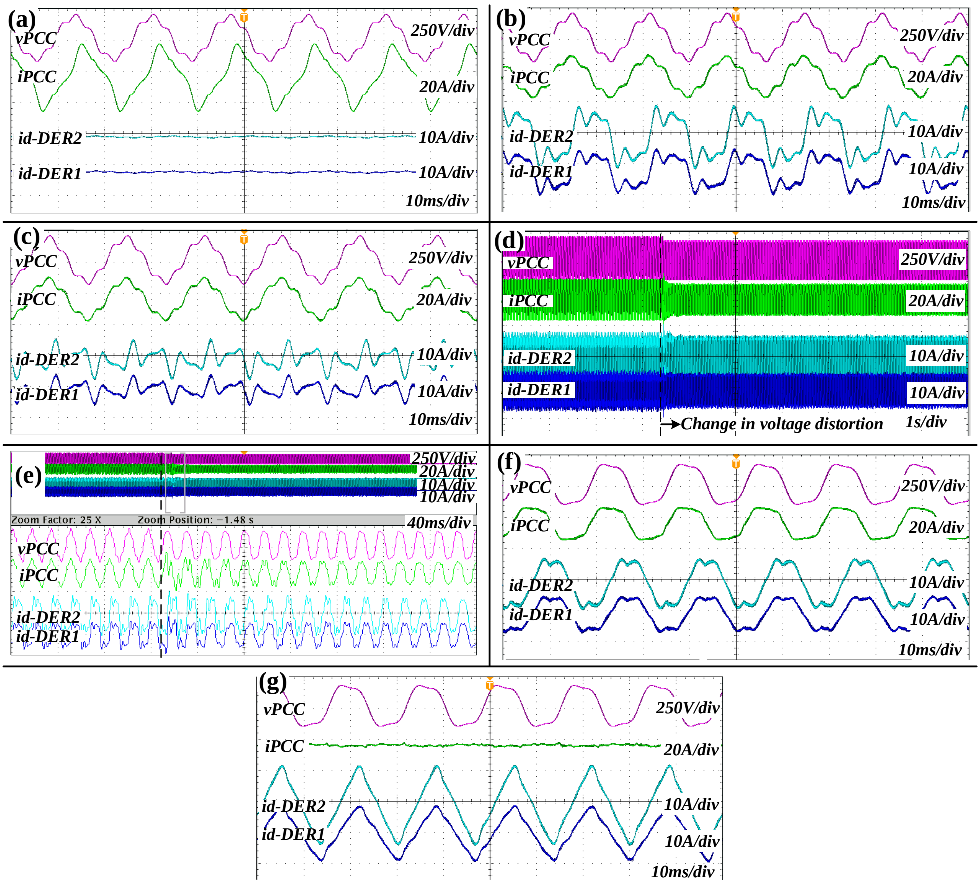

Figure 6.7: Experimental results of the RLS-based coordination of inverters in a single-phase MG operating under distorted voltages. (a) d-DERs* disabled; (b) d-DERs* performing the RLS functionality; (c) load step in (b); (d) change in voltage distortion from 5th to 3rd harmonic order; (e) zoom-in-view of (d); (f) steady state result of (e); and (g) full current sharing. From top to bottom: PCC voltage and current, d-DER$_2^\star$ and d-DER$_1^\star$ currents.

current became proportional to the PCC voltage, indicating operation under high PF (i.e., 0.99, see Table 6.2). A complementary case is demonstrated in Fig. 6.7(c), in which the inductive load L_2 was switched off by CB_{L2}. It can be seen that the compensation performance of the non-proportional current harmonics remained similar to the previous case, presenting $r_{dDERs} = 1.32$, and maintaining high PF operation.

During another experiment shown in Figs 6.7(d) and 6.7(e), considering that the load L_2 was switched on, a dynamic change in the voltage distortion was emulated. The grid emulator was set to present the 3rd harmonic order in the voltage, instead of the 5th. Note in Fig. 6.7(d) that the changes in voltage and current waveforms (i.e., at the PCC and at d-DERs*) occurred without causing any overvoltage or overcurrent. The zoom-in-view for this transition, seen in Fig. 6.7(e), shows that the two inverters were able to reach steady state operation after a few cycles (i.e., around 14 cycles). This occurred due to the dynamics of the calculations of the GCBC algorithm, of the RMS calculation required for Eq. 6.1, and also due to the transient response of the current controllers.

The steady state result comprising this new distortion in voltages is shown in Fig. 6.7(f), where it is clearly seen that the strategy was able to shape the MG PCC to emulate a resistor. The PCC current presented proportional distortions to the voltage, being primarily composed of the 3rd harmonic order. This feature is also evident in Table 6.2, where a significant amplitude at the 3rd harmonic order can be observed. As a result of the RLS operation, a $PF = 0.99$ was achieved, while d-DERs* presented ratio of $r_{dDERs} = 1.36$, ensuring proportional current sharing.

A final experiment is shown in Fig. 6.7(g) to verify the capability to share active currents under highly distorted voltages. Thus, the active, reactive, and harmonic (proportional and non-proportional) currents are set as references. Note that DERs were able to proportionally (i.e., $r_{DERs} = 1.32$) inject the load currents, resulting in a practically null current at PCC in steady state (see Table 6.2). Such a result reinforces the idea that MG full self-consumption mode can be offered regardless of distortions in the grid voltage.

6.3 Coordinated Overvoltage Control Fully Exploiting Energy Resources

Intense penetration of decentralized active power generation is known to commonly lead to overvoltage conditions, both for MGs and distribution networks [192, 193]. This is particularly noticeable at terminal feeders of radial electric systems, due to consecutive voltage drops over line impedances. Such a matter of voltage regulation is highly important, to the point of motivating new operation requirements for inverters, demanding them to offer grid-support ancillary services, as found in standards such as the IEEE 1547-2018 [8], and others [194].

Control functionalities for Volt/Watt and Volt/VAR support, also called active and reactive power control, respectively, are two of the most common examples of how inverters should respond to voltage regulation in active distribution systems or MGs. Nonetheless, although effective and fairly easily implemented, the capability to offer non-coordinated Volt/Watt and Volt/VAR functionalities by each inverter is usually tied to active power curtailment (APC) at nd-DERs [192]. Consequently, APC leads to reduced energy efficiency, also bringing lower profitability from the prosumers' perspective, as part of the generated power is usually disposed of.

In the literature, many strategies aim to provide overvoltage control in LV grids and MGs [80]. For instance, overvoltage regulation and minimization of power losses is proposed in [195] by using a Volt/VAR control that is adaptively adjusted according to voltage levels. In addition, fair APC devised by the identification of voltage patterns is considered as a secondary countermeasure when DERs' generation is high. The concept of fair APC, as in [195], is studied to balance power curtailment among DERs, given their different locations in a MG, and their significance for impairing steady voltage profiles.

The authors of [196] present a distributed method to increase the penetration of PV-based inverters by combining Volt/Watt and Volt/VAR control with smooth droop functions. The location of DERs and their distance from the distribution transformer determine if an operation occurs with a power factor close to unity or limited to ± 0.90. Thus, [196] is a model-based approach that requires information on line impedances and distances between nodes. Likewise, robust optimization is applied in [197] to attain proportional Volt/VAR and Volt/Watt coefficients to drive droop-based nd-DERs, considering their location, load placements and power injections.

A multi-objective genetic algorithm is used in [198] to provide coordinated Volt/VAR control of nd-DERs, also increasing the participation in the reactive power support of inverters close to the distribution transformer (i.e., the DST). This is an interesting feature since DERs close to such a transformer tend to not contribute to voltage regulation when local Volt/Watt or Volt/VAR control are implemented [198]. The authors of [199] adopt multi-objective optimization, along with the concept of sensitivity matrix, to steer droop-based DERs. The goal in [199] is to minimize APC and control the reactive power absorption of nd-DERs to tackle overvoltage in a grid-connected MG. It uses a hierarchical scheme in which the primary layer locally regulates droop curves according to voltage setpoints given by the secondary layer.

A master/slave approach is presented in [200] to steer DERs to achieve voltage regulation based on active power control and offering controlled power flow dispatchability at the PCC of the LV MG. Such an approach uses a model-free concept that does not require information about the electrical infrastructure and provides voltage control by adjusting the active power injection of inverters based on their output voltage and on commands from a centralized controller. However, reactive power control is not considered in [200]. Finally, active power limit prediction is proposed in [201] to overcome overvoltage using dynamic computations of Thévenin equivalent circuits of the MG. Although the self-adaptive power/voltage control slopes devised lead to maximized energy production, in relation to pure local Volt/Watt strategies, APC is not prevented.

6.3.1 Overvoltage Control Integrated to the GCBC Strategy

Considering the above-mentioned aspects found in the literature, in this thesis, an automatic overvoltage control approach is presented, considering integration with the GCBC strategy. Such a strategy is able to coordinate DERs to offer Volt/VAR and Volt/Watt functions that strive for voltage regulation, ensuring reduced APC. The previous attractiveness of the GCBC strategy remains valid, making the approach model-free. Moreover, the control approach is able to accommodate DERs that do not comprise a communication interface and operate only based on local measurements.

The strategy is superior to the implementation of Volt/Watt and Volt/VAR curves used only locally at DERs, since it can reduce APC and equalize the participation of d-DERs. Consequently, it can be interpreted as an advanced control functionality offered by the MG. This control scheme integrates local and coordinated features of DERs, depending on their nature of operation. A detailed explanation about how both nd- and d-DERs are steered is presented as follows, and will later be complemented by explanations about the proposed automatic overvoltage control scheme.

6.3.1.1 Control of nd-DERs During Voltage Regulation

The role of nd-DERs is herein explained for both categories (i.e., types A and B explained in Section 3.3). For type A nd-DERs, the absence of communication interface determines that Volt/Watt and Volt/VAR curves coming as default functionalities are only activated based on local goals. However, for type B nd-DERs, communication means allow the MGCC to remotely activate their built-in Volt/Watt and Volt/VAR [8] actions when desired.

Let us now consider the variable γ_{OV}^{nd-DER}, which is sent by the MGCC to each type B nd-DER (see Fig. 6.8). Such a variable represents the above-mentioned remote command for activating voltage control curves. Moreover, a premise for using γ_{OV}^{nd-DER} is that the MGCC knows the voltage status of the respective nd-DERs. Thus, to cope with that perspective, one additional piece of information is incorporated

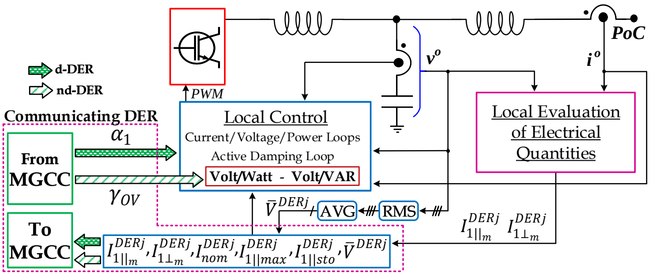

Figure 6.8: Single-phase equivalent circuit for the local control of nd- or d-DERs considering voltage control capabilities.

to data packets being exchanged among communicating entities. This is the average (AVG) value of the three-phase RMS PoC voltages of a j-th DER [8], namely $\bar{V}^{DER_j}$. For single-phase MGs, $\bar{V}^{DER_j}$ is simply the RMS PoC voltage of that inverter.

The variable γ_{OV}^{nd-DER} is responsible for determining which of the local voltage control curves is enabled, if needed. Thus, under the occurrence of overvoltage at the PoC of a type B nd-DER, the MGCC remotely sets either $\gamma_{OV}^{nd-DER} = 1$ to activate the inverter's Volt/Watt action, or $\gamma_{OV}^{nd-DER} = 2$ for Volt/VAR. The Volt/Watt and Volt/VAR splines, presented in Fig. 6.9, are only locally implemented at each nd-DER, and if $\gamma_{OV}^{nd-DER} = 0$, both are disabled. For type A nd-DERs, it is herein considered that only local Volt/Watt control is activated at all times, resulting in the fact that $\gamma_{OV}^{nd-DER} = 1$ is always set, also following the active power control spline from Fig. 6.9.

The Volt/Watt and Volt/VAR splines in Fig. 6.9 mitigate overvoltage as follows [202]. If the local voltage of an nd-DER exceeds the voltage limit ($\bar{V}^{lim}$), the active power injection performed by that inverter is adjusted to constrain the voltage rise. For type A nd-DERs, since Volt/Watt control is always set as default and no remote intervention is possible, local APC must inherently take place under overvoltage. Thus, that nd-DER must reduce its active power injection to avoid the voltages exceeding $\bar{V}^{lim}$. For cases in which voltage exceeds a critical limit, namely $\bar{V}^{lim}_{upper}$, inverters may end up curtailing all, or most of, its generated active power.

Nonetheless, type B nd-DERs act differently. For that case, the MGCC knows if an nd-DER operates aiming to inject active power at nominal capacity (i.e., $P_{max}^{nd-DER_j} = P_{nom}^{nd-DER_j}$) or not. Such a feature is known, as each inverter periodically transmits its local currents to the MGCC (e.g., $I_{1||max}^{nd-DER_j}$, $I_{1||nom}^{nd-DER_j}$, so forth). In case full active power injection is intended, Volt/VAR cannot be offered. This is only possible if an nd-DER is designed with additional power margins for specific use in voltage regulation purposes [203] (i.e., $P_{max}^{nd-DER_j} < P_{nom}^{nd-DER_j}$ is always true). Thus, for this case, Volt/Watt must be set by stating $\gamma_{OV}^{nd-DER} = 1$, inherently causing local APC.

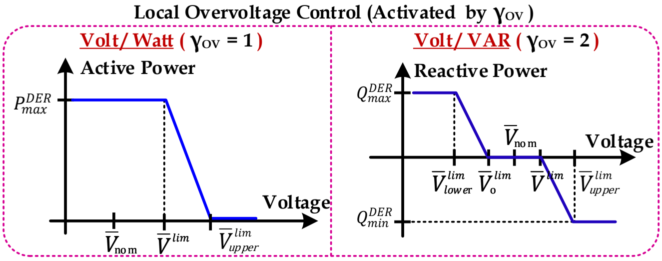

Figure 6.9: Volt/Watt and Volt/VAR splines for the local voltage control at nd-DERs.

On the other hand, if remaining power capability is available for nd-DERs suffering overvoltage, the status of the variable γ_{OV}^{nd-DER} is changed to 2 by the MGCC, so Volt/VAR control can be enabled. This allows us to use reactive control as first measure, consequently avoiding APC. Hence, such inverters can slide in reactive power curves, as seen in Fig. 6.9, in which deadbands may or may not exist around the nominal voltage ($\bar{V}_{nom}$). The reactive power processed by each type B nd-DER is limited to $Q_{max}^{DER_j}$ and $Q_{min}^{DER_j}$, according to their remaining power capabilities.

If nd-DERs can tackle overvoltage locally without causing APC, as it occurs for the aforementioned reactive power splines, higher penetration of distributed generation can be achieved for the MG. Unfortunately, in general, voltage rise is most critical during the peak hours of energy generation [201], meaning that remaining power capability is usually not available for nd-DERs to perform Volt/VAR control.

6.3.1.2 Control of d-DERs During Voltage Regulation

The employment of d-DERs on voltage control is supported by the GCBC strategy, relying on the fact that active and reactive power dispatchability at the MG PCC can be flexibly controlled. The power flow at the PCC can be incorporated into coordinated Volt/VAR or Volt/Watt curves, while accounting for the MG's internal voltage conditions. Thus, the GCBC formulation from Section 3.5.2 can be slightly adapted to extend the MG functionalities to offer voltage regulation.

Let us consider that a control cycle "k" starts at a given instant, allowing the MGCC to assess the overall condition of the MG, by means of the data packets received from the participating DERs. If any voltage measurement (i.e., from DERs: $\bar{V}^{DER_j}$; or from the PCC: $\bar{V}^{PCC}$) is above $\bar{V}^{lim}$, the overvoltage status is activated for the MG. Therefore, the MGCC has two main possibilities to deploy d-DERs to tackle overvoltages under a coordinated approach: *i)* to provide reactive power dispatch through the PCC (i.e., coordinated Volt/VAR); or *ii)* to either reduce active current injection, or to store the energy being injected by nd-DERs (i.e., coordinated Volt/Watt).

To provide such coordinated actions, the references for the reactive and active currents flowing through the PCC (i.e., $I_{1\perp_m}^{Grid*}$ and $I_{1||_m}^{Grid*}$) are used, respectively. Under the detection of any overvoltage condition, the GCBC is processed following the same initial steps explained in Section 3.5.2, up to the calculation of $I_{1||_m}^{L}(k)$ and $I_{1\perp_m}^{L}(k)$ in Eqs. 3.9 and 3.10, respectively. However, the proceeding calculation given by Eqs. 3.15 and 3.16, which would allow us to determine $I_{1||_m}^{*}(k+1)$ and $I_{1\perp_m}^{*}(k+1)$, is postponed. This is done to adequately select values for $I_{1||_m}^{Grid*}$, or for $I_{1\perp_m}^{Grid*}$, so the expected coordinated Volt/Watt, or Volt/VAR, actions can be performed, respectively.

Upon overvoltage detection, the active and reactive current control curves shown in Fig. 6.10 can be adopted to adjust the power dispatch at the PCC. Note that such

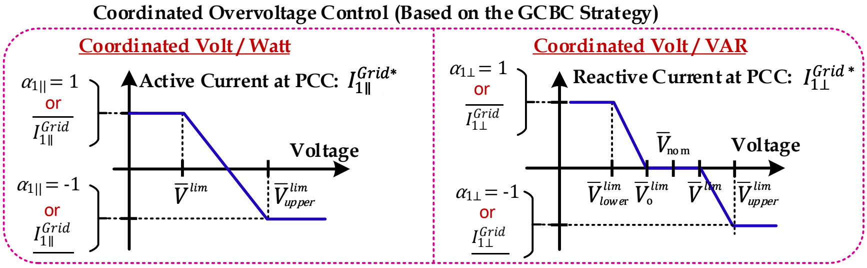

Figure 6.10: Volt/Watt and Volt/VAR splines for the coordinated voltage control at d-DERs.

curves are similar to the ones from Fig. 6.9. However, the coordinated perspective for the Volt/Watt, or Volt/VAR, actions allow the d-DERs to act concomitantly on a common goal. Thus, due to the homogeneity of the MG, the voltage profiles at each node of the MG can all be controlled together. This allows us to achieve voltage regulation without performing only local Volt/Watt or Volt/VAR control. Consequently, the method ensures that all DERs participating of the GCBC strategy contribute to maintaining voltage profiles within established limits. Additionally, in contrast to strategies such as [198], all inverters contribute to voltage regulation, even if they are placed close to the DST of the MG and do not suffer from overvoltage.

If coordinated Volt/Watt is desired, the active current term $I_{1||_m}^{Grid*}$ is iteratively adjusted by Eq. 6.3. Likewise, $I_{1\perp_m}^{Grid*}$ can be adjusted by Eq. 6.4 to provide coordinated Volt/VAR. The variables $\delta_{1||_m}$ and $\delta_{1\perp_m}$ are set as constants, ranging from 0 to 1, to regulate the steps of, respectively, the active and reactive currents dispatched at the PCC at each control cycle "k + 1". Moreover, note that such constants are multiplied by $\sqrt{\Delta I_m}$ to make sure that at each adjustment of $I_{1||_m}^{Grid*}$ or $I_{1\perp_m}^{Grid*}$ occurs proportionally to the current capabilities of the participating inverters.

$$I_{1||_m}^{Grid*}(k+1) = I_{1||_m}^{Grid*}(k) + \delta_{1||_m} \cdot \sqrt{\Delta I_m} \tag{6.3}$$

$$I_{1\perp_m}^{Grid*}(k+1) = I_{1\perp_m}^{Grid*}(k) + \delta_{1\perp_m} \cdot \sqrt{\Delta I_m} \tag{6.4}$$

It is also worth reinforcing that such active and reactive power dispatchability at the PCC is, however, constrained to upper ($\overline{I_{1||_m}^{Grid}}$ and $\overline{I_{1\perp_m}^{Grid}}$) and lower ($\underline{I_{1||_m}^{Grid}}$ and $\underline{I_{1\perp_m}^{Grid}}$) limits given by contractual relations between the MG and upstream grid. Hence, the MG cannot freely dispatch/absorb power as desired by its operational manager, being also constrained by the d-DERs power capabilities.

Thus, in possession of the adequate active or reactive current dispatch references that will support coordinated Volt/Watt or Volt/VAR, respectively, the GCBC algorithm can proceed with the calculations, just as in Section 3.5.2. This means that Eq. 6.3 and Eq. 6.4 are used to feed Eqs. 3.15 and 3.16, respectively. This consequently results in the current sharing references of $I_{h||_m}^{*}(k+1)$ and $I_{h\perp_m}^{*}(k+1)$, which now incorporate the voltage control feature to the steering of d-DERs. Additionally, such a procedure allows the possibility to maintain all the previous features of the GCBC strategy described throughout this thesis (e.g., model-free aspect and plug-and-play capabilities).

From the aforementioned discussions, one can note that such coordinated Volt/Watt or Volt/VAR control is incorporated within the scaling coefficients $\alpha_{1||}$ and $\alpha_{1\perp}$, which does not change how inverters are steered. This is also visible in Fig. 6.8, as the control structure of d-DERs does not change, not even requiring the implementation of voltage control curves locally, as conducted for the nd-DERs. The control approach for d-DERs is entirely processed at the MGCC. Finally, it is mentioned that coordinated Volt/Watt and Volt/VAR control can be performed independently, also being implementable at the same time, if desired by the MGCC. Nonetheless, an automatic scheme presented in the following section brings a proposal to integrate nd- and d-DERs to tackle overvoltages while offering reduced APC.

6.3.1.3 Automatic Overvoltage Control Scheme

The scheme of the proposed automatic control is summarized in Fig. 6.11. The main concept behind this approach is to use the local and coordinated Volt/VAR features of nd- and d-DERs, respectively, in such a way that reactive power control takes precedence over APC whenever possible. It is reinforced that this scheme is not applicable to type A nd-DERs, as they do not present a communication interface. Nevertheless, such approach indirectly affects their nodal operation, reducing local APC.

Let us refer to Fig. 6.11 to explain the control scheme, which is only processed at the MGCC at the beginning of a control cycle "*k*". As all communicating inverters transmit $\bar{V}^{DER_j}$, when an overvoltage condition occurs, the MGCC knows which *j*-th DER requires intervention. Thus, if this is a type B nd-DER that is not injecting active power at nominal rating, local Volt/VAR control is first enabled by setting $\gamma_{OV}^{nd-DER} = 2$. This is done instead of local Volt/Watt control (i.e, $\gamma_{OV}^{nd-DER} = 1$) to avoid APC. Usually, after setting $\gamma_{OV}^{nd-DER} = 2$ to any nd-DER, a wait time of t_{wait} is implemented to consider steady state accommodation before moving onto the next possible action in Fig. 6.11. t_{wait} should be set according to the MG's needs (i.e., as for safety and stability reasons) or based on grid codes [194].

Hence, if the local Volt/VAR control of an nd-DER is either not enabled or not capable of solving the overvoltage issue, d-DERs are deployed to iteratively increase the dispatch of reactive power through the PCC, according to Eq. 6.4, and based on the GCBC strategy. This results in the coordinated Volt/VAR control seen in Fig. 6.10. In the case of reaching either the maximum reactive (i.e., inductive) current allowed to flow through the upstream grid ($\underline{I_{1\perp_m}^{Grid}}$) or the overall power capability of d-DERs (i.e., resulting in $\alpha_{1\perp_m} = 1$), such coordinated Volt/VAR feature is constrained.

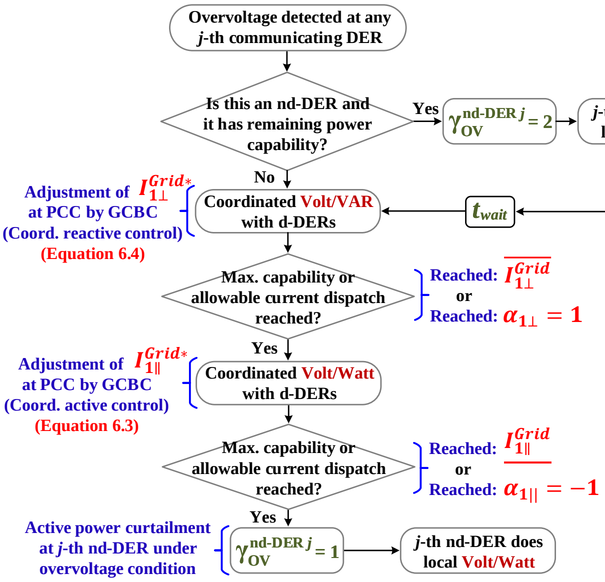

Figure 6.11: Proposed scheme for automatic overvoltage control running at the MGCC.

Although Volt/VAR control is effective, it is known that Volt/Watt control is more efficient at mitigating overvoltage in LV MGs [200], due to the low *X/R* ratio of line impedances. Hence, when Volt/VAR cannot be further processed, and the overvoltage issue has not been solved, the scheme in Fig. 6.11 enables Volt/Watt action by controlling $I_{1||m}^{Grid*}$ based on Eq. 6.3. This action can occur until: *i)* full SoC is reached (i.e., $I_{1||stom}^{DERt} = 0$; e.g., for battery-based DERs); or *ii)* the power dispatch limit ($\underline{I_{1||m}^{Grid}}$) is reached; or *iii)* overvoltage is mitigated.

Note that, up to this stage in Fig. 6.11, APC does not occur at type B nd-DERs. Moreover, the scheme automatically induces type A nd-DERs to reduce local APC according to the lowering of the overall MG voltage profile. Finally, in case none of the previous actions can maintain voltage profiles below the established limit ($\bar{V}^{lim}$), active power can be locally curtailed at type B nd-DERs. This is achieved by setting $\gamma_{OV}^{nd-DER} = 1$ for them.

6.3.2 Simulation Results

To study the effectiveness of the proposed automatic control scheme on mitigating overvoltages in LV MGs, the simulation results will now be presented. The testbench of Fig. 3.1, which had its parameters discussed in Section 4.2.1, is adopted for simulations, considering that all loads are disconnected from the MG. Loads are disregarded to allow the active power injections from nd-DERs to cause significant overvoltage conditions within the MG.

All eight DERs are considered for simulations, although particularly for this section, d-DER$_2$ does not participate in the GCBC and operates only injecting active power as a type A non-dispatchable inverter. This is done to more easily depict overvoltage conditions within the MG. Thus, the simulations consider six non-dispatchable units (i.e., nd-DER$_1$ to nd-DER$_5$, as well as d-DER$_2$), plus two dispatchable units (i.e., d-DER$_1$ and d-DER$_3$) controlled by the GCBC strategy. All non-dispatchable inverters present the Volt/Watt curve from Fig. 6.9 activated as default (i.e., $\gamma_{OV}^{nd-DER} = 1$). Moreover, since nd-DER$_1$, nd-DER$_2$ and d-DER$_2$ emulate type A inverters, they only consider $\gamma_{OV}^{nd-DER} = 1$ at all times.

Data exchange between the MGCC and communicating DERs is emulated to occur once per line period (i.e., 20 ms). Moreover, t_{wait} is 0.2 s (i.e., 10 fundamental cycles), and the upper threshold that characterizes overvoltage is set to $\bar{V}^{lim} = 243.8$ V. The contractual current dispatch limits at the MG PCC are initially set to $\overline{I_{1||_m}^{Grid}} = \overline{I_{1\perp_m}^{Grid}} = 200$ A and $\underline{I_{1||_m}^{Grid}} = \underline{I_{\perp_m}^{Grid}} = -200$ A. Yet, a current step of 4% is considered for Eqs. 6.3 and 6.4 (i.e., $\delta_{1||_m} = \delta_{1\perp_m} = 0.04$). The additional parameters adopted for the Volt/Watt and Volt/VAR curves, according to Fig. 6.9, were $\bar{V}_{upper}^{lim} = 253$ V, $\bar{V}_{o}^{lim} = 230$ V, and $\bar{V}_{lower}^{lim} = 220$ V.

The simulations consider three main scenarios. The first scenario demonstrates how the strategy operates when non-dispatchable inverters are injecting active power at nominal capacity. For the second scenario, the reactive current dispatch limit ($\overline{I_{1\perp_m}^{Grid}}$) is reduced, demonstrating the concomitant coordinated Volt/VAR and Volt/Watt features of the strategy. Finally, the last scenario presents a brief comparison between the proposed method against pure local Volt/Watt and Volt/VAR control.

Initially, a preliminary result shows how the MG voltage profiles would behave if no overvoltage control was considered at all (i.e, $\gamma_{OV}^{nd-DER} = 0$ and $\alpha_{1||_m} = \alpha_{1\perp_m} = 0$). Such a result is presented in Fig. 6.12, and it comprises the following four intervals: *i)* at Interval I, all DERs were idle (i.e., not injecting currents); *ii)* at Interval II, nd-DER$_1$, nd-DER$_4$, nd-DER$_5$ and d-DER$_2$ were injecting nominal active power; *iii)* at Interval III, nd-DER$_2$ and nd-DER$_3$ also injected nominal active powers; and *iv)* at Interval IV, d-DER$_2$ abruptly interrupted active power injection. Moreover, d-DER$_1$ and d-DER$_3$ were idling during all intervals.

From such simulation results, it is clearly seen that, as DERs operated injecting active power at full capacity, most of the MG nodes operated with voltages significantly above $\bar{V}^{lim}$. For the worst case, which was during Interval III, the maximum voltage values reached approximately 251 V, which is significantly above the overvoltage threshold. Thus, the results indicate that voltage regulation strategies need to be considered for the management of the MG.

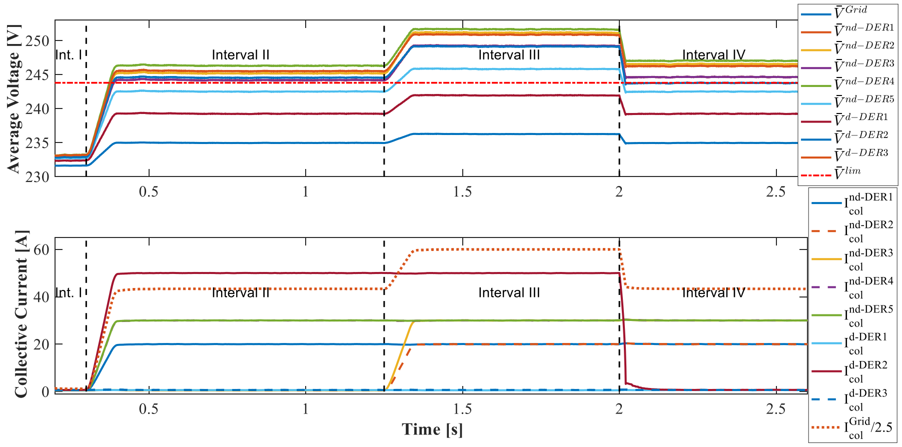

Figure 6.12: Simulation results: MG operation when all nd-DERs operate injecting power at full capacity and no overvoltage control is implemented. From top to bottom: Average voltages for the PCC ($\bar{V}^{Grid}$) and DERs ($\bar{V}^{DERj}$), and collective currents for DERs and the PCC (I_{col}^{Grid} is divided by 2.5).

6.3.2.1 Scenario 1: MG Operation with nd-DERs at Full Generation Capability

The results for this scenario are shown in Fig. 6.13 and in Table 6.3, considering the same previous four intervals depicted in Fig. 6.12. However, the proposed overvoltage control scheme is adopted herein for simulations. Thus, during Interval I in Fig. 6.13, all DERs were idling and the voltage profiles were steady and below $\bar{V}^{lim}$.

As some inverters (i.e, nd-DER$_1$, nd-DER$_4$, nd-DER$_5$, and d-DER$_2$) started to inject active power during Interval II, the voltages at certain MG nodes began to deviate, exceeding $\bar{V}^{lim}$. Consequently, nd-DER$_4$ and d-DER$_2$ started to curtail active power due to their default Volt/Watt control (i.e., see the patterns of I_{col} in Fig. 6.13, at the beginning of Interval II). Since such inverters intended to inject active power at full capability, the automatic control scheme of Fig. 6.11 could not assign $\gamma_{OV}^{nd-DER} = 2$ to allow local Volt/VAR control. Consequently, t_{wait} was not required, and the GCBC promptly strived for coordinating d-DER$_1$ and d-DER$_3$, aiming at dispatching inductive currents through the PCC to limit voltage rise.

From Fig. 6.13, one can observe that, since d-DER$_1$ and d-DER$_3$ had the same nominal capabilities, they proportionally shared reactive currents to force voltage profiles to be below $\bar{V}^{lim}$. Such an operation was initiated smoothly, without imposing abrupt current references for the d-DERs. Besides, no intervention was required for the nd-DERs. As a result, the steady state reactive powers processed by the two d-DERs were practically the same, as shown in Table 6.3, being around 7500 VAR. This result was expected, as d-DER$_1$ and d-DER$_3$ presented the same nominal capabilities.

Interval II shows additional consequences of the coordinated Volt/VAR performed

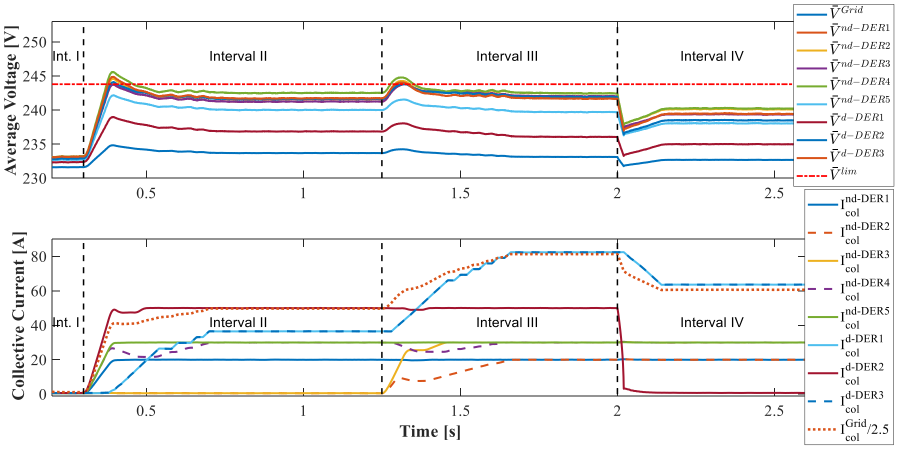

Figure 6.13: Simulation results for Scenario 1: MG operation considering nd-DERs at full capacity and with the proposed automatic overvoltage control enabled. From top to bottom: Average voltages for the PCC ($\bar{V}^{Grid}$) and DERs ($\bar{V}^{DERj}$), and collective currents for DERs and the PCC (I_{col}^{Grid} is divided by 2.5).

by the d-DERs. Since the reactive power dispatch through the PCC brought the MG voltages below $\bar{V}^{lim}$, the nd-DERs returned to nominal active power injection due to their local Volt/Watt control. This occurred because they sensed that their PoC voltages were within the acceptable range, allowing them to feed-in more power to the MG. From Table 6.3 it can be seen that practically null APC occurred, as nd-DERs injected P at nominal capacity. An inherent consequence of the coordinated voltage regulation, however, is that the MG losses over line impedances tend to increase, due to the higher power dispatch. For this interval, 1249 W was obtained for losses.

During Interval III in Fig. 6.13, as nd-DER$_2$ and nd-DER$_3$ were enabled to inject active power, their local Volt/Watt curves led them to suffer APC, due to voltage rises at their PoCs. Nonetheless, the automatic control sensed that the voltages were exceeding $\bar{V}^{lim}$, and the coordinated Volt/VAR action provided by d-DERs was adjusted by increasing the dispatch of reactive current through the PCC. Therefore, such an operation allowed the possibility to mitigate overvoltages, as well as to avoid APC at all nd-DERs (see in Table 6.3 that they injected nominal active power in steady state condition). Since nd-DERs were fully injecting P, and most of the nominal capabilities of the d-DERs were utilized for reactive current sharing, higher losses were naturally obtained, being 3348 W for this case.

For the last simulated case (i.e., Interval IV), an abrupt disconnection was emulated for d-DER$_2$, ceasing its active power injection. Since this inverter was the one with higher nominal capacity operating as a non-dispatchable unit, its impact in voltage rise was significant. This can be evidenced at the beginning of Interval IV in Fig. 6.13, by the abrupt voltage drops that occurred for all MG nodes. Thus, as d-DER$_2$ was

Table 6.3: Steady state results for Scenarios 1 and 2 in Figs. 6.13 and 6.14, respectively. Units: active power (P) [W], reactive power (Q) [VAR], collective currents (I_{col}) [A], average RMS voltage ($\bar{V}$) [V], and Losses [W].

	Scenario 1														Scenario 2			
	Int. I		**Interval II**				**Interval III**				**Interval IV**				**Interval III**			
	P ***Q***	$\bar{V}$	***P***	***Q***	I_{col}	$\bar{V}$	***P***	***Q***	I_{col}	$\bar{V}$	***P***	***Q***	I_{col}	$\bar{V}$	***P***	***Q***	I_{col}	$\bar{V}$
PCC	0	231	-51030	16120	149	233	-67180	26060	244	233	-48880	27320	182	232	-52830	24610	179	233
nd-DER$_1$	0	233	8324	0	20	241	8360	91	20	242	8283	87	20	239	8362	87	20	241
nd-DER$_2$	0	233	0	0	0	241	8392	88	20	242	8302	93	20	240	8351	81	20	242
nd-DER$_3$	0	233	0	0	0	241	12560	129	30	242	12430	129	30	239	12540	127	30	241
nd-DER$_4$	0	233	12580	131	30	242	12590	129	30	242	12440	128	30	240	12540	128	30	242
nd-DER$_5$	0	233	12430	125	30	240	12460	134	30	240	12360	121	30	238	12440	130	30	239
d-DER$_1$	0	232	318	7481	36	237	717	16840	82	236	544	12940	63	235	-9008	11450	60	235
d-DER$_2$	0	233	20890	209	50	242	223	20930	50	242	0	0	0	238	20890	210	50	241
d-DER$_3$	0	233	306	7621	36	242	733	17230	82	242	551	13190	63	239	-9211	11700	60	241
Losses	804		1249				3348				1903				2012			

disabled, the previous amount of reactive power dispatched by the MG was no longer required. Consequently, the automatic control scheme steered d-DERs to reduce injection of reactive currents, without letting voltages rise over $\bar{V}^{lim}$. This operation occurred in such a way that the APC was still not required by the nd-DERs.

6.3.2.2 Scenario 2: Constrained Reactive Power Dispatch

To show the concomitant provision of coordinated Volt/Watt and Volt/VAR functionalities, a more conservative reactive current dispatch limit was adopted, being $\overline{I_{1\perp_m}^{Grid}} = 100$ A. Simulation results are presented in Fig. 6.14 and in Table 6.3, considering the same four intervals from Scenario 1. The first two intervals in Fig. 6.14 present the same results as in Fig. 6.13, since the current dispatch limit $\overline{I_{1\perp_m}^{Grid}}$ was not achieved while mitigating overvoltages. For instance, the coordinated Volt/VAR action reached a reactive current dispatch of $\overline{I_{1\perp_m}^{Grid}} = 62.91$ A during Interval II.

During Interval III, as nd-DER$_2$ and nd-DER$_3$ were initiated to inject nominal active power, the automatic control increased the reactive current dispatch of the MG to limit voltage rise. However, since $\overline{I_{1\perp_m}^{Grid}} = 100$ A was adopted, the coordinated Volt/VAR control had to be constrained, even though d-DERs still presented nominal capability. By facing such an operational limitation, the approach interpreted that the actual reactive current dispatch was not enough to mitigate overvoltages. Thus, the MGCC followed the next step in Fig. 6.11, allowing it to steer d-DER$_1$ and d-DER$_3$ to also perform coordinated Volt/Watt, concomitantly to the offering of Volt/VAR control.

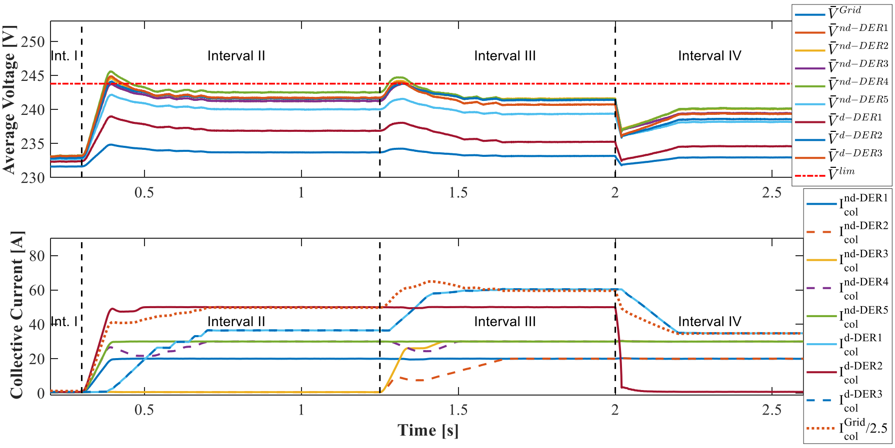

Figure 6.14: Simulation results for Scenario 2: MG operation considering nd-DERs at full capacity and with the proposed automatic overvoltage control enabled, and considering constrained reactive power dispatch. From top to bottom: Average voltages for the PCC ($\bar{V}^{Grid}$) and DERs ($\bar{V}^{DERj}$), and collective currents for DERs and the PCC (I_{col}^{Grid} is divided by 2.5).

By enabling the GCBC to also control the active current dispatch at the PCC, the d-DERs additionally shared active currents, proportionally to their remaining capabilities. Moreover, similar amounts of active currents were processed by both d-DERs during this instant. For instance, it can be seen in Table 6.3 that P and Q were similar for both d-DER$_1$ and d-DER$_3$. It is also noticed that P was negative for these d-DERs, which indicates that the approach steered them to store energy. By adding the coordinated Volt/Watt functionality, the Volt/VAR actions of the d-DERs were not affected, as shown by the similar amounts of Q power processed during Intervals II and III (see Table 6.3).

Fig. 6.14 proves that, during Interval III, the automatic scheme was able to avoid overvoltages within all monitored MG nodes, which is also shown in Table 6.3. Additionally, APC did not occur at nd-DERs, since the d-DERs automatically stored part of the energy being generated within the MG. Thus, by integrating the GCBC strategy with the proposed voltage regulation scheme, the transactive aspect of the MG is also respected. Coordinated Volt/VAR and Volt/Watt can be independently or concomitantly offered, respecting the contractual relations of the MG, and supporting the offering of multiple operational features at the same time. For instance, harmonic compensation could even be offered in parallel to voltage regulation, if desired, as long as the DERs participating in the GCBC had power capabilities available.

The final simulation case in Fig. 6.14 (i.e., Interval IV) demonstrates that the coordinated approach can also endure operation if an inverter abruptly disconnects from the MG. For that case, d-DER$_2$ suddenly presented null active power injection, causing the MG voltages to drop. As the MGCC sensed such a voltage variation, the Volt/Watt intervention followed the curve of Fig. 6.10, first reducing the active power absorption of d-DER$_1$ and d-DER$_3$. Although during this case such action was already sufficient to mitigate overvoltages, the reactive power being shared by the d-DERs would also be reduced if null energy storage was reached and voltages were not below $\bar{V}^{lim}$. APC was also practically null at nd-DERs during Interval IV.

Finally, it is highlighted that the proposed control scheme is sufficiently flexible to attend to the needs of the MG manager, allowing such a sequence of coordinated Volt/VAR followed by Volt/Watt to be swapped, if desired, without losing effectiveness in overvoltage control.

6.3.2.3 Scenario 3: Comparison to Pure Local Overvoltage Control

Two final simulation results consider the implementation of pure Volt/Watt and Volt/VAR control, respectively, to demonstrate how they contrast in relation to the proposed automatic scheme. During these two simulated cases, the same four previous operational intervals were considered (i.e., as in Figs. 6.13 and 6.14).

First, for the case of voltage regulation considering pure active power control (i.e., Case 1), only Volt/Watt curves were locally implemented on all DERs, according to Fig. 6.9. Thus, even d-DER$_1$ and d-DER$_3$ had such pure local control enabled, although they did not inject active power into the MG (this was performed to achieve a fair comparison with the result from Fig. 6.13). Simulation results for this case are shown in Fig. 6.15 and in Table 6.4, knowing that during Interval I, all DERs were idling.

At the beginning of Interval II, nd-DER$_1$, nd-DER$_4$, nd-DER$_5$, and d-DER$_2$ were initiated to inject P at full capacity. Consequently, as such nd-DERs caused overvoltages at certain nodes, nd-DER$_4$ suffered APC of approximately 22%. In addition, Fig. 6.15 shows that d-DER$_2$ initially performed APC, but achieved nominal operation in steady state. This occurred because d-DER$_3$ was under overvoltage, causing it to store energy due to its local Volt/Watt action (see negative P in Table 6.4). Since d-DER$_3$ was the one placed the furthest from the DST, in addition to the fact that it presented the largest nominal power rating, its operation significantly affected voltage profiles. Observe in Table 6.4 that, by having d-DER$_3$ only absorbing -3,566 W, the MG reached steady state operation without overvoltages.

Even though d-DER$_1$ was fully available to support voltage regulation, it did not process any currents. This occurred because d-DER$_1$ was the one placed closest to the DST, and it did not face overvoltage. Besides, the other nd-DERs also did not perform APC because their voltages were practically unaffected. Thus, although effective voltage regulation was achieved with pure local Volt/Watt control, this initial condition shows that only DERs suffering from overvoltage act on interventions. Compared to

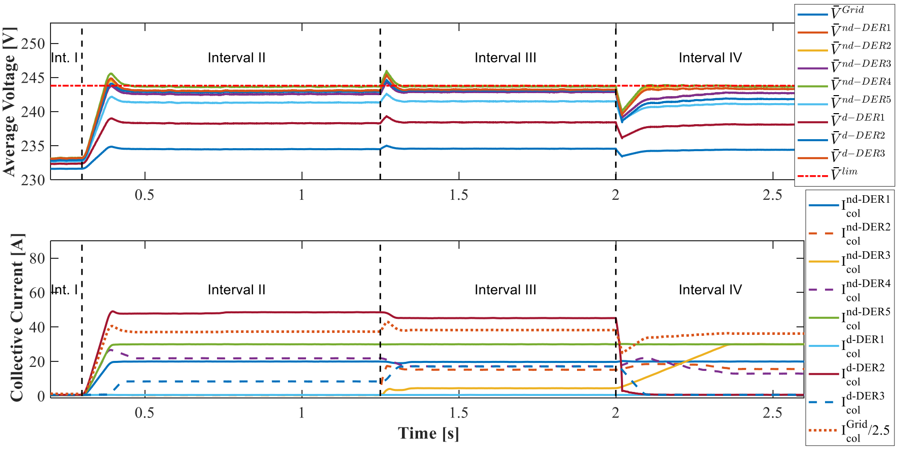

Figure 6.15: Simulation results for Scenario 3: MG operation considering pure local Volt/Watt control. From top to bottom: Average voltages for the PCC ($\bar{V}^{Grid}$) and DERs ($\bar{V}^{DERj}$), and collective currents for DERs and the PCC (I_{col}^{Grid} is divided by 2.5).

Table 6.4: Steady state results for the pure local overvoltage control in Figs. 6.15 and 6.16. Units: active power (P) [W], reactive power (Q) [VAR], average RMS voltage ($\bar{V}$) [V], and Losses [W].

	Scenario 3 - Case 1									**Scenario 3 - Case 2**								
	Interval II			**Interval III**			**Interval IV**			**Interval II**			**Interval III**			**Interval IV**		
	P	Q	$\bar{V}$	P	Q	$\bar{V}$	P	Q	$\bar{V}$	P	Q	$\bar{V}$	P	Q	$\bar{V}$	P	Q	$\bar{V}$
PCC	-45320	775	234	-46520	813	234	-4423	752	234	-47970	3474	234	-51380	6028	234	-45500	2470	234
nd-DER$_1$	8399	90	242	8328	91	243	8385	95	243	8375	82	243	8398	87	243	8399	89	243
nd-DER$_2$	0	0	243	6277	65	243	6647	72	243	0	0	243	5573	57	243	7149	79	243
nd-DER$_3$	0	0	242	1943	17	243	12590	138	243	0	0	243	2353	27	243	12600	134	243
nd-DER$_4$	9274	97	243	7403	83	243	5651	61	243	8547	91	243	6094	60	243	6537	74	243
nd-DER$_5$	12530	131	241	12560	138	243	12500	137	241	12520	125	241	12530	132	241	12510	132	241
d-DER$_1$	0	0	238	0	0	239	0	0	238	0	0	238	0	0	238	0	0	238
d-DER$_2$	20210	213	243	18810	197	243	0	0	242	20360	214	243	18690	195	243	0	0	242
d-DER$_3$	-3566	42	243	-7216	75	243	-76	0	243	-109	2637	243	-213	5066	243	-81	1680	243
Losses	684			720			674			791			957			730		

Scenario 1 (i.e., in Fig. 6.13), since less active power was injected into the MG by the nd-DERs, and no reactive power was processed by the d-DERs, lower losses were obtained. However, this occurred at the expense of having d-DER$_1$ not contributing to voltage regulation, which would not occur with the proposed automatic scheme.

The results during Interval III in Fig. 6.15 reiterate the above-mentioned discussions. As nd-DER$_2$ and nd-DER$_3$ were initiated to inject nominal active power, voltages tended to rise above $\bar{V}^{lim}$. Yet, as nd-DER$_1$ and nd-DER$_5$ were closer to the DST, they did not suffer APC. Nevertheless, the Volt/Watt control performed by the remaining DERs caused nd-DER$_3$ to only to process 16% of its nominal energy generation capability. Besides, it can be seen in Table 6.4 that nd-DER$_2$, nd-DER$_4$, and d-DER$_2$ curtailed approximately 21%, 7.5%, and 6% of their energy generations, respectively.

To conclude the simulation results for the pure Volt/Watt control, Interval IV in Fig. 6.15 shows that, when d-DER$_2$ was disabled, nd-DER$_3$ was able to reduce APC to practically zero. Besides, less absorption of active power was required from d-DER$_3$ to maintain compliant voltage profiles. However, APC still occurred for nd-DER$_2$ and nd-DER$_4$, and d-DER$_1$ still did not participate on voltage regulation.

For the final simulated scenario (i.e., Case 2), which is presented in Fig. 6.16 and in Table 6.4, pure local Volt/VAR control was considered for d-DER$_1$ and d-DER$_3$, as given by Fig. 6.9. The non-dispatchable inverters (i.e., all nd-DERs and d-DER$_2$) still presented pure Volt/Watt control locally implemented. This case is shown because it contrasts to Scenario 1 in Fig. 6.13, in which d-DERs provided coordinated Volt/VAR

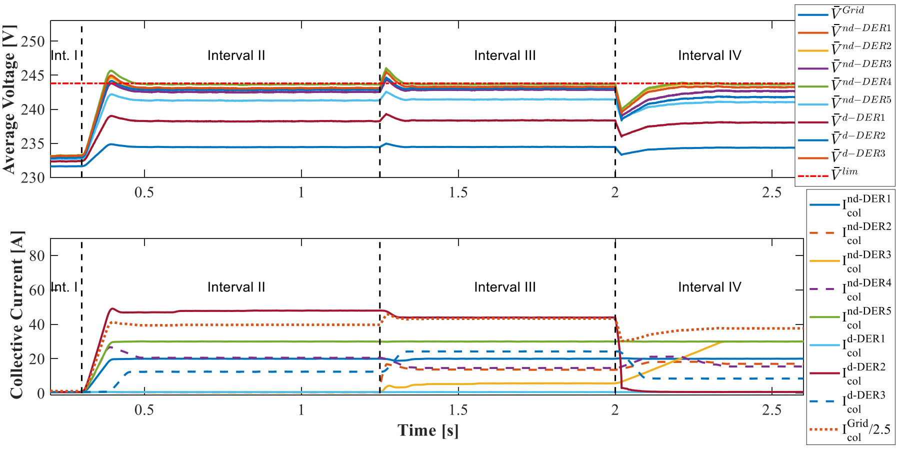

Figure 6.16: Simulation results for Scenario 3: MG operation considering pure local Volt/VAR control. From top to bottom: Average voltages for the PCC ($\bar{V}^{Grid}$) and DERs ($\bar{V}^{DERj}$), and collective currents for DERs and the PCC (I_{col}^{Grid} is divided by 2.5).

instead of local voltage control. Again, four intervals were simulated for this local perspective.

In general, the results for Case 2 (i.e., Fig. 6.16) were similar to the ones in Case 1 (i.e., Fig. 6.15), indicating that concomitant Volt/Watt and Volt/VAR local controls were able to tackle overvoltage. For instance, Table 6.4 shows that during all intervals for Case 2, when a small portion of d-DER$_3$'s nominal capability was employed in Volt/VAR actions, its operation significantly supported voltage regulation. However, APC always occurred for some nd-DERs during each of the simulated intervals. An overall reduction in energy generation of 6%, 25% and 12% was obtained for the MG during Intervals II, III, and IV, respectively. Moreover, d-DER$_1$ did not process active or reactive power at any interval, even though its local Volt/VAR control was enabled.

Such results demonstrate that the proposed automatic overvoltage control scheme allows us to exploit all DERs able to communicate with the MGCC, in contrast to classic strategies based on pure local voltage regulation. Consequently the voltage regulation burden of the MG can be balanced over all available inverters, and APC can be reduced even for nd-DERs not comprising a communication interface. One drawback, however, is that losses are generally higher for the proposed method. This occurs because: *i)* the method allows higher penetration of distributed generation, which results in higher currents flowing through line impedances; and *ii)* even DERs far from the nodes most susceptible to suffer overvoltage participate on Volt/VAR or Volt/Watt actions. For example, comparing Interval III from Fig. 6.13 with the one from Fig. 6.15, which is the worst scenario attained during simulations, losses were approximately 4.6 times higher for the automatic scheme. However, it is reiterated that, in LV grids, higher losses are usually a natural consequence of surplus energy injection not consumed by loads.

6.3.3 Experimental Results

Herein, the experimental results aim to demonstrate that the proposed automatic voltage regulation scheme can tackle overvoltage conditions in real-life applications. The main single-phase MG prototype shown in Fig. 4.2 was used once more, considering that the three DERs* were operating. For instance, nd-DER$_1^\star$ operated constantly injecting 950 W, without Volt/Watt locally implemented, being responsible for causing voltage rise internally to the MG. On the other hand, d-DER$_1^\star$ and d-DER$_2^\star$ operated coordinated by the GCBC strategy, implementing the proposed voltage regulation scheme. All loads were switched off during experiments to facilitate voltage rise. A digital voltage meter [204] was used to measure and datalog voltages at several locations of the MG (see Fig. 4.3).

For the following results, the voltage threshold determined for stating overvoltage condition (i.e., $\bar{V}^{lim}$) was set to 130 V$_{\text{RMS}}$. Yet, d-DERs* exchanged information with the MGCC based on a rate of 16.66 ms. The experimental results are divided into three intervals: at *Interval I)* only nd-DER$_1^\dagger$ injected active power; at *Interval II)* d-DERs* began to mitigate overvoltage according to the proposed automatic control; and at *Interval III)* a voltage step was applied by the grid emulator, abruptly raising the MG voltages. The experimental voltage profiles for the nodes of interest are shown in Fig. 6.17(a), and transitions between the intervals are illustrated in Fig. 6.17(b). The steady state operation is shown in Figs. 6.17(c) to 6.17(e) for Intervals I, II and III, respectively. It is highlighted that experiments considered $\delta_{1\perp} = 0.1$.

Interval I in Fig. 6.17(a) presents the voltage profiles when nd-DER$_1^\dagger$ operated alone. One can observe the impact in voltage rise caused by the active power injection from nd-DER$_1^\dagger$, as the nominal voltage of the MG was 127 V$_{\text{RMS}}$ and all nodes were above such value. Such an operation led some of the MG nodes to be close to the

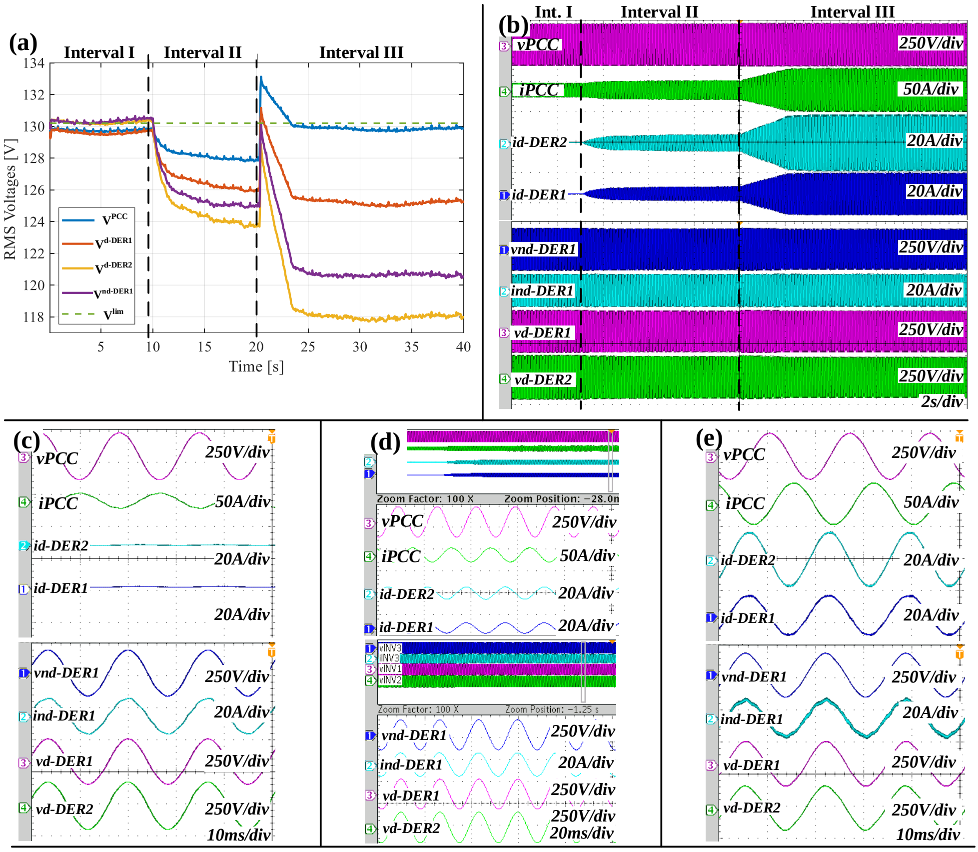

Figure 6.17: Experimental results for automatic overvoltage regulation. (a) RMS voltages of the MG nodes comprising inverters; (b) Experimental results of the three intervals tested; (c) Zoom-in-view of Interval I; (d) Zoom-in-view of Interval II; (e) Zoom-in-view of Interval III.

voltage threshold $\bar{V}^{lim}$ (e.g., as in the case of the PCC and d-DER$_1^\star$), whereas the other two locations (i.e., nd-DER$_1^\star$ and d-DER$_2^\star$'s nodes) presented voltages above the expected limit. It can also be noted from Figs. 6.17(b) and 6.17(c) that d-DER$_1^\star$ and d-DER$_2^\star$ were not processing any currents at this instant. As a consequence, mainly active current was dispatched from the MG to the upstream grid (see the 180^{o} phase shifted current at the PCC).

At the beginning of the Interval II, the GCBC was enabled, allowing d-DERs* to operate according to the scheme of Fig. 6.11. Since such inverters were initially idling, they had nominal capability available to perform Volt/VAR. Thus, observe in Fig. 6.17(b) that the d-DERs* started to iteratively increase the reactive current dispatch of the MG at each control cycle. This operation occurred smoothly, without causing undesired transients, neither for any voltages in the MG, nor for currents. Moreover, Fig. 6.17(d) shows that the PCC current was lagging in relation to the PCC voltage, which indicates that reactive current dispatch was incorporated into the MG operation.

Since d-DER$_1^\star$ and d-DER$_2^\star$ processed 3.08 A$_{\text{RMS}}$ and 3.84 A$_{\text{RMS}}$, respectively, it is indicated that proportional current sharing occurred. Therefore, even when performing overvoltage control, the inverters reached a proportion ratio of $r_{dDERs^\star} = 1.24$, which is fairly close to the expected 1.33 value. Most importantly, Fig. 6.17(a) shows that the voltages at all measured nodes were below $\bar{V}^{lim}$. This indicates that the strategy was capable of tackling the overvoltage condition, without impacting on the active current injection performed by nd-DER$_1^\star$. For instance, comparing Figs. 6.17(c) and 6.17(d), one can note that nd-DER$_1^\star$ practically injected the same current.

Lastly, a more challenging scenario was tested on the MG. At the beginning of Interval III, an abrupt voltage step to 133 V$_{\text{RMS}}$ was applied to the upstream grid, emulating a quick voltage rise during the voltage regulation provided by the proposed automatic scheme. From Fig. 6.17(a), it can be noted that a significant voltage rise occurred at all nodes of the MG, leading most of them to overvoltage conditions. Nevertheless, after sensing such a voltage rise at different nodes, the GCBC smoothly increased the reactive current dispatch supported by d-DER$_1^\star$ and d-DER$_2^\star$, as shown in Fig. 6.17(b). As a consequence, after approximately 2 s, the voltage profiles of the MG were adjusted (see Fig. 6.17(b)).

The result in Fig. 6.17(e) shows that d-DERs* increased their reactive current dispatch (see their lagging currents), also indicating that nd-DER$_1^\star$ practically maintained its active current injection. Thus, the coordinated operation allowed us to regulate voltage profiles without requiring the implementation of power curtailment at nd-DER$_1^\star$. During this case, d-DER$_1^\star$ and d-DER$_2^\star$ processed 9.83 A$_{\text{pk}}$ and 12.98 A$_{\text{pk}}$, respectively, reaching an adequate proportion ratio of 1.32. Finally, the MG voltages presented in Fig. 6.17(a) prove that all nodes were below $\bar{V}^{lim}$, ensuring overvoltage mitigation.

However, it is highlighted that, since d-DER$_2^\star$ was the inverter presenting higher power capability and it was placed at the terminal point of the feeder, its voltage was the one most affected by the coordinated reactive power dispatch. Thus, for cases in which undervoltage thresholds are reached, this inverter should have its current injection constrained to avoid exceeding operational limits. This condition can also typically be avoided if concepts of fair control [205] were integrated into the GCBC, as d-DERs* would contribute to voltage regulation proportionally to their PoC voltages.

6.4 Distributed Compensation of Unbalanced Currents

LV grids and MGs commonly present diversified scenarios of loads and DERs, requiring flexibility from coordinated control strategies, as multiple operational purposes are needed at different instants. Among such scenarios, the existence of current or voltage unbalance is a probable condition, since three-phase MGs can incorporate single-phase, two-phase, and asymmetrical three-phase loads. Besides, the presence of single-phase DERs arbitrarily connected to three-phase [68] grids is also a common cause of asymmetries. From a power quality perspective, unbalances in voltages and currents ought to be avoided whenever possible, as they may increase losses, cause stress on transformers, also resulting in neutral currents for three-phase four-wire grids, and many other complications [206].

Due to the importance of achieving mitigation of unbalances in MGs, several approaches have been proposed to steer inverters to that purpose [206, 207]. In [208], a decentralized method is presented for compensation of voltage unbalance, being integrated to a damping strategy that operates in specific P-V droop regions, in which inverters act as resistors in relation to the negative- and zero-sequence components. However, harmonic compensation is not supported by [208], and the MG power dispatchability is not addressed. Besides, extraction of sequence components is, in general, compromised due to noise and harmonic distortions [209].

Another decentralized approach relying on decomposition of negative sequence components is found in [210], steering DERs as virtual synchronous generators and based on model predictive control, presenting similar limitations to [208]. A two-layer hierarchical strategy coordinates four-leg DERs to compensate for unbalances in [211], based on single-phase droop control, as well as on three independent secondary controllers. Such a proposal uses virtual impedance loops and needs to extract negative and zero sequence components of voltages. In addition, distributed harmonic compensation is not addressed in [211], and the use of the virtual impedance concept may limit the power output capacity of DERs [212].

A power-based approach in [71] coordinates both single- and three-phase inverters to mitigate current unbalances, also achieving accurate power sharing and power flow control at the MG PCC. However, a three-phase three-wire topology is aimed at in the method, and concomitant harmonic compensation is not realizable. Coordinated unbalance mitigation in four-wire MGs based on the Conservative Power Theory (CPT) [45] is proposed in [213], not requiring decomposition of sequence components, consequently enhancing the robustness of the coordinated operation of inverters under distorted voltage conditions.

The authors of [213] use droop control and virtual impedance shaping, along with the balanced and unbalanced current parcels defined by the CPT, for steering voltage-controlled DERs. Although the CPT's unbalanced current definition is adopted [45], such a term is controlled as a single component that considers the contribution of both active and reactive unbalance currents [45], not addressing the flexibility to provide decoupled compensation of unbalanced conductances and susceptances. The CPT is also adopted in [214], relying on a four-layer hierarchical architecture and a supervisory controller for load sharing purposes. The strategy uses instantaneous electrical quantities, also not offering current sharing capabilities according to the proportional ratings of DERs. Additionally, load currents need to be directly measured in [214], which makes implementation difficult in MGs with multiple nodes and dispersed loads.

As can be noted from the literature, the CPT presents interesting features when the purpose of unbalance compensation is intended for the MGs [207]. Thus, herein, concepts from the CPT are considered, aiming at providing a framework for the GCBC strategy to also support distributed compensation of unbalanced currents in MGs. The resulting coordinated control approach compensates unbalance currents without requiring decomposition of sequence components, nor the implementation of virtual impedance loops. Moreover, reduction of neutral currents is inherently achieved in four-wire MGs, while proportionally steering DERs.

6.4.1 Distributed Compensation of Unbalanced Currents based on the CPT

The mathematical formulation of the CPT [45] is presented in Appendix A.1 and, for the scope of this thesis, its three current parcels are of interest. Given a generic electric circuit composed of *m* phases, and comprising instantaneous phase voltage v_m and line current i_m, the three parcels defined by the CPT are the active (i_{a_m}), reactive (i_{r_m}) and void currents (i_{v_m}). This first current term (i.e., i_{a_m}) relates to the active power transfer from source to load. The second parcel (i.e., i_{r_m}) characterizes the reactive power circulation at that particular section of the electric circuit, and the third parcel (i.e., i_{v_m}) indicates distortion components that are present either in voltage or current.

Most importantly, for what concerns unbalance compensation, the CPT definitions allow the terms i_{a_m} and i_{r_m} to be further decomposed in time domain into balanced and unbalanced currents, which herein use the superscripts "^{b}" and "^{u}", respectively. For instance, the active current of a phase *m* can be re-written as Eq. 6.5, whereas the reactive parcel is given by Eq. 6.6.

$$i_{a_m}(t) = i^b_{a_m}(t) + i^u_{a_m}(t) \tag{6.5}$$

$$i_{r_m}(t) = i^b_{r_m}(t) + i^u_{r_m}(t) \tag{6.6}$$

Based on the definitions in Eqs. 6.5 and 6.6, the CPT provides a means to identify unbalanced currents resulting from unequal phase conductances (i.e., $i^u_{a_m}$), as well as from unequal phase susceptances (i.e., $i^u_{r_m}$). Therefore, if a control strategy is capable of steering one or multiple inverters to suppress the terms $i^u_{a_m}$ and $i^u_{r_m}$ at a certain section of an electric circuit, the behavior of balanced conductances and susceptances are obtained, respectively [42, 215].

Let us now recall the GCBC strategy, particularly the calculations performed at the MGCC when the MG load currents (i.e., $I^L_{h||_m}$ and $I^L_{h\perp_m}$) are reconstructed during a control cycle "*k*" by Eqs. 3.9 and 3.10. From the CPT definitions, one can understand that within the fundamental components of the reconstructed load currents (i.e., $I^L_{1||_m}$ and $I^L_{1\perp_m}$) two terms exist: *i)* one corresponding to balanced active and reactive currents, namely $I^{L(b)}_{1||_m}$ and $I^{L(b)}_{1\perp_m}$; and another one respective to the unbalanced terms, namely $I^{L(u)}_{1||_m}$ and $I^{L(u)}_{1\perp_m}$. Thus, at a given control cycle, the loads' active and reactive peak currents can be re-written as in Eqs. 6.7 and 6.8.

$$I^L_{1||_m}(k) = I^{L(b)}_{1||_m}(k) + I^{L(u)}_{1||_m}(k) \tag{6.7}$$

$$I^L_{1\perp_m}(k) = I^{L(b)}_{1\perp_m}(k) + I^{L(u)}_{1\perp_m}(k) \tag{6.8}$$

A direct consequence of this current decomposition is that, if the MGCC can split $I^{L(b)}_{1||_m}$ and $I^{L(u)}_{1||_m}$, as well as $I^{L(u)}_{1||_m}$ and $I^{L(u)}_{1\perp_m}$, the GCBC strategy can support distributed compensation of unbalanced currents. Such a functionality is integrated into the GCBC by adjusting the reference currents $I^*_{1||_m}$ and $I^*_{1\perp_m}$, according to Eqs. 6.9 and 6.10. Note that only balanced fundamental currents will result at the PCC, if the other current terms are shared by the DERs. Moreover, the distributed compensation of unbalanced currents can be performed individually for the in-phase and quadrature terms, leading to decoupled balancing of conductances or susceptances at the PCC, if $I^{L(u)}_{1||_m}$ or $I^{L(u)}_{1\perp_m}$ tackled, respectively. Lastly, note that the constants γ_{Na} and γ_{Nr} (i.e., with range of [0,1] $\forall \in \mathbb{R}$) further allow the possibility to compensate unbalances partially, if desired. Such a feature might be interesting in scenarios in which DERs operate close to their nominal capability, such as in [216] and [217].

$$I^*_{1||_m}(k+1) = I^{L(b)}_{1||_m}(k) + (1-\gamma_{Na}) \cdot I^{L(u)}_{1||_m}(k) + I^{Grid*}_{1||_m}(k+1) \tag{6.9}$$

$$I^{*}_{1\perp_m}(k+1) = I^{L(b)}_{1\perp_m}(k) + (1-\gamma_{Nr})\cdot I^{L(u)}_{1\perp_m}(k) + I^{Grid*}_{1\perp_m}(k+1) \tag{6.10}$$

Therefore, in order to incorporate the purpose of unbalance compensation into the GCBC strategy, a procedure based on the CPT is presented in Fig. 6.18. Such a scheme, which is only processed at the MGCC, allows us to decompose balanced and unbalanced current parcels, which can be used to obtain current references for the GCBC. Since the CPT is defined in time-domain, to perform its decomposition, the instantaneous load currents being drawn within the MG must be estimated. For such an estimation, the quantities obtained from DERs at the beginning of the control cycle "k" are used, along with the current measurements from the PCC (i^{Grid}_m).

Relying on the premise that voltage phase shifts are negligible at the MG, the total m-phase instantaneous current from DERs (i^{DERt}_m) can be reconstructed based on v^{Grid}_m. Thus, from Kirchhoff's current law, the instantaneous load currents (i^L_m) can be calculated. In possession of i^L_m, the CPT can be straightforwardly calculated, and its current terms can be decomposed. If the peaks of the balanced and unbalanced active and reactive currents are calculated, the terms $I^{L(b)}_{1||_m}$ and $I^{L(u)}_{1||_m}$, as well as $I^{L(u)}_{1||_m}$ and $I^{L(u)}_{1\perp_m}$ are finally attained for further use in the GCBC approach.

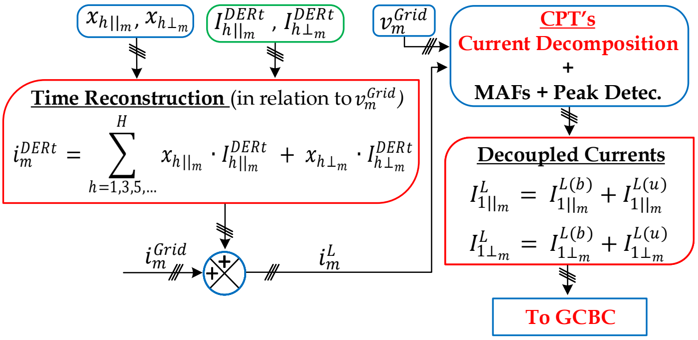

Figure 6.18: Incorporation of the CPT's unbalanced currents into the GCBC strategy.

6.4.2 Simulation Results

Simulation results are herein presented to demonstrate the features of the GCBC strategy with regard to the proposed distributed compensation of unbalanced currents. Two main simulation scenarios are presented, considering that unbalanced loads exist in the MG: *i)* the first one shows how the GCBC strategy operates, according to the classic formulation presented in Chapter 3 (i.e., without unbalance compensation capability); and *ii)* the second scenario shows the MG operating with the scheme proposed in Section 6.4.1 (i.e., with capability to compensate unbalances). The variables γ_{Na} and γ_{Nr} are considered to be 0.0, unless stated otherwise.

To constitute the scenario of a LV system with dispersed unbalanced loads, the main MG testbench used for simulations (i.e., the one in Fig. 3.1) is slightly modified. All loads previously explained in Section 4.2.1 are removed from the MG, and replaced by the loads described in Table 6.5. Thus the MG presents linear and non-linear loads, knowing that the former elements present different configurations.

For the sake of simplicity, only the previous three d-DERs are considered to operate during the following results, maintaining their original locations at the MG. Moreover, in order to demonstrate all the features related to the unbalanced compensation strategy, the d-DERs are simulated as three-phase four-leg inverters, instead of the three-phase three-leg topology. This is performed because three-phase three-leg inverters are not capable of compensating zero-sequence components circulating in four-wire circuits [129]. These four-leg DERs are simulated with inductive output filters, using PRep current regulators, with parameters shown in Table 6.5. As in previous simulations, the GCBC strategy considers communication occurring at each cycle of the 50 Hz line frequency (i.e., 20 ms), and harmonics from the 3rd to the 13th orders are tackled.

The results of the first scenario are presented in Figs. 6.19 and 6.20. Four intervals are considered during simulations. During Interval I, the d-DERs are idling, and only load currents are seen at the MG PCC. For the second interval, DERs are enabled to share active and reactive currents. At Interval III, reactive and harmonic currents are shared, and full current control is shown at the last interval. Such results are shown to

Table 6.5: Loads and control parameters adopted for the MG testbench in Fig. 3.1.

Loads	**Apparent Power** (A)
L_{B11}	$A_{bc} = 8.0$ kVA with $PF = 1.0$
L_{B15} (Y-formed with connection to neutral conductor)	$[A_a, A_b, A_c] = [2.4, 3.2, 4.0]$ kVA with $PF = 0.85$
L_{B16} (Y-formed with connection to neutral conductor)	$[A_a, A_b, A_c] = [2.4, 3.2, 4.0]$ kVA with $PF = 0.75$
L_{B17}	$A_c = 0.78$ kVA with $PF = 0.85$
L_{B18} (Y-formed with connection to neutral conductor)	$[A_a, A_b, A_c] = [0.8, 1.6, 2.0]$ kVA with $PF = 0.85$
Non-linear Loads: NL_1, NL_2, NL_3‡ (AC side inductor, DC side capacitor and resistor)	1.5 mH, 2.35 mF, 62 Ω
d-DERs L Filters and Control Parameters	
Inductor (per-phase): L_i	3.0 mH
PRep controller: KP and K_f gains	0.28 and 0.26 p.u.

‡ NL_3 is disconnected.

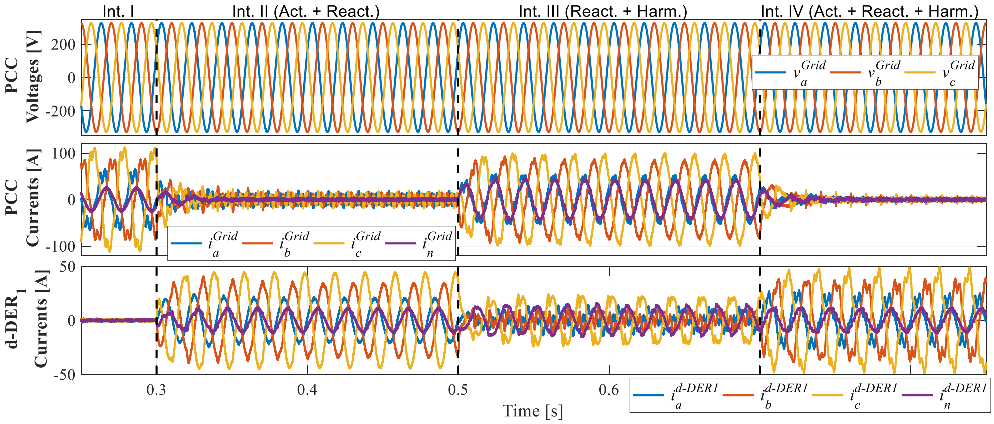

Figure 6.19: Simulation results: GCBC without the proposed compensation of unbalanced currents. Interval I: only loads operating; Interval II: d-DERs sharing fundamental currents; Interval III: d-DERs sharing reactive and harmonic currents; Interval IV: d-DERs sharing all load currents. From top to bottom: PCC voltages and currents, d-DER$_1$ currents.

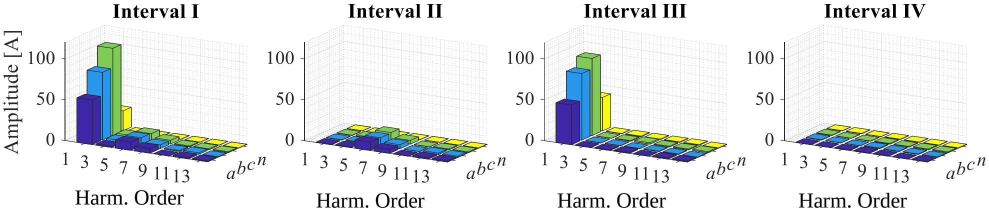

Figure 6.20: Harmonic spectrum of the PCC currents in Fig. 6.19.

briefly demonstrate that, if unbalanced loads or DERs exist in the MG, the formulation of the GCBC strategy presented in Chapter 3 does not allow us to achieve balanced currents at the PCC.

At Interval I, one can note that, despite the fact that the grid voltages were sinusoidal, the PCC currents were highly distorted and presented significant unbalance among the phases *a*, *b*, and *c*. In addition, a current with considerable amplitude circulated at the PCC. The GCBC strategy was enabled at the beginning of Interval II, allowing the fundamental currents to be shared by the DERs. Observe in Fig. 6.20 that the harmonic selectivity of the GCBC is not affected by unbalances. It is interesting to note that, even though the loads were unbalanced, both the active and reactive current terms were shared by the d-DERs (see that d-DER$_1$'s currents were unbalanced), resulting in the fact primarily harmonics flowed through the PCC. Hence, the GCBC strategy was able to detect the amplitudes of the active and reactive currents at the PCC, for the three independent phases.

Nevertheless, in Interval III the inherent limitation of the GCBC is evidenced. By commanding DERs to share the reactive and selected harmonic currents, the currents at the PCC became low distorted during steady state condition, although they were unbalanced. This occurred because the GCBC, implemented as in Chapter 3, cannot distinguish between balanced and unbalanced current terms. Thus, if unbalanced conductances or susceptances exist in the MG, the resulting PCC currents will be unbalanced if the active or reactive terms are not shared by the DERs, respectively. Fig. 6.20 shows that, even though the amplitude of the fundamental terms decreased due to the compensation of reactive currents, the unbalanced active currents remained unchanged.

At Interval IV, it also proved that all selected current terms can be shared by the DERs, if desired (see Figs. 6.19 and 6.20). The GCBC approach does not allow us to achieve only balanced currents at PCC, if unbalances exist, but all currents can be provided by the DERs without losing effectiveness in current sharing. Yet, since a per-phase analysis is performed by the method, proportional current sharing can be obtained independently for each phase.

Now, the second scenario is presented, in which the proposed scheme for distributed compensation of unbalanced currents is incorporated into the GCBC strategy. Simulation results are provided in Fig. 6.21, considering the same first interval presented in Fig. 6.19. A quantitative baseline is presented for this interval in Table 6.6, in which it is seen that significant amounts of active, reactive, distortion, and unbalanced (N) powers were measured at the PCC. It is reinforced that such power terms are given by the CPT, and can be calculated as shown in Appendix A.1. Yet, a low power factor was calculated for the PCC during this case, being 0.88.

At the beginning of Interval II, the distributed unbalance compensation provided by the proposed method is demonstrated. During this case, the balanced reactive, as well as the unbalanced active and reactive currents decomposed by the CPT were demanded to be shared by the d-DERs. The zoom-in-view of this case in Fig. 6.21 shows that the resulting PCC currents became practically balanced when in steady state (see that the fundamental bars in the harmonic spectrum for this case presented similar amplitudes).

Table 6.6: Steady state powers and PF at the PCC for Fig. 6.21.

	Interval I	**Interval II**	**Interval III**	**Interval IV**
A [kVA]	41.42	36.99	36.48	5.21
P [kW]	36.83	36.58	36.47	-0.2
Q [kVAR]	13.94	0.03	0.03	0.82
D [kVA]	5.63	5.47	0.87	0.66
N [kVA]	11.52	0.27	0.24	5.08
PF	0.88	0.98	0.99	0.00

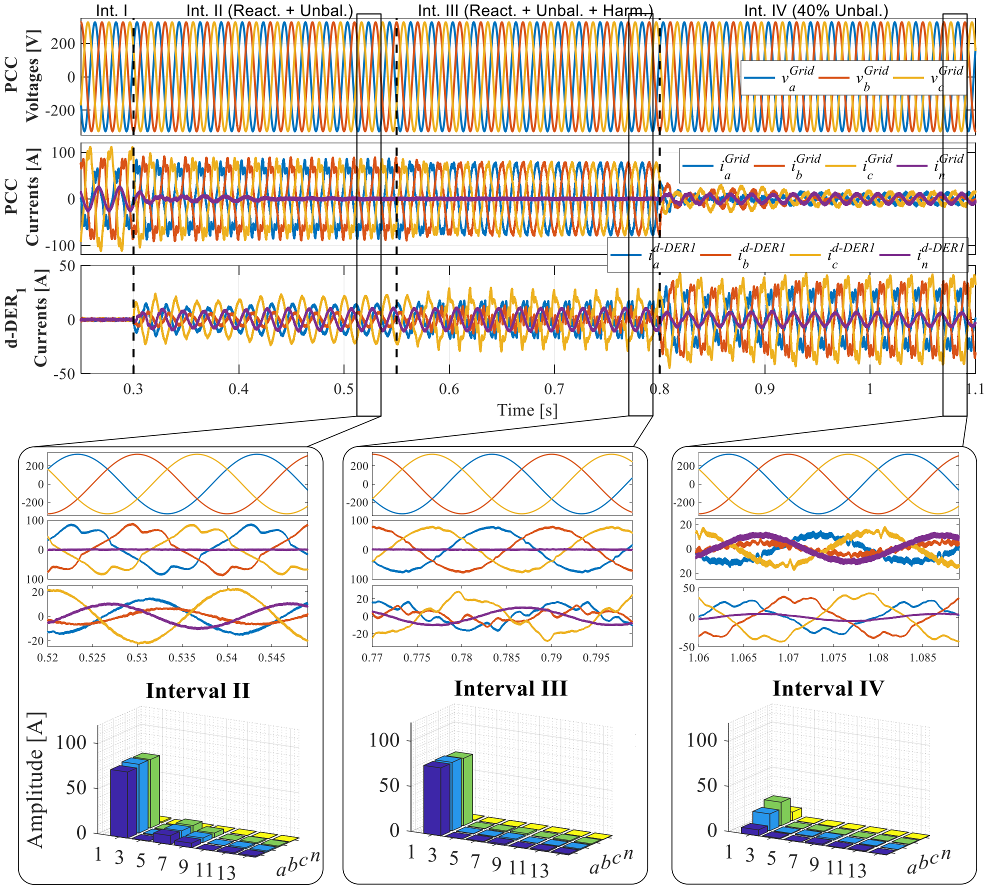

Figure 6.21: Simulation results: GCBC with the proposed compensation of unbalanced currents. Interval I: only loads operating; Interval II: d-DERs sharing reactive and unbalanced currents; Interval III: d-DERs sharing reactive, unbalanced, and harmonic currents; Interval IV: d-DERs sharing reactive, harmonic, and 60% of unbalanced currents. From top to bottom: PCC voltages and currents, d-DER$_1$ currents.

Additionally, currents and voltages were in-phase at the PCC, even though distortions were not mitigated.

Table 6.6 also indicates that the circulation of reactive and unbalances components were practically mitigated at the PCC, as small values were obtained for them. Yet, such an operation occurred without affecting P and D, providing that decoupled compensation was performed. From the d-DER$_1$'s currents, it is also evidenced that inverters operated unbalanced, processing three-phase currents, as well as neutral currents. This operation caused practically null circulation of neutral currents at the PCC. The collective currents for d-DER$_1$, d-DER$_2$ and d-DER$_3$ were 18.90 A, 10.82 A and

18.83 A, respectively. Thus, it is indicated that proportional current sharing was attained, as the proportion ratio was 1.74 (i.e., between d-DER$_1$ and d-DER$_2$, as well as between d-DER$_3$ and d-DER$_2$), and the expected value was 1.75.

During the next stage (i.e., Interval III), sharing of the selected harmonic currents was added to MG operation. As a consequence, the resulting PCC currents became practically balanced. Note from the zoom-in-view and harmonic spectrum in Fig. 6.21 that such currents presented similar amplitudes, certifying an effective distributed compensation of the unbalanced currents. Moreover, since the PCC currents became in-phase and low-distorted, it is demonstrated that the MG operated as a balanced resistor, as seen from the upstream grid perspective. Thus, note that the proposed distributed compensation of unbalanced currents can also be interpreted as an ancillary service for grid support functions, which is able to be traded in transactive markets.

The quantitative analysis provided in Table 6.6 shows that mostly active power was measured during Interval III, which led the MG PCC to operate under a high power factor (i.e., $PF = 0.99$). The collective currents processed were 19.96 A, 11.47 A and 20.00 A, respectively for d-DER$_1$, d-DER$_2$ and d-DER$_3$, leading to a proportion ratio of 1.74 (i.e., between d-DER$_1$ and d-DER$_2$, as well as between d-DER$_3$ and d-DER$_2$). Hence, such results demonstrate that the proposed scheme for compensation of unbalanced currents was integrated to the GCBC strategy, thus allowing it to maintain all of its previous operational features.

A final experiment is depicted in Interval IV, in which the variables γ_{Na} and γ_{Nr} were set to 0.4. This case represents a scenario in which only 40% of the unbalanced active and reactive currents parcels are desired to flow through the PCC, allowing d-DERs to share the remaining 60% of such currents. In Fig. 6.21, it becomes evident that the PCC currents were unbalanced, causing currents to flow through the neutral conductor. Such a feature occurred without losing effectiveness in current sharing of the other components. For instance, the current spectrum in Fig. 6.21 shows that most of the harmonic components were compensated. Lastly, the quantities presented in Table 6.6 show that an overall amount of 5.08 kVA remained at the PCC for the unbalance power N. This amount represents 44% of the amount calculated for the initial stage, indicating that the GCBC strategy was able to adequately compensate approximately 60% of the unbalanced currents, as set by imposing $\gamma_{Na} = \gamma_{Nr} = 0.4$.

6.4.3 Experimental Results

The experimental results herein validate the capability of the GCBC strategy to steer inverters for the purpose of achieving distributed compensation of unbalanced currents. For the following results, a third MG prototype is introduced, being composed of a three-phase four-wire (i.e., three-phase plus neutral) electric circuit, which presented a similar operational layout to the main single-phase prototype (i.e., Fig.

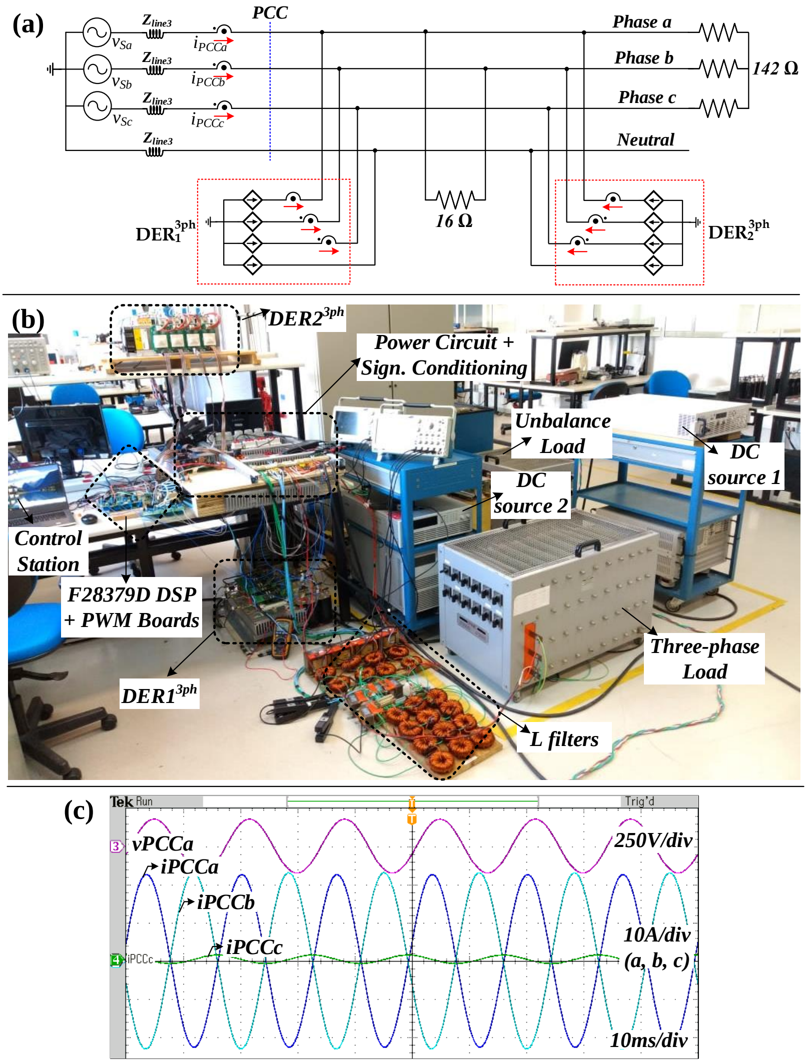

Figure 6.22: Three-phase MG prototype used for experiments of unbalance compensation. From top to bottom: (a) MG circuit; (b) picture of the prototype; and (c) Phase *a* voltage and three-phase currents at the PCC considering the unbalanced load.

4.3). The MG circuit and a picture of the prototype are shown in Fig. 6.22. The REGATRON® grid emulator once again played the role of the upstream grid, indicating that the MG operated under grid-connected mode during the following experiments. The nominal phase-to-neutral voltage of the MG was set to 127 $\mathrm{V_{RMS}}$ at 60 Hz. Yet, line impedances (i.e., $Z_{line3} = 0.11 + j.10^{-3}$) connected the MG to the upstream grid.

Such a MG comprised one three-phase balanced resistive load of 143 Ω, as well as an unbalanced resistive load of 16 Ω that was connected between phases a and b. Moreover two DERs^{3ph} were considered for experiments, both being based on three-phase four-leg inverters [218], using only inductive output filters at each at leg (i.e., being 2.0 mH per leg). The nominal capabilities of the inverters were $A^{DER_1^{3ph}} = 5kVA$ and $A^{DER_1^{3ph}} = 3.3kVA$, and constant DC voltage sources were placed at their DC buses, considering 500 V$_{\mathrm{DC}}$. A TMS320F28379D DSP from Texas Instruments® was used to embed the PR current controllers of the DERs, the CPT algorithm, as well as the GCBC strategy. The sampling and switching frequencies were 18 kHz, and communication was emulated to be 16.66 ms (i.e., once per line cycle). As performed during simulations, the GCBC strategy and current regulators controlled phases a, b, and c, being the references for the neutral leg of the DERs calculated according to Kirchhoff's current law (i.e., $i_n^* = -1 \cdot (i_a^* + i_b^* + i_c^*)$).

In Fig. 6.22(c) a first experimental result demonstrates the currents measured at the MG PCC. It is visually evident that the load connected between phases a and b caused a significant unbalance in currents. For instance, the amplitude of i_{PCC_a} was approximately 10 times higher than the one from i_{PCC_c}, Moreover, having the voltage from phase a as reference, it can be seen that the currents were phase-shifted, indicating that active and reactive unbalanced currents were demanded from the grid.

The capability of the proposed distributed compensation is demonstrated in Fig. 6.23(a). As the GCBC strategy was enabled, the DERs^{3ph} started to share the active and reactive unbalanced parcels drawn by the loads. Note that the currents processed

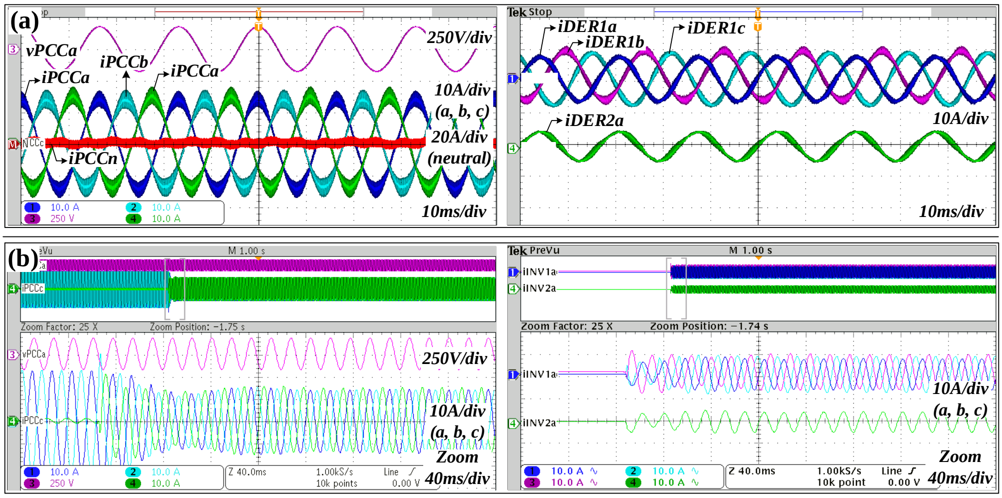

Figure 6.23: Experimental results for the distributed compensation of unbalanced currents. From top to bottom: (a) Steady state PCC voltage and three-phase currents, and DERs' currents; and (b) initialization of the results in (a).

by DER_1^{3ph} were unbalanced. In addition, the current sharing provided by the strategy was proportional to the nominal capabilities of the inverters. Such a feature can be evidenced by, for example, looking at the phase a currents from DER_1^{3ph} and DER_2^{3ph}, which were 4.92 A_{RMS} and 3.25 A_{RMS}, respectively. This thus indicates that a proportion ratio of 1.51 was obtained, keeping in mind that the expected ratio was exactly 1.51 (i.e., $A^{DER_1^{3ph}}/A^{DER_2^{3ph}}$).

Most importantly, the outcome of this coordinated operation of the inverters can be visualized in the PCC quantities in Fig. 6.23(a). It is clearly noticed that such currents became practically balanced (i.e., comparing to Fig.6.22(c)), indicating that the targeted active and reactive unbalanced currents were adequately shared by the DERs^{3ph}. Besides, as a result of the distributed compensation provided by the strategy, a null current flowed through the neutral conductor at PCC. Finally, it can also be seen at phase a that the PCC current became practically in-phase with its respective voltage, as the unbalanced reactive current parcel was supplied by the inverters.

A final remark is made with regard to the initialization of the GCBC strategy. In Fig. 6.23(b) the related transient instants of the MG operation are demonstrated, until the steady state condition of Fig. 6.23(a) was obtained. It can be seen that the coordination of the two inverters did not cause any overcurrents, at the PCC or at the DERs^{3ph}, and that steady state was achieved after approximately six fundamental cycles. If compared to the previous experimental results shown within this thesis, it can be stated that a similar performance was obtained for the MG operation, even when compensation of unbalanced currents was not imposed as operational purpose.

6.5 Highlights for Optimal Coordination of DERs in AC Microgrids

Management of AC MGs comprising multiple elements is a complex task, as many operational objectives are usually desired to be pursued at the same time [219], even though not all of them can be fully achieved. To more elegantly determine operation setpoints for MGs, the formulation of optimization problems and their incorporation into the coordination of inverters is an interesting alternative [52, 66, 150, 217, 220]. The benefits of employing optimal management in MGs are typically represented by enhanced exploitation of DERs (e.g., higher energy generation), achievement of better power quality indexes (e.g., higher PF), increased energy efficiency (e.g., smaller power losses), and many others [221, 222].

Although the implementation of optimal approaches is an attractive option to achieve enhanced MG operation, the formulation of objective functions for optimizing operational purposes is not trivial. Moreover, even when objective functions are adequately derived, it is imperative to determine which optimization algorithms will be adopted to solve the optimal problem. A careful consideration of this choice is important because many algorithms might be applicable [223], but they present different features with regard to the finding optimal solutions. Yet, one also needs to keep in mind that algorithms usually need to fit within the requirements of control architectures (e.g., processing time, computational burden, realistic use MG elements, etc.) [224].

When strategies such as the GCBC strategy are used to coordinate DERs in MGs, the derivation of the optimal problem becomes even more cumbersome, as the complexity is proportional to the number of control purposes targeted. Thus, this section aims to shed light on how an AC MG incorporating the GCBC strategy can take advantage of its formulation to derive objective functions for optimal management. More specifically, given a set of optimization purposes (OPs), it is highlighted which of the main variables of the GCBC approach would be most suitable for use. Five OPs are herein considered, knowing that they incorporate generic aspects to be optimized when an efficient and reliable MG operation is intended. The suggested usage of the GCBC variables is presented in Table 6.7.

The first purpose (i.e., OP_1) usually considered in optimal management of MGs is related to energy exploitation. Since RESs and ESSs are vital elements in MGs and they are tied to economic aspects, maximization of active power injection is commonly devised [66]. Since the GCBC variable responsible for that concern is the term $I_{1||_m}$, it

Table 6.7: Suggested usage of the main variables of the GCBC strategy to implement optimal approaches for MG control.

Optimization Purpose (OP)		$I_{1\|\|_m}$	$I_{1\perp_m}$	$I_{h\|\|_m}$ $I_{h\perp_m}$	$\sqrt{\Delta I_m}$	I_{nom_m}	$I_{1\|\|max_m}$ $I_{1\|\|sto_m}$
OP_1	*Energy Exploitation*	✓	✗	✗	✗	✓	✓
OP_2	*Economic Benefit*‡	✓	✗	✗	✗	✗	✓
OP_3	*Power Quality Performance*	✓	✓	✓	✗	✓	✗
OP_4	*Efficient Usage of DERs*	✓	✓	✓	✓	✓	✓
OP_5	*Ancillary Services*	✓	✓	✓	✓	✓	✓

‡Disregarding ancillary service provision.

needs to be taken into account into the formulation of an objective function. Moreover, it also important to incorporate the terms $I_{1||max_m}$ and $I_{1||sto_m}$, as they quantitatively constraint the amount of active current that can be injected into the MG.

Economic dispatch of MGs is one of the main drivers of optimal management [24, 150]. This occurs because a MG manager undoubtedly desires to obtain as much profit as possible from energy assets. For this purpose (i.e., OP_2), active power export and import are the main functionalities impacting on how much energy needs to be sold or bought by the MG. Hence, the term $I_{1||_m}$ is again the most important one, and $I_{1||max_m}$ represents the most ideal scenario of energy exportation. On the other hand, $I_{1||sto_m}$ incorporates important features to minimize costs in energy imports, as the MG management can consider to store energy according to electricity prices.

Some works in the literature [66, 225] also indicate that optimal management can be applied to obtain improved power quality performance. Aspects such as reactive power compensation, as well as mitigation of unbalances and harmonics, can be devised in formulations targeting OP_3. For the GCBC scenario, the terms $I_{1\perp_m}$, $I_{h||_m}$ and $I_{h\perp_m}$ (i.e., for $h > 1$) can be adopted to derive objective functions, which would usually target minimization of such quantities at a given node of the MG. In addition, since the term $I_{1||_m}$ can be adopted to tackle overvoltage conditions, it might also be an interesting variable for optimization approaches.

During practical implementations, the exploitation of DERs is not always fully achieved due to their limited power ratings or potentially intermittent energy generation features. Therefore, when inverters operate under limited capability, the formulation of optimization problems can provide a means to extract as much as possible from their functionalities. For instance, approaches similar to [216] and [217] allow us to optimally allocate the remaining capabilities of inverters to desired functionalities for the MG. This allows us to achieve efficient usage of their potentials, as desired for OP_4. Since the full exploitation of DERs is intended, all the GCBC variables gathered in Table 6.7 should be taken into account of in the optimal problem, either participating in the objective function, or being part of the formulated constraints.

Finally, ancillary services can be offered according to multiple goals internally or externally to the MG (i.e., as discussed in Chapter 2). Thus, all GCBC variables can also be considered to determine optimal setpoints for voltage/frequency regulation, peak shaving features, reactive power dispatch, and many other actions.

Based on the above-mentioned discussions, it can be concluded that the GCBC strategy can be incorporated into the optimal management of AC MGs, allowing us to achieve enhanced operational aspects.

6.6 Chapter Conclusions

In this chapter, advanced control functionalities have been presented, being integrated into the GCBC strategy, aiming at achieving enhanced MG operation. Such complementary functionalities can be employed to offer improved energy efficiency and better power quality conditions internally, as well as externally, to the MG. For instance, it has been demonstrated that, if the MG suffers from voltage distortions propagated throughout distribution systems, its PCC can be shaped as a variable resistor, guaranteeing high power factor operation. Additionally, such resistive shaping incorporates resonance damping features, which allow the possibility to increase the stiffness of the MG.

A voltage regulation approach has been presented, allowing nd- and d-DERs to be steered in synergy, integrating local and coordinated Volt/Watt and Volt/VAR actions. Based on such a functionality, overvoltages can be automatically mitigated while supporting an increased penetration of DERs, as power curtailment is avoided whenever possible. Lastly, the CPT was integrated into the formulation of the GCBC strategy, providing a means to support the compensation of unbalanced active and reactive currents, ensuring that the MG PCC operates as a balanced resistor. In addition, comments were made in regard to how the GCBC strategy can used to incorporate optimal features for the management of MGs.

All the control functionalities demonstrated in this chapter are supported without losing the main properties of the GCBC strategy, guaranteeing model-free features and plug-and-play capability. Furthermore, the proposed advanced functionalities can be interpreted as energy services that can be traded in transactive interactions of the MG.

Chapter 7

Conclusions

7.1 General Conclusions

In this thesis, a multi-purpose coordinated control strategy has been presented to flexibly steer inverter-based DERs, focusing on the scenario of LV MGs participating in transactive energy markets. Such a control approach, namely GCBC, relies on a hierarchical architecture, and it uses a centralized unit (i.e. the MGCC) to adjust the operation of inverters according to the desired MG operational goals.

The GCBC strategy is formulated based on the analysis of peak currents flowing within the MG, and it presents a model-free feature, which provides a means to coordinate DERs without previous knowledge of the MG's physical parameters (e.g, line impedances values). A synergistic interaction between both dispatchable and non-dispatchable inverters is supported by the GCBC, guaranteeing that the strategy can cope with realistic scenarios of LV MGs. In addition, the coordinated steering of DERs allows the MG to achieve internal objectives, also offering operational functionalities that support the energy planning of an upstream distribution grid.

The multifaceted perspective of transactive MGs was discussed in Chapter 2, pointing out their multiple possibilities of interactions in energy markets, under both financial and technical aspects. Besides this, a transactive control framework was presented to clarify the participation of MGs as market players, as well as highlighting their technical role in the scenario of cellular electric systems. Moreover, an extended outlook on ancillary functionalities was discussed, situating MGs as key players in the provision of grid-supporting energy services.

The infrastructure of the considered LV MG topology was presented in Chapter 3, explaining the scope of application of this thesis. The elementary local control infrastructures of nd- and d-DERs were briefly presented, showing that they can offer active power conversion from RESs or ESSs, and that smart inverters can also support the provision of ancillary services. The three-layer hierarchical architecture of the GCBC strategy was explained in detail, highlighting how the approach steers DERs, as well as explaining how the MG interacts with external agents. Additionally, the basic formulation of the GCBC strategy was also discussed, demonstrating that the analysis of peak currents can offer current sharing capabilities for DERs, as well as showing that the MG can be controlled as a single dispatchable entity.

Multiple purposes of operation for the MG were exemplified in Chapter 4, by means of simulation and experimental results. It has been demonstrated that the GCBC strategy allows us to control inverters to pursue active and reactive current sharing, supplying loads and alleviating the upstream grid from this burden. Moreover, the purpose of achieving distributed and selective compensation of harmonic currents has been demonstrated, by itself and while integrated into the control of fundamental currents. Thus, beyond controlling inverters to compensate non-active currents, the GCBC offers to the MG the possibility of operating under full self-consumption mode. Yet, as intermittency is inherent to distributed generation systems, the strategy can cope with variable generation profiles.

The MG power dispatchability has also been explored in Chapter 4, giving support to the major transactive aspect of the MG, which is related to energy trading capability. Both absorption and dispatch of active currents can be controlled at the MG PCC, as long as DERs present sufficient energy generation and nominal capabilities to support the intended goal. Yet, such a feature is conditional on the fact that MG contractual constraints should always be obeyed, as well as compliance with grid codes. Furthermore, reactive power dispatch can be offered either independently or concomitantly to active power control, giving more flexibility for the MG to sell energy services in transactive markets. Chapter 4 has also demonstrated that the MG functionalities offered by the GCBC strategy are not affected by the features of line impedances, guaranteeing that proportional sharing of currents occurs among DERs, in contrast to strategies such as the conventional droop control.

Since LV MGs are usually weak systems, they are susceptible to operating under non-ideal scenarios. Hence, Chapter 5 highlighted the particularities of the GCBC approach when inverters operate under limited power ratings. Additionally, it has been demonstrated that the strategy endures operation when voltages are highly distorted, as well as that it presents voltage ride-through capabilities. Another interesting feature related to the adoption of the GCBC strategy, particularly for homogeneous MGs, is that it provides voltage quality improvement as an indirect outcome of the proportional sharing of non-active currents. Finally, considerations on stability, communication matters and power coupling are concluded in Chapter 5, indicating that the GCBC presents operational concerns that, although not critical from a stability standpoint, need to be taken into account prior to deploying the strategy.

Advanced control functionalities have been presented in Chapter 6, providing enhanced operational features for LV MGs. It has been demonstrated that, based on a few adaptions of the GCBC strategy, the MG can be shaped to operate as a variable resistor when voltage distortions exist, allowing high power factor operation at the PCC, and supporting the damping of harmonic resonances. Voltage regulation has also been devised in Chapter 6, by means of an automatic approach that provides coordinated Volt/Watt and Volt/VAR actions, allowing us to minimize the curtailment of active power from nd-DERs. Finally, an approach based on the CPT was incorporated into the GCBC, providing a means to achieve distributed compensation of unbalanced active and reactive currents.

In summary, the overall conclusion of this thesis is that the GCBC strategy allows the possibility of offering multiple functionalities for LV MGs. Both internal and external operational purposes of MGs can be considered while exploiting DERs, and the integration of technical and market-related objectives can be taken into account. Thus, the control approach can be seen as an innovative alternative to coordinate DERs in MGs, contributing to the movement of the electric sector towards the implementation of smarter grids.

7.2 Future Works

The following scientific aspects have been identified as prospective topics for future works, aiming at expanding and giving continuity to the contributions found within this PhD thesis.

a) **Optimal regulation of the MG operation:** Even though multiple operational purposes can be offered by the GCBC strategy, MGs must dynamically adjust their goals according to real-life oriented market indexes and energy generation forecasts [220]. Thus, optimal approaches [66, 217] can be devised to efficiently exploit the capabilities of DERs, steering them to better attend to the needs of the MG. Multi-objective actions can be modeled for the MG, allowing the possibility to optimize its internal usage of energy, as well as improving economic profitability for prosumers and the MG manager;

b) **MG power dispatchability supporting cellular electric systems:** The coordinated control strategy proposed in this thesis allows us to flexibly adjust the MG power dispatchability, also shaping the PCC to emulate different behaviors for the upstream grid. Consequently, the external interactions of the MG can be included in the energy planning horizon of cellular electric systems (i.e., power systems comprising multiple interconnected and supervised MGs, such as in cluster topologies [52, 55]). Such operationality can to incorporate controllable provision of distributed energy generation in an utility scale. Moreover, ancillary services can be offered under the power system perspective, supporting voltage and frequency regulation, congestion management, as well as power quality improvement;

c) **Coordination of single- and three-phase DERs arbitrarily connected to three-phase MGs:** Although in this thesis simulation and experimental results only considered either single- or three-phase inverters, LV MGs commonly present DERs based on both topologies. Similarly to [68] and [71], the GCBC strategy can be extended to accommodate both single- and three-phase inverters in three-phase MGs to support the sharing of fundamental currents. Additionally, distributed compensation of harmonic currents using both inverter topologies, which has been rarely studied in the literature, can be investigated based on the GCBC strategy;

d) **Coordination of DERs under asymmetrical voltages:** Asymmetries in voltages often occur in weak grids, and the coordination of DERs should take that issue into account. Further studies can conducted using the GCBC strategy to understand how DERs can be steered to mitigate voltage unbalances, as well as to shape the MG PCC to achieved different operational behaviors, such as the one of balanced conductances or susceptances [148];

e) **Redesign the GCBC strategy following a distributed control architecture:** Since the GCBC strategy relies on a centralized architecture, the existence of the MGCC is unavoidable. Nevertheless, if the calculation required to attain control references can be performed under a distributed architecture [226], multi-purpose control can be supported without a central agent. Thus, improved reliability can be achieved, as communication issues become less critical;

f) **Fair voltage regulation:** The automatic voltage regulation scheme proposed in Section 6.3 coordinates d-DERs only proportionally to their nominal ratings and generation capabilities. Consequently, the natural discrepancy occurring among their voltage magnitudes, which is caused by voltage drops through line impedances, is not taken into account. Hence, if the concept of fair overvoltage [205] control is incorporated to the GCBC strategy, all d-DERs (i.e., even those placed close to the DST) can contribute to voltage regulation proportionally to their voltage magnitudes. This feature would allow us to obtain a more equalized voltage profile for all nodes of the MG.

Bibliography

[1] G. Luderer, M. Pehl, and A. Arvesen, “Environmental co-benefits and adverse side-effects of alternative power sector decarbonization strategies,” *Nature Communications*, vol. 10, pp. 1–13, 2019.

[2] IRENA, *Global Renewables Outlook: Energy Transformation 2050.* International Renewable Energy Agency, Abu Dhabi, 2020.

[3] N. Vandycke, “World Economic Forum: Can electricity decarbonize the energy sector?” https://www.weforum.org/agenda/2020/04/can-electricity-decarbonize-the-energy-sector/, Accessed: 10.09.2020.

[4] A. J. Veldhuis, M. Leach, and A. Yang, “The impact of increased decentralised generation on the reliability of an existing electricity network,” *Applied Energy*, vol. 215, pp. 479–502, 2018.

[5] S. Wang, Y. Huang, I. Vorushylo, H. Chen, D. McLarnon, P. MacArtain, and N. Hewitt, “Economic assessment of high renewable energy penetration scenario in 2030 on the interconnected irish power system,” *Energy Policy*, vol. 145, p. 111774, 2020.

[6] K. Bell and S. Gill, “Delivering a highly distributed electricity system: Technical, regulatory and policy challenges,” *Energy Policy*, vol. 113, pp. 765–777, 2018.

[7] G. P. Holdmann, R. W. Wies, and J. B. Vandermeer, “Renewable energy integration in alaska’s remote islanded microgrids: Economic drivers, technical strategies, technological niche development, and policy implications,” *Proceedings of the IEEE*, vol. 107, no. 9, pp. 1820–1837, 2019.

[8] *IEEE Standard for Interconnection and Interoperability of Distributed Energy Resources with Asiated Electric Power Systems Interfaces*, IEEE Std. 1547-2018 (Revision of IEEE Std 1547-2003), 2018.

[9] P. Jonke, B. Sumanta, F. Andrén, J. Stöckl, and T. Strasser, “Rapid prototyping of distributed energy resources integrating ICT and power electronics design,” in *IECON 2014 - 40th Annual Conference of the IEEE Industrial Electronics Society*, 2014, pp. 3591–3597.

[10] N. Mohan, T. M. Undeland, and W. P. Robbins, *Power Electronics. Converters, Applications and Design*, 3rd ed. John Wiley and Sons, Inc, 2003.

[11] J. Rocabert, A. Luna, F. Blaabjerg, and P. Rodríguez, "Control of power converters in ac microgrids," *IEEE Transactions on Power Electronics*, vol. 27, no. 11, pp. 4734–4749, 2012.

[12] A. Gopstein et al, "Draft: NIST framework and roadmap for smart grid interoperability standards, release 4.0," National Institute of Standards and Technology (NIST), Tech. Rep., July 2020.

[13] X. Fang, S. Misra, G. Xue, and D. Yang, "Smart grid — the new and improved power grid: A survey," *IEEE Communications Surveys Tutorials*, vol. 14, no. 4, pp. 944–980, 2012.

[14] B. Mirafzal and A. Adib, "On grid-interactive smart inverters: Features and advancements," *IEEE Access*, vol. 8, pp. 160 526–160 536, 2020.

[15] B. Arbab-Zavar, E. J. Palacios-Garcia, J. C. Vasquez, and J. M. Guerrero, "Smart inverters for microgrid applications: A review," *Energies*, vol. 12, pp. 1–22, 2019.

[16] Y. Yang, F. Blaabjerg, H. Wang, and M. G. Simoes, "Power control flexibilities for grid-connected multi-functional photovoltaic inverters," *IET Renewable Power Generation*, vol. 10, no. 4, pp. 504–513, 2016.

[17] B. Enayati et al, "Impact of IEEE 1547 standard on smart inverters," The Institute of Electrical and Electronics Engineers (IEEE), Tech. Rep. PES-TR67, May 2018.

[18] J. C. Vasquez, R. A. Mastromauro, J. M. Guerrero, and M. Liserre, "Voltage support provided by a droop-controlled multifunctional inverter," *IEEE Transactions on Industrial Electronics*, vol. 56, no. 11, pp. 4510–4519, 2009.

[19] F. P. Marafao, D. I. Brandao, A. Costabeber, and H. K. M. Paredes, "Multi-task control strategy for grid-tied inverters based on conservative power theory," *IET Renewable Power Generation*, vol. 9, no. 2, pp. 154–165, 2015.

[20] Y. Xue and J. M. Guerrero, "Smart inverters for utility and industry applications," in *Proceedings of PCIM Europe 2015; International Exhibition and Conference for Power Electronics, Intelligent Motion, Renewable Energy and Energy Management*, 2015, pp. 1–8.

[21] Y. Qi, P. Lin, Y. Wang, and Y. Tang, "Two-dimensional impedance-shaping control with enhanced harmonic power sharing for inverter-based microgrids," *IEEE Transactions on Power Electronics*, vol. 34, no. 11, pp. 11 407–11 418, 2019.

[22] S. Liao, M. Huang, X. Zha, and J. M. Guerrero, “Emulation of multi-inverter integrated weak grid via interaction-preserved aggregation,” *IEEE Journal of Emerging and Selected Topics in Power Electronics*, pp. 1–1, 2020.

[23] Q. Peng, Q. Jiang, Y. Yang, T. Liu, H. Wang, and F. Blaabjerg, “On the stability of power electronics-dominated systems: Challenges and potential solutions,” *IEEE Transactions on Industry Applications*, vol. 55, no. 6, pp. 7657–7670, 2019.

[24] F. Chen, M. Chen, Q. Li, K. Meng, Y. Zheng, J. M. Guerrero, and D. Abbott, “Cost-based droop schemes for economic dispatch in islanded microgrids,” *IEEE Transactions on Smart Grid*, vol. 8, no. 1, pp. 63–74, 2017.

[25] J. R. S. Junior, D. I. Brandao, N. T. D. Fernandes, W. Utuerbey, and B. Cardoso, “Multifunctional dispatchable microgrids,” *Applied Energy*, vol. 282, no. Part A, p. 116165, 2021.

[26] A. Adib and B. Mirafzal, “Virtual inductance for stable operation of grid-interactive voltage source inverters,” *IEEE Transactions on Industrial Electronics*, vol. 66, no. 8, pp. 6002–6011, 2019.

[27] A. Micallef, “Review of the current challenges and methods to mitigate power quality issues in single-phase microgrids,” *IET Generation, Transmission Distribution*, vol. 13, no. 11, pp. 2044–2054, 2019.

[28] J. He, Y. W. Li, R. Wang, and C. Zhang, “Analysis and mitigation of resonance propagation in grid-connected and islanding microgrids,” *IEEE Transactions on Energy Conversion*, vol. 30, no. 1, pp. 70–81, 2015.

[29] *IEEE Standard for the Specification of Microgrid Controllers*, IEEE Std. 2030.7-2017, 2018.

[30] L. S. De Araujo, A. M. S. Alonso, and D. I. Brandao, “Decentralized control of voltage- and current-controlled converters based on ac bus signaling for autonomous microgrids,” *IEEE Access*, vol. 8, pp. 202 075–202 089, 2020.

[31] J. M. Guerrero, J. C. Vasquez, J. Matas, L. G. de Vicuna, and M. Castilla, “Hierarchical control of droop-controlled ac and dc microgrids—a general approach toward standardization,” *IEEE Transactions on Industrial Electronics*, vol. 58, no. 1, pp. 158–172, 2011.

[32] D. E. Olivares, A. Mehrizi-Sani, A. H. Etemadi, C. A. Cañizares, R. Iravani, M. Kazerani, A. H. Hajimiragha, O. Gomis-Bellmunt, M. Saeedifard, R. Palma-Behnke, G. A. Jiménez-Estévez, and N. D. Hatziargyriou, “Trends in microgrid control,” *IEEE Transactions on Smart Grid*, vol. 5, no. 4, pp. 1905–1919, 2014.

[33] R. H. Lasseter, “Smart distribution: Coupled microgrids,” *Proceedings of the IEEE*, vol. 99, no. 6, pp. 1074–1082, 2011.

[34] Z. Li, M. Shahidehpour, F. Aminifar, A. Alabdulwahab, and Y. Al-Turki, “Networked microgrids for enhancing the power system resilience,” *Proceedings of the IEEE*, vol. 105, no. 7, pp. 1289–1310, 2017.

[35] A. Hirsch, Y. Parag, and J. M. Guerrero, “Microgrids: A review of technologies, key drivers, and outstanding issues,” *Renewable and Sustainable Energy Reviews*, vol. 90, pp. 402–411, 2018.

[36] M. Carpintero-Rentería, D. Santos-Martín, and J. M. Guerrero, “Microgrids literature review through a layers structure,” *Energies*, vol. 12, pp. 1–22, 2019.

[37] M. F. Zia, M. Benbouzid, E. Elbouchikhi, S. M. Muyeen, K. Techato, and J. M. Guerrero, “Microgrid transactive energy: Review, architectures, distributed ledger technologies, and market analysis,” *IEEE Access*, vol. 8, pp. 19 410–19 432, 2020.

[38] A. Majzoobi and A. Khodaei, “Application of microgrids in providing ancillary services to the utility grid,” *Energy*, vol. 123, pp. 555–563, 2017.

[39] Y. Wu, Y. Wu, J. M. Guerrero, and J. C. Vasquez, “Digitalization and decentralization driving transactive energy internet: Key technologies and infrastructures,” *International Journal of Electrical Power & Energy Systems*, vol. 126, no. Part A, p. 106593, 2021.

[40] D. Holmberg et al, “NIST transactive energy modeling and simulation challenge phase ii final report,” National Institute of Standards and Technology (NIST), Tech. Rep. 1900-603, May 2019.

[41] A. Micallef, M. Apap, C. Spiteri-Staines, and J. M. Guerrero, “Single-phase microgrid with seamless transition capabilities between modes of operation,” *IEEE Transactions on Smart Grid*, vol. 6, no. 6, pp. 2736–2745, 2015.

[42] A. M. S. Alonso, H. K. M. Paredes, J. A. O. Filho, J. P. Bonaldo, D. I. Brandão, and F. P. Marafão, “Selective power conditioning in two-phase three-wire systems based on the conservative power theory,” in *2019 IEEE Industry Applications iety Annual Meeting*, 2019, pp. 1–6.

[43] D. I. Brandao, R. Patric dos Santos, W. Silva, T. R. De Oliveira, and P. F. Donoso-Garcia, “Model-free energy management system for hybrid ac/dc microgrids,” *IEEE Transactions on Industrial Electronics*, pp. 1–1, 2020.

[44] SMA, “The self-consumption bonus: Information and details regarding the self-consumption of solar energy,” https://www.sma.de/en/partners/knowledgebase/the-self-consumption-bonus.html, Accessed: 2020-12-29.

[45] P. Tenti, H. K. M. Paredes, and P. Mattavelli, “Conservative power theory, a framework to approach control and accountability issues in smart microgrids,” *IEEE Transactions on Power Electronics*, vol. 26, no. 3, pp. 664–673, 2011.

[46] FAPESP. Interdisciplinary Research Activities in Electric Smart Grids. https://bv.fapesp.br/en/auxilios/97003/interdisciplinary-research-activities-in-electric-smart-grids/. Accessed on 05.01.2021.

[47] NB_POCCREI. Norwegian-Brazilian collaboration on Power Theories and Cooperative Control for Renewable Energy Integration. https://app.cristin.no/projects/show.jsf?id=568245. Accessed on 05.01.2021.

[48] H. Kim, J. Lee, S. Bahrami, and V. W. S. Wong, “Direct energy trading of microgrids in distribution energy market,” *IEEE Transactions on Power Systems*, vol. 35, no. 1, pp. 639–651, 2020.

[49] A. M. Alabdullatif, E. H. Gerding, and A. Perez-Diaz, “Market design and trading strategies for community energy markets with storage and renewable supply,” *Energies*, vol. 13, p. 972, 2020.

[50] J. M. Zepter et al, “Prosumer integration in wholesale electricity markets: Synergies of peer-to-peer trade and residential storage,” *Energy and Buildings*, vol. 184, pp. 163–176, 2019.

[51] T. Sousa et al, “Peer-to-peer and community-based markets: A comprehensive review,” *Renewable and Sustainable Energy Reviews*, vol. 104, pp. 1367–378, 2019.

[52] Y. Han, K. Zhang, H. Li, E. A. A. Coelho, and J. M. Guerrero, “Mas-based distributed coordinated control and optimization in microgrid and microgrid clusters: A comprehensive overview,” *IEEE Transactions on Power Electronics*, vol. 33, no. 8, pp. 6488–6508, 2018.

[53] L. Gkatzikis, I. Koutsopoulos, and T. Salonidis, “The role of aggregators in smart grid demand response markets,” *IEEE Journal on Selected Areas in Communications*, vol. 31, no. 7, pp. 1247–1257, 2013.

[54] M. Park, J. Lee, and D. J. Won, “Demand response strategy of energy prosumer based on robust optimization through aggregator,” *IEEE Access*, vol. 8, pp. 202 969–202 979, 2020.

[55] X. Zhou, L. Zhou, Y. Chen, J. M. Guerrero, A. Luo, W. Wu, and L. Yang, "A microgrid cluster structure and its autonomous coordination control strategy," *International Journal of Electrical Power & Energy Systems*, vol. 100, pp. 69–80, 2018.

[56] S. Li, J. Lian, A. J. Conejo, and W. Zhang, "Transactive energy systems: The market-based coordination of distributed energy resources," *IEEE Control Systems Magazine*, vol. 40, no. 4, pp. 26–52, 2020.

[57] M. Khorasany et al, "Transactive energy market for energy management in microgrids: The monash microgrid case study," *Energies*, vol. 13, pp. 1–13, 2020.

[58] O. Abrishambaf, F. Lezama, P. Faria, and Z. Vale, "Towards transactive energy systems: An analysis on current trends," *Energy Strategy Reviews*, vol. 26, p. 100418, 2019.

[59] S. M. Nosratabadi, R. Hooshmand, and E. Gholipour, "A comprehensive review on microgrid and virtual power plant concepts employed for distributed energy resources scheduling in power systems," *Renewable and Sustainable Energy Reviews*, vol. 67, pp. 341–363, 2017.

[60] T. L. Vandoorn, B. Zwaenepoel, J. D. M. De Kooning, B. Meersman, and L. Vandevelde, "Smart microgrids and virtual power plants in a hierarchical control structure," in *2011 2nd IEEE PES International Conference and Exhibition on Innovative Smart Grid Technologies*, 2011, pp. 1–7.

[61] T. Pinto et al, "Decision support for negotiations among microgrids using a multiagent architecture," *Energies*, vol. 11, p. 2526, 2018.

[62] Y. Zhao, J. Yu, M. Ban, Y. Liu, and Z. Li, "Privacy-preserving economic dispatch for an active distribution network with multiple networked microgrids," *IEEE Access*, vol. 6, pp. 38 802–38 819, 2018.

[63] P. Wu, W. Huang, N. Tai, and S. Liang, "A novel design of architecture and control for multiple microgrids with hybrid ac/dc connection," *Applied Energy*, vol. 210, pp. 1002–1016, 2018.

[64] H. Abedini, T. Caldognetto, P. Mattavelli, and P. Tenti, "Real-time validation of power flow control method for enhanced operation of microgrids," *Energies*, vol. 13, no. 5959, pp. 1–19, 2020.

[65] M. A. I. Martins, R. Fernandes, and M. L. Heldwein, "Proposals for regulatory framework modifications for microgrid insertion – the Brazil use case," *IEEE Access*, vol. 8, pp. 94 852–94 870, 2020.

[66] D. I. Brandao, W. M. Ferreira, A. M. S. Alonso, E. Tedeschi, and F. P. Marafão, "Optimal multiobjective control of low-voltage ac microgrids: Power flow regulation and compensation of reactive power and unbalance," *IEEE Transactions on Smart Grid*, vol. 11, no. 2, pp. 1239–1252, 2020.

[67] F. Rahimi and A. Ipakchi, "Using a transactive energy framework: Providing grid services from smart buildings," *IEEE Electrification Magazine*, vol. 4, no. 4, pp. 23–29, 2016.

[68] D. I. Brandao, T. Caldognetto, F. P. Marafão, M. G. Simões, J. A. Pomilio, and P. Tenti, "Centralized control of distributed single-phase inverters arbitrarily connected to three-phase four-wire microgrids," *IEEE Transactions on Smart Grid*, vol. 8, no. 1, pp. 437–446, 2017.

[69] Q. Sun, J. Zhou, J. M. Guerrero, and H. Zhang, "Hybrid three-phase/single-phase microgrid architecture with power management capabilities," *IEEE Transactions on Power Electronics*, vol. 30, no. 10, pp. 5964–5977, 2015.

[70] D. Wang, J. Qiu, L. Reedman, K. Meng, and L. L. Lai, "Two-stage energy management for networked microgrids with high renewable penetration," *Applied Energy*, vol. 226, pp. 39–48, 2018.

[71] D. I. Brandao, L. S. Araujo, A. M. S. Alonso, G. L. dos Reis, E. V. Liberado, and F. P. Marafão, "Coordinated control of distributed three- and single-phase inverters connected to three-phase three-wire microgrids," *IEEE Journal of Emerging and Selected Topics in Power Electronics*, vol. 8, no. 4, pp. 3861–3877, 2020.

[72] S. Y. Mousazadeh Mousavi, A. Jalilian, M. Savaghebi, and J. M. Guerrero, "Autonomous control of current- and voltage-controlled dg interface inverters for reactive power sharing and harmonics compensation in islanded microgrids," *IEEE Transactions on Power Electronics*, vol. 33, no. 11, pp. 9375–9386, 2018.

[73] Y. Yu, Z. Cai, and Y. Huang, "Energy storage arbitrage in grid-connected microgrids under real-time market price uncertainty: A double-q learning approach," *IEEE Access*, vol. 8, pp. 54 456–54 464, 2020.

[74] M. Soshinskaya, W. H. Crijns-Graus, J. M. Guerrero, and J. C. Vasquez, "Microgrids: Experiences, barriers and success factors," *Renewable and Sustainable Energy Reviews*, vol. 40, pp. 659–672, 2014.

[75] M. Eskandari, L. Li, M. H. Moradi, P. Siano, and F. Blaabjerg, "Optimal voltage regulator for inverter interfaced distributed generation units part i," *IEEE Transactions on Sustainable Energy*, vol. 11, no. 4, pp. 2813–2824, 2020.

[76] K. Mahmud, M. S. H. Nizami, J. Ravishankar, M. J. Hossain, and P. Siano, "Multiple home-to-home energy transactions for peak load shaving," *IEEE Transactions on Industry Applications*, vol. 56, no. 2, pp. 1074–1085, 2020.

[77] P. Tenti and T. Caldognetto, "On microgrid evolution to local area energy network (e-lan)," *IEEE Transactions on Smart Grid*, vol. 10, no. 2, pp. 1567–1576, 2019.

[78] G. V. B. Kumar and K. Palanisamy, "A review of energy storage participation for ancillary services in a microgrid environment," *Energies*, vol. 5, p. 63, 2020.

[79] R. Kabiri, D. G. Holmes, B. P. McGrath, and L. G. Meegahapola, "Lv grid voltage regulation using transformer electronic tap changing, with pv inverter reactive power injection," *IEEE Journal of Emerging and Selected Topics in Power Electronics*, vol. 3, no. 4, pp. 1182–1192, 2015.

[80] S. H. Toghroljerdi and J. Ostergaard, "Methods and strategies for overvoltage prevention in low voltage distribution systems with pv," *IET Renewable Power Generation*, vol. 11, no. 2, pp. 1–26, 2016.

[81] B. Olek and M. Wierzbowski, "Local energy balancing and ancillary services in low-voltage networks with distributed generation, energy storage, and active loads," *IEEE Transactions on Industrial Electronics*, vol. 62, no. 4, pp. 2499–2508, 2015.

[82] H. Akagi, "Control strategy and site selection of a shunt active filter for damping of harmonic propagation in power distribution systems," *IEEE Transactions on Power Delivery*, vol. 12, no. 1, pp. 354–363, 1997.

[83] J. Enslin and P. Heskes, "Harmonic interaction between a large number of distributed power inverters and the distribution network," *IEEE Transactions on Power Electronics*, vol. 19, no. 6, pp. 1586–1593, 2004.

[84] T. Wu, M. Rothleder, Z. Alaywan, and A. D. Papalexopoulos, "Pricing energy and ancillary services in integrated market systems by an optimal power flow," *IEEE Transactions on Power Systems*, vol. 19, no. 1, pp. 339–347, 2004.

[85] C. Chen, J. Wang, F. Qiu, and D. Zhao, "Resilient distribution system by microgrids formation after natural disasters," *IEEE Transactions on Smart Grid*, vol. 7, no. 2, pp. 958–966, 2016.

[86] J. Abdubannaev, S. YingYun, A. Xin, N. Makhamadjanova, and S. Rakhimov, "Investigate networked microgrids to enhance distribution network system resilience," in *2020 IEEE/IAS Industrial and Commercial Power System Asia (I CPS Asia)*, 2020, pp. 310–315.

[87] M. N. Ambia, K. Meng, W. Xiao, and Z. Y. Dong, “Nested formation approach for networked microgrid self-healing in islanded mode,” *IEEE Transactions on Power Delivery*, vol. 36, no. 1, pp. 452–464, 2021.

[88] G. Huang, J. Wang, C. Chen, J. Qi, and C. Guo, “Integration of preventive and emergency responses for power grid resilience enhancement,” *IEEE Transactions on Power Systems*, vol. 32, no. 6, pp. 4451–4463, 2017.

[89] N. Karthikeyan, J. P. Radhakrishna, B. Bak-Jensen, and J. W. Simpson-Porco, “Predictive control of flexible resources for demand response in active distribution networks,” *IEEE Transactions on Power Systems*, vol. 34, no. 4, pp. 2957–2969, 2019.

[90] A. M. S. Alonso, D. I. Brandao, E. Tedeschi, and F. P. Marafão, “Resistive shaping of interconnected low-voltage microgrids operating under distorted voltages,” *IEEE Journal of Emerging and Selected Topics in Power Electronics*, 2021.

[91] Q. Jiang, M. Xue, and G. Geng, “Energy management of microgrid in grid-connected and stand-alone modes,” *IEEE Transactions on Power Systems*, vol. 28, no. 3, pp. 3380–3389, 2013.

[92] Y. C. C. Wong, C. S. Lim, M. D. Rotaru, A. Cruden, and X. Kong, “Consensus virtual output impedance control based on the novel droop equivalent impedance concept for a multi-bus radial microgrid,” *IEEE Transactions on Energy Conversion*, vol. 35, no. 2, pp. 1078–1087, 2020.

[93] S. D. Kermany, M. Joorabian, S. Deilami, and M. A. S. Masoum, “Hybrid islanding detection in microgrid with multiple connection points to smart grids using fuzzy-neural network,” *IEEE Transactions on Power Systems*, vol. 32, no. 4, pp. 2640–2651, 2017.

[94] P. Monshizadeh, N. Monshizadeh, C. De Persis, and A. van der Schaft, “Output impedance diffusion into lossy power lines,” *IEEE Transactions on Power Systems*, vol. 34, no. 3, pp. 1659–1668, 2019.

[95] T. Caldognetto, P. Tenti, A. Costabeber, and P. Mattavelli, “Improving microgrid performance by cooperative control of distributed energy sources,” *IEEE Transactions on Industry Applications*, vol. 50, no. 6, pp. 3921–3930, 2014.

[96] K. Strunz et al, “Benchmark systems for network integration of renewable and distributed energy resources,” CIGRE, Tech. Rep. CIGRE Task Force C6.04.02, July 2009.

[97] A. M. S. Alonso, L. C. Afonso, D. I. Brandao, E. Tedeschi, and F. P. Marafao, “Considerations on communication infrastructures for cooperative operation of smart inverters,” in *2019 IEEE 15th Brazilian Power Electronics Conference and 5th IEEE Southern Power Electronics Conference (COBEP/SPEC)*, 2019, pp. 1–6.

[98] R. Torquato, G. R. Tessmer Hax, W. Freitas, and A. B. Nassif, “Impact assessment of high-frequency distortions produced by pv inverters,” *IEEE Transactions on Power Delivery*, pp. 1–1, 2020.

[99] Q. Liu, T. Caldognetto, and S. Buso, “Review and comparison of grid-tied inverter controllers in microgrids,” *IEEE Transactions on Power Electronics*, vol. 35, no. 7, pp. 7624–7639, 2020.

[100] S. Buso, T. Caldognetto, and Q. Liu, “Analysis and experimental characterization of a large-bandwidth triple-loop controller for grid-tied inverters,” *IEEE Transactions on Power Electronics*, vol. 34, no. 2, pp. 1936–1949, 2019.

[101] Y. Guan, Y. Wang, Y. Xie, Y. Liang, A. Lin, and X. Wang, “The dual-current control strategy of grid-connected inverter with lcl filter,” *IEEE Transactions on Power Electronics*, vol. 34, no. 6, pp. 5940–5952, 2019.

[102] S. Buso and P. Mattavelli, *Digital Control in Power Electronics*, 2nd ed. Morgan & Claypool, 2015.

[103] P. Mattavelli and F. P. Marafao, “Repetitive-based control for selective harmonic compensation in active power filters,” *IEEE Transactions on Industrial Electronics*, vol. 51, no. 5, pp. 1018–1024, 2004.

[104] J. P. Bonaldo, H. K. Morales Paredes, and J. A. Pomilio, “Control of single-phase power converters connected to low-voltage distorted power systems with variable compensation objectives,” *IEEE Transactions on Power Electronics*, vol. 31, no. 3, pp. 2039–2052, 2016.

[105] Q. Ouyang, Z. Wang, K. Liu, G. Xu, and Y. Li, “Optimal charging control for lithium-ion battery packs: A distributed average tracking approach,” *IEEE Transactions on Industrial Informatics*, vol. 16, no. 5, pp. 3430–3438, 2020.

[106] J. P. Bonaldo, J. A. O. Filho, A. M. S. Alonso, F. P. Marafao, and H. K. M. Paredes, “Modeling and control of a single-phase grid-connected inverter with lcl filter,,” *IEEE Latin America Transactions*, vol. 100, no. 1, pp. 1–10, 2020.

[107] L. Zhou et al, “Harmonic voltage distortion damping method for parallel-connected lcl-type inverters in islanded operation,” *IEEE Transactions on Industrial Electronics*, vol. 66, no. 11, pp. 9032–9044, 2019.

[108] Y. Han, H. Li, P. Shen, E. A. A. Coelho, and J. M. Guerrero, “Review of active and reactive power sharing strategies in hierarchical controlled microgrids,” *IEEE Transactions on Power Electronics*, vol. 32, no. 3, pp. 2427–2451, 2017.

[109] F. P. Marafão, A. M. d. S. Alonso, F. A. S. Gonçalves, D. I. Brandão, A. C. G. Martins, and H. K. Morales Paredes, “Trends and constraints on brazilian photovoltaic industry: Energy policies, interconnection codes, and equipment certification,” *IEEE Transactions on Industry Applications*, vol. 54, no. 5, pp. 4017–4027, 2018.

[110] H. M. A. Antunes et al, “A new multifunctional converter based on a series compensator applied to ac microgrids,” *International Journal of Electrical Power & Energy Systems*, vol. 102, pp. 160–170, 2018.

[111] M. Raeispour, H. Atrianfar, H. R. Baghaee, and G. B. Gharehpetian, “Resilient h∞ consensus-based control of autonomous ac microgrids with uncertain time-delayed communications,” *IEEE Transactions on Smart Grid*, vol. 11, no. 5, pp. 3871–3884, 2020.

[112] I. Ziouani et al, “Hierarchical control for flexible microgrid based on three-phase voltage source inverters operated in parallel,” *International Journal of Electrical Power & Energy Systems*, vol. 95, pp. 188–201, 2018.

[113] A. Chaouachi, R. M. Kamel, R. Andoulsi, and K. Nagasaka, “Multiobjective intelligent energy management for a microgrid,” *IEEE Transactions on Industrial Electronics*, vol. 60, no. 4, pp. 1688–1699, 2013.

[114] I. Serban, S. Céspedes, C. Marinescu, C. A. Azurdia-Meza, J. S. Gómez, and D. S. Hueichapan, “Communication requirements in microgrids: A practical survey,” *IEEE Access*, vol. 8, pp. 47 694–47 712, 2020.

[115] M. Saleh et al, “Impact of information and communication technology limitations on microgrid operation,” *Energies*, vol. 12, pp. 1–24, 2019.

[116] T. Caldognetto, S. Buso, P. Tenti, and D. I. Brandao, “Power-based control of low-voltage microgrids,” *IEEE Journal of Emerging and Selected Topics in Power Electronics*, vol. 3, no. 4, pp. 1056–1066, 2015.

[117] D. Wu, F. Tang, T. Dragicevic, J. C. Vasquez, and J. M. Guerrero, “Autonomous active power control for islanded ac microgrids with photovoltaic generation and energy storage system,” *IEEE Transactions on Energy Conversion*, vol. 29, no. 4, pp. 882–892, 2014.

[118] T. Vandoorn, B. Meersman, J. De Kooning, and L. Vandevelde, “Controllable harmonic current sharing in islanded microgrids: Dg units with programmable

resistive behavior toward harmonics," *IEEE Transactions on Power Delivery*, vol. 27, no. 2, pp. 831–841, 2012.

[119] I. Lorzadeh, H. A. Abyaneh, M. Savaghebi, and J. M. Guerrero, "A hierarchical control scheme for reactive power and harmonic current sharing in islanded microgrids," in *2015 17th European Conference on Power Electronics and Applications (EPE'15 ECCE-Europe)*, 2015, pp. 1–10.

[120] F. Najafi, M. Hamzeh, and M. Fripp, "Unbalanced current sharing control in islanded low voltage microgrids," *Energies*, vol. 1, no. 10, pp. 1–22, 2018.

[121] Z. Afshar, M. Mollayousefi, S. M. T. Bathaee, M. T. Bina, and G. B. Gharehpetian, "A novel accurate power sharing method versus droop control in autonomous microgrids with critical loads," *IEEE Access*, vol. 7, pp. 89 466–89 474, 2019.

[122] Z. Cheng, J. Duan, and M. Chow, "To centralize or to distribute: That is the question: A comparison of advanced microgrid management systems," *IEEE Industrial Electronics Magazine*, vol. 12, no. 1, pp. 6–24, 2018.

[123] M. S. Padua, S. M. Deckmann, and F. P. Marafao, "Frequency-adjustable positive sequence detector for power conditioning applications," in *2005 IEEE 36th Power Electronics Specialists Conference*, 2005, pp. 1928–1934.

[124] A. V. Oppenheim and R. W. Schafer, *Discrete-Time Signal Processing*, 3rd ed. Upper Saddle River, NJ, USA: Prentice Hall Press, 2009.

[125] S. Park et al, "A current control scheme based on multiple synchronous reference frames for parallel hybrid active filter," in *Proceedings IPEMC 2000. Third International Power Electronics and Motion Control Conference (IEEE Cat. No.00EX435)*, vol. 1, 2000, pp. 218–223 vol.1.

[126] L. Xavier et al, "Adaptive current control strategy for harmonic compensation in single-phase solar inverters," *Electric Power Systems Reserach*, vol. 142, pp. 84–95, 2017.

[127] Q. Xu, J. Xiao, X. Hu, P. Wang, and M. Y. Lee, "A decentralized power management strategy for hybrid energy storage system with autonomous bus voltage restoration and state-of-charge recovery," *IEEE Transactions on Industrial Electronics*, vol. 64, no. 9, pp. 7098–7108, 2017.

[128] A. M. S. Alonso, D. I. Brandao, F. P. Marafão, and E. Tedeschi, "Coordinated control of parallel power conditioners synthesizing resistive loads in single-phase ac microgrids," in *2019 21st European Conference on Power Electronics and Applications (EPE '19 ECCE Europe)*, 2019, pp. 1–9.

[129] E. V. Liberado, J. A. Pomilio, A. M. S. Alonso, E. Tedeschi, F. P. Marafão, and J. F. Guerreiro, “Three/four-leg inverter current control based on generalized symmetrical components,” in *2018 IEEE 19th Workshop on Control and Modeling for Power Electronics (COMPEL)*, 2018, pp. 1–7.

[130] A. M. S. Alonso, D. I. Brandao, E. Tedeschi, and F. P. Marafão, “Distributed selective harmonic mitigation and decoupled unbalance compensation by coordinated inverters in three-phase four-wire low-voltage networks,” *Electric Power Systems Research*, vol. 186, pp. 1–14, 2020.

[131] A. M. S. Alonso, L. O. Arenas, R. T. Hock Jr., H. Guillardi Jr., H. K. M. Paredes, F. A. S. Goncalves, and F. P. Marafão, “Experimental implementation of a single-phase microgrid comprising multiple inverters to validate coordinated control strategies,” in *14th IEEE International Conference on Industry Applications (INDUSCON)*, 2021, pp. 7–11.

[132] M. Depenbrock, “Quantities of a multiterminal circuit determined on the basis of Kirchhoff’s laws,” *European Transactions on Electrical Power*, vol. 8, no. 4, pp. 249–257, 1998.

[133] J. Arrillaga and N. R. Watson, *Power System Harmonics*, 2nd ed. John Wiley and Sons Ltd, 2003.

[134] H. Akagi, “New trends in active filters for power conditioning,” *IEEE Transactions on Industry Applications*, vol. 32, no. 6, pp. 1312–1322, 1996.

[135] L. Chen, X. Xu, L. Yao, and Q. Xu, “Study of a distribution line overload control strategy considering the demand response,” *Electric Power Components and Systems*, vol. 42, no. 9, pp. 970–983, 2014.

[136] G. Cavraro, T. Caldognetto, R. Carli, and P. Tenti, “A master/slave approach to power flow and overvoltage control in low-voltage microgrids,” *Energies*, vol. 12, no. 14, pp. 1–22, 2019.

[137] D. Prudhviraj, P. B. S. Kiran, and N. M. Pindoriya, “Stochastic energy management of microgrid with nodal pricing,” *Journal of Modern Power Systems and Clean Energy*, vol. 8, no. 1, pp. 102–110, 2020.

[138] U. Karki, D. Gunasekaran, and Fang Zheng Peng, “Reactive compensation of overhead ac transmission lines using underground power cables,” in *2015 IEEE Power Energy Society General Meeting*, 2015, pp. 1–5.

[139] M. Ganjian-Aboukheili, M. Shahabi, Q. Shafiee, and J. M. Guerrero, “Seamless transition of microgrids operation from grid-connected to islanded mode,” *IEEE Transactions on Smart Grid*, vol. 11, no. 3, pp. 2106–2114, 2020.

[140] M. Amin and Q. Zhong, “Resynchronization of distributed generation based on the universal droop controller for seamless transfer between operation modes,” *IEEE Transactions on Industrial Electronics*, vol. 67, no. 9, pp. 7574–7582, 2020.

[141] T. L. Vandoorn, B. Meersman, J. D. M. De Kooning, and L. Vandevelde, “Transition from islanded to grid-connected mode of microgrids with voltage-based droop control,” *IEEE Transactions on Power Systems*, vol. 28, no. 3, pp. 2545–2553, 2013.

[142] S. D’Arco and J. A. Suul, “Equivalence of virtual synchronous machines and frequency-droops for converter-based microgrids,” *IEEE Transactions on Smart Grid*, vol. 5, no. 1, pp. 394–395, 2014.

[143] M. A. Awal and I. Husain, “Unified virtual oscillator control for grid-forming and grid-following converters,” *IEEE Journal of Emerging and Selected Topics in Power Electronics*, pp. 1–1, 2020.

[144] C. Li, C. Cao, Y. Cao, Y. Kuang, L. Zeng, and B. Fang, “A review of islanding detection methods for microgrid,” *Renewable and Sustainable Energy Reviews*, vol. 35, pp. 211–220, 2014.

[145] P. Tenti, T. Caldognetto, S. Buso, and D. I. Brandao, “Control of utility interfaces in low-voltage microgrids,” *Brazilian Journal of Power Electronics (SOBRAEP)*, vol. 20, no. 4, pp. 373 – 382, 2015.

[146] J. Kwon, S. Yoon, and S. Choi, “Indirect current control for seamless transfer of three-phase utility interactive inverters,” *IEEE Transactions on Power Electronics*, vol. 27, no. 2, pp. 773–781, 2012.

[147] D. I. Brandao, “Coordinated power-based control and utility interface converter in low voltage microgrids,” Ph.D. dissertation, University of Campinas, Campinas, 9 2015.

[148] Z. Zeng, R. Zhao, and H. Yang, “Coordinated control of multi-functional grid-tied inverters using conductance and susceptance limitation,” *IET Power Electronics*, vol. 7, no. 7, pp. 1821–1831, 2014.

[149] A. H. Yazdavar, M. A. Azzouz, and E. F. El-Saadany, “A novel decentralized control scheme for enhanced nonlinear load sharing and power quality in islanded microgrids,” *IEEE Transactions on Smart Grid*, vol. 10, no. 1, pp. 29–39, 2019.

[150] F. Dorfler, J. W. S. Porco, and F. Bullo, “Breaking the hierarchy: Distributed control and economic optimality in microgrids,” *IEEE Transactions on Control of Network Systems*, vol. 3, no. 3, pp. 241–253, 2016.

[151] P. Sreekumar and V. Khadkikar, “Direct control of the inverter impedance to achieve controllable harmonic sharing in the islanded microgrid,” *IEEE Transactions on Industrial Electronics*, vol. 64, no. 1, pp. 827–837, 2017.

[152] X. Wang, Y. W. Li, F. Blaabjerg, and P. C. Loh, “Virtual-impedance-based control for voltage-source and current-source converters,” *IEEE Transactions on Power Electronics*, vol. 30, no. 12, pp. 7019–7037, 2015.

[153] F. Gothner, O. Midtgård, R. Torres-Olguin, and J. Roldan-Perez, “Virtual impedance design for power quality and harmonic sharing improvement in microgrids,” in *2019 20th Workshop on Control and Modeling for Power Electronics (COMPEL)*, 2019, pp. 1–7.

[154] A. Micallef, M. Apap, C. Spiteri-Staines, J. M. Guerrero, and J. C. Vasquez, “Reactive power sharing and voltage harmonic distortion compensation of droop controlled single phase islanded microgrids,” *IEEE Transactions on Smart Grid*, vol. 5, no. 3, pp. 1149–1158, 2014.

[155] W. Deng, N. Dai, K. W. Lao, and J. M. Guerrero, “A virtual-impedance droop control for accurate active power control and reactive power sharing using capacitive-coupling inverters,” *IEEE Transactions on Industry Applications*, vol. 56, no. 6, pp. 6722–6733, 2020.

[156] A. Adib and B. Mirafzal, “Virtual inductance for stable operation of grid-interactive voltage source inverters,” *IEEE Transactions on Industrial Electronics*, vol. 66, no. 8, pp. 6002–6011, 2019.

[157] T. E. Nunez-Zuniga and J. A. Pomilio, “Shunt active power filter synthesizing resistive loads,” *IEEE Transactions on Power Electronics*, vol. 17, no. 2, pp. 273–278, 2002.

[158] R. Hiremath and T. Moger, “Comprehensive review on low voltage ride throughcapability of wind turbine generators,” *International Transactions on Electrical Energy Systems*, vol. 30, pp. 1–39, 2020.

[159] H. Tian, F. Gao, C. Ma, G. He, and G. Li, “A review of low voltage ride-through techniques for photovoltaic generation systems,” in *2014 IEEE Energy Conversion Congress and Exposition (ECCE)*, 2014, pp. 1566–1572.

[160] N. Bottrell and T. C. Green, “Comparison of current-limiting strategies during fault ride-through of inverters to prevent latch-up and wind-up,” *IEEE Transactions on Power Electronics*, vol. 29, no. 7, pp. 3786–3797, 2014.

[161] M. S. Witherden, R. Rayudu, and R. Rigo-Mariani, “The influence of nonlinear loads on the power quality of the new zealand low voltage electrical power distribution network,” in *2010 20th Australasian Universities Power Engineering Conference*, 2010, pp. 1–6.

[162] A. T. Procopiou and L. F. Ochoa, “Voltage control in pv-rich lv networks without remote monitoring,” *IEEE Transactions on Power Systems*, vol. 32, no. 2, pp. 1224–1236, 2017.

[163] Z. Xin, P. Mattavelli, W. Yao, Y. Yang, F. Blaabjerg, and P. C. Loh, “Mitigation of grid-current distortion for lcl-filtered voltage-source inverter with inverter-current feedback control,” *IEEE Transactions on Power Electronics*, vol. 33, no. 7, pp. 6248–6261, 2018.

[164] Z. Shuai et al, “Microgrid stability: Classification and a review,” *Renewable and Sustainable Energy Reviews*, vol. 58, pp. 167–179, 2016.

[165] R. Majumder, “Some aspects of stability in microgrids,” *IEEE Transactions on Power Systems*, vol. 28, no. 3, pp. 3243–3252, 2013.

[166] E. F. Alves, G. Bergna, D. I. Brandao, and E. Tedeschi, “Sufficient conditions for robust frequency stability of ac power systems,” *IEEE Transactions on Power Systems*, pp. 1–1, 2020.

[167] A. K. Singh, R. Singh, and B. C. Pal, “Stability analysis of networked control in smart grids,” *IEEE Transactions on Smart Grid*, vol. 6, no. 1, pp. 381–390, 2015.

[168] M. N. Alam, S. Chakrabarti, and A. Ghosh, “Networked microgrids: State-of-the-art and future perspectives,” *IEEE Transactions on Industrial Informatics*, vol. 15, no. 3, pp. 1238–1250, 2019.

[169] K. Ogata, *Discrete-time Control Systems*, 2nd ed. Prentice-Hall, 1995.

[170] A. Angioni et al, “Coordinated voltage control in distribution grids with lte based communication infrastructure,” in *2015 IEEE 15th International Conference on Environment and Electrical Engineering (EEEIC)*, 2015, pp. 2090–2095.

[171] H. Han, X. Hou, J. Yang, J. Wu, M. Su, and J. M. Guerrero, “Review of power sharing control strategies for islanding operation of ac microgrids,” *IEEE Transactions on Smart Grid*, vol. 7, no. 1, pp. 200–215, 2016.

[172] T. J. Mary and P. Rangarajan, “Delay-dependent stability analysis of microgrid with constant and time-varying communication delays,” *Electric Power Components and Systems*, vol. 44, no. 13, pp. 1441–1452, 2016.

[173] K. C. Budka, J. G. Deshpande, and M. Thottan, *Communication Networks for Smart Grids*, 1st ed. Springer, 2014.

[174] B. Francis et al., "Sunspec plant information exchange: Sunspec alliance interoperability specification," Sunspec Alliance, Tech. Rep. Draft, July 2015.

[175] Z. Peng, J. Wang, D. Bi, Y. Wen, Y. Dai, X. Yin, and Z. J. Shen, "Droop control strategy incorporating coupling compensation and virtual impedance for microgrid application," *IEEE Transactions on Energy Conversion*, vol. 34, no. 1, pp. 277–291, 2019.

[176] T. L. Vandoorn, J. D. M. De Kooning, B. Meersman, J. M. Guerrero, and L. Vandevelde, "Automatic power-sharing modification of $p/\ v$ droop controllers in low-voltage resistive microgrids," *IEEE Transactions on Power Delivery*, vol. 27, no. 4, pp. 2318–2325, 2012.

[177] P. Jintakosonwit, H. Fujita, H. Akagi, and S. Ogasawara, "Implementation and performance of cooperative control of shunt active filters for harmonic damping throughout a power distribution system," *IEEE Transactions on Industry Applications*, vol. 39, no. 2, pp. 556–564, 2003.

[178] S. A. R. Konakalla, A. Valibeygi, and R. A. de Callafon, "Microgrid dynamic modeling and islanding control with synchrophasor data," *IEEE Transactions on Smart Grid*, vol. 11, no. 1, pp. 905–915, 2020.

[179] M. S. Golsorkhi, D. D. Lu, and J. M. Guerrero, "A gps-based decentralized control method for islanded microgrids," *IEEE Transactions on Power Electronics*, vol. 32, no. 2, pp. 1615–1625, 2017.

[180] G. Yang, K. E. Martin, and J. Østergaard, "Investigation of pmu performance under tve criterion," in *2010 5th International Conference on Critical Infrastructure (CRIS)*, 2010, pp. 1–7.

[181] O. B. Fosso, M. Molinas, K. Sand, and G. H. Coldevin, "Moving towards the smart grid: The norwegian case," in *2014 International Power Electronics Conference (IPEC-Hiroshima 2014 - ECCE ASIA)*, 2014, pp. 1861–1867.

[182] F. Yang, X. Feng, and Z. Li, "Advanced microgrid energy management system for future sustainable and resilient power grid," *IEEE Transactions on Industry Applications*, vol. 55, no. 6, pp. 7251–7260, 2019.

[183] J. He, B. Liang, Y. W. Li, and C. Wang, "Simultaneous microgrid voltage and current harmonics compensation using coordinated control of dual-interfacing converters," *IEEE Transactions on Power Electronics*, vol. 32, no. 4, pp. 2647–2660, 2017.

[184] H. Pezeshki, P. J. Wolfs, and G. Ledwich, “Impact of high pv penetration on distribution transformer insulation life,” *IEEE Transactions on Power Delivery*, vol. 29, no. 3, pp. 1212–1220, 2014.

[185] D. J. Hogan, F. J. Gonzalez-Espin, J. G. Hayes, G. Lightbody, and R. Foley, “An adaptive digital-control scheme for improved active power filtering under distorted grid conditions,” *IEEE Transactions on Industrial Electronics*, vol. 65, no. 2, pp. 988–999, 2018.

[186] A. Arguello, R. Torquato, W. Freitas, and A. Padilha Feltrin, “A graphical method to assess component overload due to harmonic resonances in wind parks,” *IEEE Transactions on Power Delivery*, pp. 1–1, 2020.

[187] S. Devassy and B. Singh, “Performance analysis of solar pv array and battery integrated unified power quality conditioner for microgrid systems,” *IEEE Transactions on Industrial Electronics*, pp. 1–1, 2020.

[188] Y. Chen, J. M. Guerrero, Z. Shuai, Z. Chen, L. Zhou, and A. Luo, “Fast reactive power sharing, circulating current and resonance suppression for parallel inverters using resistive-capacitive output impedance,” *IEEE Transactions on Power Electronics*, vol. 31, no. 8, pp. 5524–5537, 2016.

[189] M. Depenbrock, “The fbd-method, a generally applicable tool for analyzing power relations,” *IEEE Transactions on Power Systems*, vol. 8, no. 2, pp. 381–387, 1993.

[190] L. S. Czarnecki, “What is wrong with the Budeanu concept of reactive and distortion power and why it should be abandoned,” *IEEE Transactions on Instrumentation and Measurement*, vol. 36, no. 3, pp. 834–837, 1987.

[191] S. Fryze, “Active, reactive and apparent power in circuits with nonsinusoidal voltage and current,” *Przegl. Elektrotech*, vol. 7, pp. 193–203, 1931.

[192] J. H. Braslavsky, L. D. Collins, and J. K. Ward, “Voltage stability in a grid-connected inverter with automatic volt-watt and volt-var functions,” *IEEE Transactions on Smart Grid*, vol. 10, no. 1, pp. 84–94, 2019.

[193] A. Anzalchi, A. Sundararajan, A. Moghadasi, and A. Sarwat, “High-penetration grid-tied photovoltaics: Analysis of power quality and feeder voltage profile,” *IEEE Industry Applications Magazine*, vol. 25, no. 5, pp. 83–94, 2019.

[194] A. Hoke, J. Giraldez, B. Palmintier, E. Ifuku, M. Asano, R. Ueda, and M. Symko-Davies, “Setting the smart solar standard: Collaborations between hawaiian electric and the national renewable energy laboratory,” *IEEE Power and Energy Magazine*, vol. 16, no. 6, pp. 18–29, 2018.

[195] S. H. Toghroljerdi and J. Ostergaard, “Prevention of distribution network overvoltage by adaptive droop-based active and reactive power control of pv systems,” *Electric Power Systems Research*, vol. 113, pp. 313–327, 2016.

[196] S. Pukhrem, M. Basu, M. F. Conlon, and K. Sunderland, “Enhanced network voltage management techniques under the proliferation of rooftop solar pv installation in low-voltage distribution network,” *IEEE Journal of Emerging and Selected Topics in Power Electronics*, vol. 5, no. 2, pp. 681–694, 2017.

[197] K. Baker, A. Bernstein, E. Dall’Anese, and C. Zhao, “Network-cognizant voltage droop control for distribution grids,” *IEEE Transactions on Power Systems*, vol. 33, no. 2, pp. 2098–2108, 2018.

[198] M. Juamperez, G. Yang, and S. B. Kjær, “Voltage regulation in lv grids by coordinated volt-var control strategies,” *Journal of Modern Power Systems and Clean Energy*, vol. 2, no. 4, pp. 319–328, 2014.

[199] T. T. Mai, n. Haque, H. T. Vo, and P. H. Nguyen, “Methods and strategies for overvoltage prevention in low voltage distribution systems with pv,” *IET Renewable Power Generation*, vol. 2019, no. 18, pp. 5007–5011, 2019.

[200] G. Cavraro, T. Caldognetto, R. Carli, and P. Tenti, “A master/slave approach to power flow and overvoltage control in low-voltage microgrids,” *Energies*, vol. 12, p. 2760, 2019.

[201] Y. Wang, P. Zhang, W. Li, W. Xiao, and A. Abdollahi, “Online overvoltage prevention control of photovoltaic generators in microgrids,” *IEEE Transactions on Smart Grid*, vol. 3, no. 4, pp. 2071–2078, 2012.

[202] H. Lee, K. Yoon, J. Shin, J. Kim, and S. Cho, “Optimal parameters of volt–var function in smart inverters for improving system performance,” *Energies*, vol. 13, p. 2294, 2020.

[203] Y. Yang, H. Wang, and F. Blaabjerg, “Reactive power injection strategies for single-phase photovoltaic systems considering grid requirements,” *IEEE Transactions on Industry Applications*, vol. 50, no. 6, pp. 4065–4076, 2014.

[204] L. De Oro Arenas, G. d. A. e Melo, and C. A. Canesin, “A methodology for power quantities calculation applied to an FPGA-based smart-energy meter,” *IEEE Transactions on Instrumentation and Measurement*, vol. 70, pp. 1–11, 2021.

[205] S. Alyami, Y. Wang, C. Wang, J. Zhao, and B. Zhao, “Adaptive real power capping method for fair overvoltage regulation of distribution networks with high penetration of pv systems,” *IEEE Transactions on Smart Grid*, vol. 5, no. 6, pp. 2729–2738, 2014.

[206] F. H. M. Rafi, M. J. Hossain, M. S. Rahman, and S. Taghizadeh, “An overview of unbalance compensation techniques using power electronic converters for active distribution systems with renewable generation,” *Renewable and Sustainable Energy Reviews*, vol. 125, p. 109812, 2020.

[207] A. S. Vijay, S. Doolla, and M. C. Chandorkar, “Unbalance mitigation strategies in microgrids,” *IET Power Electronics*, vol. 13, no. 9, pp. 1687–1710, 2020.

[208] D. V. Bozalakov, J. Laveyne, J. Desmet, and L. Vandelvelde, “Overvoltage and voltage unbalance mitigation in areas with high penetration of renewable energy resources by using the modified three-phase damping control strategy,” *Electric Power Systems Research*, vol. 168, pp. 283–294, 2019.

[209] M. Savaghebi, A. Jalilian, J. C. Vasquez, and J. M. Guerrero, “Autonomous voltage unbalance compensation in an islanded droop-controlled microgrid,” *IEEE Transactions on Industrial Electronics*, vol. 60, no. 4, pp. 1390–1402, 2013.

[210] J. Liu, Y. Miura, and T. Ise, “Cost-function-based microgrid decentralized control of unbalance and harmonics for simultaneous bus voltage compensation and current sharing,” *IEEE Transactions on Power Electronics*, vol. 34, no. 8, pp. 7397–7410, 2019.

[211] E. Espina, R. Cárdenas-Dobson, M. Espinoza-B., C. Burgos-Mellado, and D. Sáez, “Cooperative regulation of imbalances in three-phase four-wire microgrids using single-phase droop control and secondary control algorithms,” *IEEE Transactions on Power Electronics*, vol. 35, no. 2, pp. 1978–1992, 2020.

[212] Z. Hou, Y. Sun, W. Yuan, H. Han, C. Hong, and J. M. Guerrero, “Conventional p-ω/q-v droop control in highly resistive line of low-voltage converter-based ac microgrid,” *Energies*, vol. 9, p. 943, 2016.

[213] C. Burgos-Mellado, R. Cárdenas, D. Sáez, A. Costabeber, and M. Sumner, “A control algorithm based on the conservative power theory for cooperative sharing of imbalances in four-wire systems,” *IEEE Transactions on Power Electronics*, vol. 34, no. 6, pp. 5325–5339, 2019.

[214] T. D. C. Busarello, A. Mortezaei, A. Péres, and M. G. Simões, “Application of the conservative power theory current decomposition in a load power-sharing strategy among distributed energy resources,” *IEEE Transactions on Industry Applications*, vol. 54, no. 4, pp. 3771–3781, 2018.

[215] F. P. Marafao, D. I. Brandao, F. A. S. Gonçalves, and H. K. M. Paredes, “Decoupled reference generator for shunt active filters using the conservative power

theory," *Journal of Control, Automation and Electrical Systems*, vol. 24, p. 522–534, 2013.

[216] D. I. Brandao, H. Guillardi, H. K. Morales-Paredes, F. P. Marafão, and J. A. Pomilio, "Optimized compensation of unwanted current terms by ac power converters under generic voltage conditions," *IEEE Transactions on Industrial Electronics*, vol. 63, no. 12, pp. 7743–7753, 2016.

[217] A. M. S. Alonso, B. R. Pereira Jr., D. I. Brandao, and F. P. Marafao, "Optimized exploitation of ancillary services: Compensation of reactive, unbalance and harmonic currents based on particle swarm optimization," *IEEE Latin America Transactions*, vol. 100, no. 1, pp. 1–12, 2020.

[218] T. C. Monteiro et al, "Dynamic voltage restorer development and testing," in *XI Brazilian Power Electronics Conference*, 2011, pp. 1–1.

[219] G. Carpinelli, F. Mottola, D. Proto, and A. Russo, "A multi-objective approach for microgrid scheduling," *IEEE Transactions on Smart Grid*, vol. 8, no. 5, pp. 2109–2118, 2017.

[220] M. N. Costa, F. Gonzalez-Longatt, D. Topic, and M. A. Andrade, "Optimal microgrid–interactive reactive power management for day–ahead operation," *Energies*, vol. 14, p. 1275, 2021.

[221] A. H. Fathima and K. Palanisamy, "Optimization in microgrids with hybrid energy systems – a review," *Renewable and Sustainable Energy Reviews*, vol. 45, pp. 431–446, 2015.

[222] A. A. Anderson and S. Suryanarayanan, "Review of energy management and planning of islanded microgrids," *CSEE Journal of Power and Energy Systems*, vol. 6, no. 2, pp. 329–343, 2020.

[223] B. Khan and P. Singh, "Selecting a meta-heuristic technique for smart microgrid optimization problem: A comprehensive analysis," *IEEE Access*, vol. 5, pp. 13 951–13 977, 2017.

[224] L. I. Avila, L. E. Castanon, A. V. Martinez, and Y. Zhang, "A review of optimal control techniques applied to the energy management and control of microgrids," *Procedia Computer Science*, vol. 52, pp. 780–787, 2015.

[225] J. Alshehri and M. Khalid, "Power quality improvement in microgrids under critical disturbances using an intelligent decoupled control strategy based on battery energy storage system," *IEEE Access*, vol. 7, pp. 147 314–147 326, 2019.

[226] D. M. Ferreira, D. I. Brandao, G. Bergna-Diaz, E. Tedeschi, and S. M. Silva, "Distributed control strategy for low-voltage three-phase four-wire microgrids: Consensus power-based control," *IEEE Transactions on Smart Grid*, pp. 1–1, 2021.

[227] P. Tenti and P. Mattavelli, "A time domain approach to power term definitions under non sinusoidal conditions," *L'Energia Elettrica*, vol. 81, 2004.

[228] D. De Roover and O. H. Bosgra, "An internal-model-based framework for the analysis and design of repetitive and learning controllers," in *Proceedings of the 36th IEEE Conference on Decision and Control*, vol. 4, 1997, pp. 3765–3770 vol.4.

Appendix A

A.1 The Conservative Power Theory: Current Decomposition and Power Terms

The Conservative Power Theory (CPT) is a time-domain power theory applicable to single- or poly-phase electric systems with periodic quantities, being suitable for analyzing circuits under sinusoidal or non-sinusoidal conditions, as well as under symmetrical or asymmetrical voltage scenarios. Current and power components are decoupled based upon the conservativeness of the active and reactive power terms.

The CPT's definition of power terms and corresponding decomposed current parcels is thoroughly discussed in [45] and [227]. The most important definitions taken into account within this thesis are as follows.

Considering instantaneous phase voltages (v_m) and currents (i_m), the active power (*P*) defined by the CPT in a three-phase circuit is given by Eq. A.1, where *T* is the period of these signals.

$$P = \frac{1}{T} \cdot \sum_{m=a,b,c} \int_0^T v_m \cdot i_m \cdot dt \tag{A.1}$$

$$P = \frac{1}{T} \cdot \int_0^T \left(v_a \cdot i_a + v_b \cdot i_b + v_c \cdot i_c \right) dt \tag{A.2}$$

The reactive power (*Q*) is similarly defined, being given by Eq. A.3, where $\hat{v}_m$ is the unbiased-time integral of voltage. Such a term $\hat{v}_m$ is calculated by obtaining the integral of v_m and removing its mean value, as given by Eq. A.5, in which ω_o is the fundamental angular frequency.

$$Q = \frac{\omega_o}{T} \cdot \sum_{m=a,b,c} \int_0^T \hat{v}_m \cdot i_m \cdot dt \tag{A.3}$$

$$Q = \frac{\omega_o}{T} \cdot \int_0^T \left(\hat{v}_a \cdot i_a + \hat{v}_b \cdot i_b + \hat{v}_c \cdot i_c \right) dt \tag{A.4}$$

$$\hat{v}_m = \int_0^t v_m \cdot d\tau - \frac{1}{T} \cdot \int_0^T v_m \cdot dt \tag{A.5}$$

In possession of *P* and *Q*, the CPT decomposes the *m*-phase currents into orthogonal terms, characterizing both balanced and unbalanced features. Moreover, a remaining component (namely, void), which stands for non-linearities in currents is also defined. Considering the subscripts *a*, *r*, and *v*, respectively, for the active, reactive and void terms, and the superscripts *b* and *u* for the balanced and unbalanced features of such parcels, the instantaneous current decomposition of the CPT is given by Eq. A.6. Note that Eq. A.6 allows us to obtain the void current of each *m*-phase, as in Eq. A.7.

$$i_m = i_{a_m} + i_{r_m} + i_{v_m} = i^b_{a_m} + i^b_{r_m} + i^u_{a_m} + i^u_{r_m} + i_{v_m} \tag{A.6}$$

$$i_{v_m} = i_m - \left(i^b_{a_m} + i^b_{r_m} + i^u_{a_m} + i^u_{r_m} \right) \tag{A.7}$$

By using the collective value (V_{col}) of the RMS voltages, which is given by the Euclidian norm [45] in Eq. A.8, along with *P*, the balanced active currents are calculated according to Eq. A.10. Analogously, by calculating the collective value ($\hat{V}_{col}$) of the RMS unbiased voltages with Eq. A.9, and using *Q*, the balanced reactive currents are given by Eq. A.11. Under these definitions, the unbalanced active currents characterize the difference between the phase conductance and the equivalent conductance as seen in Eq. A.12, where V_{RMS_m} and P_m are, respectively, the RMS *m*-phase voltage and active power. Similarly, the unbalanced reactive currents can be obtained by Eq. A.13.

$$V_{col} = \sqrt{V^2_{RMS_a} + V^2_{RMS_b} + V^2_{RMS_c}} \tag{A.8}$$

$$\hat{V}_{col} = \sqrt{\hat{V}^2_{RMS_a} + \hat{V}^2_{RMS_b} + \hat{V}^2_{RMS_c}} \tag{A.9}$$

$$i^b_{a_m} = \frac{P}{V^2_{col}} \cdot v_m \tag{A.10}$$

$$i^b_{r_m} = \frac{Q}{\omega_o \cdot \hat{V}^2_{col}} \cdot \hat{v}_m \tag{A.11}$$

$$i^u_{a_m} = \left(\frac{P_m}{V^2_{RMS_m}} - \frac{P}{V^2_{col}} \right) \cdot v_m \tag{A.12}$$

$$i^u_{r_m} = \left(\frac{Q_m}{\omega_o \cdot \hat{V}^2_{RMS_m}} - \frac{Q}{\omega_o \cdot \hat{V}^2_{col}} \right) \cdot \hat{v}_m \tag{A.13}$$

Lastly, the collective current (I_{col}) can be calculated based on the collective values of all the CPT's current parcels, as shown in Eq. A.14, due to the orthogonality existing among them. In addition, the unbalanced currents can be integrated into one current parcel (I^u_{col}), since $(I^u_{col})^2 = (I^u_{a_{col}})^2 + (I^u_{r_{col}})^2$.

$$I^2_{col} = (I^b_{a_{col}})^2 + (I^b_{r_{col}})^2 + (I^u_{col})^2 + (I_{v_{col}})^2 \tag{A.14}$$

The CPT also defines power terms that quantify the active, reactive, unbalance and distortion quantities, being respectively termed as *P*, *Q*, *N*, and *D*. The terms *N* and *D* are given by Eqs. A.15 and A.16, respectively, and the apparent power (*A*) can also be calculated according to Eq. A.17.

$$N = V_{col} \cdot \sqrt{(I^u_{a_{col}})^2 + (I^u_{r_{col}})^2} = V_{col} \cdot I^u_{col} \tag{A.15}$$

$$D = V_{col} \cdot I_{v_{col}} \tag{A.16}$$

$$A^2 = V^2_{col} \cdot I^2_{col} = P^2 + Q^2 + N^2 + D^2 \tag{A.17}$$

Appendix B

B.1 Complementary Information about the Main Simulation Testbench

B.1.1 Pictures of the MG Implemented in MATLAB/Simulink

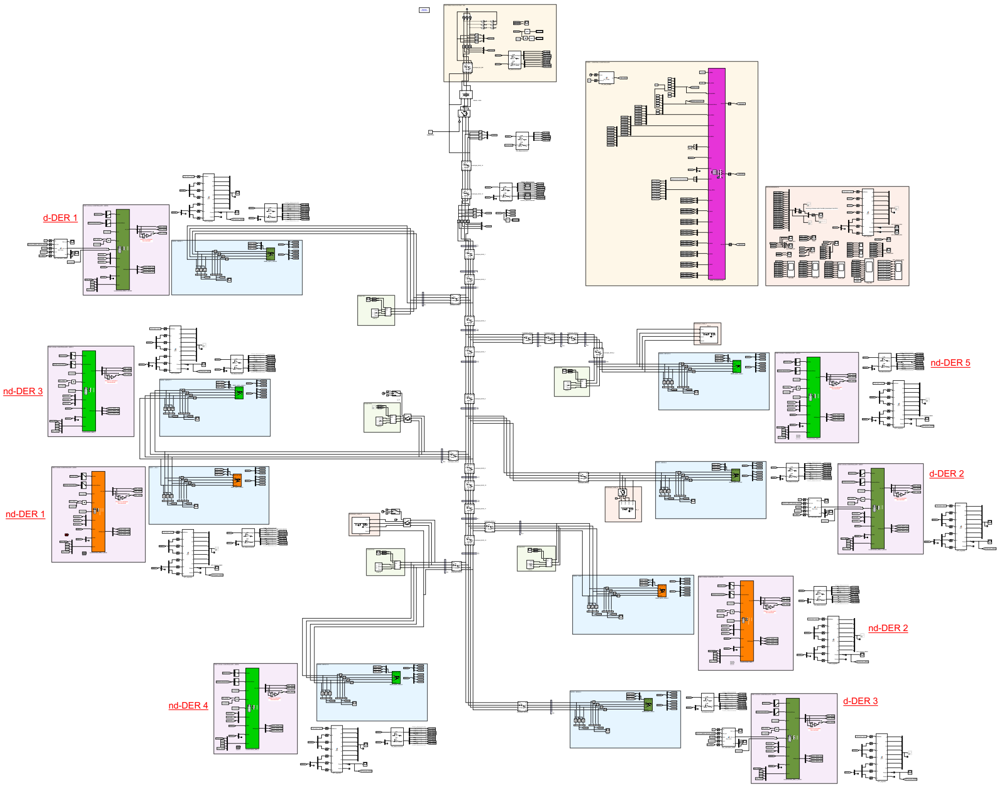

Figure B.1: Overall layout of the main MG testbench used for simulation results.

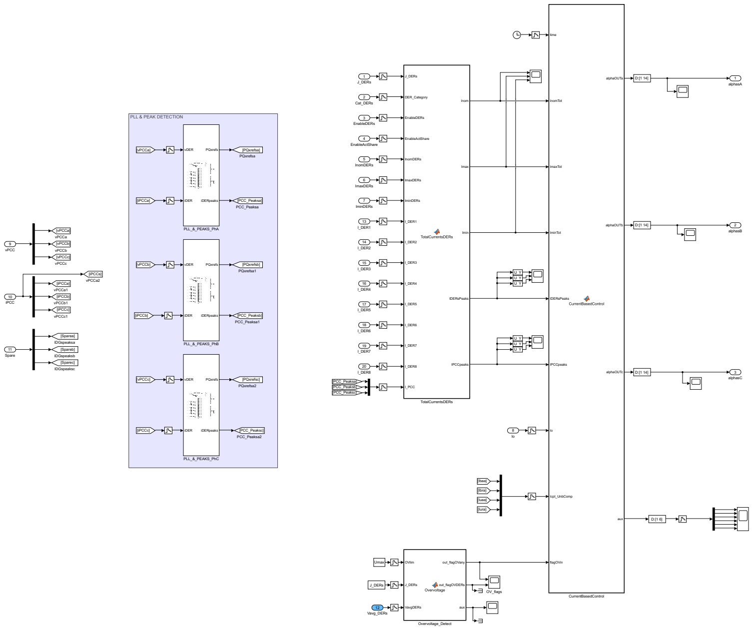

Figure B.2: Layout of the MGCC implemented for simulation results.

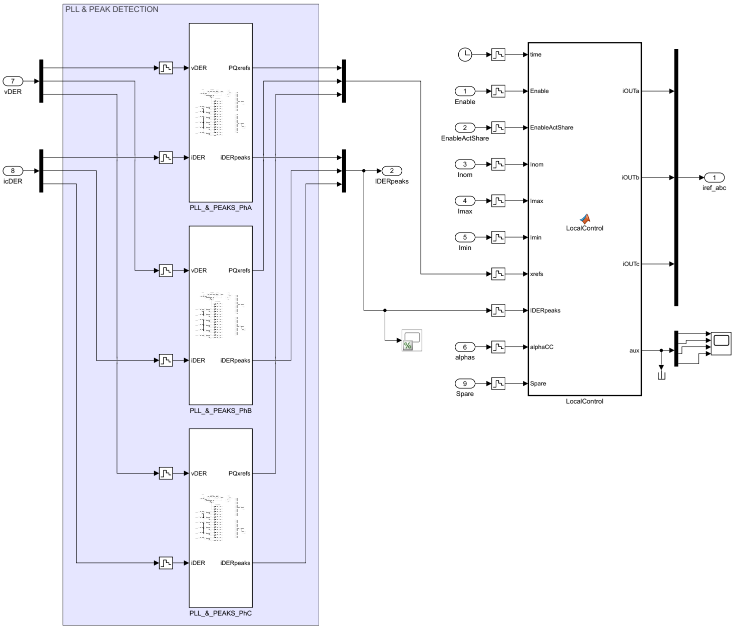

Figure B.3: Local control layer of an d-DER implemented for simulation results.

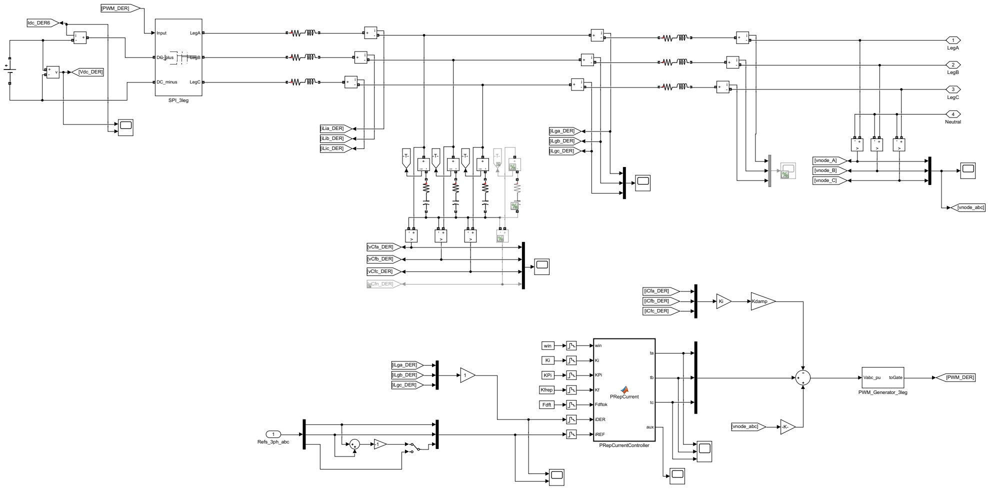

Figure B.4: Topology of an d-DER and its control loops implemented for simulation results.

B.1.2 Line Impedance Parameters

The line impedance parameters adopted for the simulation results, based on the main MG testbench of Fig. 3.1, is presented in Table B.1.

Table B.1: Line impedance parameters for the MG testbench in Fig. 3.1.

Node from	Node to	R [Ω/km]	X [Ω/km]	$R_{neutral}$ [Ω/km]	$X_{neutral}$ [Ω/km]	Length [m]
B1	*B2*	0.163	0.136	0.490	0.471	35
B2	*B3*	0.163	0.136	0.490	0.471	35
B3	*B4*	0.163	0.136	0.490	0.471	35
B4	*B5*	0.163	0.136	0.490	0.471	35
B5	*B6*	0.163	0.136	0.490	0.471	35
B6	*B7*	0.163	0.136	0.490	0.471	35
B7	*B8*	0.163	0.136	0.490	0.471	35
B8	*B9*	0.163	0.136	0.490	0.471	35
B9	*B10*	0.163	0.136	0.490	0.471	35
B3	*B11*	1.541	0.206	2.334	1.454	30
B4	*B12*	0.266	0.151	0.733	0.570	35
B12	*B13*	0.266	0.151	0.733	0.570	35
B13	*B14*	0.266	0.151	0.733	0.570	35
B14	*B15*	0.326	0.158	0.860	0.630	30
B6	*B16*	0.569	0.174	1.285	0.865	30
B9	*B17*	1.541	0.206	2.334	1.454	30
B10	*B18*	1.111	0.195	1.926	1.265	30

B.1.3 Design of the PRep Current Controllers

The modeling of the proportional plus repetitive current regulators used for the control of the inverters during simulations is summarily presented. Such an approach is based on [103] and it provides the design of current controllers that track time-domain references with zero steady state error. Moreover, such PRep controller is formulated based on the internal model principle [228], and its block diagram is presented in Fig. B.5.

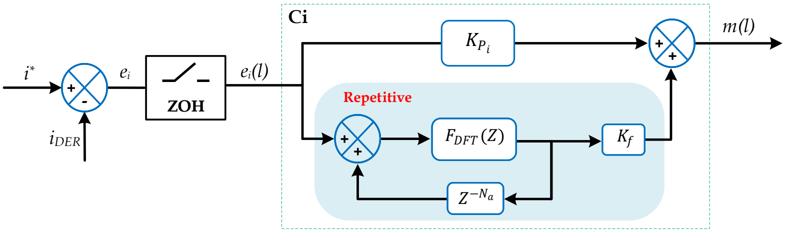

Figure B.5: Block diagram of the proportional repetitive (PRep) controller.

One can note that the controller (C_i) relies on two independent regulators; which are one proportional controller (K_{P_i}), and one repetitive controller. The first can be designed similarly to any other classic PI controller [102]. For instance, given an open loop transfer function of a DER in s-domain ($G_{OL}(s)$), and the transfer of a PI controller ($G_{PI}(s)$), one can obtain the proportional gain by calculating Eq. B.1, knowing that K_{I_i} is the integral gain.

$$\mid G_{PI}(s) \cdot G_{OL}(s) \mid = \mid \left(K_{P_i} + \frac{K_{I_i}}{s} \right) \cdot G_{OL}(s) \mid = 1 \tag{B.1}$$

The repetitive controller, on the other hand, relies on the idea of summing up the error reference ($e_i(l)$) at the l^{th} sampling interruption, with its delayed samples (e.g., $e(l-1)$). Consequently, note that a discrete implementation needs to be considered, as represented by the zero-order-holder (ZOH) in Fig. B.5. A DFT-based implementation of band-pass filters is implemented for this repetitive procedure, being designed based on a Z-domain cosine transform, which is given by Eq. B.2.

$$F_{DFT}(Z) = \frac{2}{N} \cdot \sum_{i=0}^{N-1} \left(\sum_{h \in N_h} \cos \left[\frac{2\pi \cdot h \cdot (i + N_a)}{N} \right] \right) \cdot Z^{-1} \tag{B.2}$$

In Eq. B.2, N stands for the filter window (i.e., number of samples in one cycle of the fundamental frequency), and N_h represents the set of selected harmonics processed by the band-pass filters. In addition, the variable N_a is the number of delay steps of the PRep controller, being usually chosen to be between one and three sampling periods [103]. Finally, the gain K_f relates to the integral gain of PI controllers, affecting the transient response and steady state performance of the repetitive regulator. K_f can be calculated by Eq. B.3, in which $n_{oh} \cdot T_o$ is the desired transient response time of the controller, and w_s is the angular frequency of highest harmonic order of the filter.

$$K_f = \frac{2.2}{0.32 \cdot n_{oh} \cdot T_o \cdot w_s} \tag{B.3}$$

B.1.4 Parameters of the Utility Interface Converter

The UI adopted to operate as a grid-interactive converter in Section 4.4.1 has its control modeling and design thoroughly explained in [145] and [147]. However, to provide an overview of its operation, its equivalent single-phase circuit and the simplified block diagram of its triple loop controller is presented in Fig. B.6.

The UI is a voltage-controlled converter, and its triple loop control relies on: *i)* a fast inner current loop, which offers improved dynamic response (i.e., when compared to classic VCM converters [11]), being usually designed with PRes, PRep, deadbeat, or hysteresis controllers [99]; *ii)* an output voltage loop, which allows us to regulate the voltage at the output capacitor of the UI, usually incorporating PRes or PI controllers [99]; and *iii)* a slow outer current loop ($Z_{i_{Grid}}$), offering precise control over the grid current (i.e., active and reactive power setpoints can also be translated into current references for this loop [71]).

During simulations, the UI was emulated by a three-phase ideal current source,

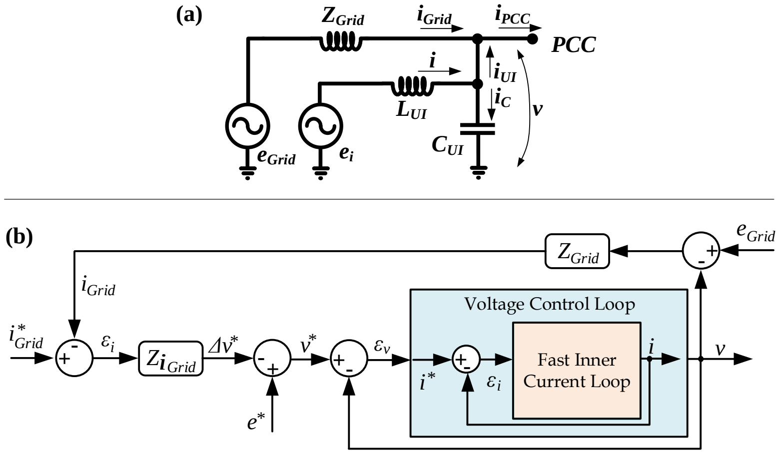

Figure B.6: (a) Equivalent single-phase representation of the UI; and (b) Simplified block diagram of the triple loop control of the UI.

comprising parallel RC output filters with per-phase parameters equal to $C_{UI} = 470\mu F$ and $R_{UI} = 0.003\Omega$. A PI controller was used for the UI's grid current loop, and a PRes + integral (PIRes) controller [102], designed similarly to the explained in Appendix C.1.2, was adopted for the voltage control loop. This resonant voltage controller was tuned to the fundamental, additionally to the following harmonic orders: 2nd, 3rd, 4th, 5th, 7th, 9th and 11th. The gains of the controllers are shown in Table B.2, considering current and voltage sensor gains of 1/350 [1/A] and 1/400 [1/V], respectively.

Table B.2: Controller gain parameters of the UI.

PI (Grid Current Loop)		
Proportional Gain		0.006
Integral Gain		0.006
PIRes (Voltage Loop)		
Proportional Gain		8
Integral Gain		0.15
	a_h	b_h
$h = 1$	0.0015	1.999412
$h = 2$	0.0015	1.998672
$h = 3$	0.0015	1.997439
$h = 4$	0.0015	1.995715
$h = 5$	0.0005	1.993501
$h = 7$	0.0005	1.987608
$h = 9$	0.001	1.979777
$h = 11$	0.0005	1.970032

Appendix C

C.1 Complementary Information about the Main MG Prototype

C.1.1 Circuit Layout and Digital Control Implementation

The single-phase MG prototype assembled as the main testbench for experiments, which is seen in Fig. 4.3, has a more detailed presentation of its circuit in Fig. C.1. Note that more details are provided about how the physical infrastructure of the DERs* was implemented. All the three DERs* were built using power switches from SEMIKRON®, based on a full-bridge topology (i.e., two-level inverter). Moreover, d-DERs* were assembled with SKM 75GB128D IGBT modules and SKHI 23/12 gate drivers, whereas the nd-DER* used SEMiX 403GB128Ds IGBT modules and Skyper 32PRO gate drivers. The maximum switching frequency allowed for these IGBT modules was 20 kHz, with V_{CES} equal to 1200 V.

The digital voltage meter used was the one presented in [204], and it can be used to datalog electrical quantities at different nodes of the MG. Additionally, this smart

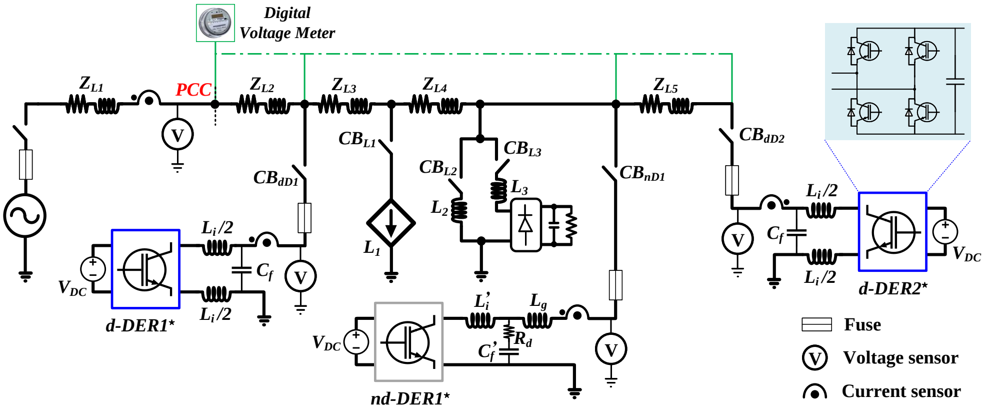

Figure C.1: Detailed implementation of single-phase MG prototype as the main setup for experimental results in this thesis.

meter is capable of processing a range of power theories, although this feature was not used. With regard to the implementation of control algorithms, a detailed scheme is presented in Fig. C.2. This figure summarizes the digital control logic embedded to one of the F28335 DSPs, being responsible for managing the operation of d-DER$_1^\star$ and d-DER$_2^\star$ in the MG. For the other control station, which was responsible for controlling nd-DER$_1^\star$, a similar approach to Fig. C.2 was implemented, although the GCBC was not considered since this inverter operated only based on local goals.

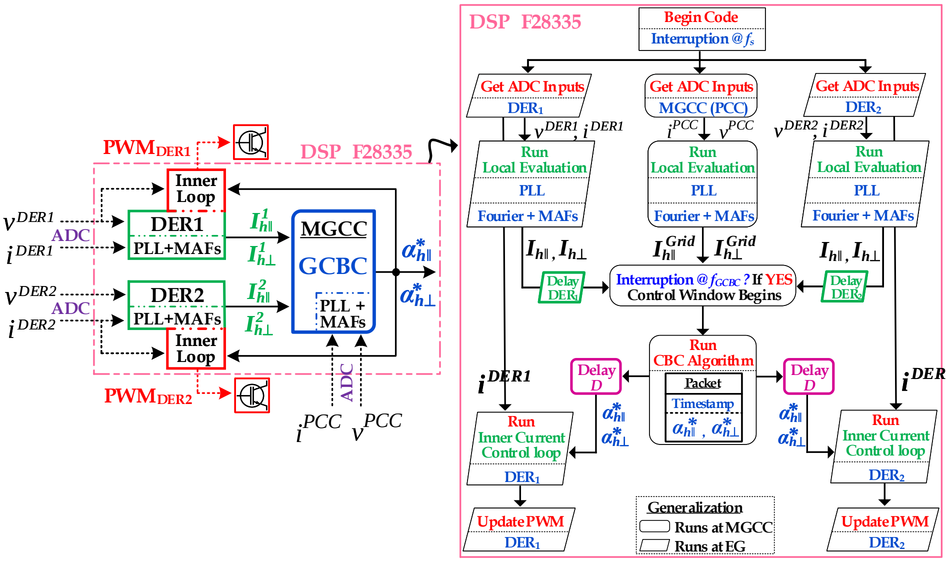

Figure C.2: Control logic implemented on the F28335 DSP.

C.1.2 Design of the PRes Current Controllers

The proportional plus resonant current controllers implemented for the single-phase MG setup are based on the design found in [102]. Similarly to the PRep controllers, PRes regulators are interesting because they are able to track periodic references with zero steady state error. Moreover, in general, they present a lower computational burden that PRep controllers, although they need to be tuned for each harmonic frequency to be tracked. The block diagram of this PRes controller is presented in Fig. C.3.

It can be noted that this regulator is also composed of two main elements, which are the proportional controller (K_{P_i}) and the resonant controller. The former can be designed as explained for the PRep controller, being calculated according to Eq. B.1. On the other hand, the resonant controller is composed of a set of resonant filters tuned at certain frequencies "h" of interest. As demonstrated in [102], the s-domain idealized representation of this PR controller can be realized by Eq. C.1, in which H stands for

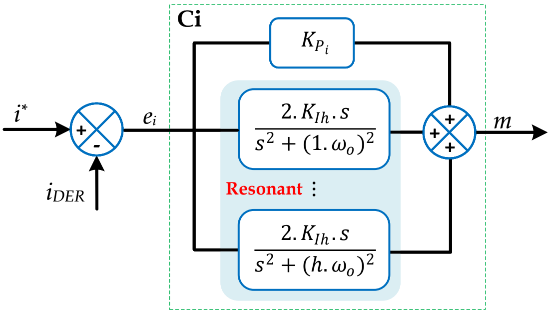

Figure C.3: Block diagram of the proportional resonant (PRes) controller.

the highest harmonic order of interest.

$$G_{PRes}(s) = K_{P_i} + \sum_{h}^{H} \frac{2 \cdot K_{I_h} \cdot s}{s^2 + (h \cdot w_o)^2} \tag{C.1}$$

The variable K_{I_h} represents the integral gain adopted for each of the resonant filters, and it can be calculated according to Eq. C.2 [102]. Besides, the term $n_{oh} \cdot T_o$ is again defined as the desired transient response of the controller, knowing that w_o and T_o are the angular frequency and time period of the fundamental frequency.

$$K_{I_h} = \frac{2.2 \cdot K_{P_i}}{n_{oh} \cdot T_o} \tag{C.2}$$

One important aspect about this PRes controller is that it needs to be discretized, in order to be implemented in applications of digital control. Consequently, the Tustin's discretization method based on a bilinear transformation [124] can be used, allowing us to obtain Eq. C.3, which represents the output of the PRes regulator (m). The coefficients a_h and b_h of this discretized implementation of the PRes controller can be calculated by Eqs C.4 and C.5, in which T_s is the sampling period.

$$m(Z^{-1}) = a_h \cdot e_i(Z^{-1}) - a_h \cdot e_i(Z^{-1}) \cdot Z^{-2} + b_h \cdot m(Z^{-1}) \cdot Z^{-1} - m(Z^{-1}) + K_{P_i} \cdot e_i(Z^{-1}) \tag{C.3}$$

$$a_h = \frac{2 \cdot K_{I_h} \cdot T_s}{4 + (h \cdot w_o)^2 \cdot T_s^2} \tag{C.4}$$

$$b_h = \frac{-8 + 2 \cdot (h \cdot w_o)^2 \cdot T_s^2}{4 + (h \cdot w_o)^2 \cdot T_s^2} \tag{C.5}$$

ISBN 978-82-326-6603-4 (printed ver.)
ISBN 978-82-326-5663-9 (electronic ver.)
ISSN 1503-8181 (printed ver.)
ISSN 2703-8084 (online ver.)

NTNU
Norwegian University of
Science and Technology